Triple Oxygen Isotopes of Cherts : Implications for the δ¹⁸O and Temperatures of Early Oceans

Dissertation

zur Erlangung des mathematisch-naturwissenschaftlichen Doktorgrades
"Doctor rerum naturalium"
der Georg-August-Universität Göttingen

im Promotionsprogramm Geowissenschaften / Geographie
der Georg-August University School of Science (GAUSS)

vorgelegt von

Sukanya Sengupta

aus Kalkutta, Indien

Göttingen 2016

Betreuungsausschuss:

     Prof. Dr. Andreas Pack, Abteilung Isotopengeologie, Geowissenschaftliches Zentrum,
     Georg August Universität Göttingen

     Prof. Dr. Jochen Hoefs, Geowissenschaftliches Zentrum,
     Georg August Universität Göttingen

Mitglieder der Prüfungskommission

     Referent:
     Prof. Dr. Andreas Pack, Abteilung Isotopengeologie, Geowissenschaftliches Zentrum, Georg August Universität Göttingen

     Korreferent:
     Prof. Dr. Jochen Hoefs, Geowissenschaftliches Zentrum, Georg August Universität Göttingen

weitere Mitglieder der Prüfungskommission:

- Prof. Dr. Joachim Reitner, Abteilung Geobiologie, Geowissenschaftliches Zentrum, Georg August Universität Göttingen
- Prof. Dr. Volker Thiel, Abteilung Geobiologie, Geowissenschaftliches Zentrum, Georg August Universität Göttingen
- Prof. Dr. Alexander Knohl, Abteilung Bioklimatologie, Georg August Universität Göttingen
- Prof. Dr. Zachary D. Sharp, Department of Earth and Planetary Sciences, University of New Mexico
- Dr. Daniel Herwartz, Institut für Geologie und Mineralogie, Universität zu Köln

Tag der mündlichen Prüfung: 07.07.2016

Name: Sukanya Sengupta
Anschrift: Robert Koch Str. 38 (Zr.Nr. 21) 37075 Göttingen

Mail: sukanya.sengupta@geo.uni-goettingen.de
Tel. Nr.: +4917630648530

An das Dekanat
der Fakultät für Geowissenschaften und Geographie
Goldschmidtstrasse 3
37077 Göttingen

                                            Göttingen, den 07.06.2016

Acknowledgments

I would first like to extend my gratitude and thanks to my supervisor Prof. Dr. Andreas Pack for providing me with this exciting research topic and his continuous support during my time as a PhD student. I thoroughly enjoyed working together with him and learning something new at every step. His scientific bend of mind and encouragement helped me immensely throughout the duration of my PhD. I also thank his family for making me feel at home in Germany.

I thank Prof. Dr. Jochen Hoefs for being my co-supervisor and for his useful insights on various topics regarding the thesis.

I would like to thank Prof. Zachary D. Sharp for highly motivating me and guiding me while working together in our laboratory.

I would like to thank wholeheartedly Daniel Herwartz and Tommaso Di Rocco, my very first colleagues in Germany, who introduced me to the university, the laboratory and assisted me at every step.

I thank Magdalena Hofmann, Jan Peter Duda, Stefan Peters for their advice and suggestions whenever I approached them.

I thank Reinhold Przybilla, Ingrid Reuber, Dennis Kohl and Axel Dierschke for their technical support in the laboratory.

I also thank our Masters students, especially Maximilian Troche who underwent long days of running experiments in the lab, along with me for many months.

I am thankful to the German Academic Exchange Service (DAAD) for awarding me the scholarship that gave me the opportunity to work in a modern laboratory far away from my country and stay in Germany with my spouse.

Moreover, I thank my mentors and professors, Prof. Pulak Sengupta and Prof. Subir Sarkar from Jadavpur University, India.

I thank my parents Mr. Abhijit Sengupta and Mrs. Sucharita Sengupta for inspiring me to travel abroad pursue my dreams. They are the motivation and support behind this incredible journey I have had.

Finally, I thank my beloved husband Sumit Roy for his constant support and encouragement through thick and thin of my professional and personal life.

I would finally like to thank the many wonderful people I met from all around the world during my PhD period. They are fondly acknowledged.

Table of Contents

Acknowledgements

Abstract

The temperature of Earth's earliest oceans, in which life may have first originated, remains a controversial issue in Earth science. Over the last 50 years, many studies have attempted to apply the temperature dependent fractionation of oxygen isotopes $^{18}O/^{16}O$ to ancient marine chemical sediments in order to infer the temperatures of the ancient oceans. The $\delta^{18}O$ composition of marine chemical sediments progressively decrease with increasing age leading to the suggestions that either the Precambrian oceans were also strongly depleted in ^{18}O (~-13‰) but had the same temperature as modern day, or that they had the same $\delta^{18}O$ value but were extremely hot (up to 80°C). A third opinion is that these chemical sediments are all diagenetically altered and unsuitable for paleoenvironmental studies. The current study introduces and demonstrates the use of a new additional parameter in resolving the classical problem – triple oxygen isotope composition of modern and ancient cherts. Mass dependent $^{18}O/^{16}O$ and $^{17}O/^{16}O$ fractionations result in resolvable unique curves in the triple oxygen isotope space, which may be used to identify individual equilibrium and kinetic processes.

This thesis comprises, 1) a general introduction to the thesis; 2) a description of the general terminology and the technique for extraction as well as gas cleaning to obtain impurity free oxygen gas from cherts and silicates, suitable for high-precision $\delta^{17}O$ analysis; 3) a geochemical mass balance model for $\delta^{17}O$ and $\delta^{18}O$ values of present and ancient seawater; 4) high-precision triple-oxygen isotope analyses and trace element analyses of cherts and amorphous silica samples – their implications for $\delta^{18}O$ and temperature of Earth's early oceans and 5) a general conclusion. This is followed by the Appendix, containing four manuscripts on which I am co-author. These are (I) manuscript entitled "Revealing the climate of snowball Earth from $\Delta^{17}O$ systematics of hydrothermal rocks" by Herwartz et al. (2015); (II) manuscript entitled "A calibration of the triple oxygen isotope fractionation in the $SiO_2–H_2O$ system and applications to natural samples" by Sharp et al. (2016); (III) manuscript entitled "The oxygen isotope composition of San Carlos olivine on the VSMOW2-SLAP2 scale" by Pack et al. (2016) and (IV)

manuscript entitled "Tracing the oxygen isotope composition of the upper Earth's atmosphere using cosmic spherules" by Pack et al. (2017).

Chapter 1 is an introduction into the aim of the thesis and the discussion about low $\delta^{18}O$ oceans vs. hot oceans.

Chapter 2 first describes the terminology and data normalization methods used in the current study. A two-point calibration method of normalizing oxygen isotope data on the VSMOW2-SLAP2 scale is described and adopted. The next section of the chapter describes method that was used to extract oxygen from cherts, amorphous silica and silicates. After the oxygen gas is liberated from the sample, a critical step is cleaning it using a gas chromatography column to get rid of impurities like NF_3, CF_4, N_2 and other trace gases in order to obtain pure oxygen gas. This pure gas is then suitable for analyses of triple oxygen isotopes composition it the dual-inlet mode of our mass spectrometer. Repeated measurements of the same gas over long periods of time yield high precision $\Delta'^{17}O$ data ($\sim$10 ppm SD).

Chapter 3 presents a geochemical mass balance model for the present and past triple oxygen isotope composition of the oceans. This chapter includes analyses of modern oceanic crust samples that have been altered by seawater at different temperatures. High-T: low-T alteration of oceanic crust is the main control on the present day oxygen isotope composition of seawater. Other fluxes that help maintain a steady-state oxygen isotope composition of seawater over time have also been discussed in the chapter. Finally, a projection is made on how these different processes could have varied in the past and resulted in a low $\delta^{18}O$ and $\delta^{17}O$ ocean, mainly via decreasing the ratio of high- to low-T oceanic crust alteration. This modeled trend provides the basis for the interpretation of the triple oxygen isotope data of our chert samples.

Chapter 4 of this thesis presents high-precision triple oxygen isotope data of chert and amorphous silica (diatoms and sponges) samples from different geological locations, ages (Phanerozoic to Archean) and settings. The oxygen isotope data are used to revisit the relationship between temperature and $^{17}O/^{16}O$, $^{18}O/^{16}O$ equilibrium fractionation in the silica-water system. Trace element analyses for most of the chert samples are also presented. This data along with the oxygen isotope data, are used to infer depositional and diagenetic histories of the individual chert samples with implications for the $\delta^{18}O$ and temperature conditions of

Precambrian ocean. The results reveal that many of the Precambrian samples are not in equilibrium with modern seawater composition at any temperatures; they also do not display equilibrium with an extreme light $\delta^{18}O$ and light $\delta^{17}O$ ocean. Most of the sample can be explained by equilibration with modern meteoric water or hydrothermal water –seawater mixtures.

The current study, thus, provides an additional parameter for interpreting the oxygen isotope data of cherts and application to estimate Precambrian ocean $\delta^{18}O$ and temperatures. The possibility of a hot Precambrian ocean remains, but equilibration with extremely light $\delta^{18}O$ oceans ($\sim$-13‰) is excluded at least for most of the chert samples analyzed in this study.

Chapter 5 is a chapter on the conclusions of the current study.

Four manuscripts on which I am co-author have been included in the Appendix– (I) Herwartz et al. (2015), (II) Sharp et al. (2016) and (III) Pack et al. (2016). The contribution to the manuscript by Herwartz et al. (2015) is help with triple oxygen isotope analysis in the laboratory and writing some parts of the paper. For the manuscript by Sharp et al. (2016) I analyzed triple oxygen isotope values of diatom samples via laser fluorination using F_2. My contribution to the third manuscript by Pack et al. (2016) is running oxygen extraction experiments from air, VSMOW2 and VSLAP2. My contribution to the fourth manuscript by Pack et al. (2017) is extracting and measuring air oxygen along with students (also as a part of their Bachelor thesis).

1. General Introduction

1.1 Aim of study

This study addresses the long debated topic of $\delta^{18}O$ and temperature (T) evolution of oceans with time. The aim of this study is to use the triple oxygen isotope compositions, i.e., $^{17}O/^{16}O$ and $^{18}O/^{16}O$ ratios of cherts in order to infer whether the Archean oceans were hot (up to 80°C suggested by Knauth and Epstein, 1976) than today or had extreme low $\delta^{18}O$ values (e.g., ~12‰ according to Perry, 1967) compared to modern oceans. A geochemical model for modern day $\delta^{17}O$ of seawater and its evolution with time, in case of a variable $\delta^{18}O$, is presented for the first time in this study.

1.2 Cherts over geological time

Fine grained chemical sediments, composed mostly or entirely of silica (SiO_2), are called cherts. The origin of the term "chert" dates back to the seventeenth century and was probably derived from a local English term – "Chert, perhaps originally chirt, is believed to be a local English term that was taken into geological use. It may be of onomatopoeic origin. The name chert may be of more recent origin than flint, and unlike flint, is not found in literary usage. It was well established in meaning in 1679" (Frondel, 1962).

Folk (1974) gave the scientific definition of a chert as "a chemically precipitated sedimentary rock, essentially monominerallic and composed chiefly of microcrystalline and/or chalcedonic quartz, with subordinate megaquartz and minor amounts of impurities". Common impurities present within cherts are clay minerals, silt, carbonate, pyrite and organic matter. They are compact rocks with low porosity (Folk et al 1952; Smith 1960), highly insoluble, highly impermeable and very resistant to alteration (Knauth, 1973).

Cherts or flints were first used by prehistoric man as tools and later as weapons, employing the nature of the rock to naturally break to produce conchoidal fractures and sharp edges. The rock was frequently fashioned into knife blades, spear points, arrowheads, scrapers, axes, drills and other sharp tools (Fig 1).

Figure 1 Two principle types of chert and prehistoric usage of the rock. (A) Bedded chert from Governors beach, Cyprus. Image source: sandatlas.org (B) Nodular chert from Cyprus. Image source: sandatlas.org (C) Chert or flint tools from about 14,000 years ago. Image source: Historic Scotland, historicagraphica.com

Naturally occurring authigenic silica exists in a wide variety of forms – from X-ray amorphous to well ordered α-quartz. Amorphous silica or "opal" can be of three types – opal-A, opal-CT and opal-C (Jones and Segnit, 1971). Of these, opal-A, precipitated in abundance by modern

organisms like diatoms and sponges etc., is the most common form. It is isotropic, its diffuse X-ray peak lies at 4.1 Å and contains up to 12 weight % H_2O within its structure (Knauth, 1992). The crystalline varieties of sedimentary silica are microcrystalline quartz, chalcedony or fibrous silica, mesocrystalline quartz and megaquartz (e.g., Knauth, 1994; Maliva et al., 2005). Petrographical studies have demonstrated most cherts to be mostly composed of microquartz (Knauth, 1994). Descriptions of the types of silica can be found in Chapter 3.
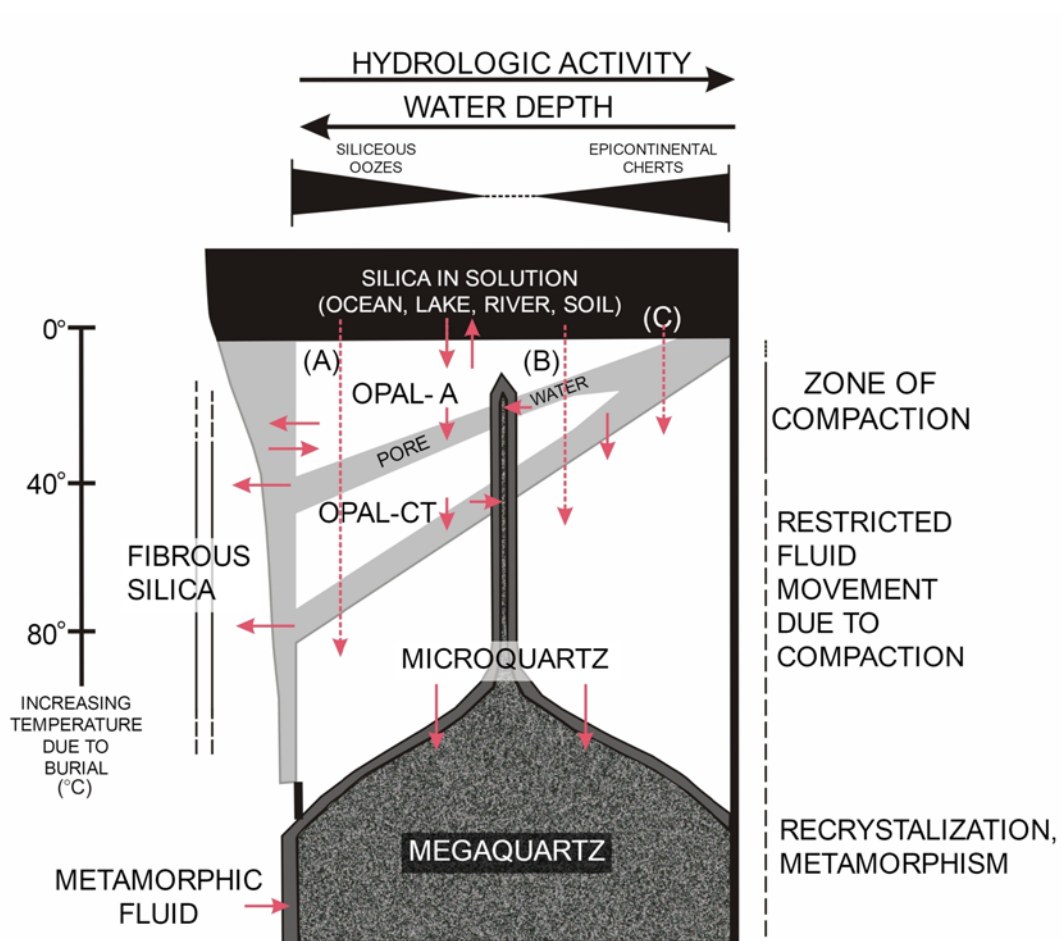
Figure 2 Schematic diagram of major authigenic silica phases and their possible diagenetic transformations. Vertical dimension represents qualitative burial depth with associated increase in temperature and loss of permeability. Horizontal scale represents qualitative depth of initial depositional environment. In general, deep sea oozes lie to the left of the diagram, while epicontinental deposits lie toward the right. Diagenetic path (A) represents silica initially deposited as opal-A (diatoms, radiolarians) which then transforms to opal-CT and then microquartz via solution – reprecipitation steps. Path (C) represents early diagenetic cherts, in which microquartz forms during shallow burial. Megaquartz forms by metamorphic re-crystallization of microquartz or

The origin of authigenic quartz is highly variable and complicated. Broadly speaking, cherts may form as pure orthochemical precipitates from silica rich fluids (C-type cherts) or via replacement of a precursory volcanic or sedimentary rock (S-type cherts) (e.g., Van den Boorn et al., 2007). Figure 2 shows the common forms of authigenic silica, hydrologic activity dissolving and precipitating the silica, and different diagenesis pathways. At room temperature (25°C) all forms of silica are soluble at pH >9. Fluids containing >6 µg/g dissolved silica are potentially silicifying fluids. At high silica concentrations of >80,000 µg/g, however, it is more likely that opal-A (>120,000 µg/g) or opal-CT (>80,000 µg/g) will precipitate instead of quartz (Knauth, 1992). It is also possible for quartz to precipitate directly from water, but only with high silica concentration, >4 µg/g, as shown by Mackenzie and Gees (1971) in laboratory experiments.

Modern concentration of silica in seawater is very low, < 1 µg/g in surface water and ∼ 15 µg/g in some bottom waters (Hesse 1988) – in stark contrast to a 60 µg/g concentration suggested by Siever (1992) in Precambrian ocean water.

The Phanerozoic silica cycle is controlled by an immense number of silica-secreting organisms like diatoms (70% of the silica secreting population - Lisitzin, 1972) (oldest accepted fossil evidence from Lower Jurassic - Barron, 1993), followed in importance by radiolaria (fossils discovered in strata as old as Middle Cambrian - Won and Below, 1999) and silica sponges (oldest fossil records in Proterozoic - Li, Chen and Hua, T., 1998). Higher organisms like silicoflagellates (oldest fossils from Early Cretaceous – McCartney, 1993) also contribute to the Phanerozoic silica budget but on a much smaller scale. Rivers, pore water reflux, submarine weathering and submarine volcanism/hydrothermal activity provide silica input into the oceans. The silica output flux is controlled by biogenic precipitation of silica and the total present day silica production by marine organisms is about 25 times the input of silica to the oceans (e.g., Heath, 1974; Edmond, 1979; Hesse, 1989). The imbalance in the silica budget is not a real one because 90-99% of silica extracted from surface seawater by silica secreting organisms redissolves before burial and is returned to the ocean (e.g., Hurd, 1973).

The silica secreting organisms produce shells or "tests" or "frustules" that are made of the amorphous opal-A. This amorphous polymorph of silica contains a large amount of water, up to 12 weight percent (wt %), taking into account both hydroxyl and molecular water (Knauth and Epstein, 1982). Opal-A is unstable in seawater and dissolves easily because of the very low silica concentrations of Phanerozoic oceans and only up to ~15 ppm in some bottom waters. This is way smaller than the equilibrium solubility of amorphous silica, which is between 70-150 ppm at 25°C and pH < 9 (Iler, 1979). The silica secreting microorganisms, while producing silica, raise the otherwise highly undersaturated seawater to silica saturation levels (on a local micro-scale) with the help of the catalyzing influence of enzyme controlled bio-reactions (Hesse, 1989). As the organisms die, the enzyme aided reactions cease and the micro-environment of silica-supersaturation is lost. As a result, the unstable opal-A begins to dissolve back into seawater. Thus, silica concentration of ocean surface waters is lowest due to the biogenic silica extraction, and the value gradually increases downwards with increasing water depth due to post-mortem settling and dissolution of the siliceous microorganism tests. The silica concentration of seawater attains a "mid-depth maximum" from which point downwards seawater loses its silica concentration as it mixes with silica poor surface water masses from the Poles, especially in the North Atlantic (Hesse, 1989).

Extensive chert formations are amongst some of the oldest rocks found on earth, e.g., 3.5 Ga Onverwacht Group in South Africa represents the least metamorphosed Archean cherts. Precambrian sedimentary rocks contain cherts in abundance, in the form of distinct beds / stratiform bedded deposits, or as lenses or nodules within other sediments like carbonate. Cherts are found as replacement nodules or silicified laminae in stromatolitic carbonate rocks, silica rich layers or cements in iron formations, beds and veins in greenstone belts and volcanic sequences, and as beds within argillites. Their occurrence almost throughout earth's history and in a variety of different geological settings renders them important candidates for looking into the ancient geological past.

Principle questions involved in studying cherts are the origin of silica, the depositional environment of the silica or siliceous sediments and their subsequent diagenesis (Hesse, 1988). The method of silica deposition has varied over time, "present is key to the past" not

holding true in this respect. The modern silica cycle is governed by opal secreting diatoms but they have been active only for the past 50 Ma (Siever, 1991; Knauth, 1992) and have formed thick bedded chert sequences since then. In fact, biogenic silica is common throughout the Phanerozoic – until the diatom explosion ~50 Ma ago, the primary sources of silica were radiolaria, sponges and vascular plants. All silica secreting organisms deposit silica in its amorphous opal-A form which then undergoes digenetic maturation and transformation to stable microquartz via opal-CT (Calvert, 1971). Oxygen isotope studies ($^{18}O/^{16}O$ fractionations) suggest these changes are associated with a rise in burial temperature. Temperatures of 45°C for the opal-A to opal-CT conversion and 80°C for the final transformation to quartz have been suggested by oxygen isotopic studies on deep sea drilled cores (Knauth and Epstein, 1975; Kolodny and Epstein, 1976; Murata et al., 1977; Pisciotto 1981) and by studying the geothermal gradient therein (Kastner, 1981).

Precambrian cherts could not have been deposited the same way as the Phanerozoic counterparts, simply because of the absence of diatom, radiolarian opal-A and lack of firm evidence suggesting that such microorganisms may have existed during that time. Thus, inorganic pathways for the deposition and origin of Precambrian chert are required (Hesse, 1989; Siever, 1991). Within the Precambrian sedimentary rocks chert is found in abundance and in different forms, e.g. chertified stromatolitic carbonates, iron formations, beds within argillites etc. Both bedded and vein type cherts are seen, for e.g. within the Dresser Formation, Pilbara Group, Western Australia. Deposition from big hydrothermal plumes spreading out on the ocean floor may have formed some of these thick chert beds (e.g., van den Boorn et al., 2007), which are often found associated with volcanics, but it is still controversial. Moreover, some chert types like the chert layers within thick iron formations e.g., within the Gunflint Range, Canada have no modern analogues. It is possible that bacterial precipitation of silica gel (opal-A) played a major role in the Precambrian (Konhauser and Ferris, 1996; Konhauser et al., 2002) or that the ancient oceans were supersaturated in silica, leading to direct precipitation of microquartz but none of these mechanisms have been confirmed so far (Knauth, 1992; Knauth, 1994).

Despite the origin and diagenesis of cherts being complicated, advances in isotope geology have made cherts, along with other marine sediments, important for information regarding ancient

ocean water chemistry (e.g., Perry 1967), temperature (e.g., Knauth and Epstein, 1976) and paleoclimatic conditions. An oxygen isotope record of past earth surface might be partially preserved in cherts, even though it is controversial. However, the possibility of finding information on paleoenvironments of the early Earth from cherts important because oxygen fractionation between silica and water is a function of temperature.

In his classic paper Urey (1947) first calculated stable isotope fractionation factors between species of geochemical interest. The silica-water oxygen isotope exchange - T relationship is expressed in the form $1000 \ln \alpha = \dfrac{a \times 10^6}{T^2} + \dfrac{b \times 10^3}{T} + c$, where $\alpha^{18/16O}_{SiO_2-Water}$ is the fractionation factor between the two phases (silica – water) and a,b, c are constants. The first experimentally determined quartz-water thermometer was given by O'Neil and Clayton (1964). So, the oxygen isotope composition of cherts can potentially tell us about the oyxgen isotope composition of ancient hydrosphere as well as its temperature.

This study focuses on the oxygen isotope study of cherts and the information regarding ancient seawater that may be obtained from that. In this thesis and additional parameter, the $\delta^{17}O$ compositions of cherts, shall be introduced to resolve this enigmatic topic. This parameter is described in Section 1.4 of this chapter.

1.3 The seawater problem

The solar system originated at 4.57 Ga (Allègre et al., 1995) and accretion of small bodies in the solar nebula followed within the next 10 Myr (Lugmaier and Shukolyukov, 1998). The Earth accreted to its present mass between 4.52 and 4.45 Ga (Halliday, 2000; Sasaki and Nakazawa, 1986; Porcelli et al., 1998) and this is where the Hadean era starts, along with Earth formation. The planet was then probably still covered by a magma ocean (Tonks and Melosh, 1993) but formation of continental crust followed soon (4.00 – 4.03 Ga, Bowring and Williams, 1999). The oldest rocks found on Earth's surface are 4.03 Ga old (Bowring and Williams, 1999) but older detrital zircons (e.g., 4.1 – 4.4 Ga) have been reported from within quartzitic rocks of the

Murchison District of Western Australia (Froude et al., 1983 and others). A single 4.40 Ga zircon has been reported by Wilde et al. (2001). These zircons were found to be enriched in ^{18}O respective to mantle derived ones (Mojzsis et al., 2001; Wilde et al.,2001; Peck et al., 2001) and are indicative of "an active hydrological cycle, a significant quantity of water on Earth surface, and an early continental crust"(c.f. Holland, 2004).

The Archean era starts at 3.8 Ga. By then the Earth cooled down significantly and early Archean greenstone terranes began to form. The Isua supracrustal belt in W. Greenland contains volcanic rocks and a variety of sediments and metasediments (Nutman et al., 1997). The supracrustal, mafic and ultramafic rocks here are aged ≥ 3.87 Ga to 3.6 Ga. They are interpreted to be of deep marine origin and the metamorphosed BIF deposits in this belt provide best evidence for an early Archean ocean (Holland, 2004).

According to stellar evolution models the Archean sun was 20 – 25 % fainter than today (Gough 1981) and thus, lower surface temperatures are expected at that time on Earth. But a dense greenhouse atmosphere rich in CO_2 could have led to higher temperatures (Kasting and Ackerman, 1986). Conflicting views on this topic exists and different proxies have been studied so far to arrive at a conclusion regarding this.

The evolution of temperature and chemistry of earth's early oceans is particularly interesting since it is suspected that life may have originated in the ocean or near hydrothermal vents (Bada and Lazcano, 2002). It is not known when exactly life originated on Earth but light $\delta^{13}C$ values, indicative of biological activity, have been measured in carbonaceous inclusions within apatite grains from a ∼ 3.8 Ga old banded iron formation from the Isua supracrustal belt, western Greenland and nearby Akilia island (Mojzsis et al., 1996). Recently, Bell et al. (2015) found graphite of biogenic origin within 4.4 Ga old detrital zircons, suggesting that terrestrial life may have originated by 4.4 Ga - about 300 Ma older than previously postulated (e.g., Battistuzzi et al., 2004). Some of the oldest evidences of early life in the form of putative microfossils were reported in cherty metasedimentary rocks, ∼3.5 Ga old, from the Pilbara Craton (Awramik et al., 1983; Schopf, 1992, 1999 and others) even though some of these claims have been later doubted (Garcia-Ruiz et al., 2003; Bower et al., 2016). This makes marine sediments, particularly cherts even more attractive candidates for paleoenvironmental studies.

1.3.1 Oxygen isotope studies

The term $\delta^{18}O$ is defined as follows, where i = 18 :-

$$\delta^i O^{sample}_{standard} = \left(\frac{\frac{^iO}{^{16}O}sample}{\frac{^iO}{^{16}O}standard} - 1 \right) \times 1000$$

In order to tap into the plethora of information that marine sediments may provide, several studies have been performed on their oxygen isotope compositions so far and a characteristic trend has been noted in their $\delta^{18}O$ values – a secular trend of decreasing $\delta^{18}O$ values of sediments with increasing age (Fig. 2) (Perry, 1967; Longinelli and Nutti, 1968; Knauth and Epstein, 1976; Degens and Epstein, 1962 and others). This could be a direct reflection of the $\delta^{18}O$ of the ancient oceans, i.e., a lighter $\delta^{18}O$ earlier ocean would precipitate chemical sediments with lighter $\delta^{18}O$ values than today, considering that the average temperature of the ocean remained the same as present day. Veizer et al. (1999) displayed this gradually low to high $\delta^{18}O$ values in well-preserved calcitic and phosphatic shells from Cambrian to Cretaceous, inferring dramatically low $\delta^{18}O$ of seawater ($\delta^{18}O_{SW}$) of -22‰ in the Cambrian. Shemesh et al., 1983 and 1988 displayed a similar trend in phosphates; they also showed that phosphates are least resistant to alteration amongst other chemical sediments. In cherts, $\delta^{18}O$ values, lower by several tens of per mils than their younger counterparts, were observed first by Perry (1967) who also attributed this to a lighter $\delta^{18}O_{sw}$ in the past, about -12‰ in the Archean.

A light $\delta^{18}O^{SW}$ in the past, gradually progressing to higher values up to the present is not the only possible explanation for the oxygen isotopic variations seen in these sediments. Studies suggest that the ancient oceans were very hot, up to 80°C (e.g., Knauth and Epstein, 1976; Knauth and Lowe, 2003) but the $\delta^{18}O^{SW}$ remained unchanged. This has serious implications on the origin and evolution of life. At such high temperatures only hyperthermophilic organisms, i.e., ones that survive in extreme hot environments of > 60°C, would have survived. General arguments against this idea of hot surface temperatures are the concept of the 25% fainter Archean sun and therefore the incredibly high pCO_2 levels, 2-6 bars, required to maintain such high surface temperatures on Earth in that case (Kasting and Howard, 2006). The convincing records of glacial ages during intervals 0.75 - 0.58 Ga, 2.45 - 2.22 Ga and evidence hinting at possible

regional glaciations at 2.9 Ga (Hoffman, 2013; Pierrehumbert et al., 2011) are also incompatible with the continuous high-T surface conditions.

A third interpretation of the sediment data is that the low $\delta^{18}O$ data of the older marine chemical sediments is simply an effect of post-depositional alteration or diagenesis (e.g., Degens and Epstein, 1962) and does not provide any information about the enigmatic Precambrian world.

Geochemical modelling has been applied to try and replicate how $\delta^{18}O_{SW}$ may have varied over time and to see if this correlates with the information provided by the rock record. The $\delta^{18}O^{SW}$ is controlled by interactions of the lithosphere with the hydrosphere which lead to oxygen isotope exchange between the two reservoirs. It has been concluded by some authors (Muehlenbachs and Clayton, 1976; Muehlenbachs, 1998) that $\delta^{18}O_{SW}$ is presently in steady-state at 0 ± 2‰ and it is not probable that it varied greatly in the past, assuming that seafloor spreading and plate tectonics operated back then. Isotopic and trace element studies of oldest crustal samples sets the time of plate tectonics initiation to as early as shortly after the end of the Hadean, i.e., very early Archean (Shirey et al., 2008). Mantle derived Archean placer diamonds (age 3.1 to 3.5 Ga) from the Kaapval craton, South Africa have enriched nitrogen isotopic compositions which may be due to contamination of the mantle by nitrogen-rich Archean sediments, thus indicating active plate tectonics in the Archean (Smart et al., 2016).

The geological rock record also provides clues that indicate that the isotopic composition of the oceans may indeed not have been much different in the past than it is today. Oldest ophiolite complexes have been dated to $\sim$ 3.8 Ga (Furnes et al., 2007). Ophiolites are obducted oceanic crust sections emplaced onto continental margins (Pearce 2003) and are indicative of plate tectonics and seafloor spreading. If seawater $\delta^{18}O$ did change in the past, an effect should also have been seen in the $\delta^{18}O$ vales of the ophiolites through time. However, alteration patterns similar to that seen in modern oceanic crust have been observed in altered oceanic pillow lavas from Archean greenstone terranes (Smith and O'Neil, 1984), in $\sim$ 2 Ga old ophiolites (Holmden and Muehlenbachs, 1992) as well as in younger ophiolites. These observations have been commonly used as evidence that seawater isotopic composition remained constant over time.

Other modelling studies (Wallmann, 2001; Kasting et al., 2006; Jaffrés et al., 2007) argue that the fluxes controlling the total oxygen budget of the oceans could have varied in time and ancient

oceans may have had significantly lower $\delta^{18}O_{SW}$ values than today. Kasting et al. (2006) suggests a secular rise in sea level through time as a reason why the $\delta^{18}O_{sw}$ varied through time. If ridge crests were less deeply submerged than today then the pressure within the hydrothermal system would have been lower, leading to less convective heat transfer upwards. This would mean lesser penetration depth and temperature of water within the hydrothermal circulation system, thus reducing the amount of oceanic crust altered due at high-T. At reduced pressures the seawater circulating through the ridges may have boiled more easily, thus also reducing high-T alteration. A reduced high-T alteration flux would relatively increase the low-T alteration flux and preferentially pull down the $\delta^{18}O_{SW}$.

The Archean atmosphere may have had higher pCO_2 levels than today. The Archean would also have had greater availability of greenstones, which are more readily weathered than other lithologies. Jaffres (2007) argues that these two factors coupled together would lead to higher continental weathering rates. She also supports the lower ridge crest depth or even emergent ridge crests hypotheses and overall lesser high-T : low-T ratios in the past driving $\delta^{18}O^{SW}$ to lower values.
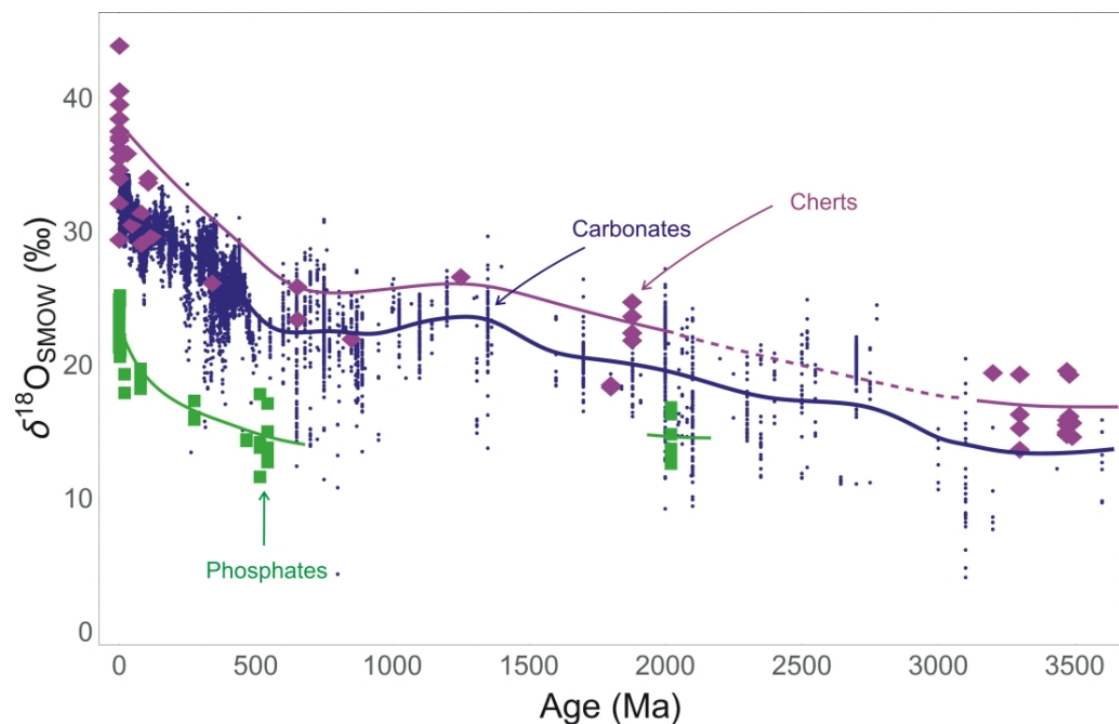

Figure 3 A plot of $\delta^{18}O$ of carbonates (blue dots) from the archived data of Jan Veizer, chert samples from this study (pink diamonds), and phosphates (green squares) from Shemesh et al. (1983) vs.

14

1.4 New approach - triple oxygen isotope study

Clearly, from the $\delta^{18}O$ alone, it is not possible to choose amongst the three explanations provided for the varying $\delta^{18}O$ of marine sediments over time. In this study, we use an additional parameter, in the form of the high-precision ($\Delta'^{17}O$, defined later in text, resolvable on the ppm scale) analysis of $\ln(^{17}O/^{16}O)/\ln(^{18}O/^{16}O)$ ratios of cherts, in order to resolve this classical problem.

The very first paleo-ocean temperature calculations were made by Urey et al. (1951) by measuring the oxygen isotope of marine carbonates. He employed a geochemical thermometer based on the $^{18}O/^{16}O$ fractionation between calcite and water, when both phases are in equilibrium with each other. He recognized that these calculated temperatures were dependent on a "best estimate" of ^{18}O composition of the water equilibrating with these carbonates. Thus, an inherent drawback of this paleothermometer emerges – both the $\delta^{18}O$ and temperature of the equilibrating water being unknown, which is the case for most samples, it is impossible to determine one independent of the other. This may introduce a bias in the interpretation of sediment data, depending on the assumption made for either of the two parameters in the first step of calculations. Thus, we cannot say for sure if the ancient oceans were hotter or had lighter $\delta^{18}O$ values than today, by using the $^{18}O/^{16}O$ fractionation and T relation alone.

The measurement of the third isotope of oxygen, ^{17}O, and the $^{17}O/^{16}O$ fractionation has been ignored for a long time. This is partly due to analytical challenges – high precision data are required not only on $\delta^{18}O$ but also on $\delta^{17}O$ of samples. Another reason for not studying $^{17}O/^{16}O$ fractionations was the view that ^{17}O value of a substance provides no additional information to ^{18}O alone (Bigeleisen, 1952; Craig, 1957).

In terrestrial rocks, variations in $\delta^{17}O$ are generally half of the respective variations in $\delta^{18}O$ (Craig, 1957). Thus, $\delta^{17}O$ vs $\delta^{18}O$ of terrestrial materials appear to define a line with slope of ~0.5

15

in a linearized plot. Such a line has been called the Terrestrial Fractionantion Line (TFL) (Clayton, 2003; Rumble et al., 2007). On closer inspection, and with high precision measurements, the TFL can be split into a number of different slopes that are denoted by co-genetic sample suites and are representative of individual processes – meaning, the TFL is an average of all these individual slope values (Pack and Herwartz, 2014; Herwartz et al., 2015). Such slopes within this plot are denoted by θ and the range of possible θ values for triple oxygen isotope fractionation is 0.5 to 0.5305 (Matsuhisa et al., 1978; Young et al., 2002; Cao and Liu, 2011). Such purely mass dependent variations in slopes of fractionation lines were first anticipated by Matsuhisa et al., 1978 and later theoretically predicted by Young et al., 2002 and Cao and Liu, 2011.

Pack and Herwartz (2014) reported high-precision triple-oxygen isotope data on terrestrial materials and demonstrated that low and high-T equilibrated rocks define different lines with distinct slopes in the triple oxygen isotope space. A temperature dependence of the triple oxygen isotope fractionation, demonstrating how the different θ values between silica and water in the triple oxygen isotope space vary with temperature, was also discussed.

Levin et al. (2014), Passey et al. (2014) and Sharp et al. (2016) have also reported triple oxygen isotope data on terrestrial sediments and shown that the different θ values defined by co-genetic suite of minerals or mineral-water pairs provide information on the origin of the minerals.

In this study, triple oxygen isotope composition of chert samples from various locations and ages were measured in order to suggest some feasible equilibrium conditions for the sediments. Previous studies on the seawater puzzle have reported only $\delta^{18}O$ values of sediments. Further analysis for and discussion on the $\alpha_{\mathrm{SiO_2-Water}}^{^{18/16}\mathrm{O}}$ -T relation for silica-water equilibrium is also included. A combination of the classical $^{18}O/^{16}O$ fractionation –T relation and the relatively new $\theta_{\mathrm{SiO_2-Water}}^{\mathrm{equilibrium}} - T$ relations may help resolve temperature and $\delta^{18}O$ values of silica precipitating waters without the need to assume a particular value for any one of the two parameters (as demonstrated in Sharp et al., 2016). In combination with evolution of triple oxygen isotope composition of seawater through time, obtained from a geochemical model presented in this study, the temperature dependence of triple oxygen isotope fractionations may

yield results not biased or constrained by presumptions on either of the two important parameters - the $\delta^{18}O$ and temperature of ancient oceans.

1.5 Trace element studies

In order to charactrize the studied chert samples better and infer more about their depositional comditions a trace element analysis study was performed on them. Sediments like cherts, carbonate, banded iron formations, that precipitate directly from seawater, serve as good proxies of ocean water chemistry (e.g., Van Kranendonk et al., 2003 and references therein). Significant information regarding geochemical evolution of the hydrosphere and atmosphere of the Earth, from Archean to Modern, may be extracted from geochemical studies of such sediments, for e.g., marine oxidation states and changes therein maybe interpreted using Ce anomalies of marine BIFs, as demonstrated by some early studies (Fryer et al., 1977). BIFs have also been used to assess hydrothermal input into oceans with time (Danielson e al., 1992).

Typical features of normalized REE (rare earth elements) + Y patterns of modern seawater include (e.g., Elderfield and Greaves, 1982; Bau et al., 1995):

 1) LREE (light REE) depletion relative to HREE (heavy rare earth elements)

2) negative Ce-anomalies ($Ce\ anomaly = \frac{Ce}{Ce^*} = \left[\frac{Ce}{Pr\ (Pr/Nd\ )}\right]_{PAAS}$)

3) positive La anomalies (elevated relative to Pr and Nd) ($La\ \ anomaly = \frac{La}{La^*} = \left[\frac{La}{Pr(Pr/Nd)^2}\right]_{PAAS}$)

4) super-chondritic Y/Ho ratios (> 44 for pure marine chemical sediments) (chondrite Y/Ho value is 26-27 according to Pack et al., 2007)

5) variable Eu anomalies, with a positive anomaly indicating hydrothermal input

$$(Eu \quad anomaly = \frac{Eu}{Eu^*} = S\left[\frac{Eu}{\frac{2}{3}Sm+\frac{1}{3}Tb}\right]_{PAAS})$$

The equations for the anomalies are according to Lawrence et al. (2006), and indices $[x]_{PAAS}$

Indicate values of element "x" normalized to Post Archean Australian Shale (PAAS) (Taylor and McLennan, 1985). Earth's seawater signature has, for the most part, remained constant through time except for a negative Ce anomaly, which has not been commonly found prior to the great oxidation event ~1.8 Ga (Van Kranendonk et al., 2003).

Extensive work on trace element patters of essentially monominerallic cherts was carried out by Murray et al. (1990, 1991, 1992, 1994). The exposure time of sediments to seawater is also important for incorporating REEs (Muray, 1990). Adsorption of REEs from seawater or the fluid in which the precipitation occurs is another important way of adding REEs to cherts. Thus, cherts deposited in different tectonic settings display different trace element patterns. Murray (1990, 1994) displayed this in Phanerozoic cherts and deduced three depositional regimes – spreading ridge proximal, open ocean basin floor and continental margin settings. Al and Ti are good indicators of terrigenous input because they are affiliated with aluminosilicate phases. On the other hand, metalliferous ridge-proximal sediment is Fe rich. So, Fe can be used as indicative of hydrothermal input at oceanic spreading centres. Therefore Murray (1994) used a plot of Fe_2O_3 / TiO_2 vs $Al_2O_3/(Al_2O_3 + Fe_2O_3)$ in order to classify the depositional environments of cherts into continental margin proximal, pelagic and ridge proximal groups. This plot has been used in the current study to classify the chert samples.

The information obtained from trace element studies, along with the triple oxygen isotope compositions of chert samples and the general result of the mass balance model have been considered together for interpreting $\delta^{18}O$ and temperature of seawater over time.

1.6 References

Allegre, C. J., Manhes, G., & Göpel, C. (1995). The age of the Earth. Geochimica et Cosmochimica Acta, 59(8), 1445-1456.

Awramik, S. M., Schopf, J. W., & Walter, M. R. (1983). Filamentous fossil bacteria from the Archean of Western Australia. Developments in Precambrian Geology, 7, 249-266.

Bada, J. L., & Lazcano, A. (2002). Some like it hot, but not the first biomolecules. Science, 296(5575), 1982-1983.

Battistuzzi, F. U., Feijao, A., & Hedges, S. B. (2004). A genomic timescale of prokaryote evolution: insights into the origin of methanogenesis, phototrophy, and the colonization of land. BMC Evolutionary Biology, 4(1), 44.

Bekker, A., & Holland, H. D. (2012). Oxygen overshoot and recovery during the early Paleoproterozoic. Earth and Planetary Science Letters, 317, 295-304.

Bell, E. A., Boehnke, P., Harrison, T. M., & Mao, W. L. (2015). Potentially biogenic carbon preserved in a 4.1 billion-year-old zircon. Proceedings of the National Academy of Sciences, 112(47), 14518-14521.

Bigeleisen, J. (1952). The effects of isotopic substitution on the rates of chemical reactions. The Journal of Physical Chemistry, 56(7), 823-828.

Bower, D. M., Steele, A., Fries, M. D., Green, O. R., & Lindsay, J. F. (2016). Raman Imaging Spectroscopy of a Putative Microfossil from the~ 3.46 Ga Apex Chert: Insights from Quartz Grain Orientation. Astrobiology, 16(2), 169-180.

Bowring, S. A., & Williams, I. S. (1999). Priscoan (4.00–4.03 Ga) orthogneisses from northwestern Canada. Contributions to Mineralogy and Petrology, 134(1), 3-16.

Calvert, S. E. (1971). Composition and origin of North Atlantic deep sea cherts. Contributions to Mineralogy and Petrology, 33(4), 273-288.

Cao, X., & Liu, Y. (2011). Equilibrium mass-dependent fractionation relationships for triple oxygen isotopes. Geochimica et Cosmochimica Acta, 75(23), 7435-7445.

Craig, H. (1957). Isotopic standards for carbon and oxygen and correction factors for mass-spectrometric analysis of carbon dioxide. Geochimica et cosmochimica acta, 12(1), 133-149.

Danielson, A., Möller, P., & Dulski, P. (1992). The europium anomalies in banded iron formations and the thermal history of the oceanic crust. Chemical Geology, 97(1), 89-100.

Degens, E. T., & Epstein, S. (1962). Relationship Between O^{18}/O^{16} Ratios in Coexisting Carbonates, Cherts, and Diatomites: Geological Notes. American Association of Petroleum Geologists Bulletin, 46(4), 534-542.

Edmond, J. M., Measures, C., McDuff, R. E., Chan, L. H., Collier, R., Grant, B., Gordon, L.I., & Corliss, J. B. (1979). Ridge crest hydrothermal activity and the balances of the major and minor elements in the ocean: the Galapagos data. Earth and Planetary Science Letters, 46(1), 1-18.

Elderfield, H., & Greaves, M. J. (1982). The rare earth elements in seawater. Nature, 296, 214-219.

Folk, R. L. (1974). Petrography of sedimentary rocks. Univ. Texas, Hemphill, Austin, Tex, 182.

Folk, R. L., & Weaver, C. E. (1952). A study of the texture and composition of chert. American Journal of Science, 250(7), 498-510.

Frondel, C. (1962). Dana's System of Mineralogy, Volume II. Silica Minerals.

Froude, D.E., Ireland, T.E., Kinny P.D., Williams, I.S., Compston, W., Williams, I.R., Myers, J.S. (1983). Ion microprobe identification of 4,100-4,200 Myr-old terrestrial zircons. Nature, 304, 616–618.

Fryer, B. J. (1977). Rare earth evidence in iron-formations for changing Precambrian oxidation states. Geochimica et Cosmochimica Acta, 41(3), 361-367.

Furnes, H., de Wit, M., Staudigel, H., Rosing, M., & Muehlenbachs, K. (2007). A vestige of Earth's oldest ophiolite. Science, 315(5819), 1704-1707.

García-Ruiz, J. M., Hyde, S. T., Carnerup, A. M., Christy, A. G., Van Kranendonk, M. J., & Welham, N. J. (2003). Self-assembled silica-carbonate structures and detection of ancient microfossils. Science, 302(5648), 1194-1197.

Gough, D. O. (1981). Solar interior structure and luminosity variations. In Leibacher, J., van Driel-Gesztelyi, L., Mandrini, C.H. & Wheatland, M. S. (Chief Eds.) Physics of Solar Variations, Springer, pp. 21-34.

Halliday, A. N., Lee, D. C., & Jacobsen, S. B. (2000). Tungsten isotopes, the timing of metal-silicate fractionation, and the origin of the Earth and Moon. Origin of the Earth and Moon, 1, 45-62.

Heath, G. R. (1974). Dissolved silica and deep-sea sediments. W.W. Hay (Ed.). Society of Economic Paleontologists and Mineralogists., Special Publication 20, 77–93.

Hesse, R. (1988). Diagenesis# 13. Origin of chert: Diagenesis of biogenic siliceous sediments. Geoscience Canada, 15(3).

Hesse, R. (1989). Silica diagenesis: origin of inorganic and replacement cherts. Earth-Science Reviews, 26(1), 253-284.

Hesse, R. (1989). Silica diagenesis: origin of inorganic and replacement cherts. Earth-Science Reviews, 26(1), 253-284.

Hoffman, P. F. (2013). The Great Oxidation and a Siderian snowball Earth: MIF-S based correlation of Paleoproterozoic glacial epochs. *Chemical Geology*, *362*, 143-156.

Holland, H.D. (2004). The geologic history of seawater. In Elderfield, H. (Ed.). & Holland, H.D. & Turekian, K.K. (Exec. Eds.), Treatise on Geochemistry,Vol. 6. The Oceans and Marine Geochemistry. Elsevier Pergamon, Kidlington, Oxford, pp. 583–625.

Holmden, C., & Muehlenbachs, K. (1993). The 18O/16O ratio of 2-billion-year-old seawater inferred from ancient oceanic crust. Science, 259(5102), 1733-1736.

Hu, G., & Clayton, R. N. (2003). Oxygen isotope salt effects at high pressure and high temperature and the calibration of oxygen isotope geothermometers. Geochimica et Cosmochimica Acta, 67(17), 3227-3246.

Hurd, D. C. (1973). Interactions of biogenic opal, sediment and seawater in the Central Equatorial Pacific. Geochimica et cosmochimica acta, 37(10), 2257-2282.

Iler, R. K. (1979). The chemistry of silica: solubility, polymerization, colloid and surface properties, and biochemistry. Wiley, New York.

Jaffrés, J. B., Shields, G. A., & Wallmann, K. (2007). The oxygen isotope evolution of seawater: a critical review of a long-standing controversy and an improved geological water cycle model for the past 3.4 billion years. Earth-Science Reviews, 83(1), 83-122.

Jones, J. T., & Segnit, E. R. (1971). The nature of opal I. Nomenclature and constituent phases. Journal of the Geological society of Australia, 18(1), 57-68.

Kasting, J. F., & Ackerman, T. P. (1986). Climatic consequences of very high carbon dioxide levels in the Earth's early atmosphere. Science, 234(4782), 1383-1385.

Kasting, J. F., Howard, M. T., Wallmann, K., Veizer, J., Shields, G., & Jaffrés, J. (2006). Paleoclimates, ocean depth, and the oxygen isotopic composition of seawater. Earth and Planetary Science Letters, 252(1), 82-93.

Kastner, M. (1981) Authigenic silicates in deep-sea sediments: formation and diagenesis. In: Emiliani, C. (Ed.) The Sea 7, Wiley, New York, pp. 915-980.

Kenny, R., & Knauth, L. P. (1992). Continental paleoclimates from δD and $\delta^{18}O$ of secondary silica in paleokarst chert lags. Geology, 20(3), 219-222.

Knauth, L. P. (1973). Oxygen and hydrogen isotope ratios in cherts and related rocks (Doctoral dissertation, California Institute of Technology).

Knauth, L. P. (1992). Origin and diagenesis of cherts: an isotopic perspective. In Clauer, N. & Chaudhuri, S. (Eds.), Isotopic signatures and sedimentary records, Springer Berlin Heidelberg, pp. 123-152.

Knauth, L. P. (1994). Petrogenesis of chert. Reviews in Mineralogy and Geochemistry, 29(1), 233-258.

Knauth, L. P., & Epstein, S. (1975). Hydrogen and oxygen isotope ratios in silica from the JOIDES Deep Sea Drilling Project. Earth and Planetary Science Letters, 25(1), 1-10.

Knauth, L. P., & Epstein, S. (1976). Hydrogen and oxygen isotope ratios in nodular and bedded cherts. Geochimica et Cosmochimica Acta, 40(9), 1095-1108.

Knauth, L. P., & Epstein, S. (1982). The nature of water in hydrous silica. American Mineralogist, 67(5-6), 510-520.

Knauth, L. P., & Lowe, D. R. (2003). High Archean climatic temperature inferred from oxygen

isotope geochemistry of cherts in the 3.5 Ga Swaziland Supergroup, South Africa. Geological

Society of America Bulletin, 115(5), 566-580.

Kolodny, Y., & Epstein, S. (1976). Stable isotope geochemistry of deep sea cherts. Geochimica et

Cosmochimica Acta, 40(10), 1195-1209.

Konhauser, K. O., & Ferris, F. G. (1996). Diversity of iron and silica precipitation by microbial

mats in hydrothermal waters, Iceland: Implications for Precambrian iron formations. Geology,

24(4), 323-326.

Konhauser, K. O., Hamade, T., Raiswell, R., Morris, R. C., Ferris, F. G., Southam, G., & Canfield, D. E.

(2002). Could bacteria have formed the Precambrian banded iron formations? Geology,

30(12), 1079-1082.

Lawrence, M. G., Greig, A., Collerson, K. D., & Kamber, B. S. (2006). Rare earth element and yttrium

variability in South East Queensland waterways. Aquatic Geochemistry, 12(1), 39-72.

Levin, N. E., Raub, T. D., Dauphas, N., & Eiler, J. M. (2014). Triple oxygen isotope variations in

sedimentary rocks. Geochimica et Cosmochimica Acta, 139, 173-189.

Li, C. W., Chen, J. Y., & Hua, T. E. (1998). Precambrian sponges with cellular

structures. *Science*, *279*(5352), 879-882.

Lipps, J. H. (Ed.). (1993). Fossil prokaryotes and protists. Blackwell Scientific Publications.

Lisitzin, A. P. (1972). Sedimentation in the world ocean with emphasis on the nature, distribution

and behavior of marine suspensions. K. S. Rodolfo (Ed.). Society of Economic Paleontologists

and Mineralogists, Special Publication 17, 218.

Longinelli, A., & Nuti, S. (1968). Oxygen isotopic composition of phosphorites from marine

formations. Earth and Planetary Science Letters, 5, 13-16.

Lugmair G. W., & Shukolyukov A. (1998). Early solar system timescales according to ^{53}Mn-^{53}Cr

systematics. Geochimica et Cosmochimica Acta, 62, 2863–2886.

Mackenzie, F. T., & Gees, R. (1971). Quartz: synthesis at earth-surface conditions. Science,

173(3996), 533-535.

Maliva, R. G., Knoll, A. H., & Simonson, B. M. (2005). Secular change in the Precambrian silica cycle: insights from chert petrology. Geological Society of America Bulletin, 117(7-8), 835-845.

Matsuhisa, Y., Goldsmith, J. R., & Clayton, R. N. (1978). Mechanisms of hydrothermal crystallization of quartz at 250 C and 15 kbar. Geochimica et Cosmochimica Acta, 42(2), 173-182.

Mojzsis, S. J., Arrhenius, G., McKeegan, K. D., Harrison, T. M., Nutman, A. P., & Friend, C. R. L. (1996). Evidence for life on Earth before 3,800 million years ago.

Mojzsis, S. J., Harrison, T. M., & Pidgeon, R. T. (2001). Oxygen-isotope evidence from ancient zircons for liquid water at the Earth's surface 4,300 Myr ago. Nature, 409(6817), 178-181.

Muehlenbachs, K. (1998). The oxygen isotopic composition of the oceans, sediments and the seafloor. Chemical Geology, 145(3), 263-273.

Muehlenbachs, K., & Clayton, R. N. (1976). Oxygen isotope composition of the oceanic crust and its bearing on seawater. Journal of Geophysical Research, 81(23), 4365-4369.

Murata, K. J., Friedman, I., & Gleason, J. D. (1977). Oxygen isotope relations between diagenetic silica minerals in Monterey Shale, Temblor Range, California. American Journal of Science, 277(3), 259-272.

Murray, R. W. (1994). Chemical criteria to identify the depositional environment of chert: general principles and applications. Sedimentary Geology, 90(3), 213-232.

Murray, R. W., Ten Brink, M. R. B., Gerlach, D. C., Russ, G. P., & Jones, D. L. (1991). Rare earth, major, and trace elements in chert from the Franciscan Complex and Monterey Group, California: Assessing REE sources to fine-grained marine sediments. Geochimica et Cosmochimica Acta, 55(7), 1875-1895.

Murray, R. W., ten Brink, M. R. B., Gerlach, D. C., Russ, G. P., & Jones, D. L. (1992). Interoceanic variation in the rare earth, major, and trace element depositional chemistry of chert: perspectives gained from the DSDP and ODP record. Geochimica et Cosmochimica Acta, 56(5), 1897-1913.

Murray, R. W., ten Brink, M. R. B., Jones, D. L., Gerlach, D. C., & Russ, G. P. (1990). Rare earth elements as indicators of different marine depositional environments in chert and shale. Geology, 18(3), 268-271.

Nutman, A. P., Mojzsis, S. J., & Friend, C. R. (1997). Recognition of ≥ 3850 Ma water-lain sediments in West Greenland and their significance for the early Archaean Earth. Geochimica et Cosmochimica Acta, 61(12), 2475-2484.

O'Neil, J. R., & Clayton, R. N. (1964). Oxygen isotope geothermometry. Isotopic and cosmic chemistry, 157-168.

Pack, A., & Herwartz, D. (2014). The triple oxygen isotope composition of the Earth mantle and understanding variations in terrestrial rocks and minerals. Earth and Planetary Science Letters, 390, 138-145.

Pack, A., Russell, S. S., Shelley, J. M. G., & Van Zuilen, M. (2007). Geo-and cosmochemistry of the twin elements yttrium and holmium. Geochimica et Cosmochimica Acta, 71(18), 4592-4608.

Passey, B. H., Hu, H., Ji, H., Montanari, S., Li, S., Henkes, G. A., & Levin, N. E. (2014). Triple oxygen isotopes in biogenic and sedimentary carbonates. Geochimica et Cosmochimica Acta, 141, 1-25.

Pearce, J. A. (2003). Supra-subduction zone ophiolites: the search for modern analogues. Special Papers-Geological Society of America, 269-294.

Peck, W. H., Valley, J. W., Wilde, S. A., & Graham, C. M. (2001). Oxygen isotope ratios and rare earth elements in 3.3 to 4.4 Ga zircons: Ion microprobe evidence for high $\delta^{18}O$ continental crust and oceans in the Early Archean. Geochimica et Cosmochimica Acta, 65(22), 4215-4229.

Perry, E. C. (1967). The oxygen isotope chemistry of ancient cherts. Earth and Planetary Science Letters, 3, 62-66.

Pierrehumbert, R. T., Abbot, D. S., Voigt, A., & Koll, D. (2011). Climate of the Neoproterozoic. Annual Review of Earth and Planetary Sciences, 39, 417-460.

Pisciotto, K. A. (1981). Diagenetic trends in the siliceous facies of the Monterey Shale in the Santa Maria region, California. Sedimentology, 28(4), 547-571.

Porcelli, D., Cassen, P., Woolum, D., & Wasserburg, G. J. (1998). Acquisition and early losses of rare gases from the deep Earth. Acquisition and early losses of rare gases from the deep Earth. In Origin of the Earth and Moon: Lunar Planetary Institute Contribution, Report 957, 35–36.

Rumble, D., Miller, M. F., Franchi, I. A., & Greenwood, R. C. (2007). Oxygen three-isotope fractionation lines in terrestrial silicate minerals: An inter-laboratory comparison of hydrothermal quartz and eclogitic garnet. Geochimica et Cosmochimica Acta, 71(14), 3592-3600.

Sasaki, S., & Nakazawa, K. (1986). Metal-silicate fractionation in the growing Earth: Energy source for the terrestrial magma ocean. Journal of Geophysical Research: Solid Earth, 91(B9), 9231-9238.

Schopf, J. W. (1992). The Proterozoic biosphere: a multidisciplinary study. Cambridge University Press.

Sharp, Z. D., Gibbons, J. A., Maltsev, O., Atudorei, V., Pack, A., Sengupta, S., Shock, E.L., & Knauth, L. P. (2016). A calibration of the triple oxygen isotope fractionation in the SiO_2-H_2O system and applications to natural samples. Geochimica et Cosmochimica Acta, 186, 105-119.

Shemesh, A., Kolodny, Y., & Luz, B. (1983). Oxygen isotope variations in phosphate of biogenic apatites, II. Phosphorite rocks. Earth and Planetary Science Letters, 64(3), 405-416.

Shemesh, A., Kolodny, Y., & Luz, B. (1983). Oxygen isotope variations in phosphate of biogenic apatites, II. Phosphorite rocks. Earth and Planetary Science Letters, 64(3), 405-416.

Shemesh, A., Kolodny, Y., & Luz, B. (1988). Isotope geochemistry of oxygen and carbon in phosphate and carbonate of phosphorite francolite. Geochimica et Cosmochimica Acta, 52(11), 2565-2572.

Shirey, S. B., Kamber, B. S., Whitehouse, M. J., Mueller, P. A., & Basu, A. R. (2008). A review of the isotopic and trace element evidence for mantle and crustal processes in the Hadean and Archean: Implications for the onset of plate tectonic subduction. Geological Society of America Special Papers, 440, 1-29.

Siever, R. (1992). The silica cycle in the Precambrian. Geochimica et Cosmochimica Acta, 56(8), 3265-3272.

Smart, K. A., Tappe, S., Stern, R. A., Webb, S. J., & Ashwal, L. D. (2016). A review of the isotopic and trace element evidence for mantle and crustal processes in the Hadean and Archean: implications for the onset of plate tectonic subduction. Nature Geoscience, 9, 255-259.

Smith, H. S., O'Neil, J. R., & Erlank, A. J. (1984). Oxygen isotope compositions of minerals and rocks and chemical alteration patterns in pillow lavas from the Barberton greenstone belt, South Africa. In Archaean Geochemistry (pp. 115-137). Springer Berlin Heidelberg.

Smith, W. E. (1960). The siliceous constituents of chert. Geologie en Mijnbouw, 39(1), 1-8.

Taylor, S. R., & McLennan, S. M. (1985). The continental crust: its composition and evolution.

Tonks, W. B., & Melosh, H. J. (1993). Magma ocean formation due to giant impacts. Journal of Geophysical Research: Planets, 98(E3), 5319-5333.

Urey, H. C. (1947). The thermodynamic properties of isotopic substances. Journal of the Chemical Society (Resumed), 562-581.

Urey, H. C., Lowenstam, H. A., Epstein, S., & McKinney, C. R. (1951). Measurement of paleotemperatures and temperatures of the Upper Cretaceous of England, Denmark, and the southeastern United States. Geological Society of America Bulletin, 62(4), 399-416.

van den Boorn, S. H., van Bergen, M. J., Nijman, W., & Vroon, P. Z. (2007). Dual role of seawater and hydrothermal fluids in Early Archean chert formation: evidence from silicon isotopes. Geology, 35(10), 939-942.

Van Kranendonk, M. J., Webb, G. E., & Kamber, B. S. (2003). Geological and trace element evidence for a marine sedimentary environment of deposition and biogenicity of 3.45 Ga stromatolitic carbonates in the Pilbara Craton, and support for a reducing Archaean ocean. Geobiology, 1(2), 91-108.

Veizer, J., Ala, D., Azmy, K., Bruckschen, P., Buhl, D., Bruhn, F., ... & Jasper, T. (1999). 87Sr/86Sr, δ13C and δ18O evolution of Phanerozoic seawater. Chemical geology, 161(1), 59-88.

Wallmann, K. (2001). The geological water cycle and the evolution of marine δ 18 O values. Geochimica et Cosmochimica Acta, 65(15), 2469-2485.

Wilde, S. A., Valley, J. W., Peck, W. H., & Graham, C. M. (2001). Evidence from detrital zircons for the existence of continental crust and oceans on the Earth 4.4 Gyr ago. Nature, 409(6817), 175-178.

Won, M. Z., & Below, R. (1999). Cambrian Radiolaria from the Georgina Basin, Queensland, Australia. *Micropaleontology*, 325-363.

Young, E. D., Galy, A., & Nagahara, H. (2002). Kinetic and equilibrium mass-dependent isotope fractionation laws in nature and their geochemical and cosmochemical significance. Geochimica et Cosmochimica Acta, 66(6), 1095-1104.

2. Methods

2.1 Terminology

Oxygen has three stable isotopes, with the following abundances:

- ^{16}O = 99.763 %

- ^{17}O = 0.0375 %

- ^{18}O = 0.1995 %

The oxygen isotope ratios in the current study are reported in the $\delta^{17}O$ and $\delta^{18}O$ notation (McKinney et al., 1950) relative to VSMOW2-SLAP2 linearized scale as reference. The terms and $\delta^{17}O$ and $\delta^{18}O$ are defined as follows:

$$\delta^i O_{standard}^{sample} = \left(\frac{\frac{^iO}{^{16}O}\,sample}{\frac{^iO}{^{16}O}\,standard} - 1 \right) \times 1000$$

Equation 1

In terrestrial rocks, variations in $\delta^{17}O$ are generally half of the respective variations in $\delta^{18}O$ (Craig, 1957). Linearized forms of $\delta^{17}O$ and $\delta^{18}O$ are written as $\delta'^{17}O$ and $\delta'^{18}O$ (Equation 2). Small deviations from an otherwise good correlation between $\delta'^{17}O$ and $\delta'^{18}O$ are displayed in form of the $\Delta'^{17}O$ notation. Here we use a reference line with slope λ_{RL} = 0.5305 and zero intercept (Wiechert et al., 2004; Pack and Herwartz, 2014). The $\Delta'^{17}O$ of VSMOW is 0‰ on that scale. The linearized forms of the δ^i, i.e., $\delta^i O$ and $\Delta'^{17}O$ terms are defined as:

$$\delta^i O_{\text{VSMOW2-SLAP2}} = 10^3 \ln \left(\frac{\delta^i O_{\text{VSMOW2-SLAP2}}}{10^3} + 1 \right)$$

$$\Delta'^{17}O = \delta'^{17}O_{\text{VSMOW2-SLAP2}} - 0.5305 \times 10^3 \ln \left(\frac{\delta^{18}O_{\text{VSMOW2-SLAP2}}}{10^3} + 1 \right)$$

$\delta^{17}O$, $\delta^{18}O$, and $\Delta'^{17}O$ is reported in per mil (‰) throughout the text.

The fractionation of an isotope between two coexisting substances or phases A and B can be defined by the fractionation factor α^i_{A-B} (Equation 4). Equilibrium fractionation in $^{17}O/^{16}O$ and $^{18}O/^{16}O$ between the two phases, expressed by the respective fractionation factors, are related to each other by the triple O-isotope fractionation exponent, θ_{A-B} (Equation 5). A plot of the $\delta'^{17}O$ vs $\delta'^{18}O$ values of A and B defines a line with a slope of θ_{A-B} :-

$$\alpha^{^iO/^{16}O}_{\text{A-B}} = \frac{(^iO/^{16}O)_\text{A}}{(^iO/^{16}O)_\text{B}}$$

$$\alpha^{^{17}O/^{16}O}_{A-B} = \left(\alpha^{^{18}O/^{16}O}_{A-B} \right)^{\theta_{A-B}}$$

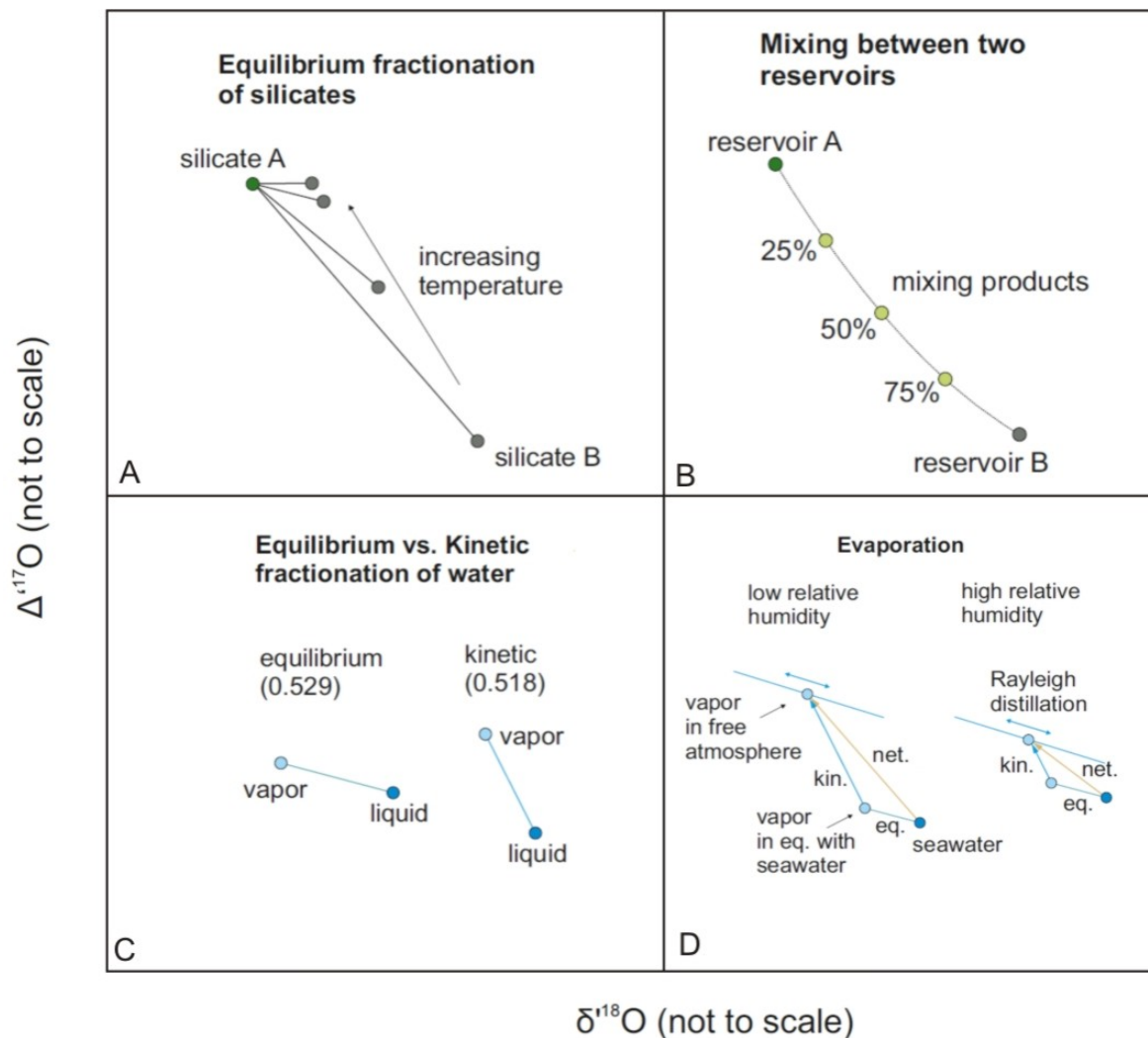A sketch showing different types of processes in the oxygen isotope systematics is shown in Figure 1

Figure 1 $\Delta'^{17}O$ vs $\delta'^{18}O$ sketches displaying different kinds of processes in the oxygen isotope systematics. Sketches are not to scale (modified after Herwartz et al., 2015, supplementary information). (A) The high-T limit of θ for equilibrium fractionation is 0.5305 (Matsuhisa et al., 1978; Young et al., 2002; Pack and Herwartz, 2014). With decreasing temperature, the equilibrium θ deceases, which is predicted by theory (Cao & Liu, 2011) and has been confirmed empirically (Pack and Herwartz, 2014; Sharp et al., 2016). (B) Mixing between two reservoirs, A and B, produces curves in δ' space (Miller, 2002). (C) Both equilibrium and kinetic fractionation processes follow straight lines in such a space. Kinetic processes have smaller θ values. According to definition, θ is the slope of lines in $\delta'^{17}O$ vs $\delta'^{18}O$ space. In $\Delta'^{17}O$ vs $\delta'^{18}O$ space these lines are transformed to lines with slope θ-0.5305 because of our definition of $\Delta'^{17}O$ and choice of reference line that has a 0.5305 slope and 0 intercept. The θ values for equilibrium and kinetic fractionations of water are well constrained. (D) Evaporation is a combination of kinetic and equilibrium fractionation processes, and the relative proportions of the two mechanisms depend on the relative humidity above the water body. Thus, the slope for net evaporation varies with relative humidity (Landais et al., 2006).

Both α and θ are, in general, functions of the phases in equilibrium (A,B) and temperature T (Matsuhisa et al., 1978; Young et al., 2002; Cao and Liu, 2011). So far only a few experimentally determined θ values have been published:

1. $\theta_{\text{CO}_2-\text{Water}}^{\text{equilibrium}}$: Hofmann et al. (2012) determined a θ value, for CO_2 - water equilibrium, of 0.522 ± 0.002, for temperature range 2 to 37°C. No temperature dependence was resolved. Barkan and Luz (2012) published a $\theta_{\text{CO}_2-\text{Water}}^{\text{equilibrium}}$ value at 25°C of 0.5229 ± 0.0001, with higher precision

2. $\theta_{\text{Vapour}-\text{Water}}^{\text{equilibrium}}$: Meijer and Li (1998) published θ values for equilibrium between water and evaporated water vapour. They determined a value of 0.5281 ± 0.0015. Later, Barkan and Luz (2005) determined a value of 0.529 ± 0.001 for $\theta_{\text{Vapour}-\text{Water}}^{\text{equilibrium}}$ over a temperature range of 11.4 to 41.5°C.

3. $\theta_{\text{Apatite}-\text{Water}}^{\text{equilibrium}}$: Using skeletal apatite of terrestrial mammals, Pack et al. (2013) published a $\theta_{\text{Apatite}-\text{Water}}^{\text{equilibrium}}$ value of 0.523 ± 0.002 at 37°C.

4. $\theta_{\text{SiO}_2-\text{Water}}^{\text{equilibrium}}$: For the silica-water equilibrium, the following two exist.

   a) $\theta_{\text{SiO}_2-\text{water}}^{\text{equilibrium}}(T) = \dfrac{-(740 \pm 290)}{T^2} + 0.5305$ by Pack and Herwartz (2014). This relation will be revised in this study.

   b) $\theta_{\text{SiO}_2-\text{water}}^{\text{equilibrium}}(T) = \dfrac{-(1.85 \pm 0.04)}{T} + 0.5305$ by Sharp et al. (2016) which is indistinguishable from a previous theoretical estimate by Cao and Liu (2011).

2.2 Normalization to the VSMOW2-SLAP2 scale

A two-point calibration scale, using reference materials VSMOW2 and SLAP2 (Coplen, 1995) was suggested in order to improve the inter-laboratory comparison of data and to account for the non-

linearity of the mass spectrometers (Gonfiantini, 1978; Schoenemann et al., 2013). Non-linearity effects of mass spectrometers come into consideration when materials having $\delta^{18}O$ tens of per mils away from that of the laboratory reference O_2 are measured. Very small non-linearity effects, in the range of 0.03 to 1.0 ppm per 1‰ $\delta^{18}O$ on the $\Delta'^{17}O$, have been noted for different laboratories (Barkan and Luz, 2005; Tanaka and Nakamura, 2013; Schoenemann et al., 2013; Lin et al., 2010; Li et al., 1988; Kusakabe and Matsuhisa, 2008).

The use of the $\Delta'^{17}O$ parameter incorporates significant discrepancies, of up to ~30 ppm (depending on $\delta^{18}O$) between laboratories when the data are not normalized on a two-point calibration scale. The idea discussed in this study, of using the $\Delta'^{17}O$ of cherts as an additional tool for answering key geological questions, requires much greater measurement precision than 30 ppm in $\Delta'^{17}O$ and accurately monitoring non-linearity effects is therefore crucial.

Vienna Standard Mean Ocean Water (VSMOW) and subsequently, VSMOW2, which was prepared to replace the exhausting VSMOW, has an assigned $\delta^{18}O$ and $\delta^{17}O$ value of 0 ‰. The $\delta^{18}O$ value of Standard Light Antarctic Precipitation 1 (SLAP2), on the basis of measurements in 114 laboratories worldwide until 1976, is -55.5 (Gonfiantini, 1978). SLAP2 has been measured later as well and the same $\delta^{18}O$ has been observed (Barkan and Luz, 2005; Schoenemann et al., 2013; Steig et al., 2014). But the $\delta^{17}O$ value of SLAP2 is an assigned value of -29.6987‰ (Schoenemann et al., 2013) and is not necessarily the true composition of SLAP2. This is one inherent problem of this normalization method and renders measured values incomparable with theory. Because of this reason Tanaka and Nakamura (2013) did not adopt the two-point calibration method of data normalization.

In this study, we have chosen the -29.6987‰ value (Schoenemann et al., 2013) for $\delta^{17}O$ of SLAP2. This value is calculated from an assigned value of 0 ppm for $\Delta'^{17}O$ of SLAP2, using a reference line with slope 0.528. The $\delta^{18}O$ value of SLAP2 is taken as -55.5‰ (Gonfiantini, 1978). We then broadly follow the strategy of Schoenemann et al. (2013) for normalizing our data. This is the same approach as followed by Pack et al. (2016) :-

$$\delta^i O_{\text{VSMOW2}-\text{SLAP2}}^{\text{sample}} = \frac{-\delta^i O_{\text{VSMOW2}}^{\text{SLAP2,assigned}}}{\delta^i O_{\text{raw}}^{\text{VSMOW2}} - \delta^i O_{\text{raw}}^{\text{SLAP2}}} \cdot$$
$$(\delta^i O_{\text{raw}}^{\text{sample}} - \delta^i O_{\text{raw}}^{\text{VSMOW2}})$$

Equation 6

We have measured both VSMOW2 and SLAP2 in our laboratory (Pack et al., 2016) using the same extraction line and mass spectrometer as those that were used for the chert samples. We observed a non-linearity of 1 ppm per 0.9‰ $\delta^{18}O$, significantly higher than the 0.2 to 0.6 ppm per 1‰ $\delta^{18}O$ range observed by (Barkan and Luz, 2005; Tanaka and Nakamura, 2013; Schoenemann et al., 2013; Lin et al., 2010; Li et al., 1988; Kusakabe and Matsuhisa, 2008;). Our non-linearity is similar to Jabeen and Kusakabe (1997) who also observed ~1 ppm per 1‰ $\delta^{18}O$. Our silica and chert data have a large spread in $\delta^{18}O$, from 15‰ to 40‰. This means for a sample with $\delta^{18}O$ = 40‰ a correction of 36 ppm on the $\Delta'^{17}O$ value of that sample is required to get rid of non-linearity effects. So, we have applied this correction and report all data on VSMO2-SLAP2 scale.

2.3 Analytical procedures

2.3.1 Fluorination in conventional Ni-bombs

Baertschi and Silverman (1951) first proposed two fluorination techniques for extracting oxygen from silicate rocks. They used ClF_3+H_2 or F_2+HF as fluorinating agents. Reactions were run at a temperature of 420°C. The method with F_2 as a reagent and HF as a catalyst was found to be more reproducible in the study and was later employed by others (e.g., Silverman, 1951). The $^{18}O/^{16}O$ ratios were determined with an uncertainty of ± 0.2 per mil via this method. Later, Taylor and Epstein (1962) extended this method to study $\delta^{18}O$ values of individual mineral phases of silicate rocks. Soon afterwards, Clayton and Mayeda (1963) introduced a fluorination technique using BrF_5 as fluorinating agent in order to release oxygen gas from oxides and silicates. Samples were fluorinated inside pure Ni reaction tubes (14 mm outer diameter, 3 mm wall thickness, 30cm length) at 450°C and for 12 hours for quartz, micas and feldspars. Better oxygen yields, consequently leading to smaller uncertainties in the measured isotope ratios, i.e., ±0.07 to ± 0.26 for sandstones, quartzites and pegmatite quartz samples were the advantages of this method over the previous ones. Additionally, BrF_5 is a reagent easier and safer to handle in the lab than F_2 and is readily purified. Most of the chert samples in the present study were fluorinated following the technique of Clayton and Maeda (1963). The steps involved are presented and discussed in brief here.
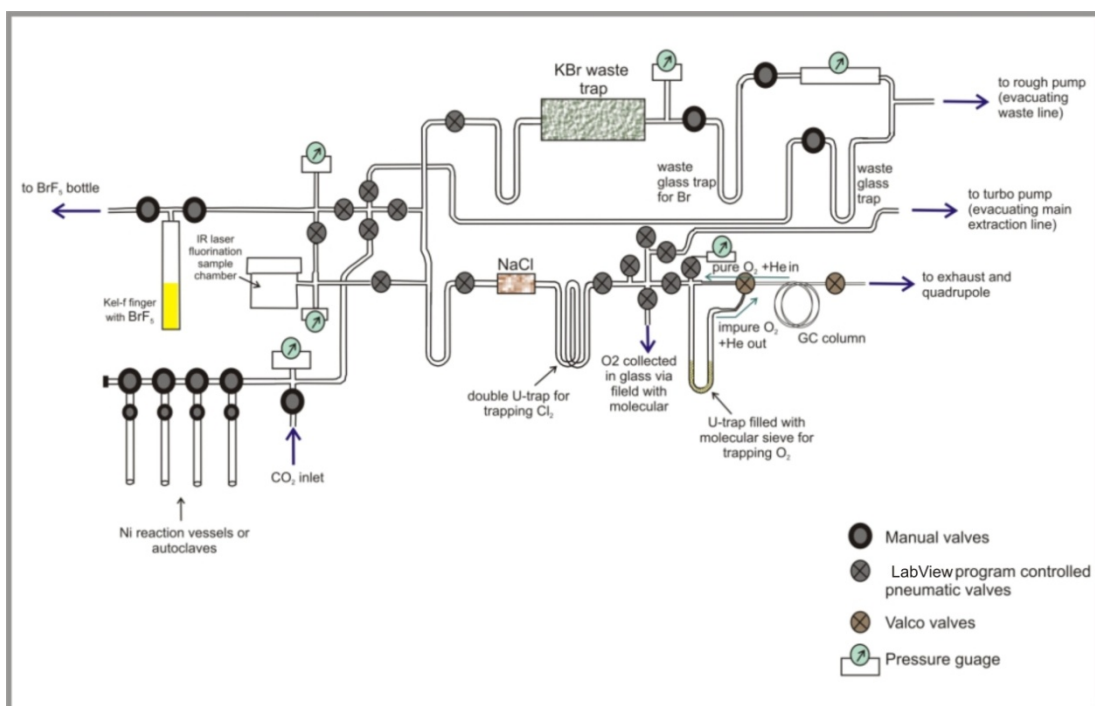
Figure 2 Schematic representation of the fluorination and extraction setup used in the study. The different U-traps are used to trap condensable gases by freezing the traps with liquid N_2. In order to trap O_2 molecular sieve balls at liquid N_2 temperatures are used. The setup consists broadly of two parts – the main extraction line, evacuated using a Turbo pump and the waste line, evacuated using a rough pump. The waste line is used to convert leftover unreacted BrF_5 to Br (by passing through heated KBr salt).

A simplified diagram of the extraction line is given in Figure 2. The reaction vessels or autoclaves, i.e., Ni-bombs (14 mm outer diameter, 3 mm wall thickness, 30 cm length), along with the entire reaction and extraction setup, are first well evacuated until the pressure in the line is in the 10^{-4} mbar range. Small chips ($\sim$5 cm) of the quartz or chert samples were first hand-picked to avoid weathered parts or coarse vein quartz. For some samples small cores ($\sim$ 3 cm long, $\sim$ 0.2 mm diameter) were drilled out from the hand specimens. Chert samples were coarsely crushed and treated with 10N HCl for 5 mins, in order to remove any carbonate components that may be present. Samples were then washed with ethanol and distilled water. The samples were dried and then crushed to a fine powder. For loading the quartz powders the bombs were filled with Ar first, then quickly unscrewed from the reaction line and set up again after pouring in the sample powder through a glass chute, such that the sample reached the bottom of the bombs. Sample powders of 5-12 mg were used. After the bombs are mounted back onto the extraction line, BrF_5 is introduced into the bombs, one at a time. By opening the valve to the BrF_5 inlet,

the BrF_5 is expanded between the cross volume and the T-volume (connecting the way to laser fluorination and NaCl cell) to a pressure of 500 mbar (in excess to that required for fluorination). The valve to the BrF_5 reservoir is then closed and the expanded BrF_5 is frozen into the bomb within a few seconds. The bomb is closed and ones all other bombs have been filled in this way, individual heating furnaces are used for each bomb to assist the reaction. The reaction is carried out at a temperature of 650°C for 18 to 20 hrs (O'Neil and Epstein, 1966).

2.3.2 Laser fluorination

Some chert samples were analyzed via laser fluorination using either F_2 or BrF_5 as fluorinating agents (Sharp, 1990). Selecting sample fractions, pre-treatment to clean and remove carbonate components is same as in Section 2.3.1. The O_2 gas was cleaned by passing it through a gas chromatography (GC) column. Oxygen isotope ratios were measured using the same method as for the other samples.

Special care was taken during the analysis of the diatoms. A stepwise fluorination was performed using F_2 in order to strip off isotopically light oxygen bound to their siliceous cells or frustules (Dodd and Sharp, 2010). It was attempted to remove this layer via stepwise pre-fluorination. The diatoms samples were allowed to react with F_2, in pulses of ~1 hour, for total two-three hours. After every ca. 1 hour step the sample chamber was evacuated and fresh F_2 was introduced.

2.3.3 O_2 collection after release via fluorination

The procedure of O_2 extraction for techniques 2.3.1 and 2.3.2 is the same.

The bombs are cooled down using liquid nitrogen, in order to freeze in all leftover excess BrF_5, HF and SiF_4. The bombs are opened one at a time, and the O_2 inside are allowed to expand. The gases are allowed to pass through a salt chamber containing NaCl, heated to 200°C , where any fragments of non-condensable F_2, which maybe a part of the reaction products, reacts away to form NaF and chlorine. The gases are then passed through a double U-trap, cooled with liquid nitrogen. Cl_2 is trapped here. The major

gas remaining now is oxygen along with impurities in trace amounts – gases like N_2 and NF fragments. These impurities need to be removed, in particular the NF fragments, which otherwise interfere with $\delta^{17}O$ measurements in the mass spectrometer.

2.3.4 GC cleaning to obtain pure O_2

The impure O_2 is cleaned by passing the gas through a 5 Å, 10 m long, 0.05 mm inner diameter packed gas chromatography column at room temperature (30°C) or at -40°C, depending on the amount of oxygen expected from the sample. The gas is carried in a He stream; the flow rate is always set to 20 ml/min and is controlled via a flow-meter. At the end of the GC cycle a mass-spectrometer, Finnigan MAT 253, is used to detect gases O_2 (mass 32), N_2 (mass 28), Ar (mass 40), CO_2 (mass 44)and NF2 fragment (mass 52) according to their mass/charge ratios and track their separation times. The gases exit the GC at different times and a set of Valco valves (Figure 2) are used to trap only the oxygen coming out of the GC and not the other impurities like N_2 and NF_3. These impurities interfere with measurement of the rare ^{17}O isotope within the oxygen gas and must be separated out before the gas is measured in the mass spectrometer.

The purified O_2 is frozen within a calibrated volume of the extraction line so that the number of moles of the extracted gas maybe quantified. The pressure of the gas in the calibrated volume is measured by an MKS Baratron manometer (reliable range: 0.01 – 140 mbar; absolute range 170 mbar). Since the number of moles of each samples used is known, the number of moles of O_2 finally extracted – calculated from the pressure measured in this step – maybe used to calculate the yield of the fluorination reaction with respect to O_2, i.e., how much percentage of the O_2 present within the sample has been successfully extracted. The aim is to reach 100% in order to avoid fractionation and be able to measure the real $\delta^{18}O$ and $\delta^{17}O$ of the sample.

The clean O_2 gas was finally analyzed in the dual inlet mode of a Thermo MAT 253 gas source mass spectrometer for at least 4 blocks of 20 cycles each in order to obtain high precision data, i.e, ~5 ppm (1σ S.D.) uncertainty on $\Delta'^{17}O$.

2.3.5 Trace element analysis

Selecting sample fractions, pre-treatment to clean and remove carbonate components is same as in Section 2.3.1. After pulverizing with an agate mortar, the sample powders (100 – 1000 mg sample size) were digested in concentrated HF + $HClO_4$ + HNO_3 (3 ml HF, 3 ml $HClO_4$, ~0.5 ml HNO_3 or H_2O_2 for 100 mg sample) at 180°C for 24 hours. The sample solutions were dried out and then diluted in 2% HNO_3 (internal standards 200 ppb ^{9}Be, 20 ppb ^{102}Rh, 10 ppb ^{115}In and 20 ppb ^{185}Re). The solution was analyzed using Perkin Elmer DRC II inductively coupled plasma mass spectrometer (ICP-MS) (SCIEX, Canada). Total 8 calibration points were used and matrix matched. The accuracy was controlled by the SRM standard JA-2 (from Japan). In total 59 elements were analyzed (Li, B, Na, Mg, Al, P, K, Ca, Sc, Ti, V, Cr,Mn, Fe, Co, Ni, Cu, Zn, Ga, Ge, As, Se, Rb, Sr, Y, Zr, Nb, Mo, Cd, Sm, Sb, Te, I, Cs, Ba, La, Ce, Pr, Nd, Sm, Eu, Gd, Tb, Dy, Ho, Er, Tm, Yb, L, Hf, Ta, W, Ir, Pt, Tl, Pb, Bi, Th, U). The detection limit was 1 ppb. The uncertainty is ~5-10%.

2.4 References

Baertschi, P., & Silverman, S. R. (1951). The determination of relative abundances of the oxygen isotopes in silicate rocks. Geochimica et Cosmochimica Acta, 1(4), 317-328.

Barkan, E., & Luz, B. (2005). High precision measurements of ^{17}O/^{16}O and ^{18}O/^{16}O ratios in H_2O. Rapid Communications in Mass Spectrometry, 19(24), 3737-3742.

Barkan, E., & Luz, B. (2012). High-precision measurements of ^{17}O/^{16}O and ^{18}O/^{16}O ratios in CO_2. Rapid Communications in Mass Spectrometry, 26(23), 2733-2738.

Cao, X., & Liu, Y. (2011). Equilibrium mass-dependent fractionation relationships for triple oxygen isotopes. Geochimica et Cosmochimica Acta, 75(23), 7435-7445.

Clayton, R. N., & Mayeda, T. K. (1963). The use of bromine pentafluoride in the extraction of oxygen from oxides and silicates for isotopic analysis. Geochimica et cosmochimica acta, 27(1), 43-52.

Coplen, T. B. (1995). Reporting of stable hydrogen, carbon, and oxygen isotopic abundances. Geothermics, 24(5), 707-712.

Craig, H. (1957). Isotopic standards for carbon and oxygen and correction factors for mass-spectrometric analysis of carbon dioxide. Geochimica et cosmochimica acta, 12(1), 133-149.

Dodd, J. P., & Sharp, Z. D. (2010). A laser fluorination method for oxygen isotope analysis of biogenic silica and a new oxygen isotope calibration of modern diatoms in freshwater environments. Geochimica et Cosmochimica Acta, 74(4), 1381-1390.

Gonfiantini, R. (1978). Standards for stable isotope measurements in natural compounds.

Herwartz, D., Pack, A., Krylov, D., Xiao, Y., Muehlenbachs, K., Sengupta, S., & Di Rocco, T. (2015). Revealing the climate of snowball Earth from $\Delta^{17}O$ systematics of hydrothermal rocks. Proceedings of the National Academy of Sciences, 112(17), 5337-5341.

Hofmann, M. E., Horváth, B., & Pack, A. (2012). Triple oxygen isotope equilibrium fractionation between carbon dioxide and water. Earth and Planetary Science Letters, 319, 159-164.

Jabeen, I., & Kusakabe, M. (1997). Determination of $\delta^{17}O$ values of reference water samples VSMOW and SLAP. Chemical Geology, 143(1), 115-119.

Kusakabe, M., & Matsuhisa, Y. (2008). Oxygen three-isotope ratios of silicate reference materials determined by direct comparison with VSMOW-oxygen. Geochemical Journal, 42(4), 309-317.

Landais, A., Barkan, E., Yakir, D., & Luz, B. (2006). The triple isotopic composition of oxygen in leaf water. Geochimica et cosmochimica acta, 70(16), 4105-4115.

Li, W., Ni, B., Jin, D., & Zhang, Q. (1988). Comparison of the oxygen-17 abundance in three international standard waters. Huaxue Tongbao, 6, 39-40.

Lin, Y., Clayton, R. N., & Gröning, M. (2010). Calibration of $\delta^{17}O$ and $\delta^{18}O$ of international measurement standards–VSMOW, VSMOW2, SLAP, and SLAP2. Rapid Communications in Mass Spectrometry, 24(6), 773-776.

Matsuhisa, Y., Goldsmith, J. R., & Clayton, R. N. (1978). Mechanisms of hydrothermal crystallization of quartz at 250 C and 15 kbar. Geochimica et Cosmochimica Acta, 42(2), 173-182.

McKinney, C. R., McCrea, J. M., Epstein, S., Allen, H. A., & Urey, H. C. (1950). Improvements in mass spectrometers for the measurement of small differences in isotope abundance ratios. Review of Scientific Instruments, 21(8), 724-730.

Meijer, H. A. J., & Li, W. J. (1998). The use of electrolysis for accurate $\delta^{17}O$ and $\delta^{18}O$ isotope measurements in water. Isotopes in Environmental and Health Studies, 34(4), 349-369

Miller, M. F. (2002). Isotopic fractionation and the quantification of ^{17}O anomalies in the oxygen three-isotope system: an appraisal and geochemical significance. Geochimica et Cosmochimica Acta, 66(11), 1881-1889.

O'Neil, J. R., & Epstein, S. (1966). A method for oxygen isotope analysis of milligram quantities of water and some of its applications. Journal of Geophysical Research, 71(20), 4955-4961.

Pack, A., & Herwartz, D. (2014). The triple oxygen isotope composition of the Earth mantle and understanding variations in terrestrial rocks and minerals. Earth and Planetary Science Letters, 390, 138-145.

Pack, A., Gehler, A., & Süssenberger, A. (2013). Exploring the usability of isotopically anomalous oxygen in bones and teeth as paleo-CO_2-barometer. Geochimica et Cosmochimica Acta, 102, 306-317.

Pack, A., Tanaka, R., Hering, M., Sengupta, S., Peters, S., & Nakamura, E. (2016). The oxygen isotope composition of San Carlos olivine on the VSMOW2-SLAP2 scale. Rapid Communications in Mass Spectrometry, 30(13), 1495-1504.

Schoenemann, S. W., Schauer, A. J., & Steig, E. J. (2013). Measurement of SLAP2 and GISP $\delta^{17}O$ and proposed VSMOW-SLAP normalization for $\delta^{17}O$ and ^{17}O excess. Rapid Communications in Mass Spectrometry, 27(5), 582-590.

Sharp, Z. D. (1990). A laser-based microanalytical method for the in situ determination of oxygen isotope ratios of silicates and oxides. Geochimica et Cosmochimica Acta, 54(5), 1353-1357.

Silverman, S. R. (1957). The isotope geology of oxygen. Geochimica et Cosmochimica Acta, 2(1), 26-42.

Steig, E. J., Gkinis, V., Schauer, A. J., Schoenemann, S. W., Samek, K., Hoffnagle, J., Dennis, K.J. & Tan, S. M. (2014). Calibrated high-precision ^{17}O-excess measurements using cavity ring-down spectroscopy with laser-current-tuned cavity resonance. Atmospheric Measurement Techniques, 7(8), 2421-2435.

Tanaka, R., & Nakamura, E. (2013). Determination of ^{17}O-excess of terrestrial silicate/oxide minerals with respect to Vienna Standard Mean Ocean Water (VSMOW). Rapid Communications in Mass Spectrometry, 27(2), 285-297.

Taylor, H. P., & Epstein, S. (1962). Relationship between O^{18}/O^{16} ratios in coexisting minerals of igneous and metamorphic rocks part 1: principles and experimental results. Geological Society of America Bulletin, 73(4), 461-480.

Wiechert, U. H., Halliday, A. N., Palme, H., & Rumble, D. (2004). Oxygen isotope evidence for rapid mixing of the HED meteorite parent body. Earth and Planetary Science Letters, 221(1), 373-382.

Young, E. D., Galy, A., & Nagahara, H. (2002). Kinetic and equilibrium mass-dependent isotope fractionation laws in nature and their geochemical and cosmochemical significance. Geochimica et Cosmochimica Acta, 66(6), 1095-1104.

3. Mass balance model for the triple oxygen isotope composition of the oceans

3.1 Introduction

Low $\delta^{18}O$ values observed in ancient marine chemical sediments, tens of per mil lower than modern day, inspired the idea of seawater with lower $\delta^{18}O$ values ($\delta^{18}O^{SW}$) in the past, as proposed first by Weber (1965). The $\delta^{18}O^{SW}$ is currently buffered primarily by low and high-T interactions of oceanic crust by seawater (e.g., Muehlenbachs and Clayton, 1976; Holmden and Muehlenbachs, 1993). But some geochemical modeling studies suspect that the high-T : low-T alteration processes on Earth may have varied over time (e.g., Wallmann, 2000). A relatively lower proportion of hydrothermal alteration, relative to low-T alteration would have lowered the $\delta^{18}O$ of the ancient oceans (Veizer et al., 1996; Lécuyer and Allemand, 1999; Wallmann, 2001; Kasting et al., 2006; Jaffrés et al., 2007). Extremely low $\delta^{18}O^{SW}$ values ($\sim$-10‰) (as modeled by studies like Wallmann, 2001 and Jaffrés, 2007) would only result from significantly different geological conditions of the early Earth for e.g., slow rates of seafloor spreading or even complete cessation of plate tectonics. A lower seafloor spreading rate would reduce magnitudes of both high and low-T alteration. Reduced crust permeability would reduce low-T weathering, whereas lower seawater recycling and hydrothermal circulation at subduction zones would lead to reduced hydrothermal alteration of the oceanic crust (Fornari and Embley, 1995; Wallmann, 2001). The net effect is a decreased high-T : low-T alteration ratio (Holland 1984, pp. 242;

Wallmann, 2001). Shallower depths of mid-ocean ridge crests (Walker and Lohmann, 1989; Kasting et al., 2006) would mean less pressure within the axial hydrothermal systems, and less effective high-T fluid circulation within the systems. Consequently, lesser penetration depths and lower water temperatures at the ridges would decrease the amount of oceanic crust exposed to hydrothermal alteration (Kasting et al., 2006). Additionally, circulating fluids operating at lower than critical pressure would boil off more frequently. Other factors like higher Archean pCO_2 levels and availability of greater proportions of greenstones would have favored greater continental low-T weathering thereby reducing the effect of hydrothermal alteration flux on seawater (Jaffrés et al., 2007 and references therein).

However, not all scientists find dramatically different $\delta^{18}O^{SW}$ in the past feasible. Instead, it is argues that seawater is buffered, in the long term, to $0 \pm 2‰$ (Muehlenbachs and Clayton, 1972a; Muehlenbachs, 1998).

In this study we investigate not only the $\delta^{18}O^{SW}$ but also the $\delta^{17}O^{SW}$ and $\Delta'^{17}O^{SW}$ values of low and high-T altered oceanic crust, shale as product of weathering and ultimately the of modern day seawater. We shall also model how $\delta^{17}O^{SW}$ would have changed in the past if the $\delta^{18}O^{SW}$ was indeed lower than at present.

3.2 The triple oxygen isotope compositions of major reservoirs - mantle, MORB and seawater

The $\delta^{18}O$ isotopic compositions of the major reservoirs on Earth (mantle, oceanic crust and seawater) are known. Recent studies have investigated the $\delta^{17}O$ composition of mantle (Pack and Herwartz, 2014; Pack et al., 2016) and seawater (Luz and Barkan, 2010). These values obtained by these studies are reviewed below and then used to estimate the $\delta^{17}O$ composition of MORB and of seawater in an ice-free world. The inferred $\delta^{17}O$ values are used for the purpose of mass balance modeling in 3.6.

3.2.1 Mantle and MORB

The present day isotopically homogenous mantle composition has an average $\delta^{18}O$ = 5.5‰ (Mattey et al., 1994) and $\Delta'^{17}O$ = -50 ± 1ppm (SE) (from study of San Carlos Olivine in Pack et al., 2016). This determines the composition of the oceanic crust, which is a huge reservoir of oxygen being constantly renewed through the processes like low and high-T alteration of oceanic crust and continental weathering. The mantle derived oceanic crust has constant worldwide $\delta^{18}O_{SMOW}$ = 5.8 ± 0.3‰ (Muehlenbachs, 1998). The $^{17}O/^{16}O$ ratio of one pristine MORB glass sample was measured by Pack and Herwartz, 2014. The triple oxygen isotope values of the sample are – $\delta^{18}O$ = 5.70 ± 0.07‰, $\delta^{17}O$ = 2.97 ± 0.04‰ and $\Delta'^{17}O$ = -0.052 ± 0.006‰ (corrected according to Pack et al., 2016) (see section 2.2 in Chapter 2, for correction procedure). The $\Delta'^{17}O$ of this sample is identical to the mantle value within uncertainty. So, we use $\Delta'^{17}O^{MORB}$ = -0.050‰ in this study. Using this $\Delta'^{17}O^{MORB}$ value, along with a $\delta^{18}O^{MORB}$ = 5.8‰ we calculate $\delta^{17}O^{MORB}$ = 3.023‰ and use this value throughout the text (Table 2).
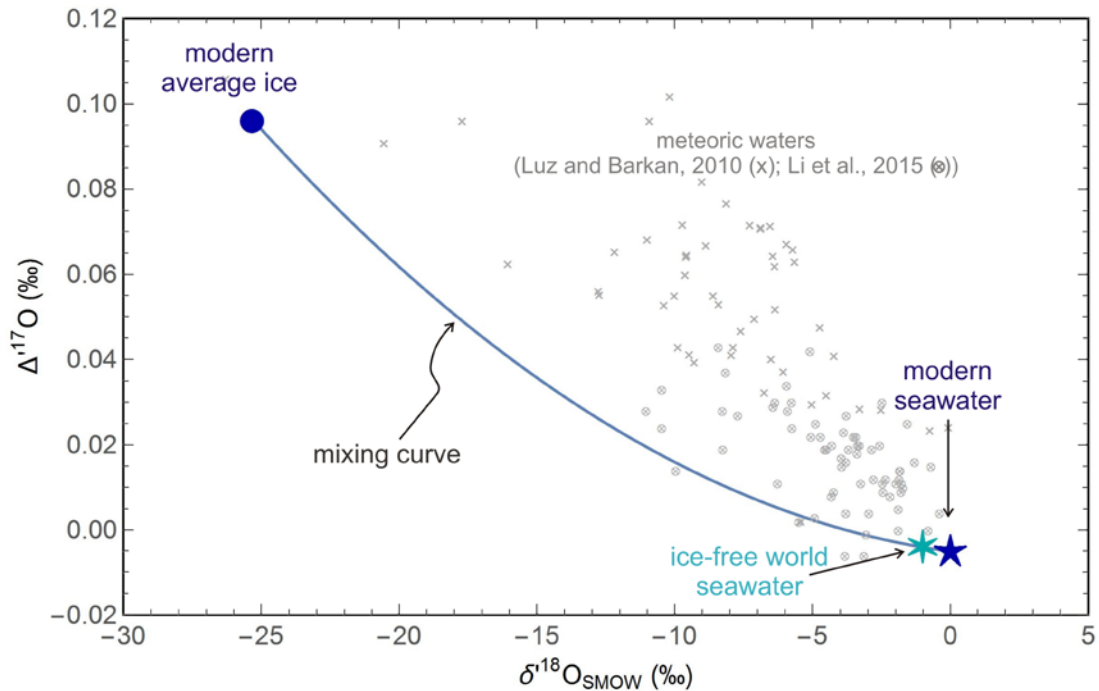
3.2.2 Modern seawater

The $\delta^{18}O$ of global seawater $\delta^{18}O^{SW}$ is currently in steady state (Li, 1972) - controlled largely by the interaction of seawater with oceanic crust and in general by isotopic exchange with silicate rocks (Muehlenbachs and Clayton, 1976; Muehlenbachs, 1998). Present day $\delta^{18}O$ values of seawater from around the globe and different water depths show a range of $\delta^{18}O$ from -1.5 to 1.8‰ with respect to VSMOW (compiled by Jaffrés et al., 2007; cf. Carpenter and Lohmann, 1995: Table 1). The average value of $\delta^{18}O^{SW}$ is ~0.28 ± 0.5‰ with respect to VSMOW (Shackleton and Kennet, 1975). A value of 0‰ is used in this study; this does not affect any results of the model within uncertainty.

The change in $\delta^{17}O$ of seawater ($\delta^{17}O^{SW}$), and subsequently the seawater $\Delta'^{17}O$ ($\Delta'^{17}O^{sw}$), is closely coupled to changes in the $\delta^{18}O^{SW}$ and guided by the slopes of the individual fractionation processes (Pack and Herwartz, 2014). Luz and Barkan (2010) carried out high-precision analyses of 38 seawater samples from Atlantic Ocean, Pacific Ocean, Mediterranean and northern Red Sea for their triple oxygen isotope composition and found average $\Delta'^{17}O^{sw}$ = -0.005 ± 0.001‰, i.e., -5 ± 1 ppm. We use this value for the ^{17}O composition of seawater in this study.

3.2.3 Ice-free world seawater

An important point to be taken into consideration while dealing with the triple oxygen isotope composition of the modern oceans is that currently about 1.7% of all water on Earth is trapped in ice and snow (Glecik, 1996). Ice caps trap the lighter oxygen isotopes preferentially over the heavier ones because high latitude precipitation is significantly depleted in heavy isotopes. Therefore, an ice-free world is expected to have lighter $\delta^{17}O^{SW}$ and $\delta^{18}O^{SW}$ values than at present. Decrease in $\delta^{18}O^{SW}$ of up to -1‰ was estimated by Shackleton and Kennet (1975). Later, Schrag et al. (2002) conducted analysis of pore fluids trapped in deep-sea sediments, from the North and South Atlantic oceans – providing direct measurements on how bottom water oxygen isotopic compositions changed during the Last Glacial Maximum (LGM) (26,500 to 19,000-20,000 years ago, Clark et al., 2009). This study confirmed the previously estimated ice-free world $\delta^{18}O^{SW}$ = -1 ± 0.1‰. Lhomme et al. (2005) employed numerical modelling of ice dynamics and tracer transport in order to estimate ice-sheets $d^{18}O$ over last 20,000 years – an ice-free world of ~-1.4‰ was proposed. Overall, secular variations in global $\delta^{18}O^{SW}$ do not exceed 0 ± 1‰ (Shackleton and Kennet, 1975). So, we take $\delta^{18}O$ of -1 ‰ for an ice-free world seawater.

Figure 1 Plot of $\Delta'^{17}O$ vs $\delta'^{18}O$ showing mixing between modern seawater (five pointed dark blue star) and modern average ice (dark blue dot). If all the ice trapped in glaciers today were to melt and mix with seawater then we would have an ice-free world with $\delta^{18}O$ = -1 ± 0.1‰ and $\Delta'^{17}O$ = -0.004‰ (light blue star).

A lower $\delta^{18}O^{SW}$ of an ice-free world means the $\delta^{17}O^{SW}$ would also have been lower than today. We assume that the average continental ice $\delta^{18}O$ is -25‰. The meteoric water dataset of Luz and Barkan (2010) includes measurements of triple oxygen isotopes in light snow ($\sim$26‰ $\delta^{18}O$). Based on their data, a light meteoric water of -25‰ would have $\delta^{17}O$ = -13.246‰ and $\Delta'^{17}O$ = 0.096‰. A mixing curve between this data point, representing average ice, and modern seawater in the $\Delta'^{17}O$ vs $\delta'^{18}O$ space is shown in Figure 1. For an ice-free world we adopt $\delta^{18}O$ value of -1‰ and the corresponding $\Delta'^{17}O$ value of an ice- free world can be calculated from this mixing relationship. The values for ice-free (IF) ocean are: $\delta^{17}O$ = -0.535‰ and $\Delta'^{17}O^{IF}$ = -0.004 ± 0.003‰.

On longer timescales, the isotopic composition of the ocean is controlled by isotopic exchange with the oceanic crust. Low temperature alteration drives the $\delta^{18}O^{SW}$ to lower values while high temperature alteration has the opposite effect. While these systematics are well understood for

δ^{18}O (Muehlenbachs, 1976; Muehlenbachs, 1998; Wallmann, 2001; Kasting et al., 2006; Jaffrés et al., 2007), empirical data for alteration processes in triple oxygen isotope fractionation is sparse (Pack and Herwartz, 2014). To quantitatively model the steady state between seawater and oceanic crust, accurate data on high and low T alteration is required. Respective analyses are presented in the following sections.

3.3 Materials and Methods

3.3.1 Oceanic crust samples

3.3.1.1 General information

We have analyzed oceanic crust samples from two boreholes of the Integrated Ocean Drilling Program (IODP) and Deep Sea Drilling Program (DSDP)/Ocean Drilling Program (ODP). Cold upper crust samples, altered at low temperatures (<50°C) were chosen from Hole U1383 in the Atlantic Ocean. From the second location, i.e., Hole 504B, an extensively studied site (Alt et al., 1986; 1995; Bach et al., 1996), hot mid-crust samples were chosen which have been hydrothermally altered at high temperatures (>250°C).

3.3.1.2 Hole U1383C

Site U1383 of the Integrated Ocean Drilling Program (IODP) is situated in 4414 m water depth in the North Pond area of the North Atlantic Ocean. The North Pond, an area of elevated conductive heat flow, is a sediments ''pond'' on the western flank of the Mid-Atlantic Ridge, overlying ~8 Ma old basaltic crust (Orcutt et al., 2013).

The borehole U1383C in this site has coordinates 22°48.1241' N ; 46°03.1662' W. The sediment/basement interface at the hole was encountered at 38.3 mbsf. The lithology within this borehole below 164 mbsf, where our samples hail from, comprises glassy to variolitic to cryptocrystalline

basalts (mostly pillow flows) with variable degrees of low temperature alteration or seafloor weathering.

3.3.1.2.1   Sample U1383C-13R1W_109-112

This sample comes from Core 13R1, section1 of the borehole and is extracted from a depth of 173.82 mbsf, within sub-unit 3-6. This sub-unit is described in the core description records of IODP as aphyric (lacking phenocrysts) to sparsely/moderately phyric pillow lava. Average vein width is ~ 0.2mm (0.6 mm maximum) with mainly grayish brown halos (~11mm average width). Vein filling is 25% smectite, 25% carbonate, 25% FeOx/iddingsite, 25% zeolite (IODP core report). Chilled margins with variable extents of palagonitization (~50%) with reddish brown to light green alteration are seen. Massive gray basalt with plagioclase phenocrysts generally develop brown alteration halos are present along exposed veins.

Based on visual estimates, sample U1383C 13R1W 109-112 is about 10% altered (IODP core report).

3.3.1.2.2   Sample U1383C-31R2W_45-49

This sample comes from core 31R, section 2 of the borehole and is extracted from a depth of 313.99 mbsf, within lithologic unit 3-28. This unit is composed of aphyric pillow lava. Veins of average and maximum width ~ 0.3 mm, with dark to grayish brown halos are present within the pillows. The vein fillings include 20% smectite, 40% carbonate, 20% FeOx/iddingsite and 20% zeolites (from core IODP core descriptions).

The degree of overall alteration in this sample, based on visual estimation, is about 20% (IODP core report).

3.3.1.2.3 Sample U1383C 32R3W 1-4

This sample is from a depth of 324.31 mbsf within Core 32R, Section 3 of U1383C borehole, lithologic unit 3-29. This unit is not well described in the IODP core description logs. It may be a breccia / pseudobreccia.

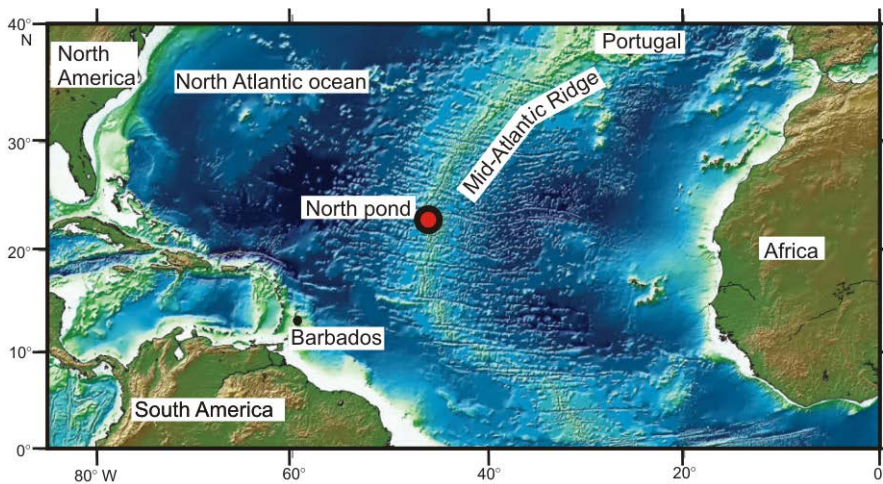The sample is very heavily altered, ~ 80% from visual estimates (IODP core report).

Figure 2 Location of the North Pond area in the North Atlantic Ocean, the site where IODP Hole U1383C is situated. The image is modifies from IODP Expidition 336 Preliminary Report.

3.3.1.3 Hole 504B

We have analyzed high temperature altered oceanic samples from Leg 83 of DSDP/ODP Hole 504B (01°13.63' N ; 83°43'.81' W). This borehole is located 200 km south of the Costa Rica Rift spreading centre in the east equatorial Pacific.

Our samples come from depths of ~1090 to 1350 m – the region of upper sheeted dolerite dikes complex (SDC) (the SDC extends from 1055 to >2111 mbsf) within a 6 Ma old oceanic crust.

The upper SDC (down to 1500 mbsf) is variably altered to the Greenschist facies. Alteration is highly heterogeneous and most intense along the chlorite ± actinolite veins in the form of cm-sized, light gray alteration patches which may represent areas of increased primary porosity (Alt

et al., 1996a; Bach et al., 2003). The sequence of vein mineral precipitation is (1) chlorite ± actinolite ± titanite, (2) quartz ± epidote ± sulfide, and (3) zeolite, prehnite, or anhydrite (Bach et al., 2003; Alt et al., 1996). An overall increasing alteration temperature >250°C and lowering water/rock ratios with increasing depth has been noted (Bach et al., 2003).

3.3.1.3.1 Sample 504B 141R1W 76-85

This sample belongs to Core 122R of Hole 504B, Section 1, Piece 7, Litho zone SDC, Litho type B. it comes from a depth of 1214.3 mbsf. The sample is a diabase breccia wherein the olivine has been completely altered to chlorite. The plagioclase fractions show high alteration to chlorite, albite, and quartz whereas the clinopyroxene is heavily altered to chlorite and actinolite. The matrix of the rock is completely chloritized. The extent of alteration, from visual estimates, is 80%.

3.3.1.3.2 Sample 504B 141R1W 50-57

This sample belongs to Core 141R of Hole 504B, Section 1, Piece 7, Litho zone SDC, Litho type B, retrieved from a depth of 1350.3 mbsf. The sample is a chilled margin breccia, which is completely chloritized and contains very fine grained rock fragments. Voids and vein fillings include cement of prehnite, chlorite, and anhydrite. Based on visual estimates this sample has been described as 100% altered (Bach et al., 2003).
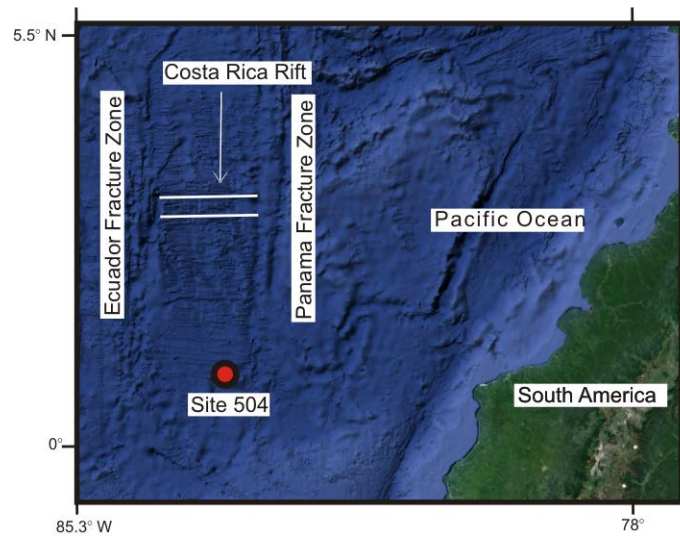
Figure 3 Location of DSDP Site 504 in the Pacific Ocean.

3.3.2 Shale

The sample is a marine shale from the Posidonia Shale formation ("Posidonienschiefer"), Wenzen Hills, Lower Saxony, Germany. The age of the formation is Lower Jurassic (Lias lithostratigraphic group of Europe, i.e., 200 to 180 Ma) (Figure 5). The formation comprises finely laminated layers of oil shales formed of fine-grained sediments intercalated with bituminous limestones (Bottjer et al., 2001). These shales are postulated to have been deposited in an anoxic (or nearly anoxic) deep water environment on the seafloor of the Paleo-Tethys Ocean.

The sample analyzed in this study is a medium to fine grained dark grey coloured rock containing 40 weight percent carbonate. It was donated by Alex Gehler, Geowissenschaftliches Zentrum, Göttingen.
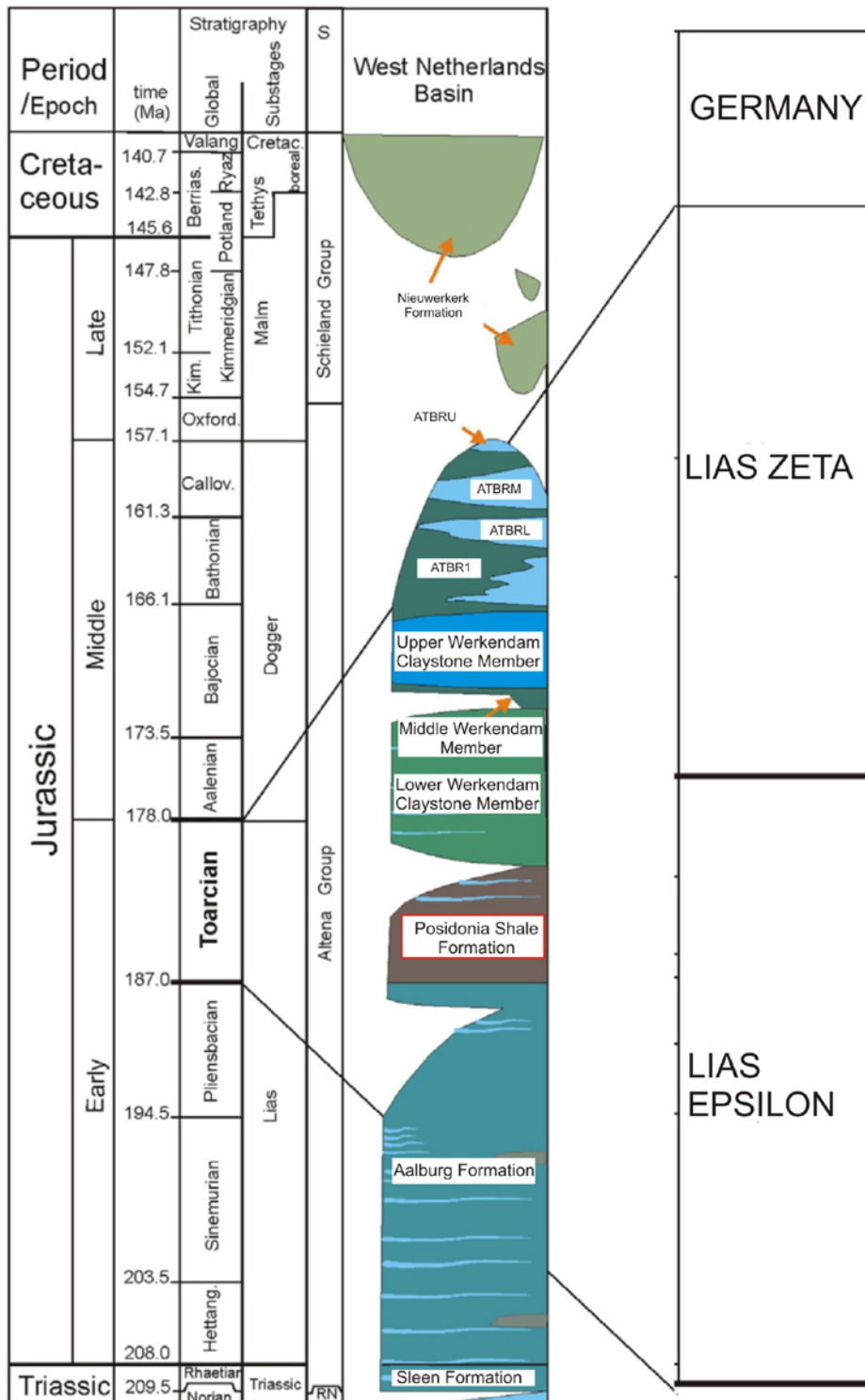
Figure 4 Stratigraphical position of the Posidonia Shale in the Netherlands and Germany. Modified after Song et al., 2015 and references therein.

3.4 Methods

Please see Ch-2 Methods, of this thesis.

3.5 Results

The results of triple oxygen isotope measurements are enlisted in Table 1. The oceanic crust data are also plotted in Figure 2 and Figure 3.

	δ¹⁷O	δ¹⁸O	δ¹⁷O	δ¹⁸O	δ¹⁷O	SD	SE	δ¹⁸O	SD	SE	Δ'¹⁷O	SD	SE
Standard	WG	WG	raw	raw	VSMOW2-	-	-	VSMOW2-	-	-	VSMOW2-	-	-
Standard 2	-	-	-	-	SLAP2	-	-	SLAP2	-	-	SLAP2	-	-
Slope of RL	-	-	-	-	-	-	-	-	-	-	0.5305	-	-
Sample	‰	‰	‰	‰	‰	‰	‰	‰	‰	‰	‰	‰	‰
Hole U1383C													
109-112	-1.123	-2.699	4.777	9.255	4.902	0.40	0.18	9.381	0.75	0.34	-0.063	0.009	0.004
	-2.077	-4.507	3.817	7.425	3.934			7.539			-0.058		
	-1.769	-3.948	4.127	7.991	4.247			8.109			-0.047		
	-2.082	-4.516	3.812	7.416	3.929			7.531			-0.059		
	-1.779	-3.923	4.116	8.016	4.236			8.134			-0.070		
45-49	-0.858	-2.199	5.043	9.761	5.171	0.30	0.15	9.890	0.57	0.28	-0.064	0.005	0.003
	-1.528	-3.475	4.369	8.469	4.491			8.590			-0.057		
	-1.186	-2.807	4.713	9.145	4.838			9.271			-0.069		
	-0.977	-2.426	4.923	9.531	5.049			9.660			-0.063		
1-4	0.328	0.113	6.236	12.101	6.374	0.62	0.22	12.246	1.18	0.42	-0.104	0.017	0.006
	0.132	-0.323	6.039	11.660	6.175			11.802			-0.068		
	0.954	1.284	6.866	13.285	7.008			13.438			-0.097		
	0.684	0.737	6.594	12.732	6.734			12.881			-0.078		
	1.558	2.352	7.473	14.366	7.621			14.526			-0.059		
	0.014	-0.572	5.920	11.407	6.055			11.548			-0.054		
	-0.122	-0.792	5.783	11.185	5.917			11.323			-0.074		
	-0.244	-1.004	5.661	10.970	5.794			11.108			-0.083		
Hole 504B													
76-85	-3.266	-6.817	2.620	5.087	2.728	-		5.187	0.90	-	-0.020	0.021	-
50-57	-3.418	-7.183	2.468	4.717	2.574	0.08	0.04	4.814	0.13	0.06	0.023	0.015	0.007
	-3.573	-7.429	2.312	4.468	2.417			4.563			-0.001		
	-3.477	-7.237	2.408	4.662	2.514			4.759			-0.008		
	-3.431	-7.204	2.455	4.696	2.561			4.793			0.021		
	-3.581	-7.436	2.303	4.461	2.408			4.556			-0.006		
Posidonian Shale													
Shale	3.197	5.522	9.122	17.574	9.284	0.93	-	17.755	1.80	-	-0.095	0.015	-
	4.499	8.028	10.432	20.11	10.604			20.307			-0.116		

Table 1 Triple oxygen isotope data of samples analyzed for the mass balance model. The δ¹⁷O and δ¹⁸O values are presented in the table in three forms – with respect to working gas (WG), the values that are obtained from the mass spectrometer (raw) and using a two-point calibration method (VSMOW2-SLAP2) (see Methods in Chapter 2 for non-linearity correction). Throughout the text the δ¹⁷O and δ¹⁸O values are reported in the VSMOW2-SLAP2 scale.
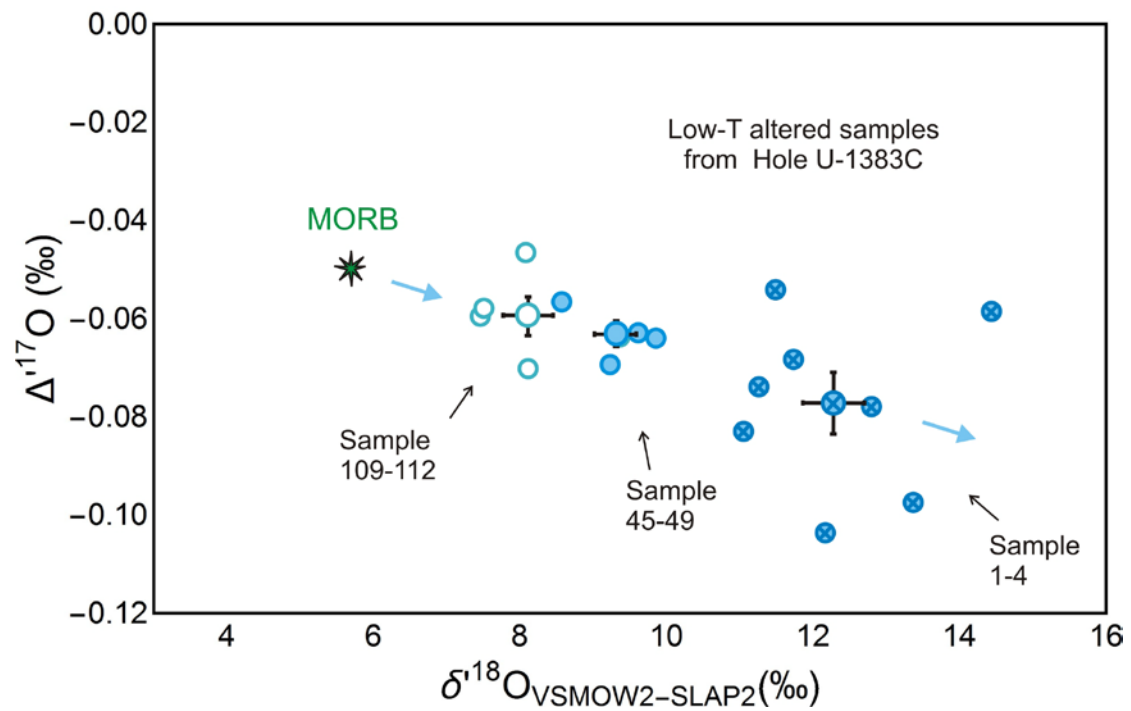
Figure 5 $\Delta'^{17}O$ vs $\delta'^{18}O$ plot of low-T altered oceanic crust samples from IODP Hole U1383C. Note that the $\delta^{18}O$ values of the samples are heavier than that of MORB while their $\Delta'^{17}O$ are more negative, as shown by the thick blue arrows. The MORB $\delta^{18}O$ value is from Muehlenbachs (1998) and $\Delta'^{17}O$ value is from Pack and Herwartz (2014) (modified after Pack et al., 2016).
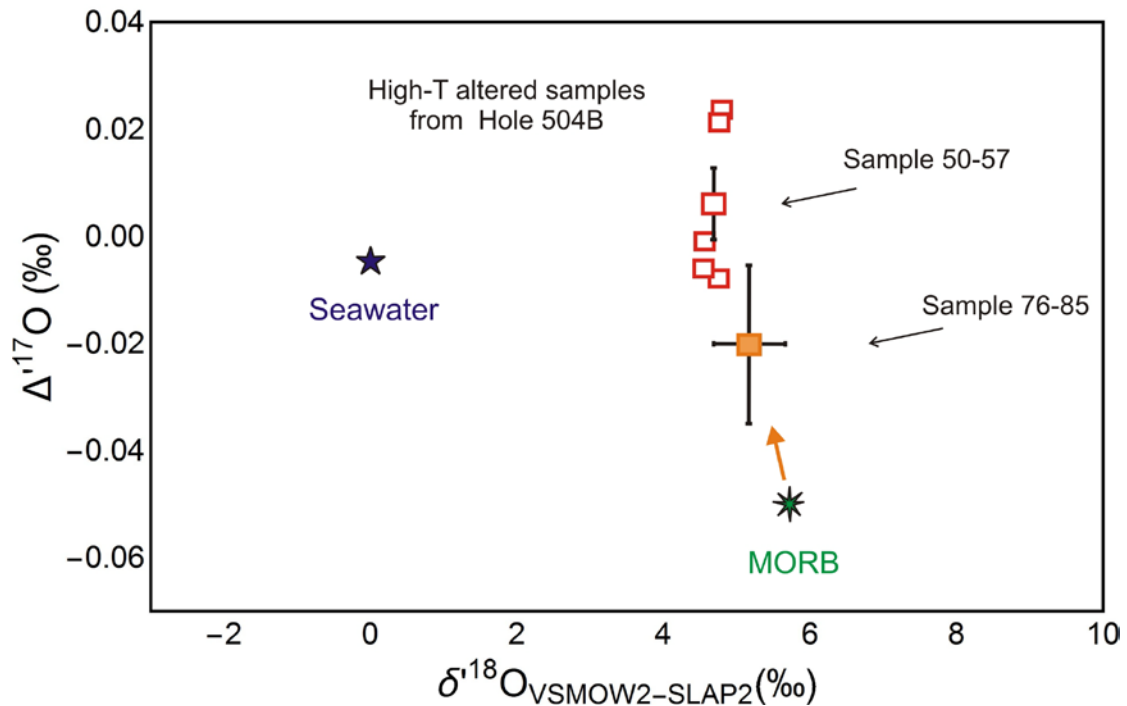
Figure 6 Δ'17O vs δ'18O plot of high-T altered oceanic crust samples from IODP Hole 504B. Note that the δ18O values of the samples are lighter than that of MORB while their Δ'17O are more positive, shown by thick orange arrow. The MORB δ18O value is from Muehlenbachs (1998) and Δ'17O value is from Pack and Herwartz (2014) (modified after Pack et al., 2016). Seawater value is from Luz and Barkan (2010).

3.6 Discussion

3.6.1 The Mass Balance Model - General formulation of the box model

The final $\delta^{18}O$ and $\delta^{17}O$ values of seawater are calculated according to the isotopic flux of ^{16}O, ^{17}O and ^{18}O to and from the oceans via geological processes. Five major geological processes affect the total oxygen budget of the oceans via lithosphere-hydrosphere interactions (Figure 4) (e.g., Muehlenbachs and Clayton, 1976; Muehlenbachs, 1998).
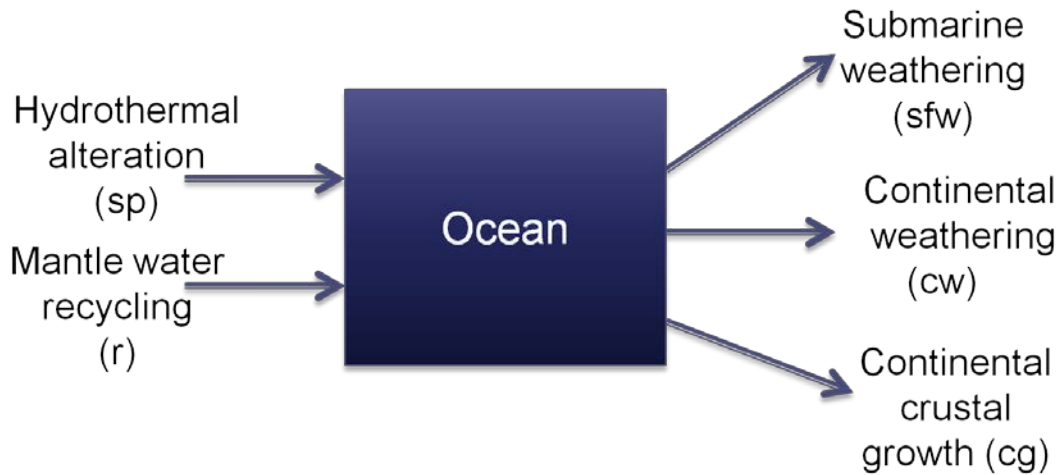
In order to quantify the effect of these major processes on the oceans' oxygen isotope budget, one has to calculate how much oxygen is exchanged per year (volume x density x %oxygen) per process. The isotopic change associated with these processes must be quantified. For this purpose, flux equations maybe written down for the individual relevant processes (Muehlenbachs and Clayton, 1972a; Muehlenbachs, 1998). We have based our model on the one presented by Muehlenbachs (1998) and have formulated flux equations for both $\delta^{18}O$ and $\delta^{17}O$ of seawater. A general form of the box model is as follows:-

$$\frac{\partial}{\partial t}\delta^i O^{Ocean} = \sum \frac{F_j^i}{m_{Ocean}} - \Delta(\delta^i O_j)$$

Equation 1

In the above equation i = mass 18 or 17 corresponding to fractionation in $^{18}O/^{16}O$ and $^{17}O/^{16}O$ respectively, j = isotope exchange reaction or process, m_{Ocean} = mass of the ocean (presently 2.8 × 10^{21} kg), and F stands for the amount of oxygen exchanged between seawater and another reservoir in the process concerned. All $\delta^{18}O$ and $\delta^{17}O$ values are on the linearized VSMOW2-SLAP2 scale.

We take the modern day values for the amount of oxygen exchanged between reservoirs, from Muehlenbachs (1998); these values are expressed in kg-oxygen/year (Table 2). For each process we calculate a difference in $\delta^{18}O$ and $\delta^{17}O$ values between the unaltered rock reservoir and altered rock reservoir, i.e., before and after interaction with seawater. This is represented by the term $\Delta(\delta^iO^j_{VSMOW})$ in the above equation. So, the definition of $\Delta(\delta^iO^j)$ is:-

$$\Delta(\delta^iO_j) = \delta^iO_j^{\text{unaltered reservoir}} - \delta^iO_j^{\text{altered reservoir}}$$

Equation 2

Please see Table 2 for a list of the input parameters of the mass balance model. These include:

1) triple oxygen isotope compositions of the major reservoirs – the mantle, MORB and modern seawater (expressed in per mil, on the VSMOW2-SLAP2 scale)

2) the magnitudes for the oxygen fluxes/ geological processes, i.e., the amount of oxygen that is exchanged annually between the reservoirs (in kg-Oxygen/year)

3) the change brought about in $\delta^{17}O$ and $\delta^{18}O$ values of the rocks (and connate water in case of "Mantle water recycling" flux) by the respective geological processes.

Parameter	Description	Values	Uncertainties on fluxes
Triple oxygen isotope compositions of individual reservoirs on VSMOW2-SLAP2 scale			
$\delta^{17}O^{SW}$, $\delta^{18}O^{SW}$, $\Delta'^{17}O^{SW}$	Seawater composition (varies with time)*	-0.005‰, 0‰, -0.005‰	-
$\delta^{17}O^{MORB}$, $\delta^{18}O^{MORB}$, $\Delta'^{17}O^{MORB}$	Composition of unaltered oceanic crust (constant, buffered by mantle)**	3.023‰, 5.8 ± 0.3‰, -0.050 ± 0.010‰	-
Oxygen exchanged between lithosphere and hydrosphere for five geological processes that control the oxygen isotope composition of seawater (flux magnitudes)			
F_{sfw}	Low T alteration/Seafloor weathering flux	2.18×10^{12} kg O year^{-1}	Depth of oceanic crust pentrated by cold seawater: 600 ± 50 m/yr
F_{ha}	High T alteration / Hydrothermal alteration flux	18.7×10^{12} kg O year^{-1}	Amount of oceanic crust altered: 5 ± 0.5 km/yr
F_{cw}	Continental weathering flux	10.2×10^{12} kg O year^{-1}	Continental weathering rate: 8 ± 0.3 km^3/yr
F_{cg}	Continental growth flux	1.53×10^{12} kg O year^{-1}	Average island arc accretion rate: 1.1 ± 0.01 km^3/yr
F_r	Mantle water recycling flux	0.8×10^{12} kg O year^{-1}	Amount of water carried by sediments to the trenches: ~1 ± 0.01 km^3/yr

*Luz and Barkan (2010)

** $\delta^{18}O^{MORB}$ value from Muehlenbachs (1998), $\delta^{17}O^{MORB}$ and $\Delta'^{17}O^{MORB}$ values from Pack and Herwartz (2014) and Pack et al. (in press)

All flux magnitudes (F_j) are based on Muehlenbachs (1998), where j=geological process

Table 2 List of input parameters for mass balance model.

Parameter	Description	Values	Uncertainties on fluxes
Difference in $\delta^{17}O_{VSMOW2\text{-}SLAP2}$ and $\delta^{18}O_{VSMOW2\text{-}SLAP2}$ values between unaltered and altered oxygen reservoirs			
$\Delta(\delta^{17}O)_{sfw}$, $\Delta(\delta^{18}O)_{sfw}$	Fractionation between unaltered and low T altered / weathered oceanic crust	$-0.34\delta^{17}O^{SW}-3.40$, $-0.34\delta^{18}O^{SW}-6.53$ (‰)	-
$\Delta(\delta^{17}O)_{ha}$, $\Delta(\delta^{18}O)_{ha}$	Fractionation between unaltered and high T altered oceanic crust	$-\delta^{17}O^{SW}+0.5$ (or 0.3), $-\delta^{18}O^{SW}-1.1$ (or 0.6) (‰)	-
$\Delta(\delta^{17}O)_{cw}$, $\Delta(\delta^{18}O)_{cw}$	Fractionation between unaltered and altered continental crust	$-0.25\delta^{17}O^{SW}-1.11$, $-0.25\delta^{18}O^{SW}-2.14$ (‰)	-
$\Delta(\delta^{17}O)_{cg}$, $\Delta(\delta^{18}O)_{cg}$	Fractionation between MORB and continental crust	$-0.16\delta^{17}O^{SW}-1.60$, $-0.16\delta^{18}O^{SW}+3.07$ (‰)	-
$\Delta(\delta^{17}O)_{r}$, $\Delta(\delta^{18}O)_{r}$	Fractionation between seawater and mantle water	$-\delta^{17}O^{SW}-0.79$, $-\delta^{18}O^{SW}+1.2$ (‰)	-

*Luz and Barkan (2010)

** $\delta^{18}O^{MORB}$ value from Muehlenbachs (1998), $\delta^{17}O^{MORB}$ and $\Delta'^{17}O^{MORB}$ values from Pack and Herwartz (2014) and Pack et al. (in press)

All flux magnitudes (F_j) are based on Muehlenbachs (1998), where j=geological process

3.6.2 The different oxygen fluxes controlling seawater composition

The 5 major geological processes affecting the total oxygen budget of the oceans are discussed below.

3.6.2.1 Low temperature alteration or weathering of oceanic crust

Interaction of rocks from the oceanic crust with seawater leads to isotope exchange reactions between the two phases. As new magma is extruded from mid-oceanic ridges and the newly formed oceanic crust gradually moves away from the source of magma output it comes in contact with cold seawater. Over time this crust suffers a weathering that raises its bulk $\delta^{18}O$ values. Anhydrous igneous material converts to high $\delta^{18}O$ hydrated secondary minerals like smectite, zeolites and clay minerals (e.g., Bach et al., 2003). This has been repeatedly seen in oceanic crust dredge-hauls (Taylor, 1968; Muehlenbachs and Clayton, 1976) and drill cores (Garlick and Dymond, 1970; Muehlenbachs and Clayton, 1972a). Individual alteration veins and secondary silicate minerals yield high $\delta^{18}O$ values in the range ~10 to 20‰, suggesting low temperatures of alteration between 0 and 50°C (Hoefs, 2008) and more commonly at 0-15°C (Muehlenbachs, 1986). This acts as an effective large sink for heavy oxygen isotopes and thus reduces the $\delta^{18}O^{SW}$ value.

Low-T alteration of oceanic crust starts as soon as the crust is formed (Böhlke et al., 1981), at high water : rock ratios. Pervasive alteration, most commonly, continues for a time span of a few million years, as deduced from the Rb/Sr dating of secondary minerals (Staudigel et al., 1981). The average bulk $\delta^{18}O$ value of low-T altered sea-floor basalts is ~8 or 9‰ but some can go up to 13‰ (values compiled by Muehlenbachs, 1986 after Alt et al., 1986). Longer periods of seawater circulation and consequent alteration may have occurred in localized high-permeability breccia zones or flow margins (Muehlenbachs, 1980; Staudigel et al., 1981). However, isotopic and ion-concentration studies on ^{18}O depleted pore-fluids of pelagic sediments suggest that some low-T

alteration of basaltic crust may also occur throughout the life of the crust (Lawrence and Gieskes, 1980).
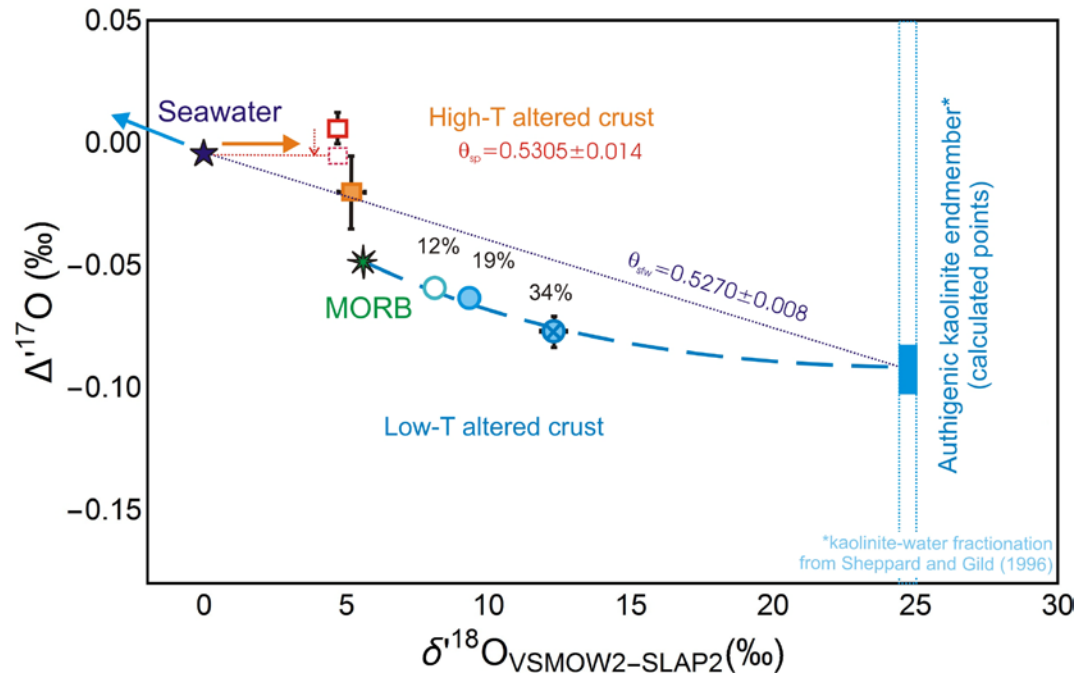

Figure 8 Plot of low and high-T altered oceanic crust samples in δ'^{18}O vs Δ'^{17}O space. The low-T altered samples are marked in blue circles, whereas the high-T altered samples are marked in orange and red squares. The mean value of each sample is plotted along with the standard errors (SE). Where error bars are not visible, the SE is smaller than the size of the symbol used. The blue dashed curve marks a mixing line between pristine MORB and 100% altered end-member clay. The high δ^{18}O of the clay, a result of low-T alteration, decreases the δ^{18}O^{SW} and increases the Δ'^{17}O^{SW}, as shown by blue arrow. High –T alteration has the opposite effect; partial alteration increases the δ^{18}O^{SW} and decreases the Δ'^{17}O^{SW}, whereas a completely altered end-member attains the Δ'^{17}O value of MORB itself (as shown by orange arrow).

Muehlenbachs (1998) estimated a bulk δ^{18}O value of 9.6‰ for an altered oceanic crust whose 100% alteration product would be a clay with δ^{18}O = 25‰ ($1000n\alpha_{kaolinite-water}^{18/16O} \approx 25‰$ at 20°C from Sheppard and Gilg, 1996). Such a basalt sample (with δ^{18}O = 9.6‰) would have

suffered 20% alteration. The bulk $\delta^{18}O$ values of the oceanic crust drill core samples from ODP Hole U1383C, in Figure 5, measured in this study are all greater than 5.8‰, i.e., they have average $\delta^{18}O_{VSMOW2\text{-}SLAP2}$ values = 8.1 ± 0.34‰, 9.4 ± 0.28‰ and 12.4 ± 0.43‰, (U1383C-109-112, 45-49 and 1-4 respectively) – all higher than that expected for pristine MORB. The high oxygen isotope values of the samples suggest that they have suffered low-T alteration. That these samples are not fresh basalts is clear even on visual inspection – they contain numerous alteration veins filled with secondary minerals like smectite, carbonates and iddingsite, which is a clay bearing alteration product of olivine. The $\delta^{18}O$ values of samples U1383C-109-112, 45-49 and 1-4 are 8.1 ± 0.34‰, 9.4 ± 0.28‰ and 12.4 ± 0.0.42‰ respectively. Following Muehlenbachs (1998) it is considered that a 100% altered basalt sample would ultimately form clay or a clay-rich rock and this considered the altered end-member. The partially altered basalt samples in this study are then mixtures between a clay-rich rock with $\delta^{18}O$ = 25‰ (Sheppard and Gild, 1996) and pristine MORB with $d^{18}O$ = 5.8‰. This means the samples U1383C-109-112, 45-49 and 1-4 are 12%, 19% and 34% altered, respectively, with regard to oxygen isotopes.

In order to write Equation 2 for this process, we consider any one altered oceanic crust sample and the percentage of alteration it has undergone according to its present $\delta^{18}O$ value (assuming a clay alteration end-member with $\delta^{18}O$ = 25‰). The most highly altered sample U-1383C-1-4 with alteration = 34% or 0.34, has been used below to write an equation for the difference in $\delta^{18}O$ between altered and unaltered oceanic crust. The abbreviation "sfw" stands for "seafloor weathering". The equation for change in $\delta^{18}O$ is as follows:-

$$\Delta(\delta^{18}O_{sfw}) = \delta^{18}O^{MORB} - [0.34 \times (\delta^{18}O^{SW} + 25) + (1 - 0.34) \times (\delta^{i}O^{MORB})] \qquad \textbf{\textcolor{blue}{Equation 3}}$$

The $\delta^{17}O$ of low-T altered oceanic crust samples are also higher than that of pristine MORB and their $\Delta'^{17}O$ decreases with increasing degree of alteration (Figure 8). The samples, in the order of least to most altered – U1383C-109-112, 45-49 and 1-4 have $\Delta'^{17}O$ values of -0.059 ± 0.004‰, -0.063 ± 0.003‰ and -0.077 ± 0.006‰ respectively. Thus, we demonstrate differences in bulk rock $\delta^{17}O$ or $\Delta'^{17}O$ values as a result of low-T (0-50°C) alteration of pure MORB forming heavier $\delta^{18}O$ and $\delta^{17}O$ minerals. The effect on seawater is a decrease in $\delta^{18}O^{SW}$ and an increase in $\Delta'^{17}O^{SW}$.

The $\delta^{18}O$ and the $\delta^{17}O$ of these altered basalts can also be expressed as a mixture of pristine unaltered end member MORB and altered end member clay. The $\delta^{17}O$ values of authigenic clays have not been published so far; but we can estimate a value for it from our altered basalt $\delta^{17}O$ and $\delta^{18}O$ results. This is possible because in the $\delta'^{17}O$ vs $\delta'^{18}O$ space the partially altered basalts that we have analyzed should fall on a mixing line between the unaltered i.e., MORB, and the fully altered authigenic clay compositions. We know the $\delta^{17}O$ and $\delta^{18}O$ values for the MORB, the partially altered basalts, the percentage of alteration the basalts have suffered and the $\delta^{18}O$ value for the clay. From these values the $\delta^{17}O$ and $\Delta'^{17}O$ values of authigenic clay is calculated to be 13.009 ± 0.005‰ and -0.091 ± 0.005‰ (SE) respectively. This hundred percent altered end member would be in equilibrium with seawater and hence, we calculate a $\theta_{seawater-clay}$ or θ_{sfw} of 0.5270 ± 0.0002. The equation corresponding to Eqn. 7 for O^{17} becomes:

$$\Delta(\delta^{17}O_{sfw}) = \delta^{17}O^{MORB} - [0.34(\delta^{17}O^{SW} + 13.009) + (1 - 0.34)(\delta^{17}O^{MORB})] \qquad \textcolor{blue}{\textbf{Equation 4}}$$

Irrespective of which particular sample we choose to write this equation, the final result of the mass balance model remains the same within uncertainty.

2.94 km^2 of oceanic crust is created and destroyed every year (Williams and Von Herzen, 1974) and seawater percolates upto 600m into the oceanic crust which leads to 1.8 km^3 of oceanic crust being altered per year and 2.2 x 10^{12} kg of oxygen is exchanged per year between the two reservoirs (Muehlenbachs and Clayton, 1976).

3.6.2.2 High temperature or hydrothermal alteration of oceanic crust

Hydrothermal alteration of the seafloor and subducted water recycling are the two processes that increase $\delta^{18}O^{SW}$ (Muehlenbachs, 1998) and accordingly, also $\delta^{17}O^{SW}$. The effect on $\delta^{17}O^{SW}$ shall be demonstrated in this study. The $\delta^{18}O$ values of greenstones and other metamorphic rocks that comprise lower $\delta^{18}O$ than fresh MORB, are products of high temperature interaction between seawater and oceanic crust (Muehlenbachs and Clayton, 1971). Circulating seawater scavenging heavier oxygen isotopes from ocean crust is also evidenced by hydrothermal fluids with $\delta^{18}O$ values enriched relative to ambient seawater. The enrichment ranges from 0.5 to 2.3‰

and is independent of spreading rates or tectonic environments (Jean-Baptiste et al., 1997). This is a major process controlling the oxygen budget of the oceans (Muehlenbachs and Clayton,1976; Gregory and Taylor, 1981). In fact, high-temperature fluids at spreading centres provide the largest ^{18}O-input into the ocean (Jean-Baptiste et al., 1997; Wallmann, 2001).

These systematics arise because oxygen-isotope fractionation factors decrease with increasing temperatures (e.g., Sheppard and Gilg, 1996). Therefore, seawater that penetrates the oceanic crust at mid-ocean ridges and reacts with oceanic crust at temperatures above 250-350°C (Muehlenbachs and Clayton, 1972b) preferentially partitions the heavier oxygen isotopes into the fluid phase (Muehlenbachs and Clayton, 1976; Holland, 1984; Veizer et al.,1986; Walker and Lohmann, 1989; Qing and Veizer, 1984; Jean-Baptiste et al., 1997; Muehlenbachs, 1998; Wallmann, 2001; Jaffrés et al., 2007). Because $\Delta^{18}O^{seawater-basalt}$ is greater than $1000ln\alpha^{seawater-baslat}$, metamorphosed basalts have lower $\delta^{18}O$ values than their pristine counterparts. The greenstones have $\delta^{18}O$ values varying between 1.8 to 7‰ depending on varying modal proportions of ^{18}O-rich (e.g., quartz $\sim$9‰, albite etc.) and ^{18}O-poor minerals (e.g., epidote $\sim$1‰) (Muehlenbachs, 1986).

The sheeted dike complex underlying the upper basaltic layer of the oceanic crust has been extensively studied at DSDP Hole 504B (Alt et al., 1986; 1995; Bach et al., 1996). Our high-T altered samples come from the "upper dike section" of the Sheeted dolerite dyke complex (SDC) of Hole 504B. This section starts directly below the end of the transition zone at 1055mbsf. Sample 504B-76-85 and 50-57 have $\delta^{18}O$ values 5.2 ± 0.5‰ (SD) (only one measurement was made, error estimate is from repeated measurements of dörentrup quartz) and 4.7 ± 0.06‰ (SE) respectively, which is lower than the value of MORB and hence, confirms high-T alteration. Previous studies have reported whole rock $\delta^{18}O$ values of 3.0 to 6.5‰ (Alt et al., 1986a; Alt et al., 1996) for the upper dike section. Our measured values have an average $\delta^{18}O = 4.9 ± 0.1$‰, which is identical to the previously reported values within uncertainty. For example, 21 samples of oceanic crust (average of layer 3) from DSDP hole 735B yielded average $\delta^{18}O$ of 4.4 ± 1‰ (ranging from 2.0 to 5.8‰) (Bach et al., 2001). Using the most altered sample from Hole 504B in our study, i.e. sample 50-57, the equation for the isotopic shifts of $\delta^{18}O$ between altered and unaltered MORB becomes:

$$\Delta(\delta^{18}O_{ha}) = \delta^{18}O^{MORB} - (\delta^{18}O^{SW} + 4.7)$$

<div style="text-align: right"></div>

We also report high precision $\Delta'^{17}O$ values for the drill site Hole 504B (Figure 5). This gives us first information on how the $\delta^{17}O$ of MORB changes when it interacts with seawater at high temperatures. The $\delta^{17}O$ of the samples 504B-76-85 and 50-57 are 2.7 ± 0.1‰ and 2.5 ± 0.04‰, respectively; their $\Delta'^{17}O$ values are, in the same order, -0.020 ± 0.015 and 0.006 ± 0.007 SE. The $\Delta'^{17}O$ of the samples are elevated with respect to MORB (-0.050 ± 0.006‰). So, the effect of high-T alteration of the ocean floor on the ^{17}O composition of the oceans is that it decreases the $\Delta'^{17}O^{SW}$, drawing it to more negative values. The direction of change of $\Delta'^{17}O$ of seawater over long term has been depicted by the bold orange arrow in Figure 11.

For the equation for $\delta^{17}O$ exchanged between reservoirs during this process we shall use the highest altered high-T sample we have, i.e., Hole 504B–50-57. The mean $\Delta'^{17}O$ of this data point (0.006 ± 0.007‰) is higher than the $\Delta'^{17}O$ of modern seawater (-0.005 ± 0.001‰, Luz and Barkan, 2010). Because this sample is entirely altered we treat it as an alteration end-member. The alteration end-member is expected to be in oxygen isotopic equilibrium with ambient fluid. If this fluid is seawater, then the θ between high-T altered crust and seawater or θ_{ha} (ha = hydrothermal or high-T alteration) is 0.5307 ± 0.0014. The high-T limit of θ for mass dependent multi-step processes at equilibrium is 0.5305 according to theoretical (Young et al., 2002; Cao and Liu, 2011) and experimental studies (Matsuhisa et al., 1978; Young et al., 2002; Pack and Herwartz, 2014). The possibility for non-canonical values of equilibrium θ, i.e., higher than 0.5305, for mass-dependent processes was displayed by Bao et al. (2015) using a modeling approach but such values have not been experimentally determined so far. The value of θ_{ha} in this study is greater than 0.5305. If we consider that the altered rock is in equilibrium with a $\delta^{18}O$ and $\delta^{17}O$ heavy pore water or ambient hydrothermal fluid then the θ_{sp} values would be even higher. In order to put the value of θ_{ha} within experimentally determined limits of equilibrium θ we assign a value of -0.005‰ to the $\Delta'^{17}O$ of the sample 504B-50-57. The calculated $\delta^{17}O$ is then 2.484‰. The assigned value is within uncertainty of the measured one. The value for θ_{sp} considering equilibrium with modern seawater is the assigned high-T limit of θ, i.e., 0.5305. This assigned value has been used for writing the following equation:

$$\Delta(\delta^{17}O_{ha}) = \delta^{17}O^{MORB} - (\delta^{17}O^{SW} + 2.5)]$$

While about 600 m of ocean floor suffers low-T alteration, high-T alteration by hydrothermal fluids alters another 1 to 5 km of oceanic crust annually, at temperatures 250 to 350°C. We consider 5 km oceanic crust alteration by high-T fluids (supported by ophiolite field studies, Gregory and Taylor, 1981) at 250 to 350°C temperature, for calculating the flux magnitude (Table 1). Considering 3 km^2 new oceanic crust production every year, the volume of high-T altered crust is ~15km^3 (Muehlenbachs, 1998).

3.6.2.3 Continental weathering

Weathering of continental rocks helps effectively lower the $\delta^{18}O$ of oceans. Continental weathering occurs mostly at low, ambient Earth near-surface temperatures. Thus, large as well as variable fractionation factors of 10 to 35‰ exist between the rock forming minerals and the meteoric water that is weathering those rocks (Muehlenbachs, 1998; Wallmann, 2001; Jaffrés et al., 2007). If excess water is involved, as usually is the case in weathering, there is a net ^{18}O and predictably, ^{17}O, transfer from hydrosphere to lithosphere. This acts as an important sink for the heavier oxygen isotopes with an ^{18}O-enrichment in weathering products and subsequent ^{18}O-depletion in meteoric and marine waters (cf. Jean-Baptiste et al., 1997). The present river load of sediment is 20 x 10^{15} g/year, based on which Holland (1984) calculated a rate of weathering at 7.4 km^3/yr. He estimated that 75% of all river load is recycled sediment which means this cannot contribute to the net flux of oxygen being exchanged with the oceans. The rest 25% is one half weathered igneous and the other half weathered metamorphic rock. For the triple oxygen isotope compositions of igneous rocks a plagioclase (from a granite) data point has been used (Pack and Herwartz, 2014; corrected according to Pack et al., 2016). The final $\delta^{18}O_{igneous}$ is 8.8 ± 0.06. For average metamorphic rocks a $\delta^{18}O$ of 12‰ assumed (similar to Muehlenbachs, 1998). The average $\delta^{18}O$ for sedimentary rocks has been assumed to be 17‰ in previous modeling studies (Li, 1972; Muehlenbachs, 1998; Jaffrés et al., 2007). In this study a lower Jurassic shale

sample has been measured. It was found to have a $\delta^{18}O$ value of 19.0 ± 1.8‰ (SD from two data points). This value has been used in model. The abbreviation "cw" has been used for "continental weathering", the equation for $\delta^{18}O$ difference between continental crust and altered product shale is as follows:-

$$\Delta(\delta^{18}O_{cw}) = [0.75(0\ ) + 0.125\left(\delta^{18}O^{\text{igneous}}_{\text{rocks}} - \delta^{18}O^{SW} - \delta^{18}O^{shale}\right)$$

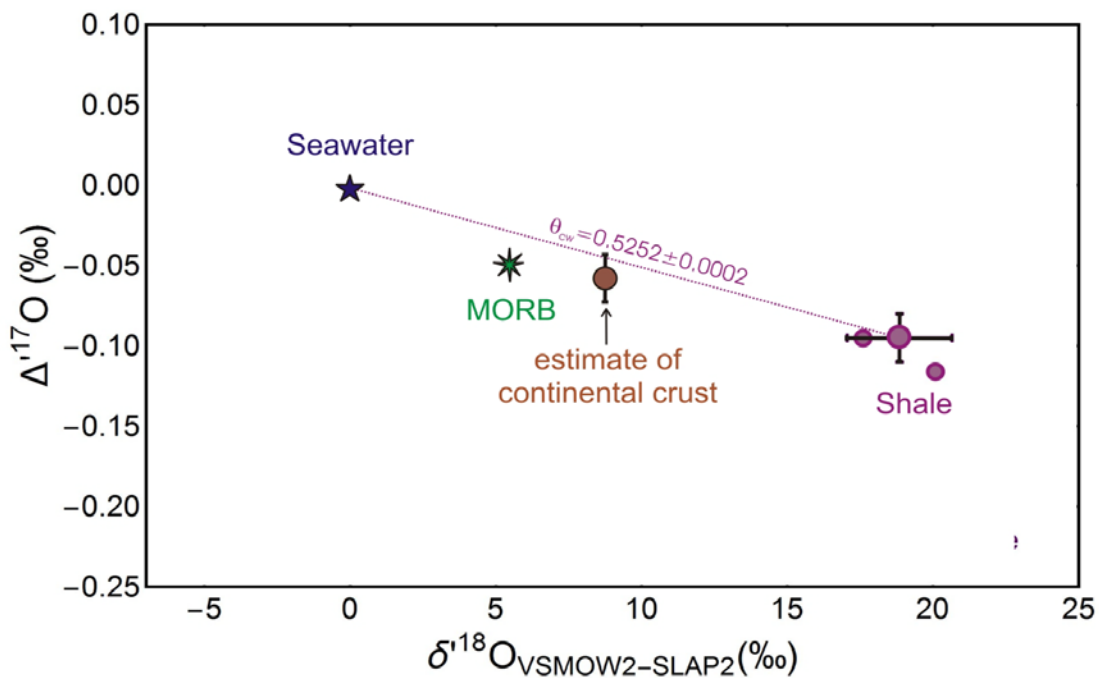$$+ 0.125\left(\delta^{18}O^{\text{metamorphic}}_{\text{rocks}} - \delta^{18}O^{SW} - \delta^{18}O^{shale}\right)$$

Figure 9 Plot of Δ'17O vs δ'18O showing marine shale data point. The average of the two measured values has been marked with error bars (1SD). Between the shale with ocean water having δ18O = 0‰ and Δ'17O = -0.005‰ (Luz and Barkan, 2010) then a slope of θcw = 0.5252 ± 0.0002 can be calculated. However, note that this is not an equilibrium slope because the shale and seawater are not in equilibrium. Modern seawater and MORB values are marked by a blue five pointed star and a green six pointed star, respectively. The data point from MORB (green star) is from Pack and Herwartz (2014) (corrected and reported on VSMOW2-SLAP2 scale following Pack et al., 2016). The data point for continental crust (brown dot) is δ18O = 8‰, assumed by Muehlenbachs (1998). The corresponding Δ'17O values is a plagioclase, sourced from a granite, measured by Pack and Herwartz

For igneous rocks' $\delta^{17}O$ composition the plagioclase data point from Pack and Herwartz (2014) (Equation 7) is used, corrected $\delta^{17}O$ = 4.60 ± 0.03‰ (Pack et al., 2016). For metamorphic rocks' composition a high-T θ of 0.527 has been assumed. For a $\delta^{18}O$ = 12‰, a $\delta^{17}O$ = 6.306‰ is obtained. The triple oxygen isotope composition of a lower Jurassic shale sample has been measured, the $\delta^{18}O$ (19.0‰) of which has been used in Equation 7 above. The shale has $\delta^{17}O$ = 9.9‰ ± 0.9‰ and $\Delta'^{17}O$ = -0.106 ± 0.015‰. It is a marine shale sample, but terrigenous input into the oceans is provided by rivers that have drained the continents, making this sample a good representative for end-member of continental weathering. Considering equilibrium with seawater a $\theta_{shale-seawater}$ or θ_{cw} maybe calculated = 0.5252 ± 0.002 which is consistent with a low-T θ (Pack and Herwartz, 2014; Herwartz et al., 2015; Sharp et al., 2016). The equation for $\delta^{17}O$ difference between continental crust and altered product shale is as follows:-

$$\Delta(\delta^{17}O_{cw}) = [0.75(0 - \delta^{17}O^{SW}) + 0.125\left(\delta^{17}O^{\substack{igneous\\rocks}} - \delta^{17}O^{SW} - \delta^{17}O^{shale}\right)$$

$$+ 0.125\left(\delta^{17}O^{\substack{metamorphic\\rocks}} - \delta^{17}O^{SW} - \delta^{17}O^{shale}\right)$$

Equation 8

Thus, continental weathering decreases the $\delta^{18}O$ and $\delta^{17}O$ of oceans (and increases $\Delta'^{17}O$ of seawater). The magnitude of the continental weathering flux, F_{cw} has been taken from Muehlenbachs et al. (1998), which is based on the present river load of sediment (20 x 10^{15} g/yr) by Holland et al. (1984).

3.6.2.4 Continental Growth

The recycling of sediments via subduction and continental growth also contributes to the $\delta^{18}O$ budget of the oceans. The continental crust is always enriched in $\delta^{18}O$ with respect to the mantle (by about 2 to 5‰) because of sediment assimilation during tectonic processes (O'Neil and Chappell, 1977). It is difficult to estimate the mass of ^{18}O-rich sediment that has been remelted and assimilated into the continental crust during tectonic event such as subduction and mountain building. But the highly heterogenous continental crust can be expressed as a mixture of sediments and MORB.

It has been suggested that ~8‰ is a good representative for $\delta^{18}O$ of accreted continental crust (cf. Taylor, 1968; Muehlenbachs, 1998). As the average value of continental crust we use the plagioclase (from granite) ($\delta^{18}O$ = 8.68‰, $\delta^{17}O$ = 4.48‰ and $\Delta'^{17}O$ = -0.057 ± 0.003‰) data point used in Equation 7 and Equation 8 pertaining to continental weathering (Pack and Herwartz, 2014; Pack et al., 2016). For deep sea sediments we take the values as calculated in section 3.6.2.1, i.e., $\delta^{18}O$ = 25.0‰, $\delta^{17}O$ = 13.0‰. According to these values the continental crust would be a mixture of 16% deep sea sediments and 84% mantle composition So, the difference between mantle and newly formed continental crust for $\delta^{18}O$ and $\delta^{17}O$ can be expressed as:-

$$\Delta(\delta^{18}O_{cg}) = \delta^{18}O^{MORB} - [0.16(\delta^{18}O^{SW} + 25) + (1 - 0.16)(\delta^{18}O^{MORB})] \qquad \textbf{Equation 9}$$

$$\Delta(\delta^{17}O_{cg}) = \delta^{17}O^{MORB} - [0.16(\delta^{17}O^{SW} + 13.009) + (1 - 0.16)(\delta^{17}O^{MORB})] \qquad \textbf{Equation 10}$$

The flux of oxygen between seawater and continental crust due to subduction and formation of new crust is based on the current crustal accretion rate of 1.1 km^3/yr (Reymer and Schubert, 1984). The flux magnitude is same as that in Muehlenbachs (1998) (Table 2).

3.6.2.5 Mantle water recycling

Seawater bound chemically within sediments, is recycled through the mantle during processes like subduction and seafloor spreading. Such recycling may return heavier oxygen isotopes to the hydrosphere (Chase and Perry, 1973). Connate water bound within sediments or hydroxyl water within altered oceanic crust have been sourced from seawater but have $\delta^{18}O$ values higher than seawater. Considering talc-water equilibrium fractionation (Saccocia et al., 2009), water trapped within the altered rocks would have $\sim 1.7‰$ lower $\delta^{18}O$ value than the host rock. This means in within bulk crustal rocks of $\delta^{18}O \sim 6‰$ (Muehlenbachs, 1998) the trapped hydroxyls and pore waters (pw used to refer to both types of water in text) would have a $\delta^{18}O^{pw}$ of 4.3‰. The difference in $\delta^{18}O$ between this water and seawater is covered under section 3.6.2.2 on high-T ocean floor alteration. However, as this water is carried to depths by subduction, it heats up and upon degassing re-equilibrates with the surrounding mantle at high temperatures ($\sim 1500°C$). Eventually it makes its way back to the hydrosphere but with a $\delta^{18}O$ that is a result of its interaction with the mantle. The temperature of interaction determines the oxygen isotope composition this water will attain. At temperatures like 1500°C, Di Rocco and Pack (2015) demonstrate via experiments that there is no fractionation in triple oxygen isotope between a silicate melt phase and water vapour. If we consider degassing at such high temperatures then the released connate water re-enters the oceans with same composition as that of mantle. Thus, the equation for shift in $\delta^{18}O$ due to subducted water recycling (r) is:-

$$\Delta(\delta^{18}O_r) = \delta^{18}O^{Mantle} - (\delta^{18}O^{SW} + 4.3) \qquad \text{\color{blue}{Equation 11}}$$

For the $\Delta(\delta^{18}O_r)$ equation we take the $\Delta'^{17}O$ value of MORB and, i.e. $\Delta'^{17}O^{MORB}$ = -0.050 ± 0.006‰ and calculate $\delta^{17}O$ of 3.128‰ for a rock that would have $\delta^{18}O$ of 6‰. The $\delta^{17}O$ value of the connate water can be estimated using a high-T θ value for silicate-water equilibrium.

Next we have to know the ^{17}O composition of bound water within bulk subducted crust. We assume that the bond water within the gabbro are in equilibrium with the rock at 350°C. But the value of $\theta_{silicate-pw}^{equilibrium}$ at 350°C is not known. We use the silica-water system as an analogue and estimate a value of $\theta_{silicate-pw}^{equilibrium}$ = 0.5272 from the $\theta_{SiO_2-H_2O}^{equilibrium} - T$ relation (θ-T relation in

Chapter 2, Cao and Liu, 2011). A $\delta^{17}O^{pw}$ can subsequently be calculated from the $\theta_{silicate-pw}^{equilibrium}$ and

$\delta^{18}O^{pw}$ values. It has been shown that at temperatures >600°C mineral-water and mineral-mineral θ values converge, the effect of temperature on θ being most prominent at lower temperatures (Pack and Herwartz, 2014; Sharp et al., 2016). Also, the process of mantle recycling has the smallest effect on buffering $\delta^{17}O^{SW}$ and $\delta^{18}O^{SW}$. Thus, estimating pore and hydroxyl water ^{17}O compositions using $\theta_{SiO_2-H_2O}^{equilibrium} - T$ relation does not change the results beyond uncertainty. The equation for the shift in $\delta^{17}O$ due to subducted water recycling (r) is as follows:-

$$\Delta(\delta^{17}O_r) = \delta^{17}O^{Mantle} - (\delta^{17}O^{SW} + 2.235)]$$ **Equation 12**

The calculation of the flux magnitude for this flux is based on the fact that ~1 km³ of water is carried to the subduction zones every year – about 50-90% is expelled by compaction and would then return to the hydrosphere (Von Huene and Scholl, 1987) (Table 2) considers 90% water expulsion, which means ~0.9 km³ water being expelled and recycled every year (Muehlenbachs, 1998).

3.6.3 Results of the mass balance model

3.6.3.1 Modern seawater

The mass balance model was run according to Equation 1, incorporating all present day flux magnitudes along with the $\Delta(\delta^{18}O)$ and $\Delta(\delta^{17}O)$ associated with each process (Table 2). The model was allowed to run over a time period of 3.8 b.y. The spreading rate was considered to be 11 times larger in the Archean than today and exponentially decreased to current rates, assuming that it is proportional to the square of heat loss (cf. Phipps Morgan, 1998; Jaffrés et al., 2007). For modern day seawater a $\delta^{18}O$ value for an ice free world is $\delta^{18}O^{IF}$ = -1 ± 0.5‰ according to the model. This matches the expected value for an ice-free world within uncertainty (e.g., by Shackleton and Kennet, 1975). The outcome for the ^{17}O composition is – present day $\delta^{17}O^{IF}$ = -0.533‰. The $\Delta'^{17}O^{IF}$, from the model, is -0.018 ± 0.015‰, identical to the expected $\Delta'^{17}O^{IF}$ = -0.004 ± 0.003‰ within uncertainty (Figure 1, calculated from Luz and Barkan, 2010).

The uncertainties on the results have been calculated using the Monte Carlo method of error propagation. A large set of random numbers were generated, using normal distribution and 100 simulations were run. The uncertainties mentioned for $\delta^{18}O^{SW}$ and $\Delta'^{17}O^{SW}$ are the standard deviations of these hundred simulations for each term. The software "Mathematica" was used for performing the simulations.

Seawater is buffered to its present day value in 2.60 x 10^8 years, according to the model results in the current study, i.e., at an average rate of $\sim$2.5‰ $\delta^{18}O$ per 10^8 years and $\sim$11 ppm $\Delta'^{17}O$ per 10^8 years.

One difference between previous models (e.g., Jaffrés et al., 2007 and references therein) and ours is that we consider primordial water composition to be equal to that of mantle, i.e., 5.5‰ instead of a higher 7‰ ($\delta^{18}O$ value adopted from Hoefs, 1997). This is because it is now known experimentally that there is 0‰ fractionation of triple oxygen isotopes between water and silicate melt at a high temperature of 1500°C (Di Rocco and Pack, 2015).. If the interaction temperature is assumed to be lower instead, $\sim$1200 - 1300°C then it may be possible that mantle water is indeed fractionated with respect to the mantle and has $\sim$7‰ $\delta^{18}O$ value. Using $\theta_{SiO_2-H_2O}^{equilibrium} - T$ (equation in Ch2) again as an approximation for the silicate-water system at high temperatures, a $\theta_{silicate-H_2O}^{equilibrium}$ = 0.5292 is obtained at 1200°C. From this we calculate that, a 7‰ $\delta^{18}O$ bearing primordial water would have $\delta^{17}O$ = 3.655‰ and $\Delta'^{17}O$ = 0.052‰, identical to mantle $\Delta'^{17}O$ composition (Pack et al., 2016). We performed a model run using these values for the initial water composition in our model instead of mantle values, but no difference was seen in the outcome for present day situation. The $\delta^{18}O^{SW}$ and $\Delta'^{17}O^{SW}$ values remained the same up to 6 decimal places. This indicates the effective buffering system that is operating today to maintain the oxygen isotopes composition of the oceans and the insensitivity of the model to small changes in the value of primordial water composition. The time taken to reach steady state varies slightly with varying $\delta^{18}O$ and $\delta^{17}O$ of primordial water. The time goes up to 2.67 x 10^8 yrs, i.e., it increases by 0.07 x 10^8 yrs.

The high-T or hydrothermal alteration process involves highest amount of oxygen exchange with seawater, amongst all the 5 processes considered, i.e., 1.87 x 10^{12} kg-Oyr^{-1} (Table 2) (Muehlenbachs, 1998). Thus, $\delta^{18}O^{SW}$ and $\delta^{17}O^{SW}$ values are expected to be most sensitive to the

input parameters involved in the $\Delta(\delta^{18}O_{ha})$ and $\Delta(\delta^{17}O_{ha})$ equations (Equation 5 and Equation 6). The data of sample 504B-50-57 have been used in both the equations because we treat the sample as a 100% altered end-member of hydrothermal seafloor alteration. However, for Equation 6, the $\Delta'^{17}O$ value for sample 504B-50-57 was decreased to -0.005 ppm (still within uncertainty range of measured data) because otherwise the θ_{sp} value between seawater or hydrothermal fluid and the sample would exceed the theoretical upper limit for θ, i.e., 0.5305 (Matsuhisa et al., 1978). Changing the $\Delta'^{17}O$ value of this sample introduces a change in the final $\delta^{17}O^{SW}$ value from the model. If we lower the $\Delta'^{17}O$ of the sample further, by 20 ppm to -25 ppm or -0.025‰, then the $\Delta'^{17}O^{SW}$ increases by 16 ppm. Thus, the $\delta^{17}O^{SW}$ becomes 0.517‰ and the $\Delta'^{17}O^{SW} = -0.004$‰ which is exactly the same as what we expect for an ice-free world. It is, therefore, worth analyzing some more heavily altered samples in the future to see if greater variation in their $\Delta'^{17}O$ values is observed.

The second most important flux, in terms of the amount of oxygen exchanged every year, is the continental weathering flux (Table 2). The $\Delta'^{17}O$ of the shale might vary the result of the mass balance for the ^{17}O composition of the oceans. So, instead of our measured shale data point we use the calculated average value for a clay rich rock ($\delta^{18}O^{clay} = 25$‰, $\delta^{17}O^{clay} = 13.009$‰), based on kaolinite-water fractionation (Sheppard and Gilg, 1996) and as described in section 3.6.2.1 on low-T seafloor alteration. Using this value yields for modern seawater: $\delta^{18}O^{IF} = -1.60$‰ and $\Delta'^{17}O^{IF} = -0.009$‰. The mean $\Delta'^{17}O$ then comes much closer to the expected -0.004‰ value for an ice-free world. So, we proceed with using these average values as our final result for modern day seawater.

3.6.3.2 Seawater variations in the past

Stable isotope exchange reactions with the oceanic crust both adds and takes away from the oceanic oxygen isotope budget and stabilizes the triple oxygen isotope composition of seawater at -0.005‰ and 1‰ for $\delta^{17}O^{SW \; and} \; \delta^{18}O^{SW}$ respectively. Thus, in the long run the $\delta^{18}O^{SW}$ is prevented from varying more than ±2 per mil, as suggested by previous models (Muehlenbachs and Clayton, 1976; Gregory and Taylor, 1981; Holland, 1984, pp. 248; Gregory 1991; Jean-

Baptiste et al., 1997; Muehlenbachs, 1998). The corresponding variation in $\delta^{17}O^{SW}$ is expected to be smaller.
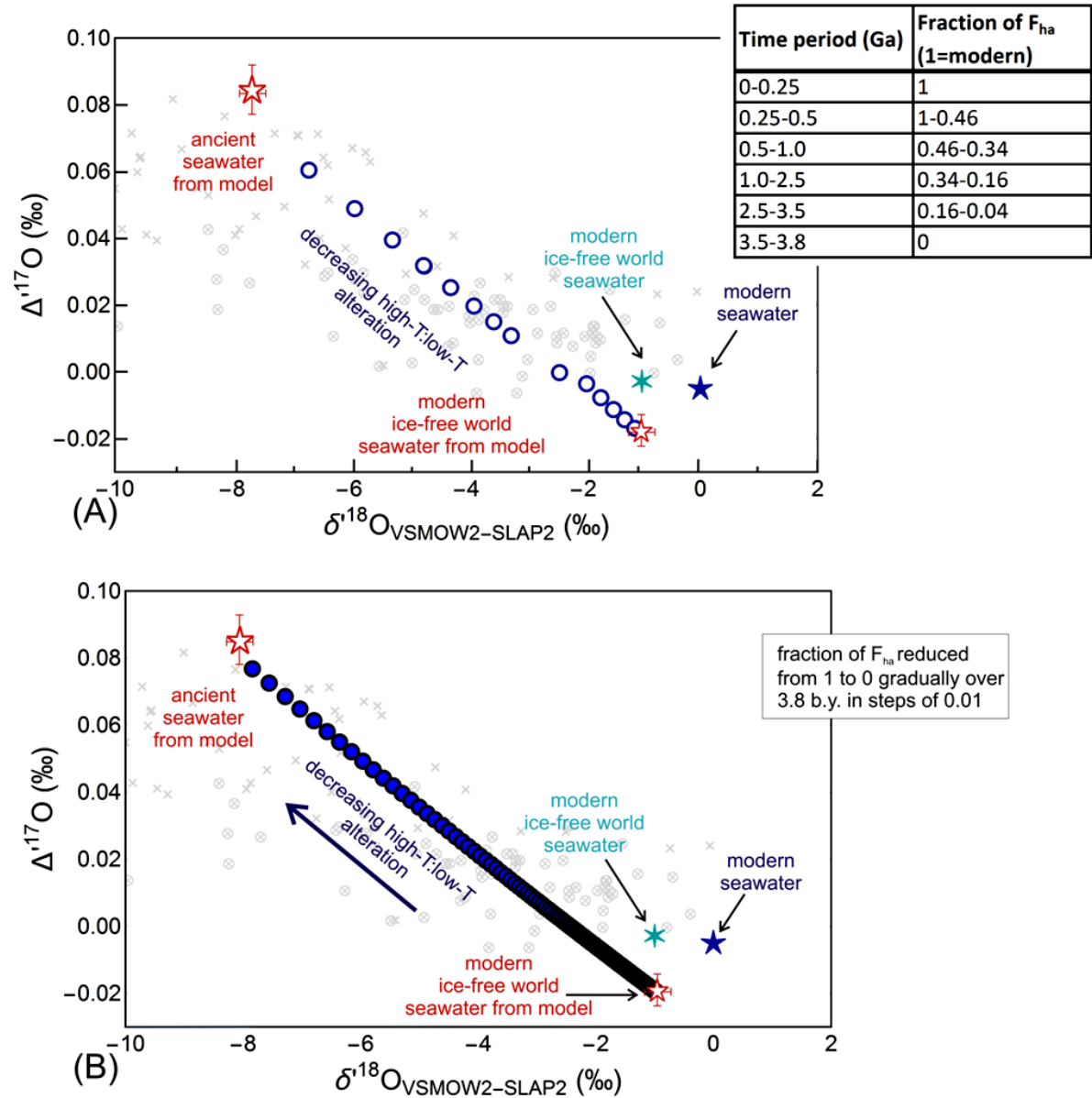
Figure 10 Plot of $\Delta'^{17}O$ vs $\delta'^{18}O$ showing seawater triple oxygen isotope composition would vary along a slope of ~0.5154 in the past (depicted by thick arrow) if the high-T alteration : low-T alteration flux ratios were to change. With decreasing F_{ha} fractions, seawater $\delta^{18}O$ decreases while $\Delta'^{17}O$ increases (corresponding to a decreasing $\delta^{17}O$). The red hollow stars depict outcomes for seawater composition from the model. Fractions of F_{ha} has been varied in bigger steps in plot (A) and more gradually in smaller regular steps in plot (B). The resulting $\Delta'^{17}O$ of the ancient oceans and the slope of variation are the same from both plots.

However, varying the magnitude of the oxygen isotope fluxes that are operating today, especially changing the ratio of high temperature to low temperature alteration of the oceanic crust would disturb the buffering effect of these fluxes. This would eventually result in a steady state value for seawater that is more than 2 per mil away from the present value. In other words, if the $\delta^{17}O^{SW}$ and $\delta^{18}O^{SW}$ was indeed different in the past, then it would be incorrect to use the modern flux magnitudes to model the ancient ocean systems (Jaffrés *et al.*, 2007). In order to model triple oxygen isotope compositions for geological past where the ratio of high-T: low-T alteration was different than today, we gradually decreased the amount of high-T alteration from present value (fraction = 1) in the Phanerozoic to zero in the Precambrian in a stepwise fashion. For each step a new model run was performed and a steady state triple oxygen isotope composition of seawater obtained, as depicted in Figure 7 by blue dots. For plot (A) in the figure the fraction of F_{ha} was decreased in large steps, ~0.1 to 0.4 at a time, covering big time periods of ~0.25 b.y. to 1.5 b.y. In plot (B), on the other hand, F_{ha} fraction was decreased more gradually in small steps of 0.01 over the entire 3.8 b.y. For both approaches, with each successive decrease in F_{ha} the seawater composition got lighter in $\delta^{18}O$, $\delta^{17}O$ and heavier in $\Delta'^{17}O$. The final result when high-T : low-T alteration approaches zero is also the same within uncertainty – $\delta^{18}O^{SW-ancient} = 7.8 \pm 0.3‰$, $\Delta'^{17}O^{SW-ancient} = 0.077 \pm 0.022‰$. Thus, seawater triple oxygen isotope composition changes along a slope of ~0.5163 in the $\delta'^{17}O$ vs $\delta'^{18}O$ space. This slope has no physical meaning, but it is important to resolve it in order to interpret triple oxygen isotope data of marine chemical sediments.

3.7 Conclusions

In this study we have measured and used high-precision $\Delta'^{17}O$ values (~0.015‰) of some altered oceanic crust samples, from ODP/IODP deep sea cores – three low-T altered and two high-T altered samples have been studied. The triple oxygen isotope composition of a marine shale sample was also analyzed, which serves as the end product of continental weathering.

A geochemical mass balance model for the $\delta^{17}O$ and $\Delta'^{17}O$ of modern day as well as a "hypothetical" ancient seawater has been presented for the first time. The mass balance model itself shows that both $\delta^{18}O$ and $\delta^{17}O$ of seawater are currently being buffered to their present day values by important geological processes involving the interaction of the hydrosphere with the lithosphere (e.g., Muehlenbachs, 1998 and references therein). In an ice-free world the calculated triple oxygen isotope compositions is: $\delta^{18}O^{IF} = -1 \pm 0.28‰$ (Schakleton and Kennet, 1975) and $\Delta'^{17}O^{IF} = -0.004 \pm 0.003‰$ (calculated from Luz and Barkan, 2010). Our model results are identical to these numbers within uncertainty. On decreasing the proportions of hydrothermal alteration, thereby changing the overall ratio of high-T : low-T alteration processes, it is possible to model a $\delta^{18}O^{SW}$ that is lighter than today. Such an ocean water bears reduced $\delta^{17}O^{SW}$ and elevated $\Delta'^{17}O^{SW}$ values compared to modern day, following a trend of 0.5163 in $\delta'^{17}O$ vs $d'^{18}O$ space. We obtain a value of $\delta^{18}O^{SW} = -7.8 \pm 0.5‰$ and $\Delta'^{17}O^{SW} = 0.077 \pm 0.015‰$ for the early Archean oceans, if the high-T alteration : low-T alteration ratio was close to zero back then (Jaffrés et al., 2007 and references therein). The trend along which seawater moves under these conditions of varying flux ratios is essential for interpreting triple oxygen isotope composition of marine chemical sediments and determining whether the Precambrian oceans were hotter than today or not. This shall be demonstrated in the following chapter.

3.8 References

Alt, J. C. (1995). Subseafloor Processes in Mid-Ocean Ridge Hydrothennal Systems. Seafloor Hydrothermal Systems: Physical, Chemical, Biological, and Geological Interactions, 85-114.

Alt, J. C., Laverne, C., Vanko, D. A., Tartarotti, P., Teagle, D. A., Bach, W., Zuleger, E., Erzinger, J., Honnorez, J., Philippe, P. A., Becker, K., Salisbury, M. H., Wilkens, R. H., & Becker, K. H. S. M. (1996). Hydrothermal alteration of a section of upper oceanic crust in the eastern equatorial Pacific: A synthesis of results from Site 504 (DSDP Legs 69, 70, and 83, and ODP Legs 111, 137, 140, and 148). Proceedings-Ocean Drilling Program Scientific Results, 148, 417-434.

Alt, J. C., Muehlenbachs, K., & Honnorez, J. (1986). An oxygen isotopic profile through the upper kilometer of the oceanic crust, DSDP Hole 504B. Earth and planetary science letters, 80(3), 217-229.

Bach, W., Alt, J. C., Niu, Y., Humphris, S. E., Erzinger, J., & Dick, H. J. (2001). The geochemical consequences of late-stage low-grade alteration of lower ocean crust at the SW Indian Ridge: Results from ODP Hole 735B (Leg 176). Geochimica et Cosmochimica Acta, 65(19), 3267-3287.

Bach, W., Erzinger, J., Alt, J. C., & Teagle, D. A. H. (1996). Chemistry of the lower sheeted dike complex, Hole 504B (Leg 148): influence of magmatic differentiation and hydrothermal alteration. Proceedings-Ocean Drilling Program Scientific Results, 148, 39-56.

Bach, W., Peucker-Ehrenbrink, B., Hart, S. R., & Blusztajn, J. S. (2003). Geochemistry of hydrothermally altered oceanic crust: DSDP/ODP Hole 504B–Implications for seawater-crust exchange budgets and Sr-and Pb-isotopic evolution of the mantle. Geochemistry, Geophysics, Geosystems, 4(3). http://dx.doi.org/10.1029/2002GC000419

Becker, R. H., Chase, C. G., & Perry, E. C. (1973). Oceanic growth models. Science, 182(4112), 601-603.

Böhlke, J. K., Honnorez, J., Honnorez-Guerstein, B. M., Muehlenbachs, K., & Petersen, N. (1981). Heterogeneous alteration of the upper oceanic crust: correlation of rock chemistry, magnetic properties, and O isotope ratios with alteration patterns in basalts from site 396B, DSDP. Journal of Geophysical Research: Solid Earth, 86(B9), 7935-7950.

Bottjer, D. J., Droser, M. L., Sheehan, P. M., & McGhee, G. R. (2001). The ecological architecture of major events in the Phanerozoic history of marine invertebrate life. Evolutionary paleoecology. Columbia University Press, New York, 35-61.

Carpenter, S. J., & Lohmann, K. C. (1995). $\delta^{18}O$ and $\delta^{13}C$ values of modern brachiopod shells. Geochimica et Cosmochimica Acta, 59(18), 3749-3764.

Clark, P. U., Dyke, A. S., Shakun, J. D., Carlson, A. E., Clark, J, Wohlfarth, B., ... & McCabe, A. M. (2009). The last glacial maximum. science, 325(5941), 710-714.

D Garlick, G., & Dymond, J. R. (1970). Oxygen isotope exchange between volcanic materials and ocean water. Geological Society of America Bulletin, 81(7), 2137-2142.

Di Rocco, T., & Pack, A. (2015). Triple oxygen isotope exchange between chondrule melt and water vapor: An experimental study. Geochimica et Cosmochimica Acta, 164, 17-34.

Expedition 336 Scientists, 2012. Expedition 336 summary. *In* Edwards, K.J., Bach, W., Klaus, A., and the Expedition 336 Scientists. Proceedings of the Integrated Ocean Drilling Program, 336: Tokyo (Integrated Ocean Drilling Program Management International, Inc.). doi:10.2204/ iodp.proc.336.101.2012

Fornari, D. J., & Embley, R. W. (1995). Tectonic and Volcanic Controls on Hydrothermal Processes at the Mid-Ocean Ridge: an Overview Based on Near-Bottom and Submersible Studies. Seafloor hydrothermal systems: physical, chemical, biological, and geological interactions, 1-46.

Gleick, P. H. Water resources in Encyclopedia of Climate and Weather. ed. SH Schneider. Vol. 2. 1996.

Gregory, R. T., & Taylor, H. P. (1981). An oxygen isotope profile in a section of Cretaceous oceanic crust, Samail Ophiolite, Oman: Evidence for $\delta^{18}O$ buffering of the oceans by deep (> 5 km) seawater-hydrothermal circulation at mid-ocean ridges. Journal of Geophysical Research: Solid Earth, 86(B4), 2737-2755.

Gregory, S. V., Swanson, F. J., McKee, W. A., & Cummins, K. W. (1991). An ecosystem perspective of riparian zones. BioScience, 41(8), 540-551.

Herwartz, D., Pack, A., Krylov, D., Xiao, Y., Muehlenbachs, K., Sengupta, S., & Di Rocco, T. (2015). Revealing the climate of snowball Earth from $\Delta^{17}O$ systematics of hydrothermal rocks. Proceedings of the National Academy of Sciences, 112(17), 5337-5341.

Hoefs J. (1997). Stable Isotope Geochemistry, 4th edition. Springer-Verlag.

Holland, H. D. (1984). The chemical evolution of the atmosphere and oceans. Princeton University Press.

Holland, H.D. (2004). The geologic history of seawater. In Elderfield, H. (Ed.). & Holland, H.D. &
Turekian, K.K. (Exec. Eds.), Treatise on Geochemistry,Vol. 6. The Oceans and Marine
Geochemistry. Elsevier Pergamon, Kidlington, Oxford, pp. 583–625.

Holmden, C., & Muehlenbachs, K. (1993). The $^{18}O/^{16}O$ ratio of 2-billion-year-old seawater
inferred from ancient oceanic crust. Science, 259(5102), 1733-1736.

Jaffrés, J. B., Shields, G. A., & Wallmann, K. (2007). The oxygen isotope evolution of seawater: a
critical review of a long-standing controversy and an improved geological water cycle model
for the past 3.4 billion years. Earth-Science Reviews, 83(1), 83-122.

Jaffrés, J. B., Shields, G. A., & Wallmann, K. (2007). The oxygen isotope evolution of seawater: a
critical review of a long-standing controversy and an improved geological water cycle model
for the past 3.4 billion years. Earth-Science Reviews, 83(1), 83-122.

Jaffrés, J. B., Shields, G. A., & Wallmann, K. (2007). The oxygen isotope evolution of seawater: a
critical review of a long-standing controversy and an improved geological water cycle model
for the past 3.4 billion years. Earth-Science Reviews, 83(1), 83-122.

Jean-Baptiste, P., Charlou, J. L., & Stievenard, M. (1997). Oxygen isotope study of mid-ocean ridge
hydrothermal fluids: Implication for the oxygen-18 budget of the oceans. Geochimica et
cosmochimica acta, 61(13), 2669-2677.

Kasting, J. F., Howard, M. T., Wallmann, K., Veizer, J., Shields, G., & Jaffrés, J. (2006). Paleoclimates,
ocean depth, and the oxygen isotopic composition of seawater. Earth and Planetary Science
Letters, 252(1), 82-93.

Kasting, J. F., Howard, M. T., Wallmann, K., Veizer, J., Shields, G., & Jaffrés, J. (2006). Paleoclimates,
ocean depth, and the oxygen isotopic composition of seawater. Earth and Planetary Science
Letters, 252(1), 82-93.

Kasting, J. F., Howard, M. T., Wallmann, K., Veizer, J., Shields, G., & Jaffrés, J. (2006). Paleoclimates,
ocean depth, and the oxygen isotopic composition of seawater. Earth and Planetary Science
Letters, 252(1), 82-93.

Lawrence, J. R., & Gieskes, J. M. (1981). Constraints on water transport and alteration in the oceanic crust from the isotopic composition of pore water. Journal of Geophysical Research: Solid Earth, 86(B9), 7924-7934.

Lécuyer, C., & Allemand, P. (1999). Modelling of the oxygen isotope evolution of seawater: implications for the climate interpretation of the δ 18 O of marine sediments. Geochimica et Cosmochimica Acta, 63(3), 351-361.

Lhomme, N., Clarke, G. K., & Ritz, C. (2005). Global budget of water isotopes inferred from polar ice sheets. Geophysical Research Letters, 32(20).

Li, Y. H. (1972). Geochemical mass balance among lithosphere, hydrosphere, and atmosphere. American Journal of Science, 272, 119-137.

Luz, B., & Barkan, E. (2010). Variations of 17 O/16 O and 18 O/16 O in meteoric waters. Geochimica et Cosmochimica Acta, 74(22), 6276-6286.

Luz, B., & Barkan, E. (2010). Variations of $^{17}O/^{16}O$ and $^{18}O/^{16}O$ in meteoric waters. Geochimica et Cosmochimica Acta, 74(22), 6276-6286.

Mattey, D., Lowry, D., & Macpherson, C. (1994). Oxygen isotope composition of mantle peridotite. Earth and Planetary Science Letters, 128(3-4), 231-241.

Matsuhisa, Y., Goldsmith, J. R., & Clayton, R. N. (1978). Mechanisms of hydrothermal crystallization of quartz at 250 C and 15 kbar. Geochimica et Cosmochimica Acta, 42(2), 173-182.

Morgan, J. P. (1998). Thermal and rare gas evolution of the mantle. Chemical Geology, 145(3), 431-445.

Muehlenbachs, K. (1980). The alteration and aging of the basaltic layer of the sea floor: oxygen isotope evidence from DSDP/IPOD Legs 51, 52, and 53. Initial Reports of the Deep Sea Drilling Project, 51, 1159-1167.

Muehlenbachs, K. (1986). Alteration of the oceanic crust and the ^{18}O history of seawater. Reviews in Mineralogy and Geochemistry, 16(1), 425-444.

Muehlenbachs, K. (1998). The oxygen isotopic composition of the oceans, sediments and the seafloor. Chemical Geology, 145(3), 263-273.

Muehlenbachs, K. (1998). The oxygen isotopic composition of the oceans, sediments and the seafloor. Chemical Geology, 145(3), 263-273.

Muehlenbachs, K. (1998). The oxygen isotopic composition of the oceans, sediments and the seafloor. Chemical Geology, 145(3), 263-273.

Muehlenbachs, K., & Clayton, R. N. (1971). Oxygen isotope ratios of submarine diorites and their constituent minerals. Canadian Journal of Earth Sciences, 8(12), 1591-1595.

Muehlenbachs, K., & Clayton, R. N. (1972a). Oxygen isotope studies of fresh and weathered submarine basalts. Canadian Journal of Earth Sciences, 9(2), 172-184.

Muehlenbachs, K., & Clayton, R. N. (1972b). Oxygen isotope geochemistry of submarine greenstones. Canadian Journal of Earth Sciences, 9(5), 471-478.

Muehlenbachs, K., & Clayton, R. N. (1976). Oxygen isotope composition of the oceanic crust and its bearing on seawater. Journal of Geophysical Research, 81(23), 4365-4369.

Muehlenbachs, K., & Clayton, R. N. (1976). Oxygen isotope composition of the oceanic crust and its bearing on seawater. Journal of Geophysical Research, 81(23), 4365-4369.

O'Neil, J. R., & Chappell, B. W. (1977). Oxygen and hydrogen isotope relations in the Berridale batholith. Journal of the Geological Society, 133(6), 559-571.

Orcutt, B. N., Wheat, C. G., Rouxel, O., Hulme, S., Edwards, K. J., & Bach, W. (2013). Oxygen consumption rates in subseafloor basaltic crust derived from a reaction transport model. Nature communications, 4, 2539.

Pack, A., & Herwartz, D. (2014). The triple oxygen isotope composition of the Earth mantle and understanding variations in terrestrial rocks and minerals. Earth and Planetary Science Letters, 390, 138-145.

Pack, A., Tanaka, R., Hering, M., Sengupta, S., Peters, S., & Nakamura, E. (2016). The oxygen isotope composition of San Carlos olivine on the VSMOW2-SLAP2 scale. Rapid Communications in Mass Spectrometry, 30(13), 1495-1504.

Perry, E. C. (1967). The oxygen isotope chemistry of ancient cherts. Earth and Planetary Science Letters, 3, 62-66.

Qing, H., & Veizer, J. (1994). Oxygen and carbon isotopic composition of Ordovician brachiopods: Implications for coeval seawater. Geochimica et Cosmochimica Acta, 58(20), 4429-4442.

Reymer, A., & Schubert, G. (1984). Phanerozoic addition rates to the continental crust and crustal growth. Tectonics, 3(1), 63-77.

Saccocia, P. J., Seewald, J. S., & Shanks, W. C. (2009). Oxygen and hydrogen isotope fractionation in serpentine–water and talc–water systems from 250 to 450° C, 50MPa. Geochimica et Cosmochimica Acta, 73(22), 6789-6804.

Schrag, D. P., Adkins, J. F., McIntyre, K., Alexander, J. L., Hodell, D. A., Charles, C. D., & McManus, J. F. (2002). The oxygen isotopic composition of seawater during the Last Glacial Maximum. Quaternary Science Reviews, 21(1), 331-342.

Shackleton, N. J., & Kennett, J. P. (1975). Paleotemperature history of the Cenozoic and the initiation of Antarctic glaciation: oxygen and carbon isotope analyses in DSDP Sites 277, 279, and 281. Initial Reports of the Deep Sea Drilling Project, 29, 743-755.

Sharp, Z. D., Gibbons, J. A., Maltsev, O., Atudorei, V., Pack, A., Sengupta, S., Shock, E.L., & Knauth, L. P. (2016). A calibration of the triple oxygen isotope fractionation in the SiO_2–H_2O system and applications to natural samples. Geochimica et Cosmochimica Acta, 186, 105-119.

Sheppard, S. M. F., & Gilg, H. A. (1996). Stable isotope geochemistry of clay minerals. Clay Minerals, 31(1), 1-24.

Sheppard, S. M. F., & Gilg, H. A. (1996). Stable isotope geochemistry of clay minerals. Clay Minerals, 31(1), 1-24.

Song, J., Littke, R., Weniger, P., Ostertag-Henning, C., & Nelskamp, S. (2015). Shale oil potential and thermal maturity of the Lower Toarcian Posidonia Shale in NW Europe. International Journal of Coal Geology, 150, 127-153.

Staudigel, H., Muehlenbachs, K., Richardson, S. H., & Hart, S. R. (1981). Agents of low temperature ocean crust alteration. Contributions to Mineralogy and Petrology, 77(2), 150-157.

Taylor Jr, H. P. (1968). The oxygen isotope geochemistry of igneous rocks. Contributions to Mineralogy and Petrology, 19(1), 1-71.

Veizer, J., Bruckschen, P., Pawellek, F., Diener, A., Podlaha, O. G., Carden, G. A., ... & Ala, D. (1997). Oxygen isotope evolution of Phanerozoic seawater. Palaeogeography, Palaeoclimatology, Palaeoecology, 132(1), 159-172.

Veizer, J., Fritz, P., & Jones, B. (1986). Geochemistry of brachiopods: oxygen and carbon isotopic records of Paleozoic oceans. Geochimica et Cosmochimica Acta, 50(8), 1679-1696.

Walker, J. C., & Lohmann, K. C. (1989). Why the oxygen isotopic composition of sea water changes with time. Geophysical Research Letters, 16(4), 323-326.

Walker, J. C., & Lohmann, K. C. (1989). Why the oxygen isotopic composition of sea water changes with time. Geophysical Research Letters, 16(4), 323-326.

Wallmann, K. (2001). The geological water cycle and the evolution of marine δ 18 O values. Geochimica et Cosmochimica Acta, 65(15), 2469-2485.

Wallmann, K. (2001). The geological water cycle and the evolution of marine δ 18 O values. Geochimica et Cosmochimica Acta, 65(15), 2469-2485.

Wallmann, K. (2001). The geological water cycle and the evolution of marine δ 18 O values. Geochimica et Cosmochimica Acta, 65(15), 2469-2485.

Weber, J. N. (1965). The O^{18}/O^{16} ratio in ancient oceans. Geokhimija, 6, 674-680.

Williams, D. L., & Von Herzen, R. P. (1974). Heat loss from the earth: new estimate. Geology, 2(7), 327-328.

Young, E. D., Galy, A., & Nagahara, H. (2002). Kinetic and equilibrium mass-dependent isotope fractionation laws in nature and their geochemical and cosmochemical significance. Geochimica et Cosmochimica Acta, 66(6), 1095-1104.

4. Cherts – study of petrography, trace elements and triple oxygen isotopes with implications on the δ¹⁸O and temperature of ancient oceans

4.1 Introduction

The trend of decreasing $\delta^{18}O$ of cherts with increasing age has been used to interpret the $\delta^{18}O$ and temperature of ancient oceans (e.g., Knauth and Lowe, 2003 and references therein). It is debated whether this trend reflects a low $\delta^{18}O$ ancient ocean with same temperature as today (e.g., Perry 1967) or a hot ocean with the same $\delta^{18}O$ as today or progressive diagenetic alteration of $\delta^{18}O$ over time. Since neither the temperature of precipitation of these cherts nor the $\delta^{18}O$ of the water they precipitate from are well constrained, the $\delta^{18}O$ value of the cherts alone is insufficient to resolve this ambiguity of a possible "hot" or "light-$\delta^{18}O$" ocean. We therefore, use the $\delta^{17}O$ of cherts as an additional parameter along with their $\delta^{18}O$ values in order to address this problem. The mass balance model from the previous section is used here as a framework to interpret the measured $\delta^{18}O$ and $\delta^{17}O$ composition of the cherts. The concept is described in more detail in Chapter 1 of this thesis and in section 5 of this chapter.

In order to characterize the depositional setting of the cherts and to detect if the studied samples are affected by detrital components, the petrography of the cherts was studied and their trace element analysis (REE, Y, Zr, Sc, Ti) was carried out. Characteristic rare earth element (REE) signatures of seawater from different tectonic regimes are recorded by the sediments deposited in the respective settings and hence, may be used to infer depositional regimes of the studied cherts (e.g., Murray, 1990; Muray, 1994). This is only possible for samples whose trace element

signatures have not been heavily disturbed by detrital contamination (e.g., Bolhar et al., 2004; Sugahara et al., 2010)

4.2 Sample description and petrographic study

Our sample set consists of cherts or silica of sedimentary origin, ranging in age from recent Quarternary- like marine diatoms and alkaline lake chert - to Archean samples including quartz from banded iron formations Figure 1. A description of the samples and their localities is provided below.

Samples with "GZG.GSP" as prefix are from the Geowissenschaftliches Museum of Geowissenschaftliches Zentrum, Göttingen.

Sample numbers such as "16 of 8-17-86" are original collection numbers from Stanley Awramik (University of California, Santa Barbara), who also provided some of the petrographic information outlined below. These samples were procured via François Robert (National Museum of Natural History, Paris).

Sample numbers starting with "PRG" belong to the samples collected by the Precambrian Paleobiology Research Group and the sample descriptions are from Schopf (1983), also procured via François Robert.

Samples with prefix "K-" were provided by Paul Knauth (Arizona State University), via Zachary Sharp (University of New Mexico, New Mexico).

Other sample providers have been specified in the description below for each sample.

The abbreviations used to refer to the samples further in the text, for simplicity, have been mentioned in parentheses.

4.2.1 Nomenclature and terminology for silica petrography

The quartz varieties seen within chert samples in transmitted light, through the optical microscope, range in size from cryptocrystalline to megaquartz, including different micro forms of quartz. A brief description of the nomenclature used in this study has been provided below. The different quartz varieties observed are all diagenetic forms of silica - seen replacing precursor minerals, forming pseudomorphs, as void - fills or simply as recrystallized rock matrix.

4.2.1.1 Microcrystalline quartz / Microquartz

Interlocking quartz crystals, in random orientation, sized < 20 μm are commonly called microcrystalline quartz (Folk and Weaver, 1952). Most cherts have microcrystalline quartz ranging in size from 3 – 5 μm. This is the dominant component of the majority of cherts (Knauth, 1992) and forms by replacing an earlier precursor phase. Individual quartz crystals typically have irregular, crenulated to diffused grain boundaries and undulose extinction (Maliva et al., 2005). Quartz crystals composed of plates of α-quartz with a mean thickness of 59 nm that are

joined by a monolayer of water might be the reason behind the undulose extinction (Micheelsen, 1966; Knauth and Epstein, 1976).

4.2.1.2 Mesocrystalline quartz

Quartz crystals > 20 μm with similar textural features as microcrystalline quartz was referred to as mesocrystalline quartz by Maliva et al., 2005 in order to distinguish it from megaquartz. This nomenclature is being followed here.

4.2.1.3 Megaquartz

Larger than 20 μm sized quartz crystals with more regular planar boundaries than crenulated ones and unit extinction are called megaquartz. They are commonly found as void fillings and carbonate replacements (Maliva et al., 2005). They are sometimes fround in the core of cavities whose walls are lined by microquartz. This is often interpreted to represent a decreased silica concentration and/or slower crystal growth rate (Folk and Weaver, 1952; Heaney, 1993), which in turn maybe due to the decrease in permeability and reduced diagenetic fluid inflow as the cavity is filling up (Knauth, 1994).

Metamorphic and hydrothermal alteration forms megaquartz with a mosaic texture, where each grain shows pinpoint extinction. This texture characterizes recrystallized cherts and distinguishes them from those that are well preserved. "Triple-point" textures of megaquartz grains can be seen within highly metamosphosed cherts (Keller et al., 1977).

4.2.1.4 Chalcedony or Microcrystalline fibrous silica

Radiating or sheaf-like bundles of quartz fibres that grow relatively rapidly in one dimension to form either radial or parallel aggregates comprise chalcedony (Folk and Weaver, 1952; Cunningham et al., 2012). Individual chalcedony fibres are a few microns in diameter and up to 200 μm or more in length (Folk and Weaver, 1952). These usually form botryoidal arrays in cavities, fractures and vugs in host rocks (Knauth, 1994). They create various patterns, e.g.,

rosette structures, which are characteristic of diagenetic silica. They are almost always a minor component in cherts.

Apart from quartz, the other phases seen within the chert samples include iron-rich materials that appear brown in plane polarised light or PPL (body colour masks interference colour in cross-polarised light or CPL), opaque minerals and organic matter. Some carbonate minerals as relict phases or even newly formed diagenetic crystals are also commonly seen within cherts.

Table 1 List of chert sample groups, abbreviations used for them throughout the text and individual samples within the groups.

Sample group	Sample Localities	Abbreviation	Sample name
	Phanerozoic cherts		
Lake Natron Chert *not marine*	Lake Natron, Tanzania, East African Ridge	LNC	LNC
Modern marine diatoms	ODP Leg 177, Site 1094, Southern Ocean	Di	Di-73
	ODP Leg 177, Site 1094, Southern Ocean		Di-34
	ODP Leg 177, Site 1093, Southern Ocean		Di7
Deep sea chert	Horizon Guyot, Pacific Ocean	HGC	HGC
Nodular Cherts	North Germany	PNC	M1
	Kreidbruch Galitz, Rügen, Germany		M7
	Hooken Cliff, Devon, United Kingdom		M6
	Aromanches-les Bains, Étreat, France		AR
Bedded Cherts	Caontons of Switzerland, Switzerland	PBC	M3
	Hainbuch valley, Hesse, Germany		M8
	Proterozoic cherts		
Doushantuo cherts	Doushantuo Formation,Yangtze Block, South China	DC	D3
			D5
Dahongyu cherts		JC	JC
Bitter Springs Chert	Bitter Springs Formation, Amadeus Basin, Australia	BS	BS
Gunflint Bedded cherts	Gunflint Iron Formation, Canada	GFBC	G1
			G3
			K-565
Chert band form BIF	Jasper Knob, Michigan, USA	BIF-2	BIF-2/a/b-chert
	Archean cherts		
Pilbara bedded cherts	Dresser formation, Pilbara craton, W. Australia	PilBC	W2
	Marble Bar Chert member		MBC/MBC-new white
Pilbara Vein Chert	Dresser formation, Pilbara craton, W. Australia	PilVC	DUC-1
			DUC-2
			DUC new
Agate in interpillow space of Mt Ada basalt	Mt Ada Basalt, Pilbara craton, W. Australia	PL-2	PL-2
Barberton bedded chert	Barberton Greenstone Belt, South Africa	BBC	Z1
			Z2
			Z3
Chert band from BIF-1	Barberton Greenstone Belt, South Africa	BIF-1	BIF-1-chert
Quartz stalactite	Barberton Greenstone Belt, South Africa	K-1100	K-1100
Nodular Chert in siderite	Barberton Greenstone Belt, South Africa	K-1113	K-1113

4.2.2 Phanerozoic samples

4.2.2.1 Lacustrine chert, Lake Natron, Tanzania

4.2.2.1.1 Natron Lake GPS-114 (NLC)

This is a modern chert sample, few hundred thousand years old, precipitated in the highly alkaline and silica supersaturated waters of Lake Natron. The location is 02° 22.426' S, 035° 54.236' E, at an altitude of 597m.

This sample was provided by Francois Robert . The water samples from Lake Natron and surrounding feeder hot springs were measured for $\delta^{18}O$ values by Francois Robert.

4.2.2.2 Modern marine diatoms

Deep sea sediment cores from the Ocean Drilling Program in the southeast Atlantic sector of the Southern Ocean were sampled at their diatoms rich zones. Both sites are located in the circum-Antarctic opal belt, which is currently an ice-free zone but was under ice cover during last glaciation (Gersonde et al., 1999). Three different diatom ooze samples from three different cores have been studied. They belong to the Pleistocene epoch.

4.2.2.2.1 ODP Leg 177, Site 1093

4.2.2.2.1.1 Sample Di7 (Di-7)

This sample is located at 50°S, mean water depth of 3626.2 m (Gersonde et al., 1999).

Hole 1093A, Core 23H-Section 4, Interval 109 to 110 cm, from about 210 m. Sample was collected from International Ocean Discovery Program (IODP) - Bremen Core Repository, Center for Marine Environmental Sciences (MARUM), Bremen, Germany.

4.2.2.2.2 ODP Leg 177, Site 1094

Two samples belong to this drilling site, located at 53°S, in the ice-free Antarctic Zone. Water depth at the location is 2807 m (Gersonde et al., 1999). Purified extracted diatom samples from these cores were donated by Aldo Shemesh, Weizmann Institute of Science, Israel.

The sample is from a depth of 21.77 m, ~111,000 yrs old and belongs to the Marine isotope stage (MIS) 5d.

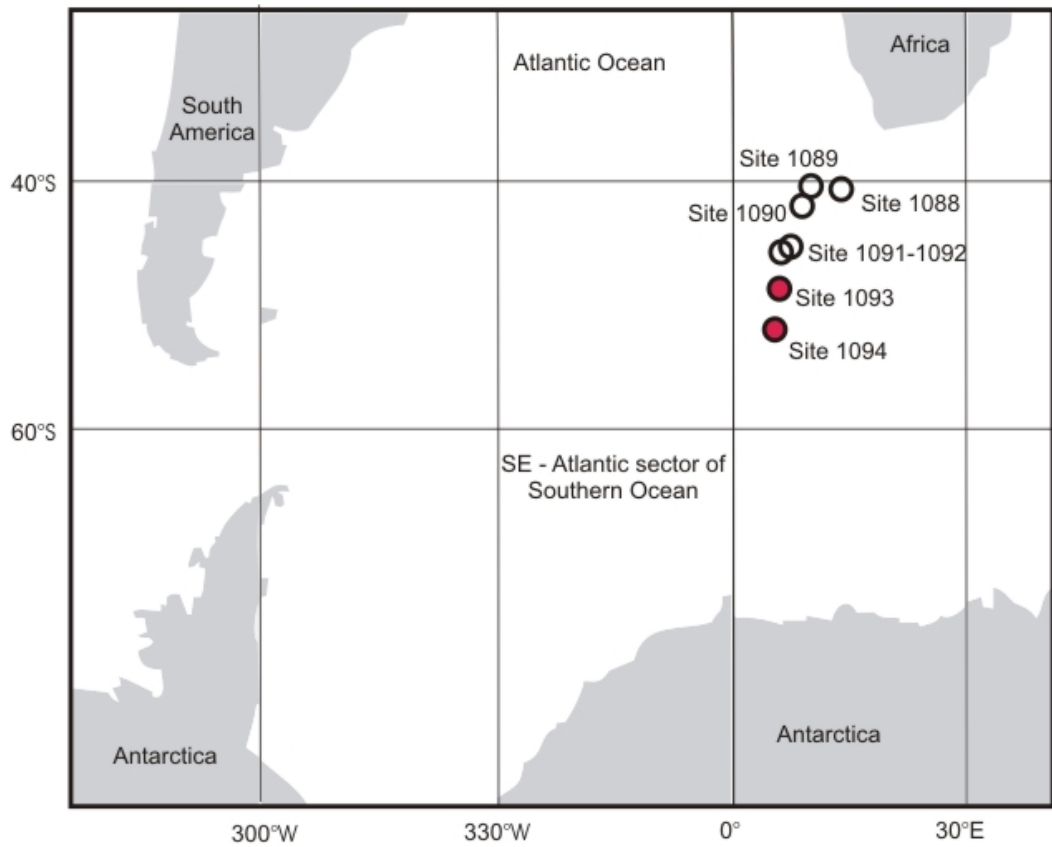 Sample from depth 19.82 m, ~92,000 yrs old, belonging to MIS 5c.

Figure 2 Map showing the location of seven sites, 1088 to 1094, drilled in the Southern Ocean as a part of Ocean Drilling Project, Leg 177. The diatom samples analyzed here belong to cores from Sites 1093 and 1094, marked here by the circles filled in red.
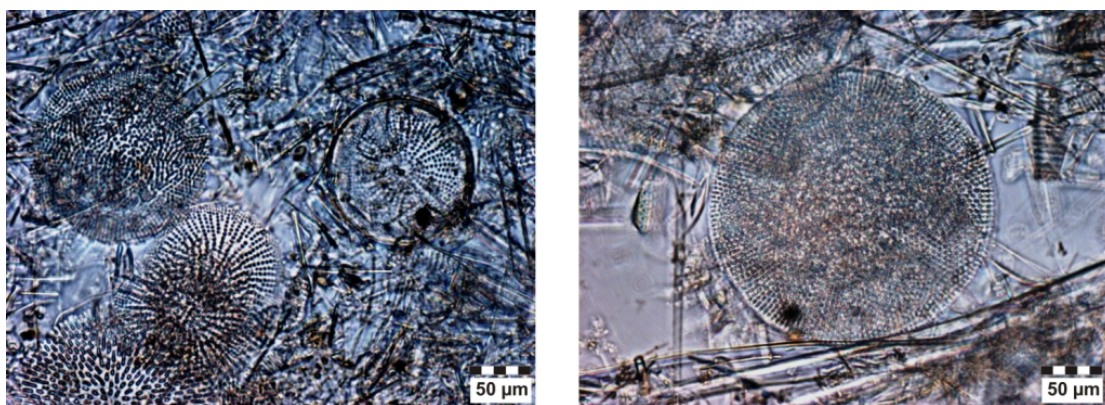

Figure 3 Diatoms, as seen under the optical microscope, within deep sea sediment core ODP Leg 177, Site 1093, Sample Di-7. Plane polarized (PPL) light image.

4.2.2.3 Deep sea chert from Horizon Guyot (HGC)

This is a microcrystalline quartz sample excavated from the Horizon Guyot in the North Central Pacific Ocean. Its location is 168°52.3'W, 10°28.0'N, at 1700 m water depth. The sample contains greater than 98% granular microcrystalline quartz (Knauth, 1973). Its $\delta^{18}O$ was measured to be 38.85‰ by Knauth (1973).

4.2.2.4 Nodular cherts in limestone (PNC)

4.2.2.4.1 Sample no. GZG.GSP 04002 (M1)

Sample is of Paleogene age, from north Germany.

4.2.2.4.2 Sample no. GZG.GSP 3998 (M7)

 Upper Cretaceous age. Locality is Kreidbruch Galitz, Jasmund, Rügen, Germany.

4.2.2.4.3 Sample no. GZG.GSP 04001 (M6)

Sample is of Upper Cretaceous age. Locality is Hooken Cliff, Beer, West Seaton, Devon, United Kingdom.

4.2.2.4.4 Aromanche chert (AC)

Sample is of Cretaceous age, from Aromanches-les Bains, France. Close to the location of cretaceous chert studied from Étretat, Upper Normandy, France in Pack and Herwartz (2014).

4.2.2.5 Bedded cherts (PBC)

4.2.2.5.1   Sample no. GZG.GSP 04000 (M3)

Lower Cretaceous age, from Zingelstraße am Lauerzee, Cantons of Switzerland, Switzerland.

Sample is a Kieselkalk / Helvetic Siliceous Limestone - a very dark coloured massive

rock containing about 40-60% silica, in the form of about 60-100 μm sized quartz crystals. The

rest of the rock is composed of partially resorbed calcite crystals. The sample is of marine origin.
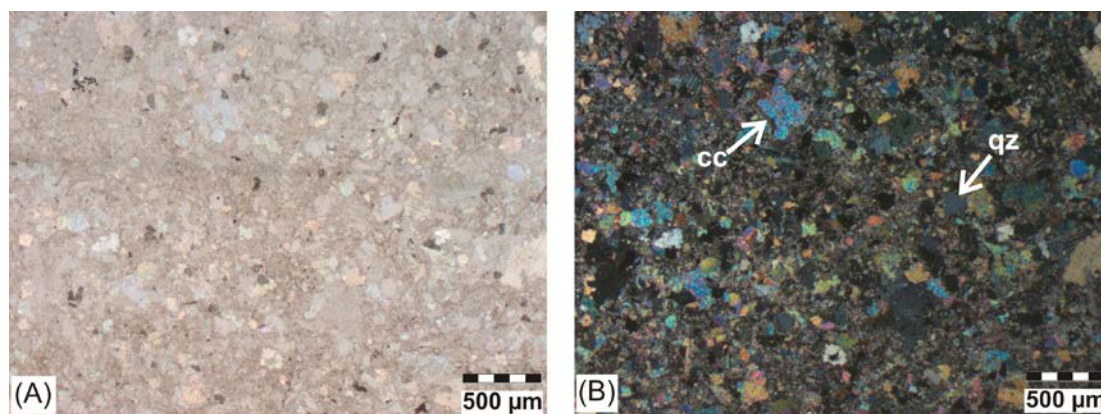
Figure 5 Photomicrographs of Sample M3, lower Cretaceous bedded siliceous limestone from Switzerland. (A) and (B) show plane polarized light (PPL) and cross polarized light (CPL) images, respectively, of the sample composed of 50-60% quartz crystals and about 30% resorbed calcite grains.

4.2.2.5.2 Sample no. GZG.GSP 03991(M8)

This is a radiolarite sample of Mississippian/Lower Carboniferous age, from Hainbuch valley, North Wallau, Hessen, Germany. The sample is a finely laminated, dark coloured deep sea sedimentary rock. Microquartz matrix with around 10% bigger detrital quartz grain aggregates floating around.

4.2.3 Proterozoic cherts
4.2.3.1 Doushantuo Formation, Yangtze Block, South China (DC)

The Doushantuo Formation is situated in the Yangtze Gorges area in the middle of the Yangtze block, Hubei Province, South China. Along with the Dengying Fmn. (ca. 551–541 Ma, Zhu et al., 2003) it represents the Ediacaran period in Earth's history and contains a plethora of well preserved microfossils (e.g., Zhu et al., 2007). Studies on Neoproterozoic successions in the Yangtze Gorges area were started by Lee, 1924 and it is the type area for late Precambrian Sinian system (c.f. Liu et al., 2013).

The Doushantuo Fmn. is between 160 and 230 metres thick and is underlain by the Cryogenian

Nantuo diamictite and overlain by upper Ediacaran dolostone of the Dengying Formation (Liu et al., 2013). The fmn. itself comprises of well defined lowermost cap carbonate unit and uppermost black shale unit (e.g., Zhu et al., 2007 and references therein), with variably carbonate and shale dominated facies in between. The middle members contain chert nodules with abundant microfossils (Yin, 1987; Yin L et al., 2007).

The samples for this study come from Tiyanjiayuanzi Section, located on the southern limb of the Huangling anticline. This section consists of medium bedded, laminated, grayish black microcrystalline dolostone with chert (Liu et al., 2013).

A passive continental margin setting on the Yangtze Block has been suggested for deposition of Ediacaran sediments in South China (Jiang et al., 2003; Li et al., 2003; Wang and Li, 2003).

Zircon U-Pb ages obtained from interbedded ash beds dates the Doushantuo Fmn. between 635.2 ± 0.6 Ma and 551.1 ± 0.7 Ma (Condon et al., 2005). The formation thus represents about 84 million years, or approximately 90% of the Ediacaran Period.

4.2.3.1.1   2a of 8-25-83 (D3)

This is a sample from top of unit 6 of Tianjiayuanzi Section. Sample is a medium-bedded, laminated, grayish-black, microcrystalline dolostone, with chert. It is composed of some continuous to fragmented Fe- rich microbial laminations (Fig. 16 A) as well as some zones almost devoid of laminations (Fig. 16 B).

4.2.3.1.2   1a of 8-25-83 (D5)

This is a sample from top of unit 3 of Tianjiayyuanzi Section. An abundance of dark kerogenous material is seen in petrographic thin-section (Fig. 16 C). This sample is also a medium-bedded, laminated, grayish-black, microcrystalline dolostone, with chert.
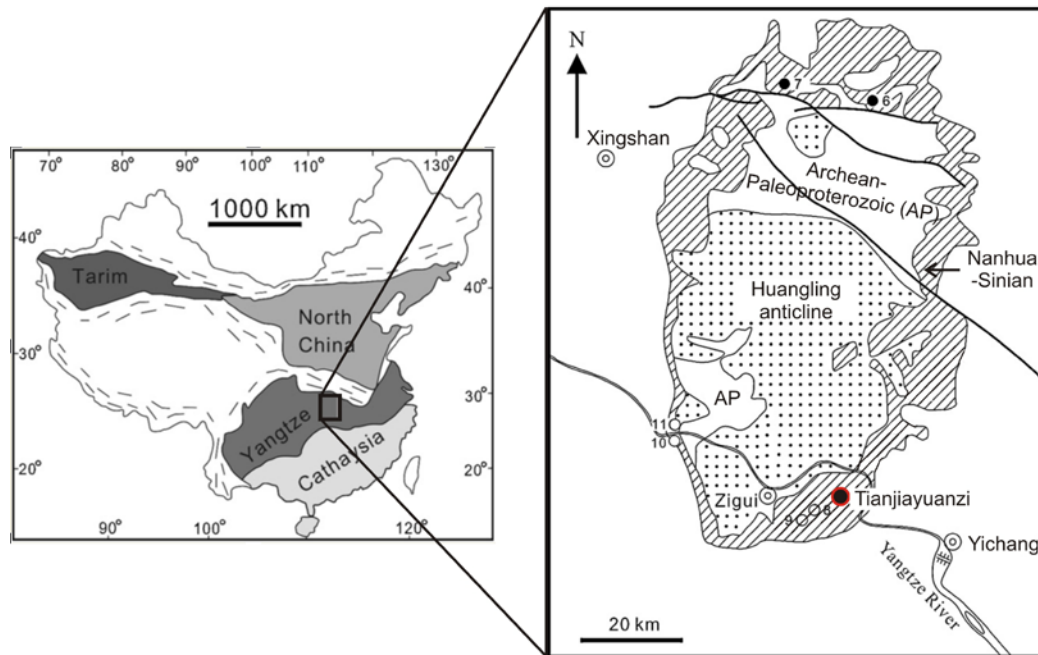
Figure 6 Map showing location of chert samples from Doushantuo Fmn. in the Yantze block of North China. The samples come from Tianjiyuanzi section, marked on map (red dot). Modifies after Liu et al., 2013.
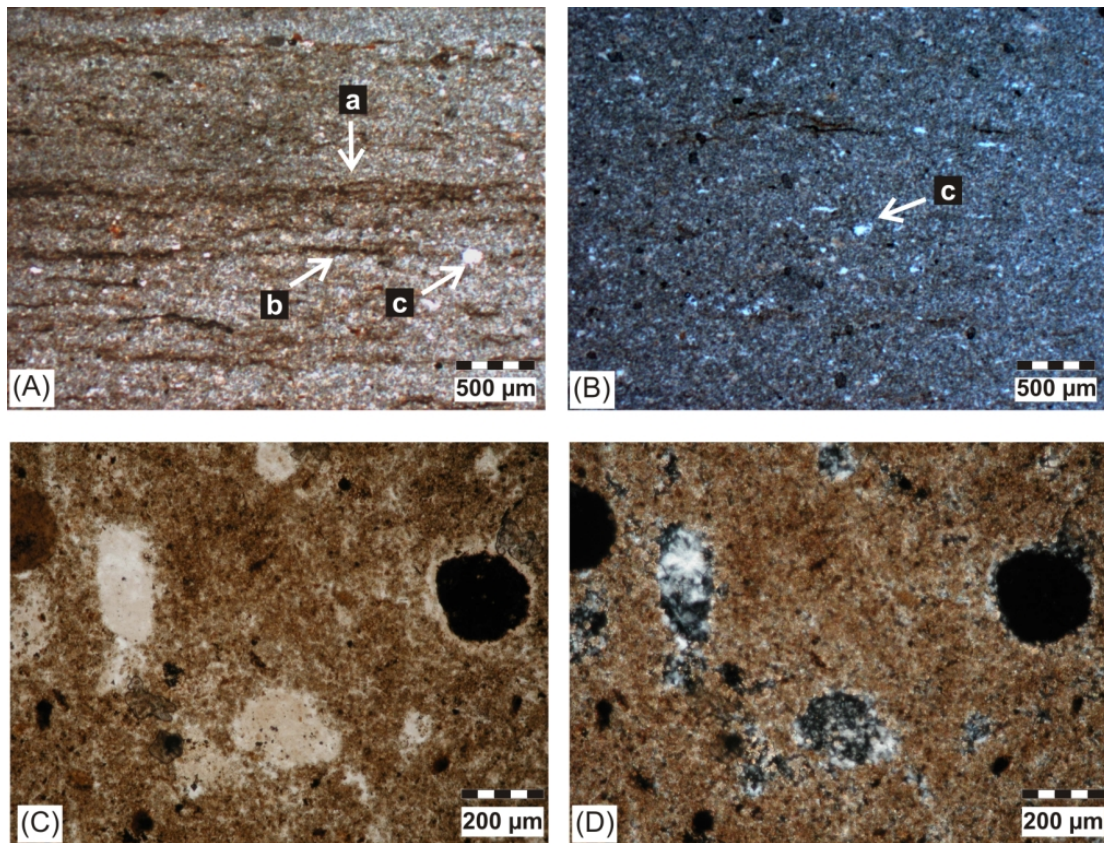
Figure 7 Photomicrographs of chert samples from the Tianjiayyuanzi Section of Doushantuo Fmn., South China. (A) plane polarized light (PPL) image of sample 2a of 8-25-83 (D3) showing preserved continuous (a) and broken/fragmented (b) microbial laminations within the silicified rock. Some detrital quartz grains (~10% by volume) (c) are found sticking to the laminations. (B) CPL image of another portion of the sample D3 within the same thin section. This portion is relatively free of microbial laminations. Silicified groundmass of microcrystalline quartz is visible. Some of the larger quartz grains may be of detrital origin (c). (C) and (D) are PPL and cross polarised light (CPL) images, respectively, of sample 1a of 8-25-83 (D5). There is an abundance of dark coloured organic matter. Recrystallized microcrystalline quartz is seen in CPL view.

4.2.3.2 Bitter Springs Formation, Australia (BS)

Located within the 24 km of predominantly shallow water sediments of the broad intracratonic Amadeus Basin in North Territory, central Australia (c.f. Southgate, 1989), the Bitter Springs Fmn. is the basal carbonate unit of the Late Proterozoic to middle Paleozoic sediment sequence (Wells et al., 1970). Estimated maximum thickness of the Fmn. is 900 m (Walther,

1972) and it is subdivided into the lower Gillen and upper Loves Creek Members (Wells et al., 1970; reviewed by Preiss et al., 1978). It conformably overlies the basal formation of the Amadeus basin sequence, called the Heavitree Quartzite.

Late Proterozoic sediments of the Amadeus basin, including those of the Bitter Springs Formation comprise a well-preserved succession of shallow water terrigenous clastic and carbonate rocks (Southgate, 1989). The Bitter Springs sediments are interpreted to have been deposited in a marine peritidal environment (Walter 1972, and unpublished observations by Malcolm R. Walther mentioned in Schopf, 1983). The formation is famous for well preserved microfossils described first by Schopf (1968).

A minimum age of 0.75 Ga (Preiss et al., 1978) and a maximum age of 0.897 ± 0.009 Ga (Black et al., 1980) is suggested for Bitter Springs Formation. The minimum age is a Rb-Sr age for dolerite from the Stuart Dyke Swarm unconformably underlying the Heavitree Quartzite.

4.2.3.2.1 PPRG 200 (BS)

The sample comes from the Loves Creek Member of the Bitter Springs Formation. It is composed of a groundmass of micro- and mesocrystalline quartz along with fibrous chalcedony (Fig. 13 A, B). Chalcedony is present as veins (Fig. 13 A and B) or as void filling cements (Fig. 13 C and D). Mesocrystalline quartz is also seen filling voids or fenestra; such quartz is called fenestral quartz (Fig. 13 E).
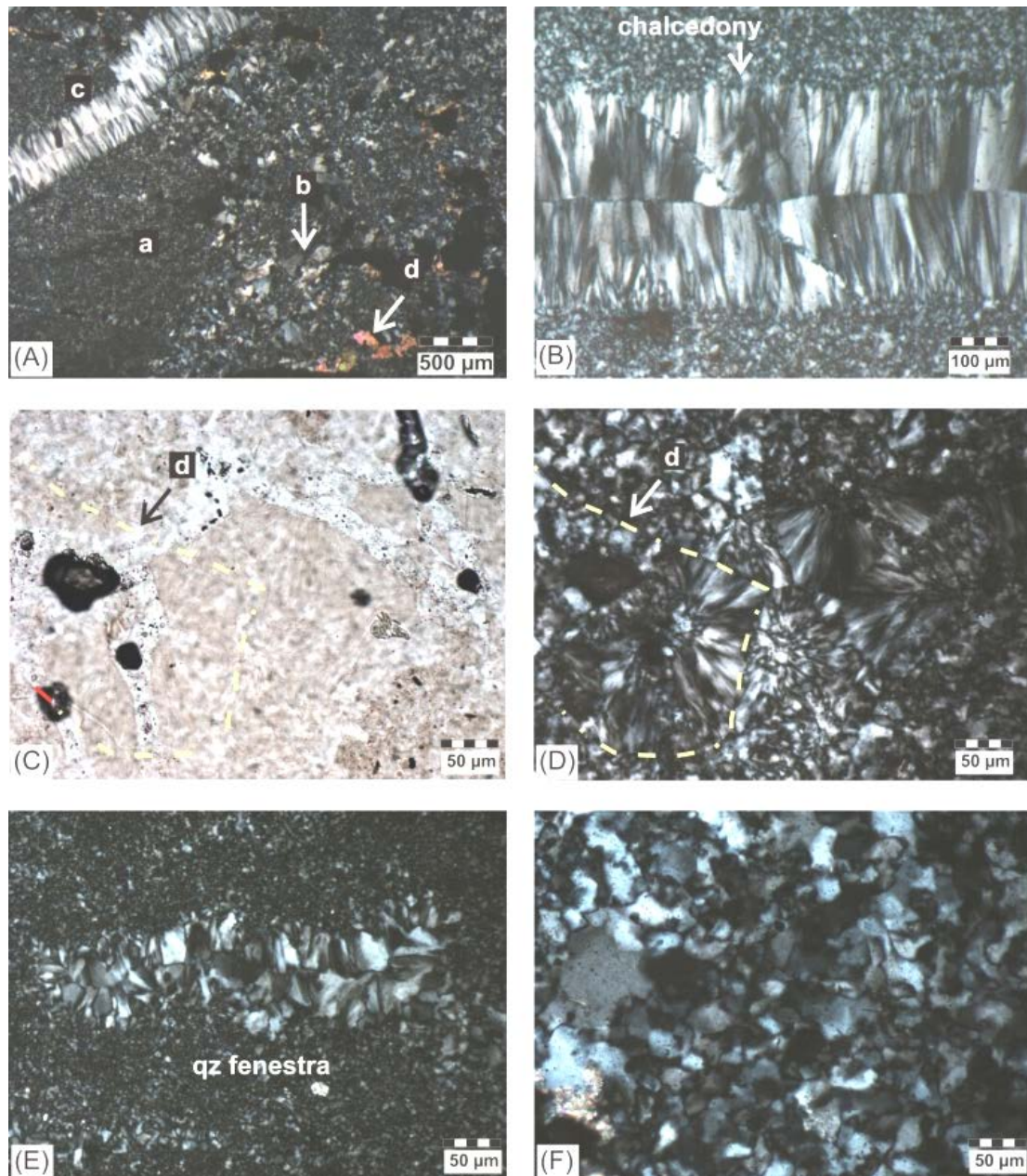
Figure 8 Photomicrographs of sample PPRG 200 (BS) from Bitter Springs Formation, Australia. (A) Overview of sample showing micro- (a) and mesocrystalline (b) quartz, fibrous chalcedony vein (c) and resorbed carbonate crystals (d). Cross polarised light image (CPL). (B) Fibrous chalcedony forming "tiger's eye" or zebraic texture. (C) and (D) Plane polarised light (PPL) and CPL images of a part of the chert matrix containing chalcedony cement and rosette pattern, which is typical of diagenetic silica. The outline of a block of recrystallized chalcedony cement has been traced by a yellow dashed line. (E) Fenestral quartz structure (F) Mesocrystalline quartz crystals with crenulated grain boundaries and undulose extinction.
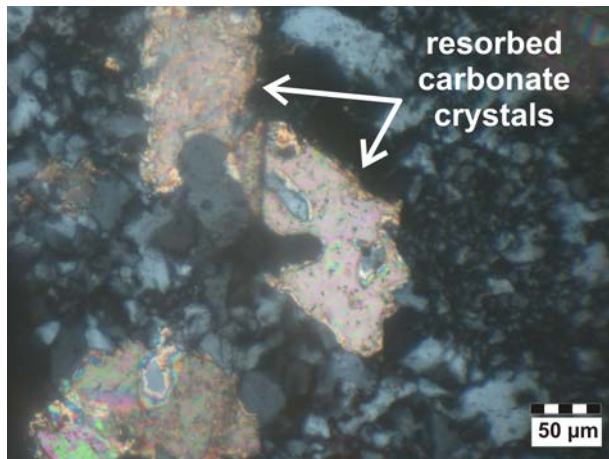
Figure 9 Resorbed crystals of carbonate minerals, probably dolomite, showing high order interference colours, surrounded by microquartz within sample PPRG 200 (BS) from bitter Springs Fmn., Australia.

4.2.3.3 Dahongyu Formation, Jixian County, North China (JC)

The Dahongyu Formation is located in the Jixian County in North China. The Proterozoic section in Jixian, North China was first reported by Kao et al., 1934 and recently is divided into 12 formations which include the Dahongyu Formation. The cherty dolostone beds of the Dahongyu Formation, containing microbiota very similar to the Gunflint type microbiota, are intercalated with volcanic sediments and lava, suggesting shallow marine environment in a region of volcanic activity (Yun, 1984).

Glauconite from the middle part of the Dahongyu Fmn. yields K-Ar age of ~1.6 Ga (Yun, 1984).

4.2.3.3.1   2 of 8-18-83 (JC)

This sample belongs to the third member of the Dahongyu Formation. Sample was collected from ~17m below boundary with Gaoyuzhang Formation. The sample is a silicified carbonate flat-pebble conglomerate and grainstone (based on thin-section study by Stanley Awramik).
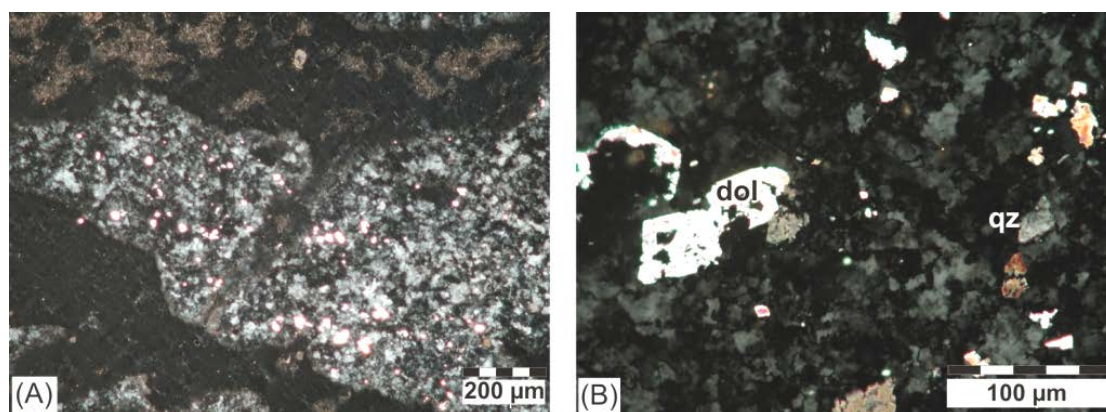
Figure 10 Photomicrographs, CPL images, of Sample 2 of 8-18-83 (JC). (A) Sample is composed of micro- and mesocrystalline quartz. (B) Some partially resorbed carbonate grains are seen within the quartz matrix.

4.2.3.4 Gunflint Iron Formation (GFBC)

The Gunflint Iron Formation, Canada was discovered in 1850 and first described by Ingall (1888). It is a part of the Animike Group of Precambrian sediments, deposited within the Animike Basin (Trendall, 1968). Almost continuous outcroups of the Gunflint Iron Fmn. are exposed from west of Gunflint Lake to Thunder Bay some 180 km to the east

continuing eastward in isolated exposures on the north shore of Lake Superior, an additional distance of some 120 km, to an area just west of Schreiber, Ontario (Fig. 9).

The Gunflint stratigraphy was determined initially by Goodwin (1956) and subsequently revised in other studies (e.g., Winter and Knauth, 1992; Fralick, 1995). It is the middle unit of the Animike Group and is conformably overlain by the Rove Fmn. (Floran and Papike, 1978). The formation consists of both stromatolitc and granular cherts, banded lutitic chert (silica with ankerite and siderite) and siderite beds (Winter and Knauth, 1992).

A shallow marine platform and shelf setting has been described for the depositional environment of the Gunflint Fmn. (Simonson, 1987: Winter and Knauth, 1992). Similarly, Fralick and Barrett (1995) interpreted the Gunflint Fmn. as representative of a wave- and tide-dominated inner shelf sequence. Alternatively, a restricted sedimentary basin with limited communication with the

open ocean has also been suggested (Carrigan and Cameron, 1991). The beautifully preserved Gunflint microbiota is an important part of early evidence of life in the Precambrian (examples of some of the early studies on the microfossils : Knoll and Barghoorn, 1975; Awramik and Barghoorn, 1977).

Zircons extracted from rainout and storm reworked volcanoclastic beds in the upper portion of the Gunflint Fmn give U-Pb ages around 1878.3 Ma (Fralick et al., 2002).

4.2.3.4.1 3 of 06-30-84 (G1)

This chert sample comes from Schreiber Reserve (classic locality of Barghoorn and Tyler, 1965) of the Gunflint Formation. The sample is a basal stromatolitic chert with columnar stromatolites (Fig. 11and B) forming directly on boulders of Kakabeka Conglomerate. The stromatolite columns are now composed of micro- (dominant component) and mesocrystalline quartz grains and lots of brown coloured iron rich material. The intercolumnar spaces are composed of reworked ooids (Fig. 4 A and B), oolite clasts (Fig. 4 C and D) and other lithoclasts embedded within a matrix of recrystallized meso- and microcrystalline quartz grains (Fig. 11 C and D).

4.2.3.4.2 16 of 8-17-86 (G3)

This is a chert of organic origin, with preserved Fe-rich stromatolitic laminations that are brown to dark brown in colour (Fig. 6 A and B). The matrix is composed of recrystallized micro- and mesocrystalline quartz grains (Fig. 6 C and D).

4.2.3.4.3 GFC-1

Typical Gunflint chert with preserved microbial mat structures indicating a relatively early silicification event.

4.2.3.4.4 K-565

Black chert from Gunflint Range composed of recrystallized micro- and mesocrystalline quartz. Sample provided by Paul Knauth via Zachary Sharp.
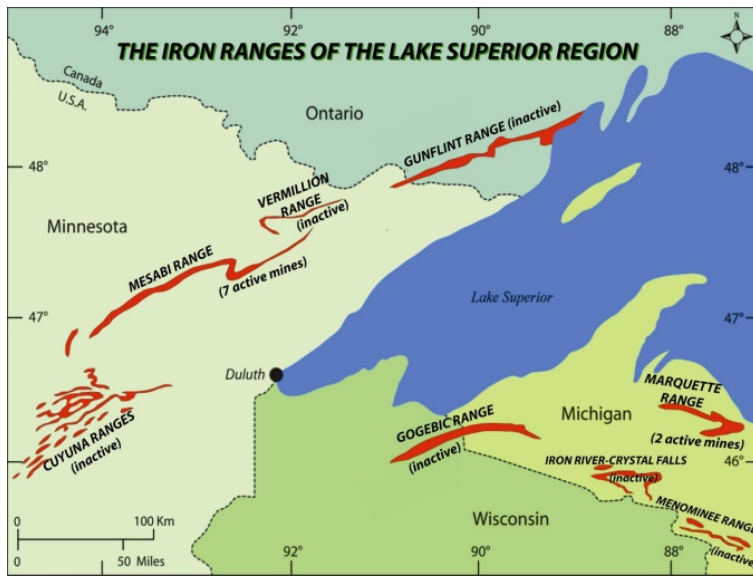
Figure 11 A geological map showing the location of the Gunflint Range in the Lake Superior Region of Ontario, Canada. Source: US Dept. of the Interior USGS report.
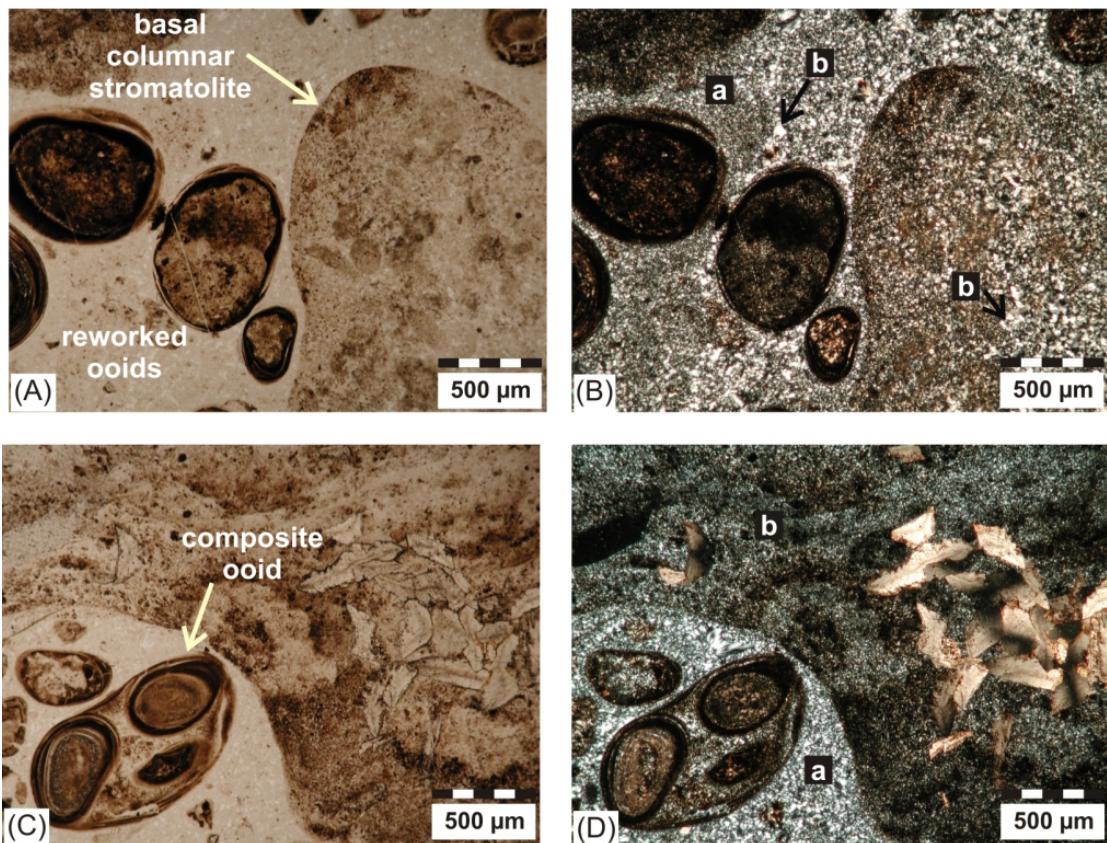
Figure 12 Photomicrographs of chert sample 3 of 06-30-84 (G1) from Gunflint Iron Formation, Animike Basin, Canada. Plane polarised light images in left column and the cross polarised light versions of the same images are in the right column. (A) Figure shows basal columnar stromatolites with reworked ooids within the intercolumnar spaces. The ooids are around 1 to 2 mm in diameter with large nucleii and very thin cortices. Only a few Fe-rich concentric laminae make up the cortex. (B) Ooids are now themselves silicified and also embedded in a recrystallized microquartz matrix, which is composed of micro- (< 20 μm) (a) and mesocrystalline quartz (> 20 μm) (b). (C) Composite ooid containing an oolite clast as nucleus with a very thin cortex is seen. The few laminae that compose the cortex are also fractured. Agitated water conditions are indicated. (D) Intercolumnar spaces often have larger quartz crystals (b) than the silicified stromatolites, which are dominantly made of microcrystalline quartz (b).
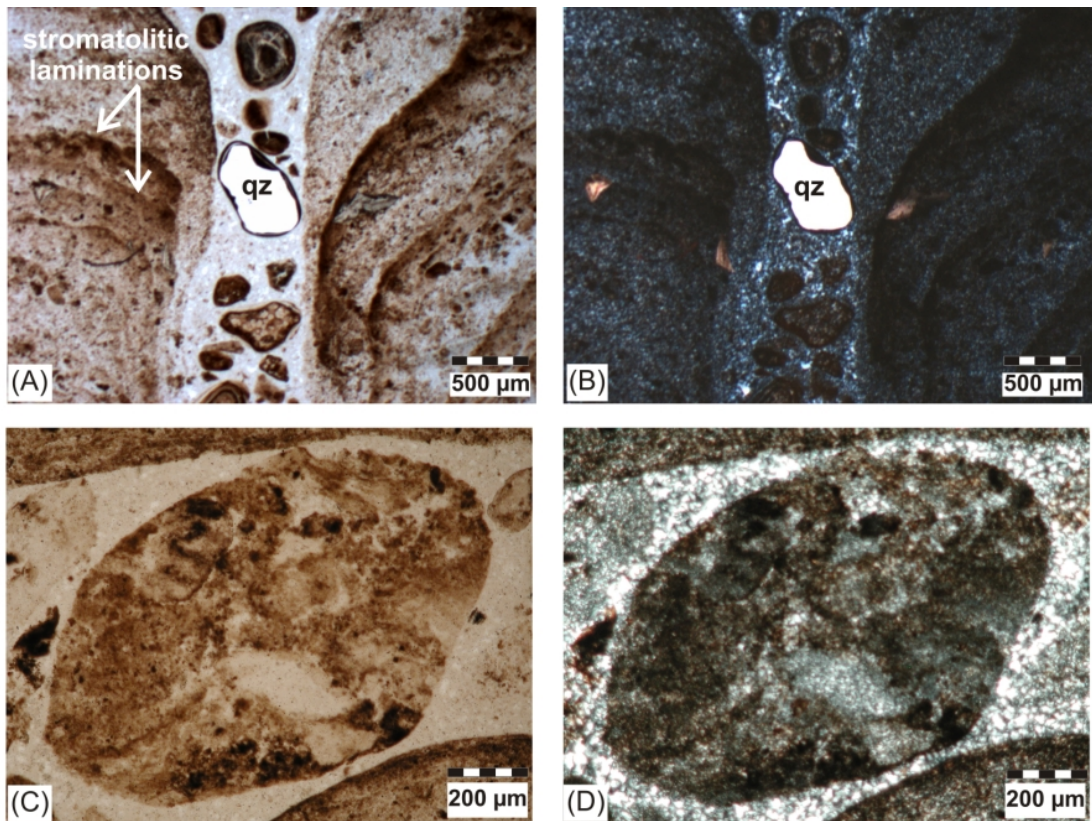
Figure 13 Photomicrographs of chert sample 3of 06-30-84 (G1) from Gunflint Iron Formation, Animike Basin, Canada. Plane polarised light images in left column and the cross polarised light versions of the same images are in the right column. (A) and (B) show columnar stromatolites with preserved laminations rich in Fe. Intercolumnar spaces contain ooids, one with detrital megaquartz as nucleus is seen. (C) and (D) Lithoclast containing Fe- rich organic matter and ghost grains of precursor minerals defined by larger sized mesoquartz crystals.
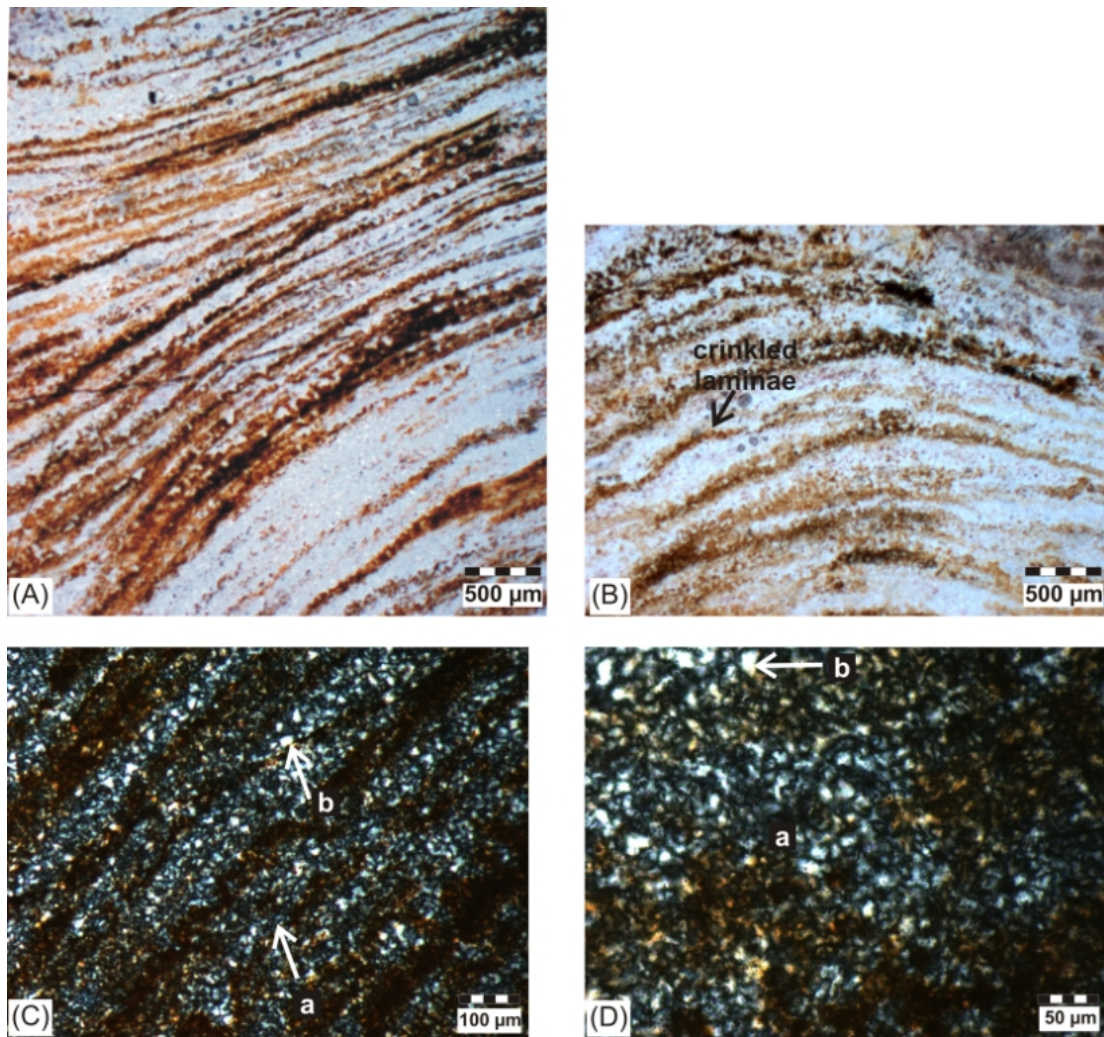
Figure 14 Photomicrograph of chert sample 16 of 8-17-86 (G3) from Gunflint Iron Formation, Animike Basin, Canada. (A) and (B) show dome like stromatolite structure with well preserved Fe-rich stromatolitic laminations. Individual laminae are 2 to 10 μm thick. Plane polarised light images. (C) The matrix of micro- (< 20 μm) (a) and mesocrystalline quartz (> 20 μm) (b) texture is visible in cross polarised light (CPL). (D) Enlarged view of the rock matrix showing crenulated grain boundaries of microquartz and partially undulose extinctions. CPL image.

4.2.3.5 Chert from Banded iron formation (BIF-2-chert)

4.2.3.5.1 BIF-2chert and BIF-2b-chert

These are two samples from the same hand-specimen of a stromatolitic ferruginous chert ("Mary Ellen Jasper") from the Biwabik Iron-Formation (Paleoproterozoic, between 1.878 – 1.836 Ga,

Addison et al., 2010) near Biwabik, Mesabi Iron Range, central St. Louis County, northeastern

Minnesota, USA. Siliceous or cherty material interbanded with iron oxide-

rich Collenia stromatolites. The sample is ~1.8 Ga old.


Figure 15 Sample BIF-2, banded iron formation of age ~1.8 Ga with iron rich Collenia stromatolites visible as grey to white columnar structures within the black chert.

4.2.4 Archean cherts

4.2.4.1 Dresser Formation, Pilbara Craton, Western Australia (PilBC)

The Warrawoona Group in the Pilbara Craton, Western Australia, is ca. 18 m thick succession

deposited over ~150 Ma (e.g., Van Kranendonk et al. 2002 and references therein) and situated

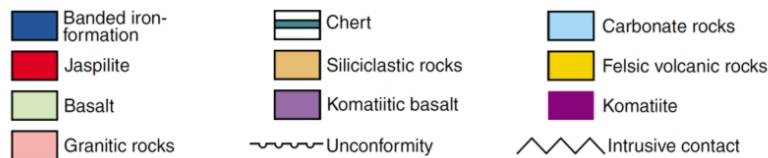in the eastern part of the Pilbara craton.
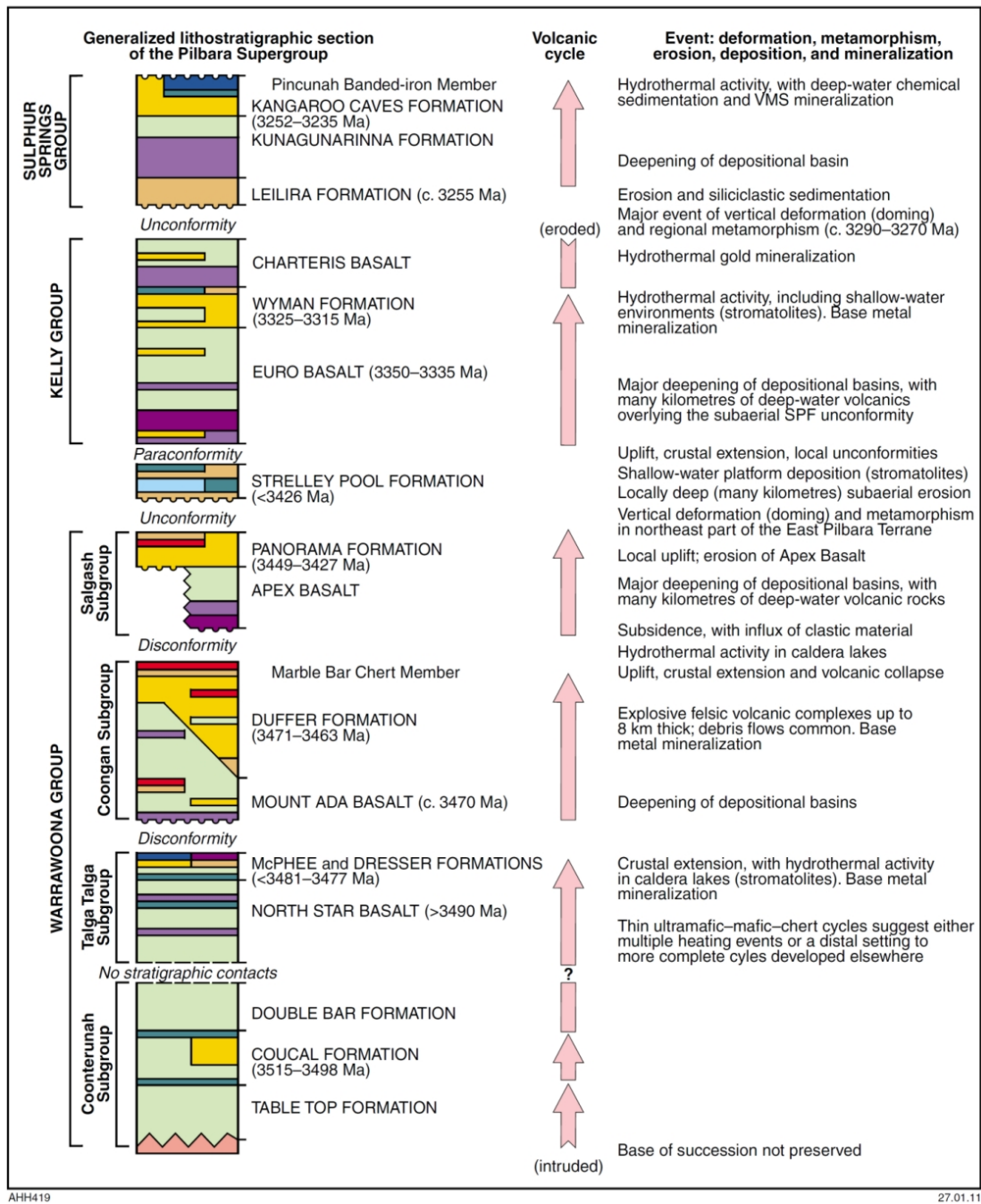
Figure 16 Generalized stratigraphic column of the Pilbara Supergroup, W. Australia (after Hickman and Van Kranendonk, 2012).

Dominantly low-grade (prehnite–pumpellyite to greenschist facies) metabasalts with interbedded felsic volcanic horizons (dominantly tuffs, some flows) and numerous chert beds (Hickman 1983; Van Kranendonk et al. 2002) make up the Warrawoona Group. It is the oldest group of the rock successions in the craton and is subdivided into four subgroups. The samples in this study come from different horizons within the Warrawoona Group.

The Dresser Fmn. is the uppermost formation of the second oldest subgroup within the Warrawoona - the Talga Talga subgroup (Hickman and van Kranendonk, 2012). This formation contains bedded cherts with interbedded pillow basalts (Van Kranendonk 2000). Within the chert horizons interlayered stratiform barite, and lesser amounts of jaspilitic chert, carbonate–chert laminates, and clastic sedimentary rocks (Buick & Dunlop 1990; Nijman et al. 1999; Van Kranendonk 2004) are found. The barite-chert intercalated units are associated with cross-cutting silica-barite veins which appear to be feeding these bedded horizons.

At least two alternative interpretations of the depositional environment of the Dresser Fmn. have been proposed. Locally observable dessication cracks and other evidences indicate shallow water deposition involving chertification of earlier carbonates or gypsum (Buick and Dunlop, 1990). Alternatively, the cross-cutting silica-barite feeder veins, apparently syndepositional with the bedded chert-barite units, indicate a primary hydrothermal origin (Nijman et al., 1999; Runnegar et al. 2001; Van Kranendonk 2004).

This formation has been attributed an age of ca. 3490 Ma based on Pb-Pb dating on barite (Thorpe et al., 1992).

Note: The sample group PilBC comprises bedded cherts from the Pilbara Craton, which also includes the sample from Marble Bar Chert Member described in the section after this.

4.2.4.1.1 4 of 03-08-85 (W2)

This sample was collected in vicinity of the locality described in Walter et al. (1980). This study described a 30 km long and 40 m thick chert-barite unit bearing metasediments at North Pole, within the Warrawoona Group. The sample W2 is a black bedded chert, containing numerous quartz veins in thin-section and few clay pockets in a finely crystallized matrix. It is possibly of hydrothermal origin.

4.2.4.1.2   UENO 2.2012 or DRESS-12613-10a (DUC-1 and DUC-2)

Approximate location of sample is 21°09.04.46' S, 119°26.09.00' E. The sample is emplaced in the field as a thick chert vein cutting across the intercalated chert and greenstone beds of the Dresser Fmn., apparently feeding into the bedded chert and probably of hydrothermal origin. DUC-1 and DUC-2 were drilled out from the same sample, spaced ~10 cm from each other. The sample was provided by Joachim Reitner.

4.2.4.2 Marble Bar Chert, Duffer Formation, Pilbara Craton, W. Australia (PilBC)

The Marble Bar Chert Member is the youngest member of the Coongan Subgroup within the Warrawoona Group. The Marble Bar is a 50- to 80-m thick sequence of beautifully bedded multicoloured interlayered cherts. Three distinct coloured interlayered (centimeters to tens of centimeters layering) varieties of thinly bedded red jasper, milky white chert and blue-black chert (Hickman and Van Kranendonk, 2012) are present (Fig. 23). The succession is metamorphosed to lower greenschist facies (Collins and Van Kranendonk, 1999). Individual beds are up to 10 m or more continuous along the strike. Different amounts of very fine-grained iron oxide impurities, with some subtle microscopic grain-size variations leads to the different colourations.

U-Pb zircon dating closely constrains the age of Duffer Fmn. from 3471 ± 5 Ma to 3465 ± 3 Ma (Thorpe et al., 1992). Sm/Nd ages of 3200 ± 300 Ma for red (or black) and white banded cherts and 2500 ± 200 Ma for yellow-grey cherts associated with quartz veins were obtained (Minami et al., 1995).

4.2.4.2.1 Marble 14613 13 (MBC)

This particular sample is from the white chert layers. This has been grouped with another bedded chert, sample W2, from the Dresser Formation; together they form sample group PilBC (bedded cherts from Pilbara Craton). This particular sample was provided by Joachim Reitner.

Figure 17 Field photographs of the Marble Bar Chert, Warrawoona group, W. Australia. (Source: internet) Interlayered red, white and blue-black chert is visible.

4.2.4.3 Mt. Ada Basalt, Pilbara Craton, Western Australia

Overlying a disconformity terminating the lower Talga subgroup is the Mt Ada Basalt formation. It is located within the Coongan Subgroup. The Mount Ada Basalt and coeval Duffer Formation have an age range of 3474–3463 Ma (Van Kranendonk et al., 2002). The Mount Ada Basalt consists of pillowed metabasalts with chert and calcite in the inter-pillow spaces.

4.2.4.3.1 Mt Ada 13613 6F (PL-2)

This sample comprises cryptocrystalline silica, in the form of white agate (PL-2), along with coarser quartz and calcite in adjacent zones, all encased together within the interspaces of pillow basalt. The sample was provided by Joachim Reitner.
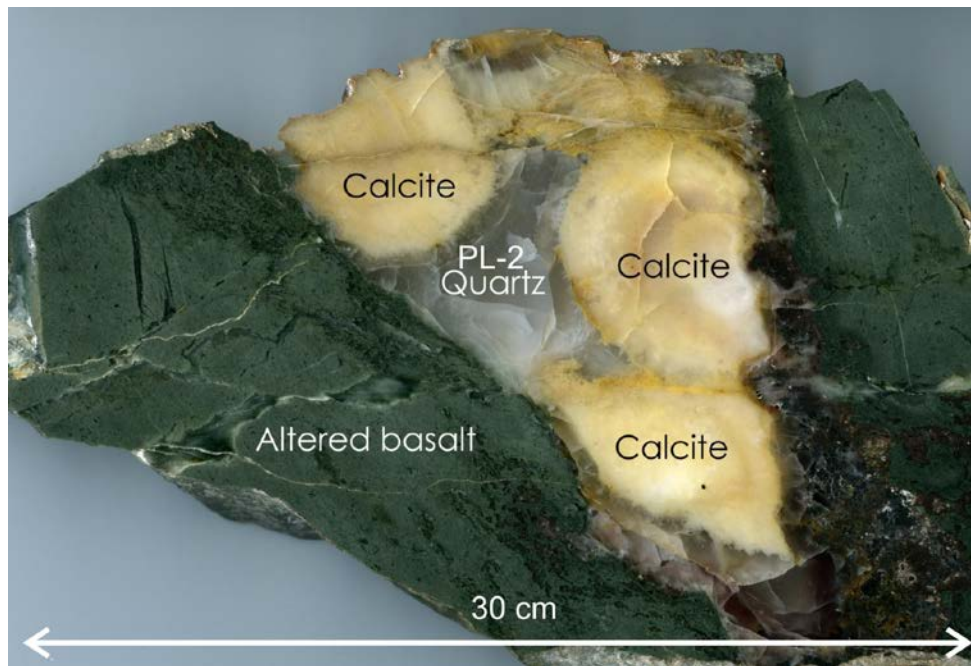

Figure 18 Photograph of hand-specimen from Mt Ada Basalt, Pilbara Craton, W. Australia. The sample comprises chert/quartz, i.e., the PL-2 sample along with calcite within the interpillow spaces of the pillow basalt.
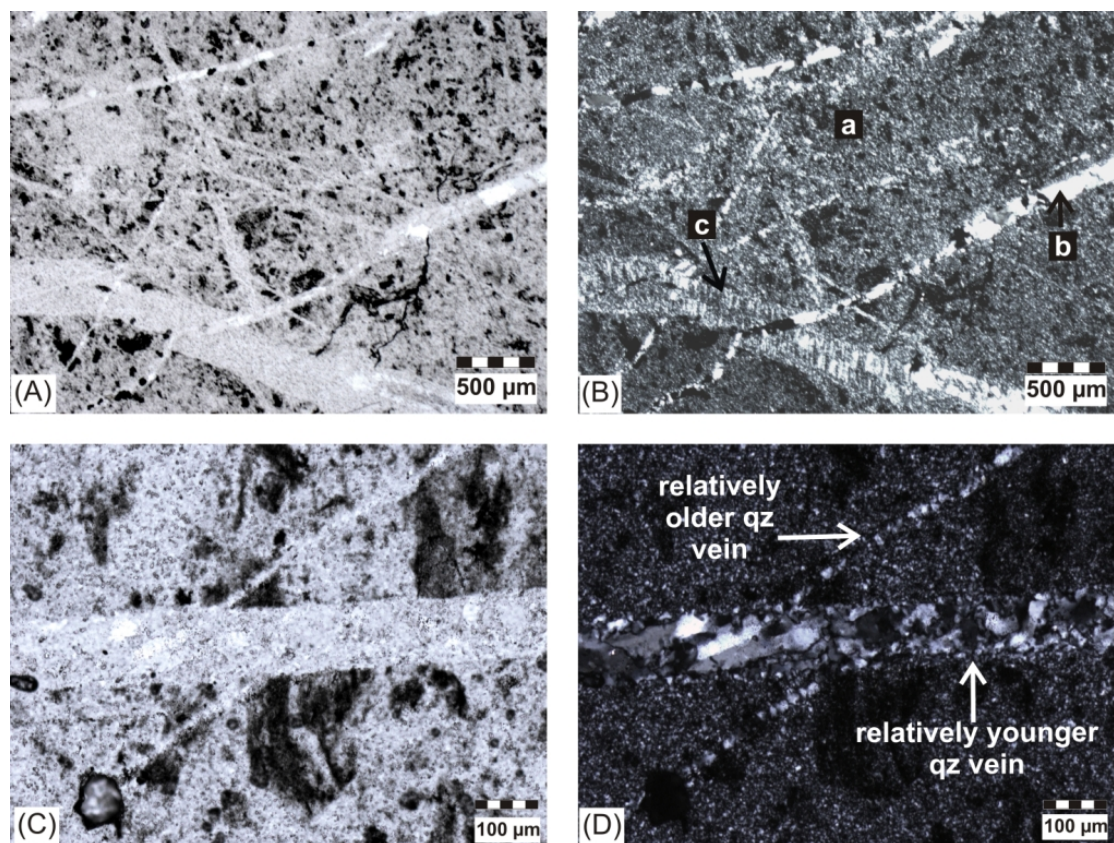
Figure 19 Photomicrographs of sample 4 of 03-08-85 (W2) from the Dresser Fmn., Pilbara Craton, Australia. (A) and (B) are PPL and CPL images offering a general view of the sample composed of cross-cutting quartz veins of different thicknesses within a groundmass of micro- and crypto-crystalline quartz (a). The veins contain mesoquartz crystals (b), some of which show undulose extinction. The thicker vein at the lower left section of the figure is filled with fibrous quartz crystals (c), referred to as 'tigers eye'. The veins are relatively younger than the silicification event and are of different generations relative to each other as well. Panels (C) and (D) are PPL and CPL images showing a thick quartz grain cutting across a relatively older thin quartz vein. The quartz grains present within the thicker vein show undulose extinction.

4.2.4.4 Swartkoppie Formation/Mendon Formation, Barberton Greenstone Belt, South Africa (BBC)

The early Archean Barberton greenstone belt is a well-preserved, generally weakly metamorphosed sequence of supracrustal volcanic and sedimentary rocks. It forms a ca. 15 km thick supracrustal sequence.
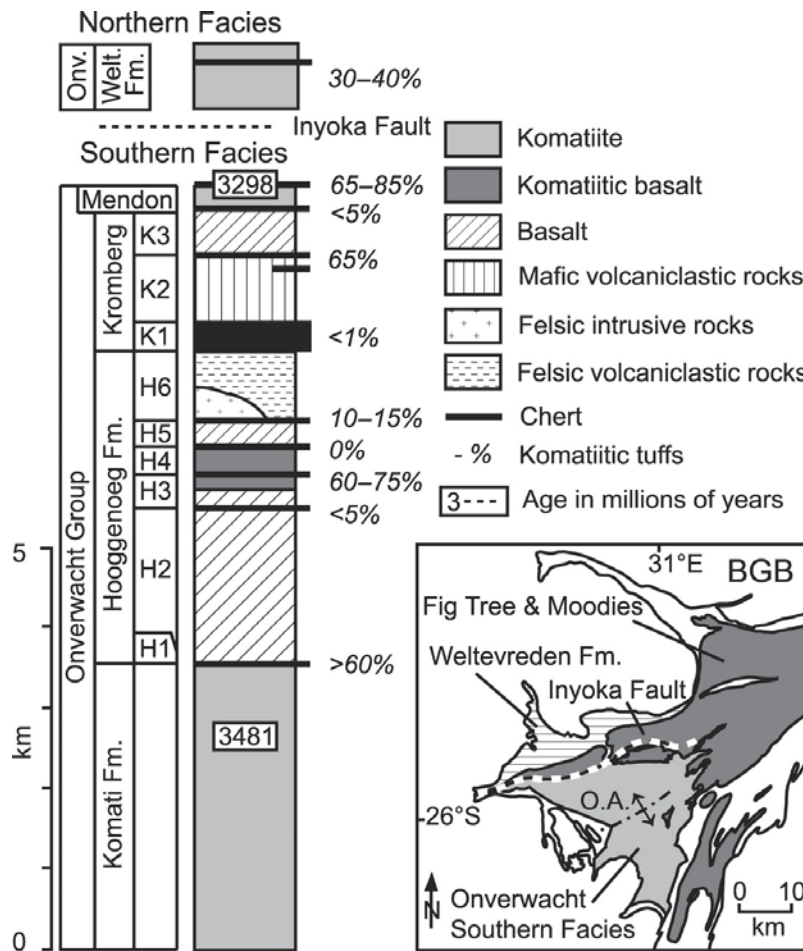
Figure 20 Generalized stratigraphic column of Onverwacht (Onv.) Group and geologic map of Barberton greenstone belt (BGB). Modified from Lowe and Byerly (1999). Ages are from Byerly et al. (1996) and Dann (2000). Percentages to right of column indicate approximate proportions of komatiitic volcaniclastic layers within each major interflow chert unit on the west limb of the Onverwacht anticline (O.A.) and interbedded within komatiitic flow sequences in the Weltevreden (Welt.) Formation (after Stiegler et al., 2008).

The Mendon Formation, composed of interbedded komatiitic lavas and cherty metasedimentary rocks, is a relatively newly defined stratigraphic unit at the top of the Onverwacht Group (Byerly, 1996 and references therein) (within Geluk Subgroup).

This formation is 3298 Ma old based on U-Pb and Pb-Pb dating of zircons within ash layers in the cherty stromatolitic metasediment Metamorphic grade of the Formation is lower Greenschist to Amphibolite facies (Viljoen and Viljoen, 1969).

4.2.4.4.1   PRG 200 (Z1)

Sample was collected from 22km NE of Barberton. The sample is a black chert containing fine grained organic material and preserved microbial mat laminations. The latter is indicative of subsequent but relatively early silica impregnation.

4.2.4.4.2   PRG 197 (Z2)

Sample collected from 11km NE of Barberton. Sample is a fine grained black chert.

4.2.4.4.3   PRG 194 (Z3)

Sample collected from 10 km NE of Barberton. The sample is a black and gray chert with visibly well preserved stromatolitic laminations, indicating early silicification.
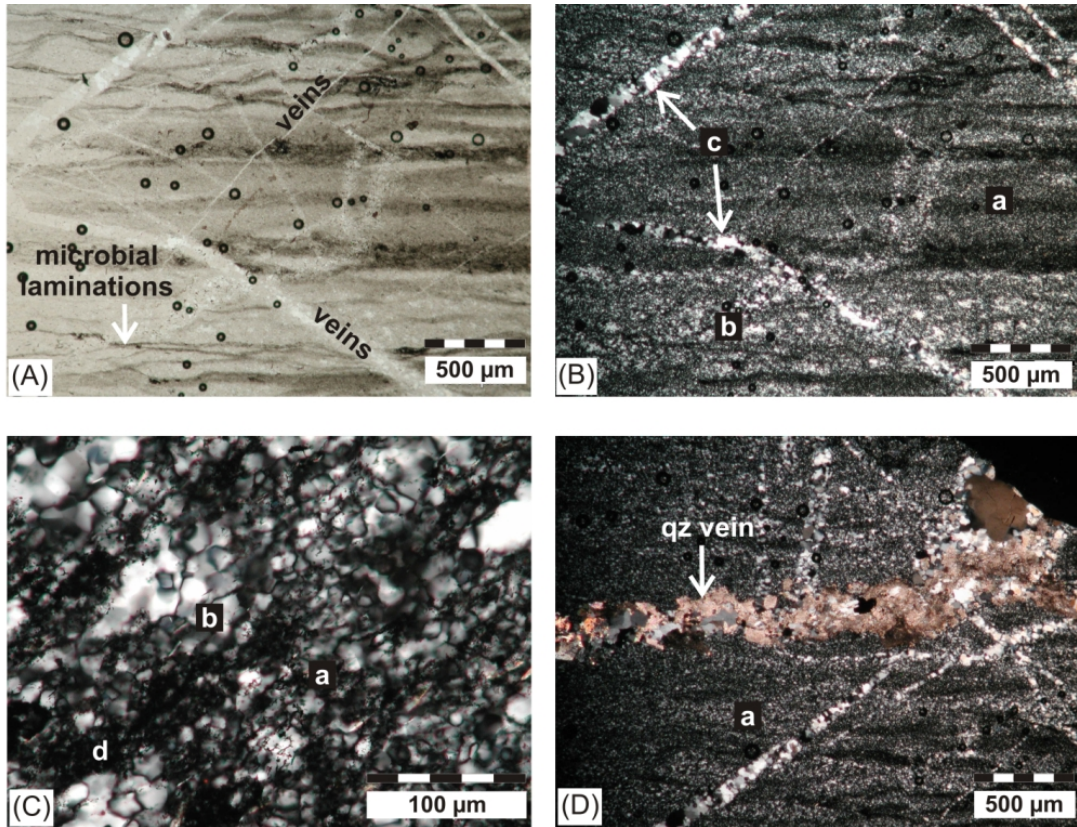
Figure 21 Photomicrographs of sample PPRG 200 (Z1), from Swartkoppie Fmn., Barberton Greenstone Belt, South Africa. The age of the chert is 3298 Ma (Viljoen and Viljoen, 1969). (A) Plane polarised light (PPL) image of sample shows well preserved microbial laminations and dark organic matter, which indicate relatively early silicification. Cross-cutting veins, of various thicknesses, are seen all over. These belong to later and possibly different generations, post the silicification event. The dark circles are an artefact of sample preparation. (B) Cross polarised light (CPL) image of A. A matrix of recrystallized microcrystalline quartz (individual crystal size < 20 μm) (a) with crenulated crystal boundaries and undulose extinction, mesocrystalline quartz (individual crystal size > 20 μm but otherwise optically similar to microcrystalline variety) (b) and cryptocrystalline quartz (crystal size not determinable with normal optical microscope) (d) is seen. Microcrystalline quartz is the dominant component of majority of cherts. The veins are composed of recrystallized macroqz (c) or cc or both?. C. Magnified view (see scale bar) of recrystallized micro and mesocrystalline quartz matrix, a major constituent of cherts. D. Quartz vein cutting through the microquartz matrix.

4.2.4.5 Other samples from Barberton Greenstone Belt, South Africa

4.2.4.5.1   K-1113

This is a nodular chert sample in siderite bed.

4.2.4.5.2   K-1100

The sample is a quartz stalactite, 3560 Ma old.

4.2.4.5.3   BIF-1

Banded iron formation of white chert layers alternating with black magnetite and red haematite bands. The sample was provided by Joachim Reitner (Georg-August-Universität-Göttingen, Göttingen).
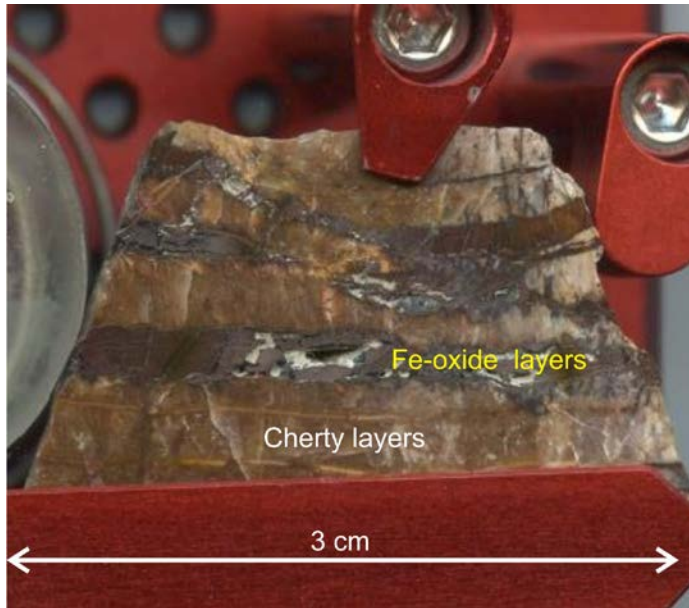
Figure 22 Small piece (~3 cm wide) of BIF-1 sample from the Barberton greenstone belt, probably close to Jasper knob, Marquette, Upper Peninsula of Michigan. This chip is a part of a bigger hand-specimen which was later crushed and crushed and clean milky – white chert fragments (from the cherty layers) were sorted out under the microscope as BIF-1-chert sample.

4.3 Methods

See Chapter 2 – Methods.

4.4 Results

4.4.1 Trace elements

4.4.1.1 Phanerozoic cherts

4.4.1.1.1 Phanerozoic nodular cherts (PNC)

The PNC cherts, samples M1, M7, M6 and AR, have almost identical PAAS normalized REE+Y patterns, as well as REE+Y concentrations (Figure 23), with small to negligible LREE depletions

in M1 and M7 – [Pr/Yb]$_{PAAS}$ and [Sn/Yb]$_{PAAS}$ ranging from 0.71 to 0.90 and 0.9 to 1.10

respectively. All three samples have negative Ce anomalies, ranging from 0.39 to 0.57. No

significant Gd anomaly is seen. Y/Ho ratios of samples are superchondritic, around 38 to 40.

Small La anomaly, from 1.11 – 1.23 is observed.
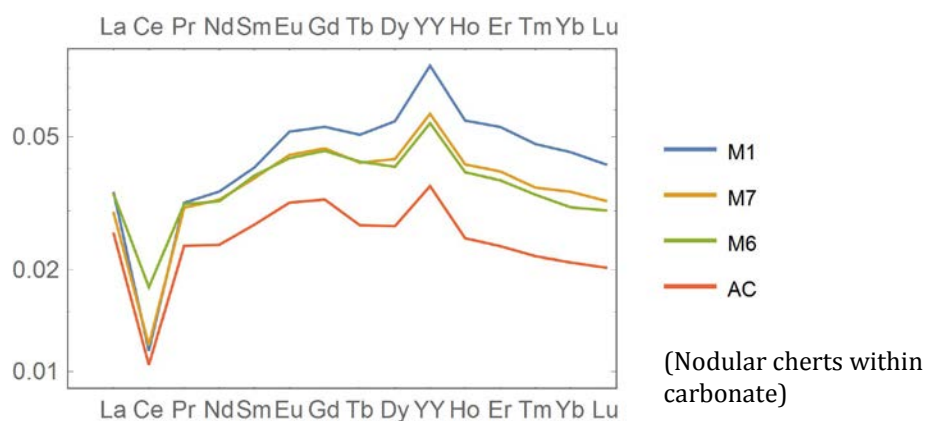

(Nodular cherts within carbonate)

Figure 23 PAAS (Pourmand et al., 2012) normalized REE+Y patterns of nodular cherts from the Phanerozoic (Phanerozoic nodular cherts). The cherts show almost identical patterns with diagnostic seawater anomalies – a small negative Ce/Ce* (0.39-0.57) and superchondritic Y/Ho molar ratios (38-40).

4.4.1.1.2   Phanerozoic bedded cherts (PBC)

The PBC cherts, samples M3 and M8, do not show LREE depletion and exhibit negative Ce

anomalies in the range 0.66 to 0.82. Sample M3 has superchondritic Y/Ho ratio of 41 but M8 has

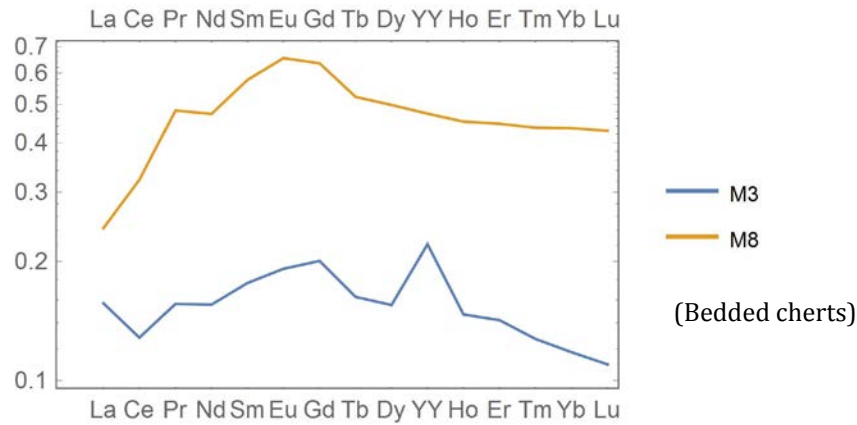chondritic Y/Ho value of 29 (Figure 24).

Figure 24 PAAS normalized REE+Y patterns of bedded cherts from the Phanerozoic (Phhanerozoic bedded cherts). Both cherts exhibit negative Ce anomalies, but only M3 exhibits a Y/Ho anomaly whereas M8 has a flatter pattern.

4.4.1.2 Proterozoic cherts

Nine Proterozoic chert samples were analyzed for their major, minor and trace elements and REE compositions out of which six (BIF-2, G1, G3, D3, D5, Jix) have relatively similar flat REE+Y patterns with LREE depletions in some and positive Eu anomaly in all samples. The samples have variable REE concentrations, ranging from <1 ppm upto ~30 ppm.

4.4.1.2.1 Doushantuo Fmn cherts (DC) and Dahongyu Fmn chert (JC)

Sample JC does not show any LREE depletions, no positive La anomaly and a small to negligible negative Ce anomaly of 0.9 (Figure 25). It has a superchondritic Y/Ho ratio of 31. The samples shows a moderately high positive Eu anomaly of 1.94.
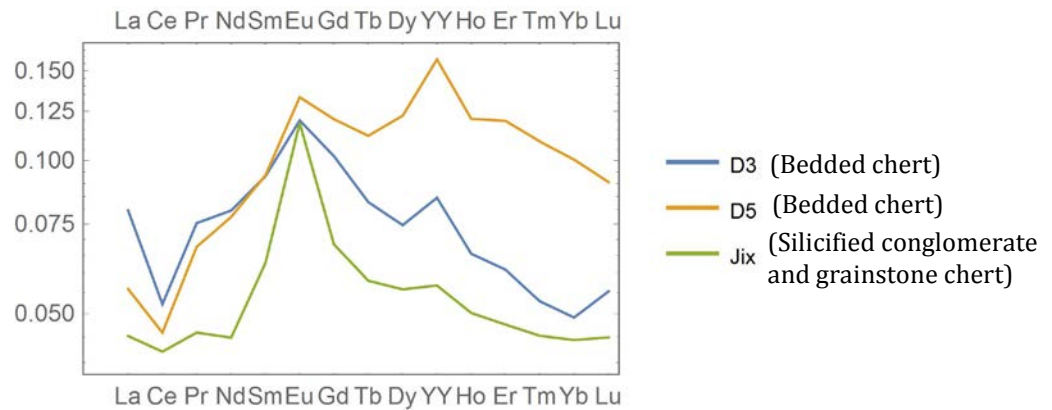
Figure 25 PAAS normalized REE+Y plots of cherts from Doushantuo Fmn (DC) and one sample from the Dahongyu Fmn (JC) showing convex patterns.

Figure 25 shows REE+Y patterns of DC and JC cherts. Samples D3 and D5 both show small positive Eu anomalies of 1.3. Sample D3 shows LREE enrichments, i.e., [Gd/Yb]$_{PAAS}$, [La/Yb]$_{PAAS}$, [Pr/Yb]$_{PAAS}$ and [Sm/Yb]$_{PAAS}$ are >1 whereas D5 shows LREE depletion with [La/Yb]$_{PAAS}$, [Pr/Yb]$_{PAAS}$ and [Sm/Yb]$_{PAAS}$ are <1. The Y/Ho ratios of both samples are superchondritic, ~ 35-36.

4.4.1.2.2   Bitter Springs Formation (Sample BSC) and Gunflint bedded cherts (GFBC)

The chert from Bitter Springs Fmn. (Sample BSC) displays a different pattern from the other samples. This sample shows no LREE depletion ([Pr/Yb]$_{PAAS}$ and [Sm/Yb]$_{PAAS}$ values are 1.34 to 1.79 respectively), negative La/La* of 0.89, small positive Ce/Ce* of 1.05, negative Eu/Eu* of 0.66 and nearly chondritic Y/Ho molar ratio of 29.
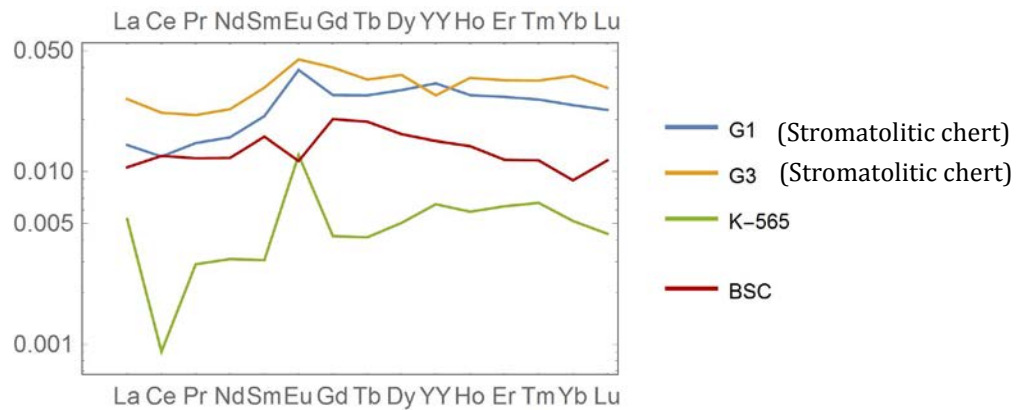
121

Figure 26 PAAS normalized REE+Y patterns of Gunflint bedded cherts (GFBC) G1, G3 and K-565 and chert from Bitter Springs Fmn, sample BSC. Sample K-565 has lowest REE concentrations amongst these samples and also has the most pronounced anomalies diagnostic of seawater.

REE + Y patterns of GFBC cherts and BSC chert have been grouped in Figure 26. The REE+Y patterns of Gunflint bedded cherts (GFBC) cherts, G1 and G3, both of which belong to the Gunflint Fmn., have positive La/La* (1.13 and 1.45 respectively), LREE depletion (both [Pr/Yb]$_{PAAS}$ and [Sm/Yb]$_{PAAS}$ is ~0.6), and small positive Eu anomalies (1.68 and 1.40 respectively). The Y/Ho ratios of the two samples are very different – while G1 has a moderately superchondritic value of 32, G1 has a sub-chondritic value of 22. Sample K-565, also a member of GFBC group, shows similar features as G1 and G3, but the REE concentration within the sample is much lower than all other Proterozoic cherts. This sample has a total ΣREE of 0.53 ppm, strong positive La/La* of 2.10, LREE depletion (both [Pr/Yb]$_{PAAS}$ and [Sm/Yb]$_{PAAS}$ is ~0.6), negative Ce/Ce* of 0.33, strong positive Eu/Eu* of 3.63 and a superchondritic Y/Ho ratio of 30.

4.4.1.2.3   Banded Iron Formation (BIF-2)

Sample BIF-2, a chert layer from within the Proterozoic banded iron formation sample, displays positive La/La* of 1.38 and LREE enriched pattern ([Pr/Yb]$_{PAAS}$ and [Sm/Yb]$_{PAA}$ >1). The sample has positive Eu/Eu* value of 1.59 and no Ce anomaly – Ce/Ce* is 0.99. The Y/Ho molar ratio for this sample is 21, which is lower than chondrites.

(Chert from banded iron formation)
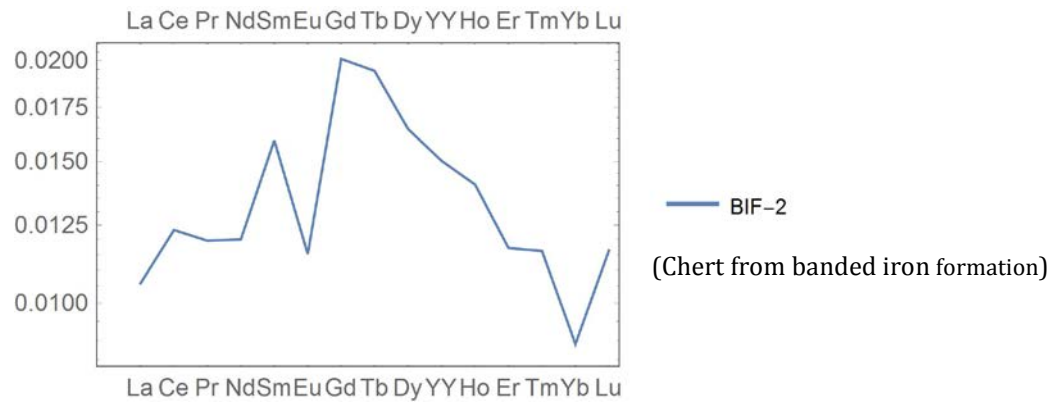
Figure 27 PAAS normalized REE+Y plot of BIF-2 with large positive Eu anomaly and no Ce anomaly. The Y/Ho ratio of the sample is sub-chondritic.

4.4.1.3 Archean cherts

REE data for two Archean samples were obtained from Joachim Reitner and six others were analyzed in this study.

4.4.1.3.1   Pilabara bedded cherts (PilBC)

Cherts from the Pilbara Craton, Austalia come from different stratigraphic locations and display variable REE+Y patterns (Figure 28).

The first group amongst the sample from Pilbara is PilBC. Sample W2, a bedded chert from the Dresser Fmn. has an LREE depleted REE+Y pattern ([Pr/Yb]$_{PAAS}$, [Sm/Yb]$_{PAAS}$, [Gd/Yb]$_{PAAS}$ are all 0.87) with a Eu anomaly, Eu/Eu* = 1.47, small negative Ce/Ce* of 0.88 and chondritic Y/Ho ratio of 28.
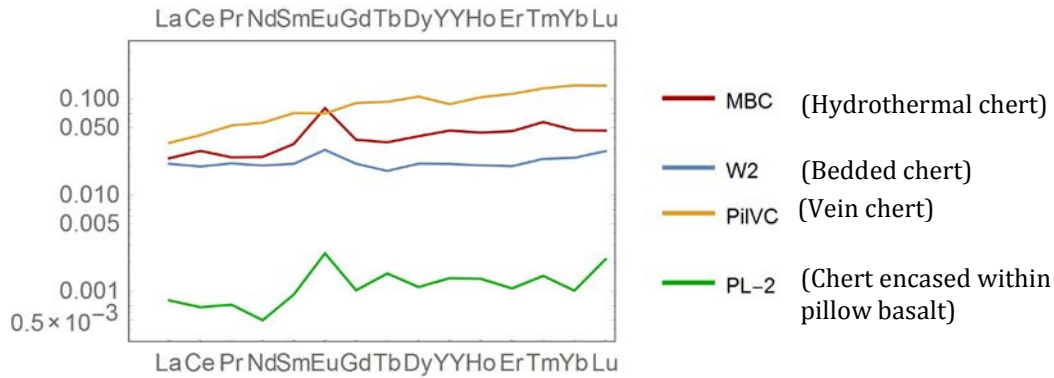
Figure 28 PAAS normalized REE+Y patterns of Archean cherts from Pilbara craton, Australia. Bedded cherts (PilBC) W2 and MBC, vein chert Sample PilVC and agate sample encased in pillow basalt Sample PL-2. The PilBC cherts show LREE depletion and positive Eu anomalies. The PilVC has a very flat pattern

Marble Bar Chert Chert sample MBC, a representative sample from the same location, exhibits an LREE depleted REE+Y pattern ($[Gd/Yb]_{PAAS}$,$[Pr/Yb]_{PAAS}$ and $[Sm/Yb]_{PAAS}$ varying between 0.52 and 0.80), a positive Eu/Eu* of 2.33 and slightly higher than chondritic Y/Ho ratio of 29. The sample has positive Ce anomaly with Ce/Ce* = 1.18.

4.4.1.3.2 Pilbara vein chert (PilVC)

A vein chert from the Dresser Formation, Sample DUC (representative of vein cherts DUC-1 and DUC2), shows LREE depletion ($[Gd/Yb]_{PAAS}$, $[La/Yb]_{PAAS}$, $[Pr/Yb]_{PAAS}$ and $[Sn/Yb]_{PAAS}$ ratios range between 0.38 and 0.66) (Figure 28). A small negative Ce/Ce* value of 0.85, no positive Eu anomaly and has sub-chondritic (correct term) Y/Ho of 23 is seen.

4.4.1.3.3 PL-2

Chert from Mt. Ada Basalt, sample PL-2 has very low REE concentration, in the range of a few ppb for individual REEs and a ΣREE of 0.135 ppm. The sample shows small LREE depletion ($[Pr/Yb]_{PAAS}$ = 0.71 and $[Sm/Yb]_{PAAS}$ =0.91), negative Ce/Ce* of 0.65, high positive Eu/Eu* of 2.20 and a chondritic Y/Ho ratio of 28.

4.4.1.3.4   Bedded Cherts from Barberton Greenstone belt South Africa (BBC)

All three chert samples from the Barberton Greenstone belt come from the Mendon Formation. The common feature between these samples is a positive Europium anomaly but of varying amounts. Sample Z1 has smallest Eu/Eu* = 1.9 whereas sample Z2 has highest Eu/Eu* = 5.76. Z1 shows LREE depletion ([Pr/Yb] $_{PAAS}$ and [Sm/Yb]$_{PAAS}$ values 0.64 and 0.83 respectively) whereas Z2 and Z3 do not show LREE depletions. All samples have negligible to small negative Ce/Ce* = 0.94 to 0.72. The Y/Ho ratios of the samples are 25, i.e., sub-chondritic for Z1, 27 for Z2 – chondritic value and 38 for Z3, which is suprachondritic. A positive La/La* is seen only in Z3, of value 1.4.
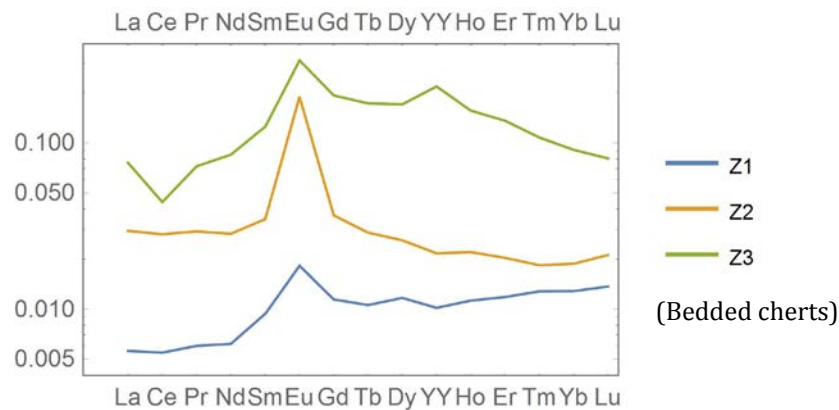
Figure 29 PAAS normalized REE+Y patterns of Barberton greenstone belt bedded chert samples (BBC). The patterns vary largely; notable variations are seen in positive Eu anomalies. A positive La anomaly is seen only in Z3.

4.4.1.3.5   Banded Iron Fmn from Barberton Greenstone belt South Africa (BIF-1)

A chert layer from the Banded iron chert formation from the Barberton Greenstone belt displays (Figure 30) no LREE depletion, no significant Ce/Ce* (~0.9) and a moderately high positive Eu/Eu* value of 1.8. The chert bears chondritic Y/Ho value of 26.

Figure 30 PAAS normalized REE+Y patterns of BIF-1-chert sample showing a pronounced positive anomaly.

All results of REE and trace element analyses are enlisted in Table 2, Table 3, Table 4. Note that the only non-marine sample in the table is Sample LNC, it is from a modern lake.

Table 2 Concentrations of REEs in samples. Note that LNC is the only non-marine sample I the table. It is from the banks of modern day Lake Natron in Tanzania.

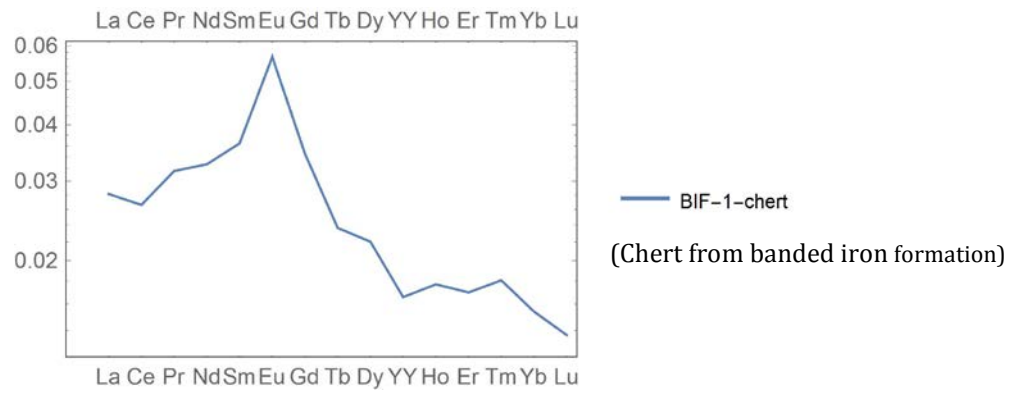| Sample group	Sample	La (ppm)	Ce (ppm)	Pr (ppm)	Nd (ppm)	Sm (ppm)	Eu (ppm)	Gd (ppm)	Tb (ppm)	Dy (ppm)	Y (ppm)	Ho (ppm)	Er (ppm)	Tm (ppm)	Yb (ppm)	Lu (ppm)
Phanerozoic																
LNC-Lake Natron chert	LNC	0.027	0.090	0.006	0.019	0.005	0.001	0.004	0.001	0.011	0.083	0.003	0.014	0.004	0.034	0.006
PNC-Phanerozoic nodular cherts	M1	1.298	0.916	0.281	1.163	0.224	0.056	0.249	0.039	0.260	2.196	0.055	0.152	0.019	0.127	0.018
	M7	1.131	0.952	0.271	1.100	0.209	0.048	0.215	0.032	0.201	1.580	0.041	0.112	0.014	0.097	0.014
	M6	1.285	1.418	0.278	1.088	0.212	0.047	0.211	0.033	0.190	1.481	0.039	0.106	0.014	0.087	0.013
	AR	0.981	0.832	0.209	0.807	0.152	0.034	0.151	0.021	0.127	0.962	0.025	0.067	0.009	0.059	0.009
PBC-Phanerozoic bedded cherts	M3	5.996	10.228	1.381	5.280	0.980	0.207	0.936	0.126	0.727	5.980	0.146	0.405	0.052	0.333	0.048
	M8	9.290	25.646	4.259	16.032	3.201	0.707	2.961	0.404	2.331	12.792	0.448	1.272	0.177	1.227	0.186
Proterozoic																
BIF-2-chert band from banded iron formation from Barberton	BIF-2/a/b chert	4.374	6.422	0.706	2.666	0.433	0.132	0.433	0.057	0.348	1.393	0.067	0.191	0.025	0.158	0.020
Greenstone Belt GFBC-Gunflint bedded cherts	G1	0.545	0.9728	0.1292	0.5344	0.1162	0.0419	0.1292	0.0214	0.1386	0.8751	0.0274	0.0771	0.0106	0.0683	0.0098
	G3	1.004	1.7432	0.1874	0.7782	0.17	0.0482	0.1866	0.0264	0.1697	0.7457	0.0346	0.0963	0.0136	0.101	0.0132
	K-565	0.2024	0.0721	0.0256	0.1055	0.017	0.0135	0.0197	0.0032	0.0236	0.1748	0.0058	0.0179	0.0027	0.0146	0.0019
DC-Doushantuo cherts	D3	3.0463	4.1541	0.665	2.7034	0.517	0.1295	0.4755	0.0641	0.3493	2.2809	0.065	0.1738	0.0214	0.1385	0.0239
	D5	2.1352	3.6505	0.5973	2.6257	0.5191	0.1439	0.5619	0.0866	0.5733	4.2701	0.1197	0.3411	0.0442	0.2832	0.0393
BS - Bitter Springs chert	BS	0.404	0.981	0.106	0.407	0.088	0.012	0.094	0.015	0.077	0.406	0.014	0.033	0.005	0.025	0.005
JC-Dahongyu cherts	JC	1.7252	3.3486	0.405	1.5193	0.3487	0.128	0.3187	0.0449	0.2612	1.5334	0.0497	0.1356	0.0183	0.1251	0.0194

Table 2 continued

Sample group	Sample	La (ppm)	Ce (ppm)	Pr (ppm)	Nd (ppm)	Sm (ppm)	Eu (ppm)	Gd (ppm)	Tb (ppm)	Dy (ppm)	Y (ppm)	Ho (ppm)	Er (ppm)	Tm (ppm)	Yb (ppm)	Lu (ppm)
Archean																
PL-2-Agate in interpillow space	PL-2	0.0306	0.0541	0.0064	0.0168	0.0051	0.0027	0.0047	0.0012	0.0052	0.0368	0.0013	0.003	0.0006	0.0028	0.0009
PilBC-Pilbara bedded cherts from Dresser Fmn	W2 MBC / MBC	0.8043	1.5715	0.1876	0.6855	0.1167	0.0317	0.0982	0.0137	0.0989	0.5659	0.0201	0.0567	0.0096	0.0686	0.0124
	MBC (new white)	0.9177	2.2833	0.217	0.842	0.188	0.0863	0.1744	0.0273	0.1908	1.259	0.0441	0.131	0.0232	0.1327	0.0202
PilVC-Pilbara vein chert from Dresser Fmn.	PilVC / DUCnew	1.3289	3.3279	0.465	1.9083	0.3939	0.0757	0.421	0.0718	0.4927	2.3727	0.1028	0.3199	0.0519	0.3883	0.0592
BBC-Barberton bedded chert from Swartkoppie Fmn	Z1	0.2139	0.4351	0.053	0.2092	0.0519	0.0197	0.0533	0.0082	0.0546	0.2747	0.0111	0.0337	0.0052	0.0362	0.0059
	Z2	1.1276	2.2413	0.2589	0.961	0.1927	0.2039	0.1705	0.0223	0.1212	0.5835	0.0218	0.0578	0.0074	0.0528	0.0091
	Z3	2.8978	3.5003	0.638	2.8777	0.6921	0.3381	0.8972	0.1335	0.7967	5.8919	0.1546	0.3864	0.0435	0.256	0.0349
BIF-1	BIF-1 chert	1.074	2.1174	0.2793	1.1098	0.2021	0.0612	0.1609	0.0183	0.1031	0.4482	0.0176	0.0485	0.0073	0.0435	0.0059

Table 3 List of anomalies observed in REE+Y patterns of samples and the concentration of some trace elements within the samples. Note that LNC is the only non-marine sample I the table. It is from the banks of modern day Lake Natron in Tanzania.

Sample group	Sample	[Pr/Yb] PAAS	[Sm/Yb] PAAS	[Gd/Yb] PAAS	[La/Yb] PAAS	Y/Ho	La/La*	Ce/Ce*	Eu/Eu*	TiO2 (wt %)	Sc (ppm)	Zr (ppm)	Hf (ppm)	Th (ppm)
Phanerozoic cherts														
LNC-Lake Natron chert	LNC	0.06	0.07	0.08	0.06	26.0	0.61	1.24	1.22	0.001	0.003	6.099	0.045	0.029
PNC-Phanerozoic nodular cherts	M1	0.71	0.90	1.19	0.76	39.7	1.25	0.39	1.18	0.003	0.18	1.13	0.03	0.06
	M7	0.90	1.10	1.35	0.86	38.6	1.08	0.41	1.13	0.004	0.18	1.75	0.03	0.09
	M6	1.02	1.24	1.47	1.09	38.2	1.11	0.58	1.09	0.009	0.25	1.94	0.05	0.19
	AR	1.12	1.30	1.54	1.22	39.0	1.10	0.45	1.16	0.004	0.21	1.14	0.03	0.09
PBC-Phanerozoic bedded cherts	M3	1.32	1.50	1.70	1.33	41.0	1.00	0.82	1.12	0.067	1.46	24.50	0.59	1.54
	M8	1.11	1.33	1.46	0.56	28.5	0.48	0.65	1.17	0.082	6.26	25.07	1.07	3.46
Proterozoic														
DC-Doushantuo cherts	D3	1.53	1.90	2.08	1.62	35.1	1.19	0.73	1.34	0.066	0.97	9.20	0.21	0.26
	D5	0.67	0.93	1.20	0.56	35.7	1.08	0.78	1.34	0.068	1.10	12.49	0.30	0.35
BS-Bitter Springs chert	BS	1.34	1.79	2.26	1.19	29.0	0.89	1.05	0.66	0.005	0.12	1.16	0.04	0.08
JC-Dahongyu cherts	JC	1.03	1.42	1.54	1.02	30.9	0.94	0.90	1.94	0.021	0.36	11.49	0.31	0.57
GFBC-Gunflint bedded cherts	G1	0.60	0.86	1.14	0.59	31.9	1.13	0.90	1.67	0.005	0.11	3.46	0.05	0.05
	G3	0.59	0.86	1.12	0.73	21.6	1.45	1.12	1.40	0.003	0.08	1.74	0.02	0.02
	K-565	0.56	0.59	0.82	1.02	30.1	2.10	0.33	3.63	0.000	0.02	0.88	0.01	0.01
BIF-2-chert band from banded iron formation from Barberton	BIF-2/a/b chert	1.43	1.39	1.66	2.05	20.8	1.38	0.99	1.59	0.005	0.29	5.98	0.03	0.03

Table 3 continued.

Sample group	Sample	[Pr/Yb] PAAS	[Sm/Yb] PAAS	[Gd/Yb] PAAS	[La/Yb]$_P$ AAS	Y/Ho	La/La*	Ce/Ce*	Eu/Eu*	TiO2 (wt %)	Sc (ppm)	Zr (ppm)	Hf (ppm)	Th (ppm)
Archean cherts														
PilBC-Pilbara bedded cherts from Dresser Fmn	W2	0.87	0.87	0.87	0.87	28.2	0.90	0.88	1.47	0.018	0.51	5.43	0.15	0.28
	MBC / MBC (new white)	0.52	0.72	0.80	0.51	28.6	1.00	1.18	2.33	-	-	-	-	-
PilVC-Pilbara vein chert from Dresser Fmn.	PilVC / DUCnew	0.38	0.52	0.66	0.25	23.1	0.75	0.85	0.90	0.005	0.49	2.85	0.05	0.07
PL-2-Agate in interpillow space	PL-2	0.71	0.91	1.01	0.79	27.7	0.53	0.65	2.20	0.001	-0.08	0.25	0.01	0.01
BBC-Barberton bedded chert from Swartkoppie Fmn	Z1	0.47	0.73	0.89	0.44	24.6	0.98	0.93	1.86	0.014	0.65	2.99	0.09	0.14
	Z2	1.57	1.86	1.95	1.58	26.8	0.94	0.93	5.76	0.017	1.93	3.15	0.08	0.13
	Z3	0.80	1.37	2.12	0.84	38.1	1.45	0.71	2.23	0.030	0.81	2.90	0.08	0.12
BIF-1	BIF-1 chert	2.05	2.36	2.24	1.82	26.0	0.93	0.87	1.81	0.003	0.21	1.70	0.04	0.09

Table 4 Al_2O_3 and Fe_2O_3 contents of samples, estimates from Al and Fe measurements via solution ICP-MS. Note that LNC is the only non-marine sample I the table. It is from the banks of modern day Lake Natron in Tanzania.

Sample group	Sample	Al_2O_3 (wt%)	Fe_2O_3 (wt%)
Phanerozoic cherts			
LNC-Lake Natron chert	LNC	0.006	0.005
PNC-Phanerozoic nodular cherts	M1	0.030	0.010
	M7	0.042	0.018
	M6	0.104	0.023
	AR	0.075	0.033
PBC-Phanerozoic bedded cherts	M3	0.569	0.121
	M8	2.337	0.509
Proterozoic			
DC-Doushantuo cherts	D3	0.302	0.156
	D5	0.604	0.282
BS-Bitter Springs chert	BS	0.119	0.182
JC-Dahongyu cherts	JC	0.255	0.057
GFBC-Gunflint bedded cherts	G1	0.037	0.293
	G3	0.032	1.252
	K-565	0.037	0.031
BIF-2-chert band from banded iron formation from Barberton Greenstone Belt (BGB)	BIF-2/a/b chert	0.044	5.292

Sample group	Sample	Al_2O_3 (wt%)	Fe_2O_3 (wt%)
Archean cherts			
PilBC-Pilbara bedded cherts from Dresser Fmn	W2	0.445	0.036
	MBC / MBC (new white)	-	-
PilVC-Pilbara vein chert from Dresser Fmn.	PilVC / DUCnew	0.077	1.404
PL-2-Agate in interpillow space	PL-2	0.010	0.010
BBC-Barberton bedded chert from Swartkoppie Fmn	Z1	0.387	0.056
	Z2	0.382	0.147
	Z3	0.201	1.215
BIF-1	BIF-1 chert	0.200	1.450

4.4.2 Triple oxygen isotopes

The Phanerozoic chert samples have $\delta^{18}O$ values 26.4 to 34.4‰ and $\Delta'^{17}O$ values ranging from -0.128 to -0.187‰. The Proterozoic samples range from $\delta^{18}O$ = 18.7 to 26.9‰ and $\Delta'^{17}O$ = -0.093 to -0.167, while the Archean cherts samples have lowest $\delta^{18}O$ values, varying from 13.9 to 19.9‰ and highest $\Delta'^{17}O$ values from -0.051 to -0.106‰. The results are enlisted in Table 5 and plotted in Figure 31, Figure 32, Figure 33.

Dörentrup quartz was used as an internal standard and analyzed several times. It has $\delta^{18}O$ = 11.5 ± 0.1‰ SE (± 0.5‰ 1σ SD for fluorination in Ni-bombs and ± 0.17‰ 1σ SD for laser fluorination) and $\Delta'^{17}O$ = - 72 ± 2 ppm SE (± 0.021‰ 1σ SD for fluorination in Ni-bombs and ± 0.006‰ 1σ SD for laser fluorination).

Table 5 List of triple oxygen isotope analyses of silica and chert samples. The δ¹⁷O and δ¹⁸O values are presented in the table in three forms – with respect to working gas (WG), the values that are obtained from the mass spectrometer (raw) and using a two-point calibration method (VSMOW2-SLAP2) (see Methods in Chapter 2 for non-linearity correction). Throughout the text the δ¹⁷O and δ¹⁸O values are reported in the VSMOW2-SLAP2 scale. The samples in italics have been used for $\theta^{\text{equilibrium}}_{\text{SiO}_2-\text{Water}} - T$ calibration. Please see next two pages for the table.

Sample	Age/Age groups	No. of analyses	δ¹⁷O WG ‰	δ¹⁸O WG ‰	δ¹⁷O raw ‰	δ¹⁸O raw ‰	δ¹⁷O VSMOW2-SLAP2 ‰	SD ‰	SE ‰	δ¹⁸O VSMOW2-SLAP2 ‰	SD ‰	SE ‰	Δ'¹⁷O VSMOW2-SLAP2 ‰	SD ‰	SE ‰
Standard 1			WG	WG	raw	raw	VSMOW2-	-	-	VSMOW2-	-	-	VSMOW2-	-	-
Standard 2			-	-	-	-	SLAP2	-	-	SLAP2	-	-	SLAP2	-	-
Slope of RL			-	-	-	-		-	-		-	-	0.5305	-	-
Phanerozoic samples															
LNC	few 100,000 yrs	4	11.702	21.816	17.677	34.063	17.910	1.1	0.5	34.351	1.1	0.5	-0.166	0.036	0.018
Di-73	~110,000 yrs	1	16.781	31.645	22.786	44.010	23.061	0.1	-	44.362	0.9	0.9	-0.228	0.021	0.021
Di-34	~92,000 yrs	1	15.066	28.279	21.061	40.604	21.322	0.1	-	40.935	0.9	0.9	-0.186	0.021	0.021
Di7	Modern	1	14.531	27.280	20.523	39.592	20.779	0.1	-	39.916	0.9	0.9	-0.197	0.021	0.021
Sponge	Modern	1	12.321	23.334	18.300	35.600	18.538	0.1	-	35.898	0.9	0.9	-0.342	0.07	0.07
spicules		2	13.415	25.311	19.400	37.600	19.647	0.5	0.3	37.911	0.9	0.5	-0.283	0.07	0.04
		2	11.924	22.445	17.900	34.700	18.134	0.5	0.3	34.992	0.9	0.5	-0.274	0.07	0.04
		2	11.725	21.852	17.700	34.100	17.933	0.5	0.3	34.388	0.9	0.5	-0.162	0.07	0.04
HGC	~ mid-Eocene	1	13.552	25.513	19.538	37.805	19.786	0.1	-	38.117	0.9	0.9	-0.252	0.021	-
Chert	Cretaceous	2	11.566	21.506	17.540	33.750	17.771	0.1	0.1	34.036	0.9	0.9	-0.140	0.021	-
M1	Paleogene	1	9.892	18.375	15.857	30.581	16.074	0.1	-	30.846	0.9	-	-0.170	0.021	-
M7	Upper Cretaceous	1	10.387	19.237	16.354	31.453	16.576	0.1	-	31.724	0.9	-	-0.128	0.021	-
M6	Upper Cretaceous	1	9.185	16.954	15.146	29.144	15.357	0.1	-	29.399	0.9	-	-0.131	0.021	-
AC	Cretaceous	4	11.741	21.841	17.716	34.089	17.949	0.1	0.5	34.377	0.9	-	-0.141	0.021	-
M3	Lower Cretacoues	1	9.463	17.561	15.425	29.758	15.639	0.1	-	30.017	0.9	-	-0.172	0.021	-
	Mississippian, Lower														
M8	Carboniferous	1	7.605	14.055	13.556	26.209	13.754	0.1	-	26.446	0.9	-	-0.187	0.021	-

Table 5 continued. Proterozoic samples.

			$\delta^{17}O$	$\delta^{18}O$	$\delta^{17}O$	$\delta^{18}O$	$\delta^{17}O$	SD	SE	$\delta^{18}O$	SD	SE	$\Delta'^{17}O$	SD	SE
Standard 1			WG	WG	raw	raw	VSMOW2	-	-	VSMOW2	-	-	VSMOW2	-	-
Standard 2			-	-	-	-	SLAP2	-	-	SLAP2	-	-	SLAP2	-	-
Slope of RL			-	-	-	-		-	-		-	-	0.5305	-	-
Sample		**No. of analyses**	‰	‰	‰	‰	‰	‰	‰	‰	‰	‰	‰	‰	‰
Proterozoic Samples															
D3	Neoptroterozoic,	2	7.530	13.798	13.481	25.949	13.679	0.1	-	26.184	0.3	-	-0.126	0.003	-
D5	635 Ma	1	6.212	11.372	12.155	23.495	12.341	0.1	-	23.714	0.9	-	-0.167	0.021	-
BS	Neoptroterozoic, 750 - 890 Ma	3	5.517	9.920	11.456	22.025	11.637	0.8	0.5	22.234	1.6	0.9	-0.096	0.028	0.016
JC	Mesoproterozoic, ~1600 Ma	1	7.922	14.524	13.875	26.684	14.076	0.1	-	26.923	0.5	-	-0.117	0.010	-
G1	Paleoproterozoic,	1	6.377	11.594	12.321	23.719	12.509	0.1	-	23.940	0.5	-	-0.119	0.010	-
G3	1878 Ma	2	5.464	9.813	11.402	21.917	11.583	1.3	-	22.125	2.5	-	-0.093	0.011	-
GFC-1		1	5.744	10.379	11.684	22.489	11.867	0.1	-	22.701	0.5	-	-0.112	0.010	-
K-565		1	6.972	12.660	12.919	24.797	13.112	0.1	-	25.025	0.9	-	-0.086	0.021	-
BIF2-avg	Paleoproterozoic, ~ 1800 Ma	2	3.672	6.437	9.600	18.500	9.765	0.1	-	18.687	0.1	-	-0.104	0.008	-

Table 5 continued. Archean samples.

Sample		no. of analyses	$\delta^{17}O$ WG ‰	$\delta^{18}O$ WG ‰	$\delta^{17}O$ raw ‰	$\delta^{18}O$ raw ‰	$\delta^{17}O$ VSMOW2-SLAP2 ‰	SD ‰	SE ‰	$\delta^{18}O$ VSMOW2-SLAP2 ‰	SD ‰	SE ‰	$\Delta'^{17}O$ VSMOW2-SLAP2 ‰	SD ‰	SE ‰
Standard 1			WG	WG	raw	raw	VSMOW2-	-	-	VSMOW2-	-	-	VSMOW2-	-	-
Standard 2			-	-	-	-	SLAP2	-	-	SLAP2	-	-	SLAP2	-	-
Slope of RL			-	-	-	-	-	-	-	-	-	-	0.5305	-	-
Archean samples															
W2	3500-3420 Ma	5	1.809	2.822	7.726	14.841	7.876	0.4	0.2	15.004	0.8	0.4	-0.055	0.025	0.011
MBC		2	4.114	7.278	10.044	19.351	10.213	0.4	-	19.543	0.9	0.1	-0.106	0.012	0.012
DUC-1	3500-3420 Ma	1	2.245	3.712	8.165	15.743	8.318	0.1	-	15.911	0.9	-	-0.091	0.021	-
DUC-2		1	1.703	2.675	7.620	14.693	7.769	0.1	-	14.855	0.9	-	-0.084	0.021	-
PL-2	3474-3463 Ma	2	1.838	2.868	7.755	14.888	7.905	0.03	-	15.051	0.1	-	-0.051	0.025	-
Z1		2	2.603	4.353	8.524	16.391	8.681	0.2	-	16.564	0.4	0.4	-0.072	0.018	0.018
Z2	3298 Ma	3	2.060	3.327	7.978	15.352	8.130	0.3	0.2	15.519	0.5	0.3	-0.072	0.008	0.005
Z3		2	1.194	1.732	7.107	13.739	7.252	0.1	-	13.894	0.2	-	-0.095	0.019	-
BIF-1-chert	N.A.	1	2.541	4.204	8.463	16.240	8.619	0.1	-	16.412	0.9	-	-0.054	0.021	-
K-1100	3560 Ma	2	4.216	7.421	10.147	19.496	10.317	0.2	-	19.689	0.3	-	-0.079	0.005	-
K-1113	N.A.	1	4.138	7.309	10.068	19.383	10.237	0.1	-	19.575	0.9	-	-0.099	0.021	-
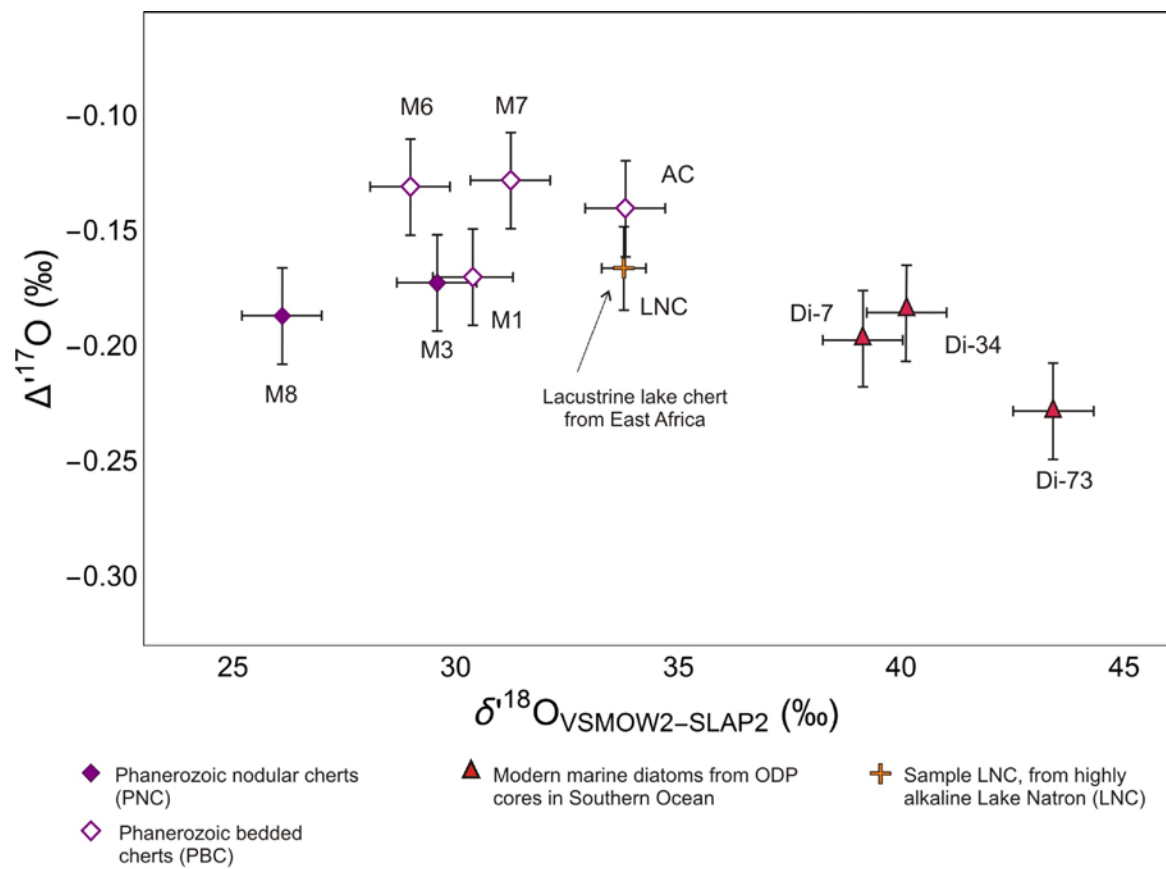
Figure 31 Plot of Δ'17O vs δ'18O of Phanerozoic chert and silica samples. The data points circled in orange represent terrestrial lacustrine cherts from East Africa. The PBC and diatom samples are marine. The PNC samples maybe have been affected by meteoric waters.
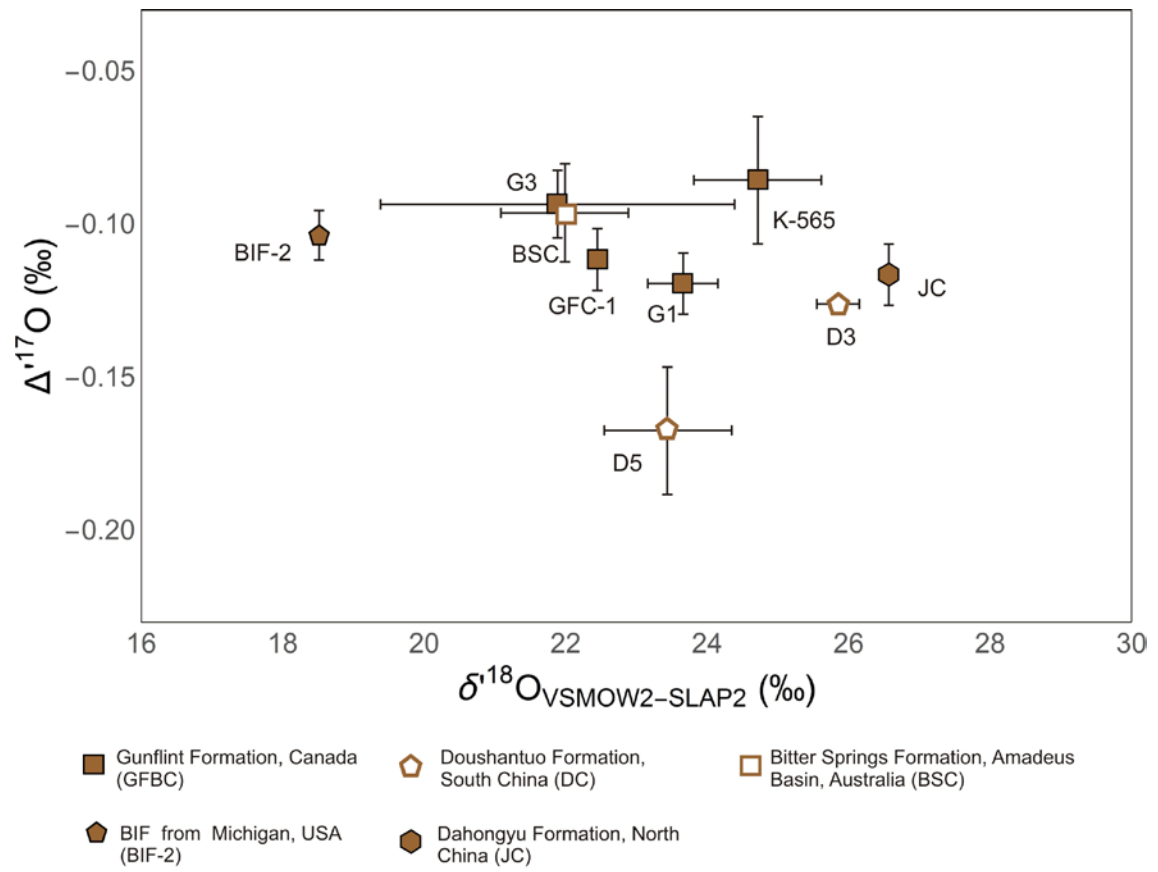
Figure 32 Plot of Δ'¹⁷O vs δ'¹⁸O of Proterozoic chert samples; data on VSMOW2-SLAP2 scale.
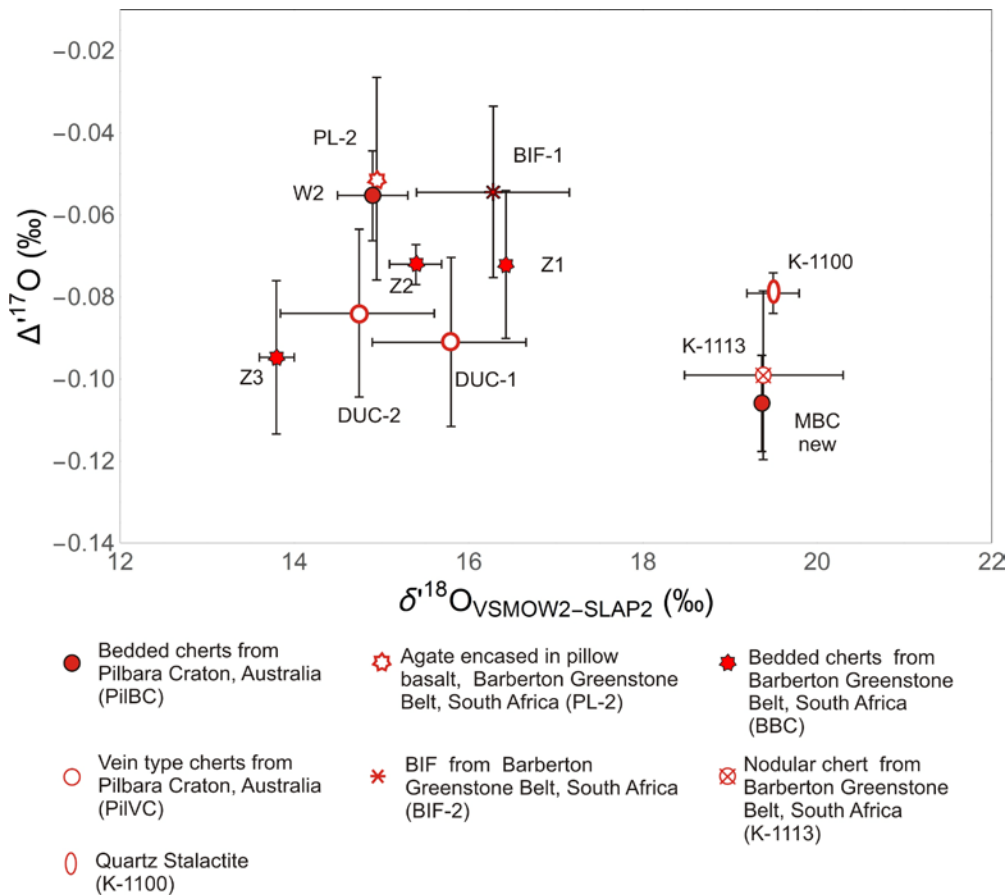
Figure 33 Plot of Δ'¹⁷O vs δ'¹⁸O of Archean cherts. All data are on VSMOW2-SLAP2 scale.

4.5 Discussion

4.5.1 The temperature dependence of the silica water ¹⁸O/¹⁶O fractionation

The ¹⁸O/¹⁶O isotope fractionation between silica and water and its temperature dependence can be used as a thermometer for paleoclimate studies (e.g., Knauth and Lowe, 2003). Defining a temperature dependent equilibrium fractionation factor for the ¹⁸O/¹⁶O fractionation between silica and water, i.e., a $\alpha_{\mathrm{SiO_2-Water}}^{18/16\mathrm{O}}$ -T relation, is essential for defining a $\theta_{\mathrm{SiO_2-Water}}^{\mathrm{equilibrium}} - T$ relation later in Section 4.10.2.

The fractionation factor between silica and water, $\alpha_{\mathrm{SiO_2-Water}}^{18/16\mathrm{O}}$, is a function of 1/T at low

temperatures or 1/T2 at high temperatures (e.g. Criss, 1991) where T is the temperature in

Kelvin. The $\alpha^{18/16\,O}_{SiO_2-Water} - T$ relation may be expressed in the following form:

$$1000 \ln \alpha = \frac{a \times 10^6}{T^2} + \frac{b \times 10^3}{T}$$

Equation 1

In the above equation a and b are constants. A short summary of the $\alpha^{18/16\,O}_{SiO_2-Water}$ - T relations

determined so far by previous studies (e.g., Sharp et al., 2016 and references therein) is given

below. The results of the studies are plotted in Figure 34.

The quartz-water fractionation was first determined experimentally by O'Neil and Clayton

(1964) for above 195°C. Later Clayton et al. (1972) re-evaluated systematic errors in mass

spectrometry. Their study measured equilibrium constants for oxygen isotope exchange between

quartz and water at 195°C ($1000 ln\alpha^{18/16\,O}_{SiO_2-Water}$ = 12.0) and 750°C ($1000 ln\alpha^{18/16\,O}_{SiO_2-Water}$ = 0.4). The

values above 500°C were incorporated by Knauth and Epstein (1976), along with data on a chert

sample from Horizon Guyot to give a new calibration.

Later, oxygen fractionation was measured in quartz precipitated under hydrothermal and high

pressure (15 kbar at 250°C) conditions, by Matsuhisa et al. (1978). Quartz was crystallized

hydrothermally between 265 to 465°C, from silicic acid by Matthews and Beckinsale (1979)

instead of directly from water.

Recently, Sharp et al. (2016) presented a revised $\alpha^{18/16\,O}_{SiO_2-Water}$ - T relation based on silica

precipitates from geothermal waters at around 50°C, marine diatoms from ocean bottom cores

(~0°C) and a marine authigenic quartz sample. For this study we choose the relation proposed by

Sharp et al. (2016), which is the latest study on this thermometry and is a synthesis of all relevant

data published so far (Figure 34):

$$1000 ln\alpha^{18/16\,O}_{SiO_2-Water}(T) = \frac{4.28(\pm 0.07) \times 10^6}{T^2} - \frac{3.5(\pm 0.2) \times 10^3}{T}$$

Equation 2

$$1000ln\alpha_{\mathrm{SiO_2-Water}}^{^{18/16}O}(T) = \frac{4.2(\pm0.07)\times10^6}{T^2} - \frac{3.3(\pm0.2)\times10^3}{T}$$

(Sharp et al., 2016)

Legend:
- Kita et al., 1985
- Leclerc and Labeyrie, 1987
- Matsuhisa et al., 1978
- Matsuhisa et al., 1979
- Matthews and Beckinsale, 1979
- Clayton et al., 1972
- Hu and Clayton, 2003
- Matthews et al., 1983
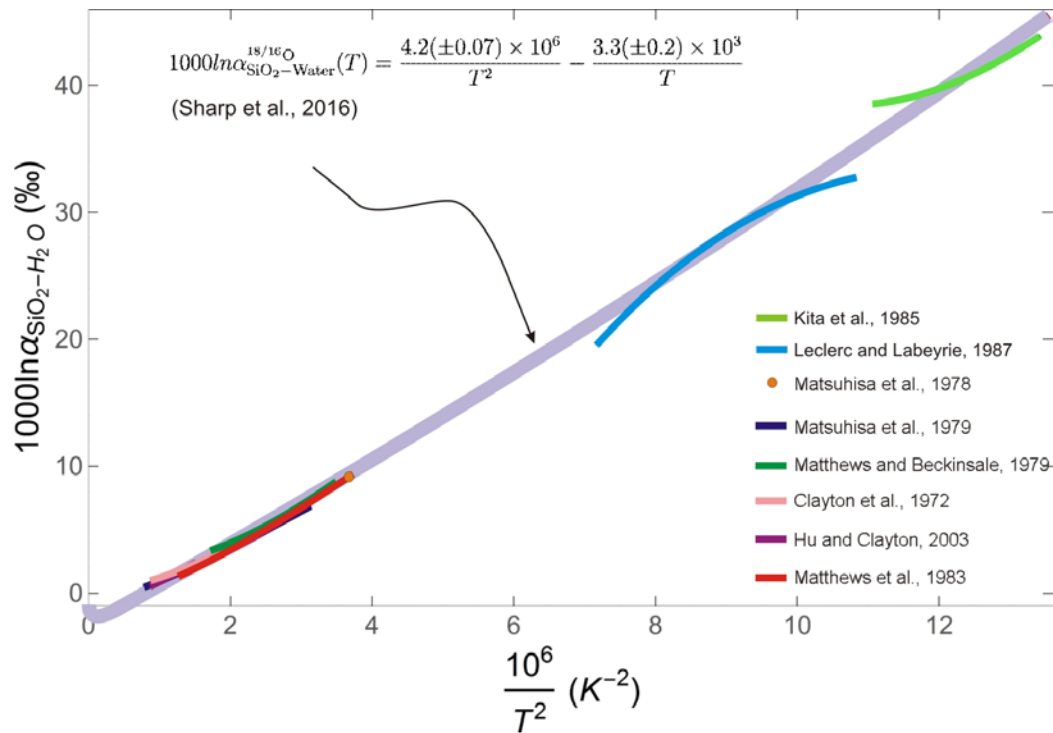
Figure 34 The $\alpha_{\mathrm{SiO_2-H_2O}}^{\mathrm{equilibrium}}$ relation recently compiled by Sharp et al. (2016) (thick curve). This equation is a best fit of the different fractionation factors published so far on quartz-water and silica-water equilibrium fractionation (thinner and smaller curves in plot). The relation is valid over the entire temperature range from 0°C to infinitely high temperatures (inferred from theory). Modified after Sharp et al. (2016).

4.5.2 The temperature dependence of θ

Matsuhisa *et al.* (1978) first used a three-isotope exchange method, combining theory and experiments, to estimate fractionation from partially exchanged samples and investigated the $^{18}O/^{16}O$ fractionation in the SiO_2-H_2O system. They carried out quartz - water exchange reactions at 250°C and measured both $^{18}O/^{16}O$ and $^{17}O/^{16}O$ fractionation ratios.

The first theoretical $\theta_{\mathrm{SiO_2-Water}}^{\mathrm{equilibrium}} - T$ equation was determined by Cao and Liu (2011). They provided θ values for oxygen isotope equilibrium fractionation between quartz and water for the temperature range of 0 to 100°C. Their data points and T – dependence curve is shown in Figure 36.

The $\theta_{SiO_2-H_2O}^{equilibrium}$ values reported by Pack and Herwartz (2014) are lower than the theoretical

values from Cao and Liu (2011). They provided a $\theta_{SiO_2-H_2O}^{equilibrium} - T$ relation based on the high-T

approximation of θ, analyses of modern marine sponge silica and a Cretaceous chert analysis, in

the form $\theta_{SiO_2-H_2O}^{equilibrium} = \frac{A}{T^2} + 0.5305$. The data reported therein needs to be corrected according to

the revisions suggested in Pack et al. (2016) and preferably reported on the SMOW2-SLAP2 scale.

The samples used for their temperature calibration were measured using an older technique, in

the 'continuous flow' mode of their mass spectrometer. The non-linearity involved in this mode is

not known but it is assumed here that the same non-linearity effects as in this study (meaning

same mass spectrometer but in the dual-inlet mode) applies to their data.

Then the two $\theta_{SiO_2-H_2O}^{equilibrium}$ values obtained for modern marine sponges and the chert increase by

0.0020 and 0.0028 respectively. As a result, the value of the constant A changes from -740 to -

573 in their $\theta_{SiO_2-H_2O}^{equilibrium} = \frac{A}{T^2} + 0.5305$ relation. The equation comes closer to the theoretical

relation by Cao and Liu (2011). The data have been discussed in greater details in the following

sections and plotted along with the other samples of this study (Figure 36).

Sponge spicules from Pack and Herwartz (2014): The modern marine sponge silica data of Pack

and Herwartz (2014) have an average $\delta^{18}O$ value of 36.1‰. This value is low because at 8°C the

expected $\delta^{18}O$ value for silica precipitating from modern seawater, according to Equation 2 is

41.7‰ (because seawater has $\delta^{18}O = 0‰$). This could be due to non – removal of isotopically

light oxygen present in the non-tetrahedral hydroxyl ions of the hydrous opaline sponge silica

(hydrated silica $SiO_2.nH_2O$) (Figure 36) during laser fluorination. Removing this structural water

from the opaline sponges is essential to extract and measure only the O-atoms that are bound to

silicon atoms, forming a part of the SiO_4 tetrahedra (the structural unit of crystalline silica). A

stepwise fluorination method is required for this purpose (Matheney and Knauth, 1989; Dodd

and Sharp, 2010). The data have a large uncertainty on their $\Delta'^{17}O$ values (40ppm SE) because

they were measured in continuous-flow mode of their mass spectrometer. However, since the

final θ value is dependent on both $\delta^{18}O$ and $\Delta'^{17}O$ of the samples, the large uncertainty on the

latter means that the $\theta_{SiO_2-Water}^{equilibrium}$ value for the sponges, as reported in Pack and Herwartz

(2014), may still be valid. $\Delta'^{17}O$ values decrease with increasing $\delta^{18}O$ values and eventually the θ

value obtained from the sponges may still remain valid, within uncertainty. The corrected sponge spicules' $\delta^{18}O$ data remains identical, within uncertainty, but their average $\Delta'^{17}O$ data changes from -0.347 to -0.265. The mean $\theta_{SiO_2-H_2O}^{equilibrium}$ value for the sponges becomes 0.5231 ± 0.007, i.e., 0.0020 higher than originally reported. Even with the large spread in $\Delta'^{17}O$ of the sponge data, the average of the corrected values is close to ($\sim$ 0.0010 lower) the theoretical values reported in Cao and Liu (2011) (Figure 36). Additionally, the growth temperature of the sponges is well constrained and hence, the corrected data has been used in this study.

<u>Chert from Pack and Herwartz (2014):</u> We also correct and use the Cretaceous chert data reported by Pack and Hewartz (2014). It is found to have $\delta^{18}O$ value 34.0‰ instead of 33.8‰ after correction to VSMOW2-SLAP2 scale. The $\Delta'^{17}O$ value increases to -0.140‰ instead of 0.221‰ and accordingly, the $\theta_{SiO_2-H_2O}^{equilibrium}$ value goes up by 0.0028 to become 0.5263. After correction of the data, the value of the constant A changes from -740 to -573 in the Pack and Herwartz (2014) $\theta_{SiO_2-H_2O}^{equilibrium} = \frac{A}{T^2} + 0.5305$ relation. The equation comes closer to the theoretical relation by Cao and Liu (2011). The corrected data have been plotted along with the other samples of this study (Figure 35).

As emphasized by Pack and Herwartz (2014), there is need for a more precise analysis of a larger sample set whose precipitating conditions are better constrained, in order to calibrate the $\theta_{SiO_2-H_2O}^{equilibrium}$ - T relation. Sharp et al. (2016) analyzed low-T silica samples and provided a calibration close to the theoretical estimate. We analyze diatom samples (from ODP deep sea cores in the Atlantic) and Horizon Guyot chert (authigenic deep sea silica from Pacific Ocean) – reported in Sharp et al. (2016) and present them here with minor modifications. We have also analyzed the triple oxygen isotope composition of a modern chert from Natron Lake, and an additional purified diatom samples from deep sea sediments of the Atlantic Ocean (see Section 88 for sample details and description). Each sample is discussed in detail next.

<u>Modern marine diatoms:</u> In order to use the $\delta^{18}O$ and $\delta^{17}O$ values of diatoms to calibrate the oxygen isotope fractionation – temperature relationship it is important to understand how oxygen isotopes of the diatom silica behave and fractionate not only during formation of diatom frustules but also as the diatom ooze settles down as a sediment package, is collected as sample

and finally purified in the laboratory for isotope analyses (Leng and Barker, 2006). Errors introduced during laboratory procedures and analysis, and how they can be removed has been described below.

Diatoms undergo a 'silica maturation' process after death and loss of organic matter, as the diatom cell settles within the sediment (Matheney and Knauth, 1989; Schmidt et al., 2001; Moschen et al., 2006; Dodd et al., 2010). This re-equilibration may occur as fast as within 0.5 years after death (Dodd et al., 2010). Modern diatoms cultured in laboratories bear $\delta^{18}O$ values 8 ‰ lower than equilibrium quartz-water fractionations (Matheney and Knauth, 1989; Sharp and Kirschner, 1994; Brandriss et al., 1998; Schmidt et al., 2001) and ~3-4‰ lower than observed silica-water fractionations in diatomaceous silica (Moschen et al., 2005, 2006). Such samples collected from sediment traps and sediment cores have not undergone this post-mortem maturation. Our samples are diatoms incorporated in sediment from depths of tens of centimetres within the deep-sea sediment cores, as old as the Pleistocene. These samples have re-equilibrated with seawater and are suitable for a temperature calibration.

The second concern while using oxygen isotope data of diatoms is related to analytical techniques, wherein it is required to successfully strip the hydrated silica shells or "tests" of these organisms of the structurally bound water within them. Diatoms, like sponges, produce "hydrated silica" tests or frustules in the form of amorphous silica polymorph opal-A, with chemical formula $SiO_2.nH_2O$ (e.g., Perry, 1989). This non-tetrahedral oxygen from within the water components (OH- or H_2O) must be removed because these are not in equilibrium with surrounding seawater but yield lighter $\delta^{18}O$ values than expected from silica-water equilibrium fractionation. Care must also be taken that this lighter non-tetrahedral oxygen does not exchange with the Si-tetrahedra bound oxygen atoms during removal. The fluorination method suggested by Dodd and Sharp (2010) was employed in order to fluorinate these samples with successive prefluorination steps (see Chapter 2 - Methods for details of prefluorination) the gradually increasing $\delta^{18}O$ and $\delta^{17}O$ values reached a plateau and did not increase any further after one point in the experiment. This is an indication that the lighter oxygen has been stripped off. Finally only those last analyses which provide temperatures close to that of Antarctic waters (~0.5°C, Gersonde et al., 1999) at ocean floors of the core sites and give reasonable $\theta_{SiO_2-H_2O}^{equilibrium}$ values

shall be chosen for calibration. Irrespective of the $\delta^{18}O$ values obtained, the calculated θ values

from the $\delta^{17}O$ and $\delta^{18}O$ remained the same within ± 0.0001 amongst multiple aliquots of a single

sample (also observed by Rumble et al., 2007; Sharp et al., 2016). Thus, even if the $\delta^{18}O$ values of

the diatoms may not be exactly true the θ values are and may safely be used for the θ-T

calibration, as shown in Sharp et al. (2016).

Purified diatom sample, Di-73, from deep sea sediment cores from the Ocean Drilling Program in

the southeast Atlantic sector of the Southern Ocean, Leg 177, Site 1094, was found to have $\delta^{17}O$ =

23.061, $\delta^{18}O$ = 43.7 ± 0.5‰ (both values on VSMOW2-SLAP2 scale) and $\Delta'^{17}O$ = -0.228 ± 0.021

ppm. The corresponding $\theta_{SiO_2-H_2O}^{equilibrium}$ value for this sample is 0.5254 ± 0.005. This particular

sample and data point has also been reported and used for $\theta_{SiO_2-H_2O}^{equilibrium} -$ T calibration in Sharp et

al. (2016) with a $\theta_{SiO_2-H_2O}^{equilibrium} -$ T value of 0.5240, calculated from normalized $\delta^{17}O$ and $\delta^{18}O$

values – this is lower than our value. They use the same data point with raw $\delta^{17}O$ and $\delta^{18}O$ values

of 22.8 and 44.0 (relative to reference O_2 gas in Universität Göttingen) but their normalized $\delta^{17}O$,

$\delta^{18}O$ and $\Delta'^{17}O$ values, i.e., 22.8‰, 44.0‰ and -0.174‰ differ from those presented in this study.

This is because they report their values normalized to San Carlos olivine values $\delta^{18}O$ = 5.3‰ and

$\Delta'^{17}O$ = -0.069‰ (or -0.054‰ using a slope of 0.528). The values for San Carlos olivine adopted

in this study instead are from Pack et al. (2016) who present an identical $\delta^{18}O$ value (within

uncertainty) but a higher $\Delta'^{17}O$ value of ~-0.050‰ (with slope 0.5305) (0.036 ± 0.009‰ using

slope 0.528). Thus, the $\Delta'^{17}O$ value of the sample in this study is lower and consequently the

calculated average number for $\theta_{SiO_2-H_2O}^{equilibrium}$ is 0.0014 higher in this study.

The temperature calculation from this diatom sample data point depends on the $\delta^{18}O$ values that

one assumes for the seawater it equilibrated with, as pointed out by Sharp et al. (2016). The

$\alpha_{SiO_2-Water}^{18/16O}$ - T relationship by the same study (Equation 2) involves a change in temperature

of 3°C for a 1‰ change in $1000\ln\alpha_{SiO_2-H_2O}^{18O/16O}$. Based on Equation 1 and a $\delta^{18}O_{sw}$ of 0‰, an average

temperature of ~3°C is obtained, which is higher than the ocean bottom temperature of 0.5°C at

the core site (Gersonde et al., 1999, Initial Reports of ODP Leg 177). Taking into consideration

that the sample is from a glacial period, MIS 5d, the seawater $\delta^{18}O$ value is an estimated 1‰

heavier than modern day because of greater amounts of lighter oxygen isotopes being trapped

144

within the greater ice volumes present then (Schrag et al., 2002 from $\delta^{18}O$ study of pore waters of Hole 1093, north of Hole 1094). Taking this heavier seawater $\delta^{18}O$ value leads to an even higher equilibration temperature of 6°C. These anomalous temperatures indicate an error in $\delta^{18}O$ analysis of the samples, which may arise due to impartial removal of lighter non-tetrahedral oxygen or due to exchange of this light oxygen with structural oxygen atoms bound to Si. The latter may have happened during the prefluorination steps if the lighter oxygen was not removed quickly enough. However, whether these calculated temperature values or the known temperature values for the geological setting, i.e., $\sim$0.5°C for deep Antarctic waters, are used for the final $\theta^{equilibrium}_{SiO_2-H_2O} -$ T calibration leads to a difference in $\theta^{equilibrium}_{SiO_2-H_2O}$ of only 0.0002 (as demonstrated in Sharp et al., 2016).This is well within the uncertainty for individual θ values in this study and therefore will have no effect on the final calibration. In this study the diatom data have been plotted using modern day deep water temperatures in the Southern Ocean instead of the calculated values simply because the former are presumably closer to the true values that these diatoms, from a glacial age, would have experienced. The arguments regarding calculated and assumed temperature values also applies to the remaining two diatom samples, to be discussed in the following sections.

The change in $\delta^{17}O$ of seawater accompanying a 1‰ heavier $\delta^{18}O$ of glacial period seawater and their combined effect on the $\theta^{equilibrium}_{SiO_2-H_2O}$ value must also be considered. Sharp et al. (2016) discuss this problem by assuming that during the glacial period $\sim$3% of the present day ocean water gets trapped in continental ice sheets, in turn be assumed to have a $\delta^{18}O$ value of $\sim$-30‰. The corresponding $\delta^{17}O$ value for the continental ice can be estimated at 15.973‰ from the list of modern meteoric waters measured by Luz and Barkan (2010). Transferring this small amount of water from the oceans has negligible effect on final $\theta^{equilibrium}_{SiO_2-H_2O}$ values, changing them only by 0.0002.

The second diatom sample comes from the same Hole 1094, Sample Di-34 – it yields values of $\delta^{18}O$ = 40.94 ± 0.5, and $\theta^{equilibrium}_{SiO_2-H_2O}$ of 0.5260 ± 0.0003. This sample is also from a glacial age. The $\theta^{equilibrium}_{SiO_2-H_2O}$ value is within uncertainty identical to the previous diatom data and an assumed temperature value close to 0°C shall be used.

Diatom sample Di7 from Leg 177, Hole 1093, situated north of 1094, shows a $\delta^{18}O$ value of 39.9 ± 0.5‰, which yields unreasonably high temperatures of ~15°C for deep seawater. It was not possible, even with prolonged prefluorination of up to 90 mins to obtain a heavier $\delta^{18}O$ value. This sample was also measured by and reported in Sharp et al. (2016), who obtained higher $\delta^{18}O$ of 42.9 and 42.5‰. Again, the $\theta_{SiO_2-H_2O}^{equilibrium}$ value obtained in this study, 0.5256 ± 0.0003 is, within uncertainty, identical to Sharp et al. (2016) and the high calculated temperature of the sample is not expected to affect within uncertainty the final calibration.

Horizon Guyot chert (HGC): Sample HGC is a deep sea chert sample from the Horizon Guyot of the mid-Pacific Mountains (Hess, 1946). It is composed of microcrystalline quartz (> 98%) and was found to have a $\delta^{18}O$ of 38.40‰ and $\Delta'^{17}O$ of -0.251‰ on the VSMOW2-SLAP2 scale. This is a nodular chert sample, from within the pelagic sediment cover over the Horizon Guyot ridge, where the silica precipitated from sediment pore waters during diagenesis. Being a dredge-haul sample, it has not been deeply buried and the pore water of the sediments would be identical to seawater (Knauth, 1973). Deep seawater in the Pacific, from where this sample comes, has $\delta^{18}O$ 0.2‰ a temperature of 2°C but this sample comes from the mid-Eocene horizon and the seawater $\delta^{18}O$ value was ~-0.6 back then (Craig and Gordon, 1965). Considering this sample is in equilibrium with modern seawater of $\delta^{18}O$ = 0‰, and $\Delta'^{17}O$ = -0.005 (Luz and Barkan, 2010) a temperature of 19°C is obtained from their ^{18}O compositions (Equation 2). Equilibration temperature increases by 2°C if the quartz equilibrated with water of -0.6‰. This variation of $\delta^{18}O$ introduces uncertainties a factor of 6 less than the error of the best fit (Sharp et al., 2016). A $\theta_{SiO_2-H_2O}^{equilibrium}$ value of 0.5240 ± 0.0004 is calculated for the sample.

Lake Natron chert from Tanzania, Africa: A lacustrine chert (LNC), few hundred thousand years old (communication from François Robert), collected from the western part of Lake Natron, a highly alkaline lake (pH up to 12) in the East African Ridge (Hay, 1968; O'Neil and Hay, 1973; François Robert, personal communication) was analyzed. This chert shows a $\delta^{18}O$ of 34.4 ± 0.5‰ and $\Delta'^{17}O$ of -0.166 ± 0.018‰ (SE) on the SMOW2-SLAP2 scale. It has been postulated that these cherts are very similar to the "Magadi-type" cherts from lake Magadi which form by replacing precursor hydrous sodium silicates hydrous sodium silicates, $NaSi_7O_{13}(OH)_3.3H_2O$ (magadiite) and $NaSi_{11}O_{20.5}(OH)_4.3H_2O$ (kenyaiite) (Eugster, 1967, 1968; Hay,1968). Such cherts, along with

the magadiite and kenyaiite minerals from the East African saline lakes are some of the heaviest $\delta^{18}O$ terrestrial material reported till date (O'Neil and Hay, 1968). In this study we report, for the first time, the $\delta^{17}O$ and corresponding $\Delta'^{17}O$ values of such "magadi-type" cherts and attempt to derive $\theta_{SiO_2-H_2O}^{equilibrium}$ values from them.

This chert from Lake Natron and also other cherts from surrounding areas are found to be forming geologically recently. It has been assumed that their temperature of formation would be close to the average annual temperature of the region, 30°C-40°C. This requires the involvement of $\delta^{18}O$ heavy saline lake waters for the chert to be precipitating in equilibrium with the water, according to the quartz-water (qz-H_2O) fractionation relation (O'Neil and Hay, 1968) (qz-H_2O fractionation relation by Sharp et al., 2016 – Equation 2 in this text). Water samples were collected and analyzed from close to the chert location (measurements by François Robert, personal communication). The water from Lake Natron was found to have a $\delta^{18}O$ of 0.17‰ on the VSMOW scale. Several hotsprings bubble up along the lake periphery and provide a small part of the freshwater supply to this lake. Water samples from two such hotsprings (A and B) were found to have $\delta^{18}O$ values -2.59‰ and -1.62‰ respectively, again on VSMOW scale. We assume the water isotopic analyses are free of mass-spectrometer related non-linearity effects. Thus, the values remain the same on VSMOW2-SLAP2 scale. Using Equation 2 for qz-H2O fractionation (Sharp et al., 2016) temperatures of 35°C are obtained if equilibrium is considered with lake water. This matches the average annual temperature of the region. The hotsprings' waters themselves have temperatures of 40 to 50°C but when considering equilibration with the chert $\delta^{18}O$ value, temperatures of only 25 and 29°C (hotsprings A and B respectively) are obtained which indicate that the chert is not in equilibrium with these freshwaters. So, the only water data point we use is the one belonging to the lake water.

The water samples were not available for $\delta^{17}O$ measurements but reasonable estimates may be made from the modern meteoric water datasets of Luz and Barkan (2010) and Li et al. (2015) compiled in Figure 35. The meteoric water dataset is a cloud of data that has a $\Delta'^{17}O$ values spread over a range of ~20 ppm for the $\delta^{18}O$ value of the lake water, i.e., 0.17‰.

The Natron lake water is recharged by incoming freshwater from the Ewaso Ngiro river and the surrounding hotsprings, but also suffers high amounts of evaporation daily. In fact, the lake is

less than 3 metres deep. Thus, the effect of the evaporation must be taken into consideration while estimating the $\delta^{17}O$ of the lake water. An equilibrium slope of 0.529 between liquid and vapour water was experimentally determined by Luz and Barkan (2005). Equilibrium and kinetic processes are straight lines in the $\delta'^{17}O$ vs $\delta'^{18}O$ and $\Delta'^{17}O$ vs $\delta'^{18}O$ spaces (see Chapter 2 for details on the triple oxygen isotope systematics). Note that this slope, as all other slopes or "θ" values, has a value of 0.529 in $\delta'^{17}O$ vs $\delta'^{18}O$ space and a value of 0.529-0.5305, i.e., -0.0015 in the $\Delta'^{17}O$ vs $\delta'^{18}O$ space. Landais et al. (2006) studied triple oxygen isotope relationships between stem and leaf water of plants in order to obtain a transpiration slope λ_{transp} between the two water compositions. This is a combination of equilibrium, kinetic and mixing processes; in the $\Delta'^{17}O$ vs $\delta'^{18}O$ space mixing processes are defined by curves and thus, a process such as evaporation or transpiration follows a curved path, whereas the net effect can be represented as a line. Landais et al. (2006) also provided a relationship between λ_{transp} and relative humidity (RH). Between RH values of 0.3 and 1 this relationship is as follows:

$$\lambda_{transp} = -0.0078 \, (\pm 0.0026) \times RH + 0.5216 \, (\pm 0.008) \qquad \text{\textcolor{blue}{Equation 3}}$$

We use Equation 3 as an approximation for evaporation of Lake Natron water. Assuming RH values of 0.3 and 0.5 for the Lake Natron area, λ_{evap} values of 0.5193 and 0.5177 are obtained from this equation. Figure 35 shows these evaporation slopes along with the $\delta^{18}O$ values of the lake water and hotsprings A and B. The possible range of $\Delta'^{17}O$ values they may have, based on global meteoric water measurements, have been marked out in blue, red and orange bars. The spread in $\Delta'^{17}O$ values for a given $\delta'^{18}O$ value is only ~ 20 to 30 ppm. Especially for the lake water of 0.17‰, $\Delta'^{17}O$ values of meteoric waters vary between 0 and 20 ppm. Lines depicting the calculated evaporation slopes of 0.5193 and 0.5177 have been plotted such that they pass through all three vertical bars and constrain a pathway for the net effect of evaporation, from lighter freshwater to a heavier lake water. We are concerned mainly with an estimate on $\Delta'^{17}O$ of the lake water that has suffered evaporation and therefore lies on an evaporation slope; a reasonable estimate for this value is 0 ± 0.010 ppm. The meteoric water data of Barkan and Luz (2010) have small non-linearity effects (1.0 ppm per 1‰ $\delta^{18}O$ on the $\Delta'^{17}O$) and the data by Li et al., 2015 were already reported on a normalized SMOW-SLAP scale.

Using the $\delta^{17}O$ and $\delta^{18}O$ values of this lake water and sample LNC we calculate a $\theta^{\text{equilibrium}}_{\text{SiO}_2-\text{Water}}$-T value of 0.5256 ± 0.0005 at 35.6°C. This value involves assumptions for many input parameters but large uncertainties have been considered at every step and a Monte Carlo method of propagation of uncertainty has been run over 100 simulations to arrive at an uncertainty of ±0.003 for the $\theta^{\text{equilibrium}}_{\text{SiO}_2-\text{Water}}$ value. Additionally, the mean θ value is close to theory – within 0.0009 of the theoretical estimate by Cao and Liu (2011).
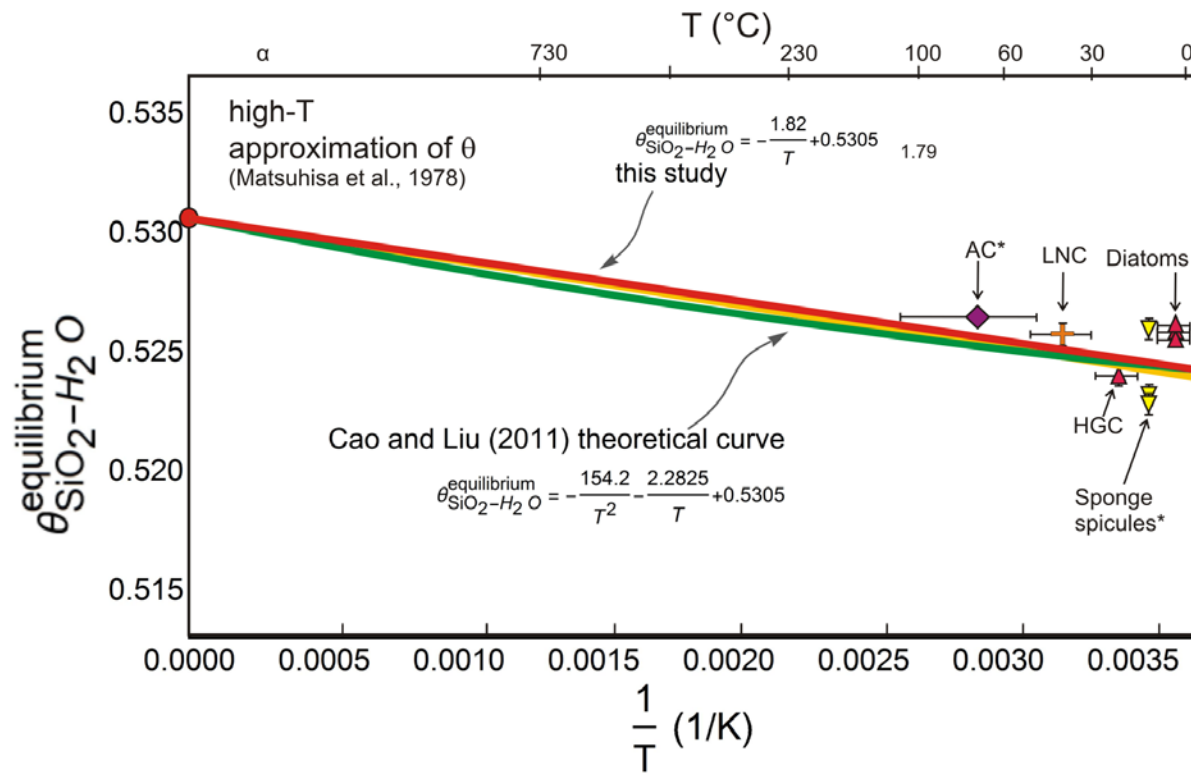
Figure 35 Figure shows the $\theta^{equilibrium}_{SiO_2-Water}$-T relationship obtained from this study (red line) and the equation determined theoretically by Cao and Liu (2011). Our equation is, within uncertainty, indistinguishable from theory. The sponge spicules' data have been taken from Pack and Herwartz (2014) and corrected according to Pack et al., 2016. The curve in yellow is the $\theta^{equilibrium}_{SiO_2-Water}$ relationship from Sharp et al., 2016.
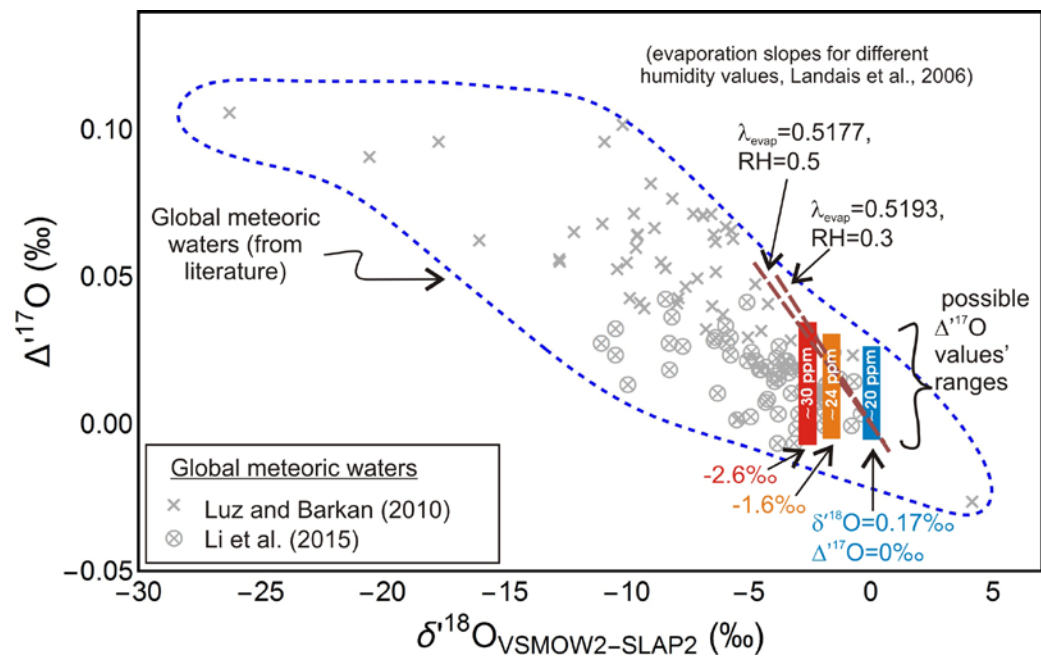
Figure 36 Δ'¹⁷O vs δ'¹⁸O plots showing the δ¹⁸O values of the Natron lake water (0.17‰) and 2 nearby hotsprings (-1.6‰ and -2.6‰). The possible range of Δ'¹⁷O values they may have, based on global meteoric water measurements, have been marked out in blue, orange and red bars. The spread in Δ'¹⁷O values for a given δ'¹⁸O value is only ~ 20 to 30 ppm. Lines depicting the calculated evaporation slopes of 0.5193 and 0.5177 have been plotted; they pass through all three vertical bars and constrain a pathway for the net effect of evaporation, from lighter δ¹⁸O freshwater to heavier lake water

Compiling the high-T approximation for θ (e.g., Matsuhisa et al., 1978) θ-T values for the sponge spicules and cretaceous chert (modified after Pack and Herwartz, 2014) along with diatom samples, Horizon Guyot chert (also reported in Sharp et al., 2016) and Lake Natron chert shows that the data points are not very well correlated and have large error bars on their θ values, but the averages are close to the theoretical estimate (Cao and Liu, 2011). Thus, the $\theta_{\mathrm{SiO_2-Water}}^{\mathrm{equilibrium}}$-T relation comes very close to the theoretical curve by Cao and Liu (2011) (Fig. 8). The $\theta_{\mathrm{SiO_2-Water}}^{\mathrm{equilibrium}}$-T calibration by Sharp et al. (2016) is also identical to the theoretical curve within uncertainty. If $\theta_{\mathrm{SiO_2-Water}}^{\mathrm{equilibrium}}$-T is expressed in the form of $\theta = \frac{a}{T} + 0.5305$ then the uncertainty on term a is 0.11, larger than the uncertainty in Sharp et al. (2016). The uncertainty was calculated following Monte Carlo error propagation.

For further discussion in this study the $\theta_{\mathrm{SiO_2-Water}}^{\mathrm{equilibrium}}$-T relation by Cao and Liu (2011) has been used. Their data fit according to the following equation, where T is in Kelvin :

$$\theta_{\mathrm{SiO_2-Water}}^{\mathrm{equilibrium}}(T) = -154.2/T^2 - 2.2825/T + 0.5305 \qquad \textbf{Equation 4}$$

4.5.3 δ^{18}O and temperature of ancient oceans

In this chapter we use the δ^{17}O of cherts as an additional parameter to investigate whether ancient ocean water was 'hot' or 'low in δ^{18}O' (see introduction). Both ^{18}O/^{16}O and ^{17}O/^{16}O fractionations between two phases in thermodynamic equilibrium with each other are temperature dependent according to the Equation 2 and Equation 4 discussed above. For every measured silica composition, a set of water compositions that the silica could have been in equilibrium with at different temperatures can be generated in the Δ'^{17}O vs δ'^{18}O triple isotope space (Sharp et al., 2016). These water compositions define an "equilibrium water curve" along which temperature varies from infinity to gradually lower values (Figure 37). At infinite or very high temperature the fractionation between water and silica is negligible and thus both phases have identical oxygen isotope compositions, which is the present triple isotope composition of the chert. Following the temperature dependence of the fractionation factors (Sharp et al., 2016)

the equilibration temperatures get successively lower, with ≈0°C marking the end of the locus in liquid water.

Such equilibrium waters' curves can be constructed for each of our chert samples. If the curve for a sample passes through modern ocean water composition at a realistic temperature then we can conclude that the chert was in equilibrium with seawater at that particular temperature. If a chert has not equilibrated with seawater then the water equilibrium curve for that chert does not pass through the composition of seawater at any temperature but rather intersects meteoric water or a mixed water composition. We attempt to apply this approach to our chert data below.
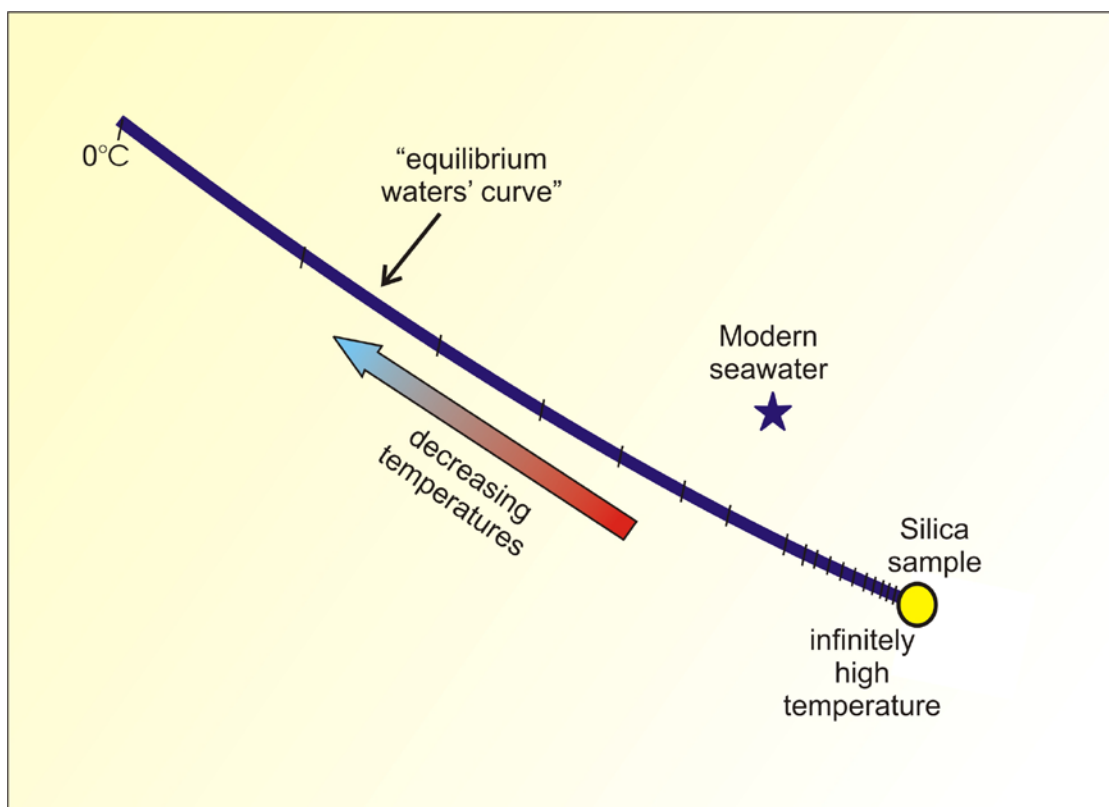
Figure 37 A schematic diagram showing a hypothetical silica (e.g., a chert) composition (yellow circle) in the triple oxygen isotope field as well as water compositions that the silica may be in equilibrium with at different temperatures. These water compositions are defined by the thick blue curve which we call the "equilibrium waters' curve". Equilibrium temperatures vary along the curve, decreasing gradually on moving away from the silica composition towards the upper left along the curve. Thus, a unique set of water compositions can be defined for every measured chert sample.

Marine cherts of different ages have been analyzed, in order to infer the triple

oxygen isotope composition of the ocean water ($\delta^{18}O^{SW}$ and $\Delta'^{17}O^{sw}$ respectively) that these

cherts equilibrated with. Phanerozoic cherts, and possibly also their Precambrian

counterparts, that we find today, have been transformed into microquartz from some form of

amorphous silica after their deposition. In that sense all cherts are products of diagenesis. But as

long as the transformation or re-precipitation occurs at a high seawater : rock ratio, the oxygen

isotopic signature retained in the rock is still that of the seawater it equilibrated. This

information can be coupled with rare earth element patterns to help decipher the depositional

environments of the samples and the oxygen isotopic composition and temperature of waters

they were in equilibrium with.

Contamination of samples by detrital quartz will affect the bulk $\delta^{18}O$ of the samples. Howevr,

petrographic studies show no significant proportions of detrital quartz in the samples. Trace

element concentrations like Ti, Zr, Sc, Hf, and Th (Table 3) have been used in the following

sections to detect terrigenous contamination that would disturb the REE+Y patterns of the

chemical precipitates. Such contamination, except for when detrital quartz is involved, will not

disturb the bulk $\delta^{18}O$ and $\delta^{17}O$ values of the cherts.
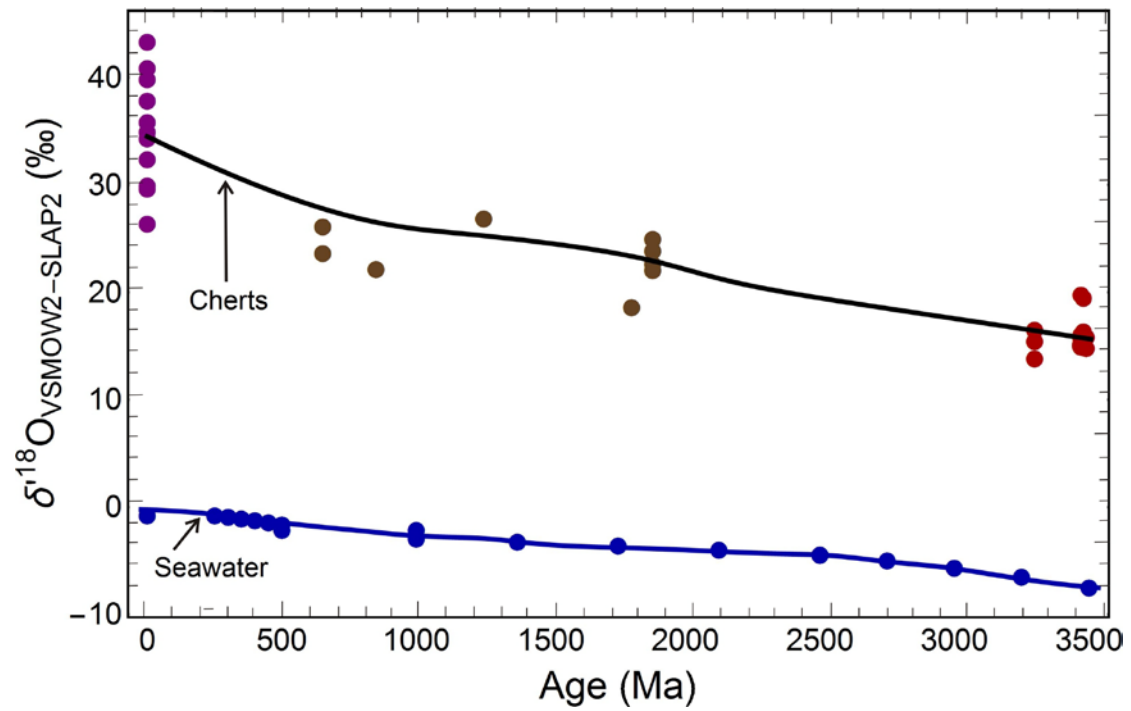
Figure 38 The chert samples in this study show overall decreasing δ'¹⁸O (or δ¹⁸O) values with increasing age. The decreasing δ¹⁸O values of seawater (blue dots) from the mass balance model (Chapter 3 of this thesis) follow the trend of the cherts. The purple dots are the Phanerozoic cherts, the brown dots are the Proterozoic cherts and the red dots are for the Archean chert samples.
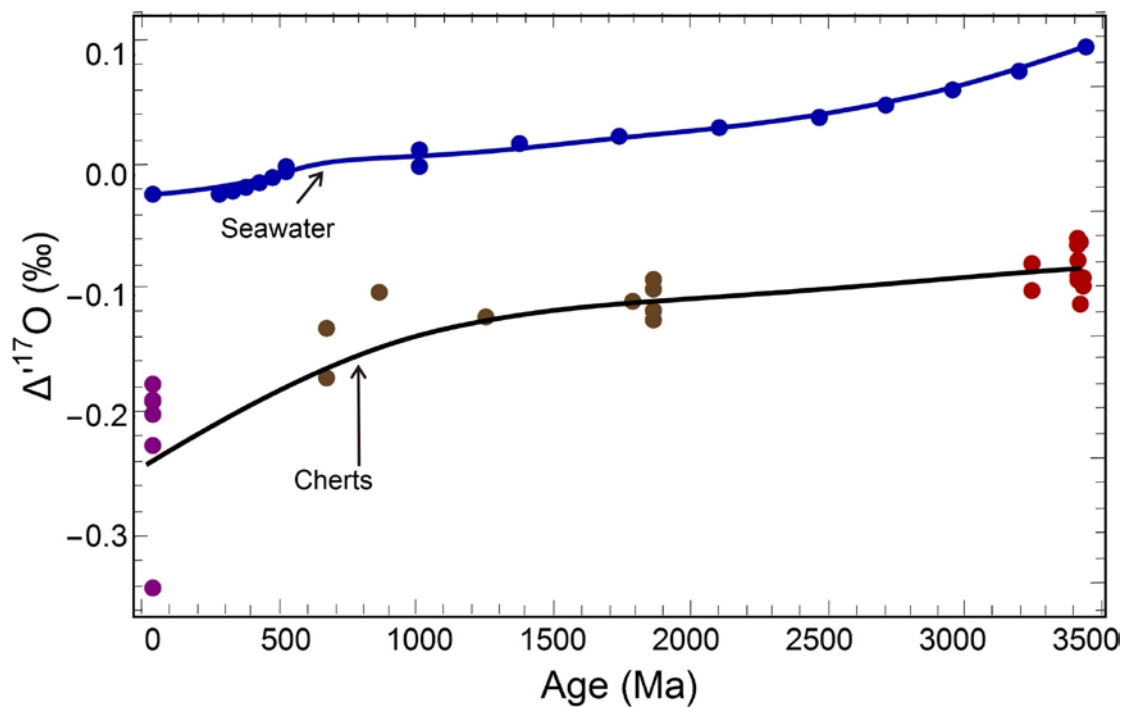
Figure 39 The chert samples in this study show overall increasing Δ'17O values with increasing age. The increasing Δ'17O values of seawater (blue dots) from the mass balance model (Chapter 3 of this thesis) follows the trend of the cherts. The purple dots are the Phanerozoic cherts, the brown dots are the Proterozoic cherts and the red dots are for the Archean chert samples.

In order to decide if the triple oxygen composition of cherts supports a hot or a low $\delta^{18}O$ ocean it is imperative to first estimate what the $\delta^{17}O$ value of a "light $\delta^{18}O$" ocean would be. With this aim, a mass balance model for present and past oceans has been presented in details in Chapter 3. In case of reduced high-T:low-T alteration ratio in the past, seawater triple oxygen isotope decreases from modern day values along a slope of ~0.5154 in the $\delta'^{17}O$ vs $\delta'^{18}O$ space. $\delta^{18}O$ of -8.5‰ and Δ'17O of 0.076‰ is obtained for ancient seawater. This trend shall be used in the following sections to interpret the oxygen isotope composition of the cherts below. Changing seawater triple oxygen isotope composition follows the overall pattern of decreasing $\delta^{18}O$ and increasing Δ'17O of the cherts analyzed in this study (Figure 38 and Figure 39).

The sections below provide a compilation of field associations, petrographic studies, trace element patterns and concentrations, and triple oxygen isotope compositions of the chert

samples in the study. Each group of chert samples (**Error! Reference source not found.**) shall

be discussed separately below.

4.5.3.1 Phanerozoic cherts

4.5.3.1.1   Phanerozoic bedded cherts (PBC)

Our Phanerozoic chert dataset consists of 6 samples. Two of them are bedded marine cherts

(PBC) whereas 4 are nodular cherts (PNC) from different locations in Europe.

The PBC samples – i.e., samples M3 (a helvetic siliceous limestone) and M8 (a radiolarite) have

total REE concentrations of 27 and 68 ppm respectively, which is very high for marine cherts

(maximum 23 ppm and majority samples <9 ppm in Suagahara et al., 2010; up to 9 ppm in Kato

and Nakamure, 2003). This indicates contamination of non-marine origin. It is not possible to use

correlation diagrams such as TiO_2 vs Zr, Th vs Sc, ΣREE vs Ti etc. as indicators of crustal

contamination for this sample group (and most of our other sample groups) because it does not

contain samples from only one single formation. Amongst all chert samples in the study the PBC

samples have highest contents of elements that indicate detrital input (Zr = ~ 25 ppm, Th = 1.54

to 3.4 ppm, Hf = 0.59 to 1.07 ppm, Sc = 1.46 to 6.26 ppm) (Figure 40). This composition indicates

contamination with shale (e.g., Van Kranendonk et al., 2003). Petrographic studies of these two

chert samples also shows detrital quartz. Thus, the trace element signatures of this group of

samples cannot be used to infer their depositional environment or depositing fluid character.

Shale normalized REE+Y patterns (Figure 24) of these two marine samples do not display strong

seawater characteristics which are probably depressed due to presence of impurities. The small

negative Ce anomalies (0.66-0.82) and slight above chondrite Y/Ho ratios (41 for M3 and 29 for

M8) (chondritic Y/Ho molar ratio is 26-27 according to Pack et al., 2007) do point toward a

marine origin, but other features like a strong positive La anomaly and strong LREE depletion are

missing. Contamination obliterating the pure trace element signature of the cherts is expected to

have little effect on the oxygen isotopes signature in them, unless a large amount of detrital
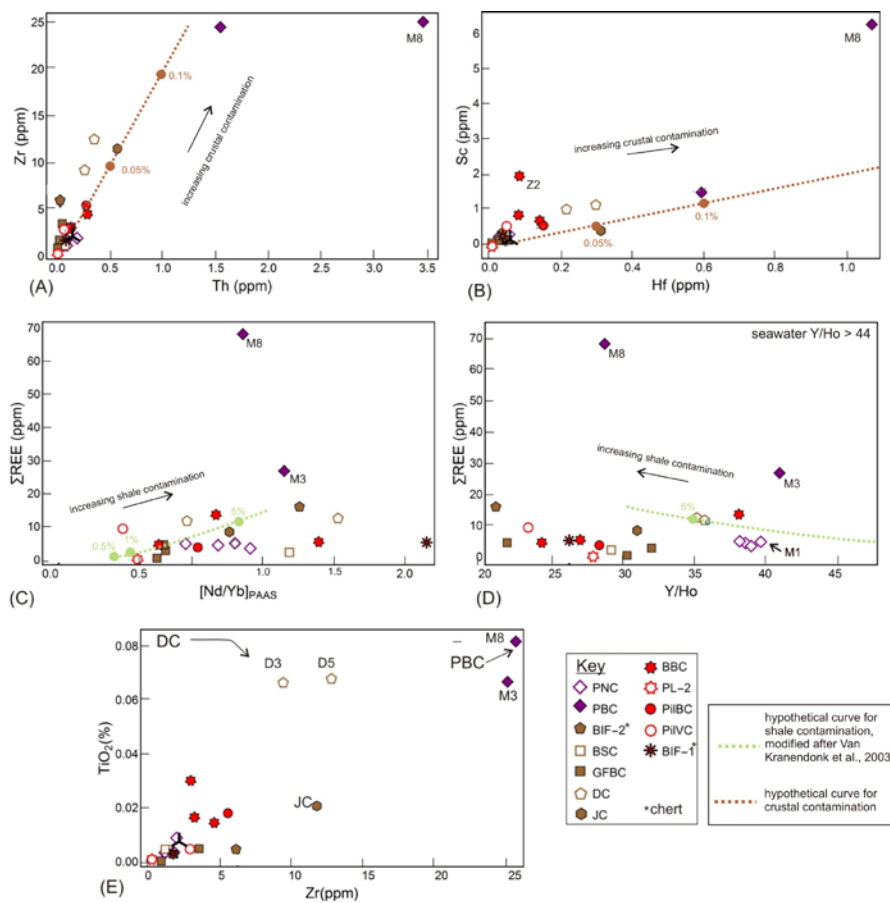
quartz is present.

Figure 40 Plots for determining non-marine contamination within studied cherts. , Plots of incompatible elements (A) Zr vs Th, (B) Sc vs Hf and (C) ΣREE vs [Nd/Yb]$_{PAAS}$ (index for LREE depletion), (E) ΣREE vs Y/Ho molar ratios can be used for detecting shale contamination within the samples (e.g., Van Kranendonk, 2003). No correlation is seen within the samples, which may be partly because almost all of them come from different geological formations (except DC and PilBC). PBC samples have higher total REE contents as well as higher concentrations of all incompatible elements followed by the DC and JC sample groups. These sample groups are contaminated with shale and their trace elements signatures cannot be used to determine their depositing environments. All other sample groups have very low concentrations of incompatible elements but characteristic seawater signatures like strong LREE depletion and high Y/Ho >44 are missing from most sample groups. So, the rest of the sample groups are likely to be contaminated with very small amounts of non-marine material. (E) Plot of TiO$_2$ vs Zr for detecting crustal contamination in samples. The inferences are exactly the same as from the previous four plots – sample groups PBC, DC and JC are highly contaminated whereas the others have minor to no impurities.
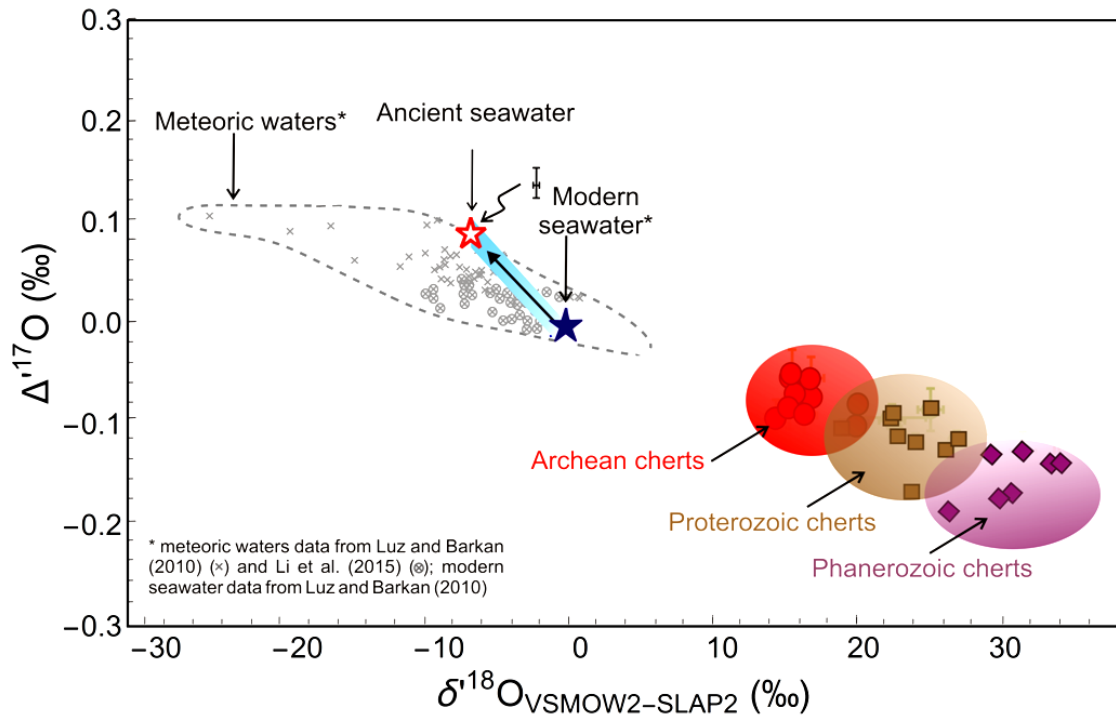
Figure 41 Plot of Δ'¹⁷O vs δ'¹⁸O values of modern seawater (ice-free) (blue solid star), modern meteoric waters (bounded by dashed gray line) and ancient seawater (outcome of mass balance model , when high-T : low-T alteration ratio approaches zero) (red hollow star). The change of δ¹⁸O and Δ'¹⁷O of seawater has been marked by the thick blue strip, taking into account the associated uncertainties on the oxygen isotope values. These values are not distinguishable from a part of the modern meteoric water field. The triple oxygen isotope compositions of the Archean (red), Proterozoic (brown) and Phanerozoic (purple) cherts have been plotted to show their relative positions in the plot.

The outcome of the mass balance model (Chapter 3) needs to be recalled at this point first in order to discuss the chert data further. This is shown in Figure 41. The red hollow star shows the value of ancient seawater if low-T : high-T alteration ratio was close to zero. The blue thick line represents the mass balance model trend, i.e., changing triple oxygen isotope values of seawater over 3.8 b.y. from modern to ancient. The line has a slope of ~0.5154 and the thickness of the line represents uncertainties on δ¹⁸O and Δ'¹⁷O associated with the modeling outcomes. All uncertainties have been calculated using Monte Carlo method of error propagation, assuming a normal distribution of data points, in "Mathematica" software. The values of light δ¹⁸O^{SW}, obtained from the model, are indistinguishable from the modern meteoric waters' field. This

figure is important for discussion of oxygen isotope values of all the following cherts.
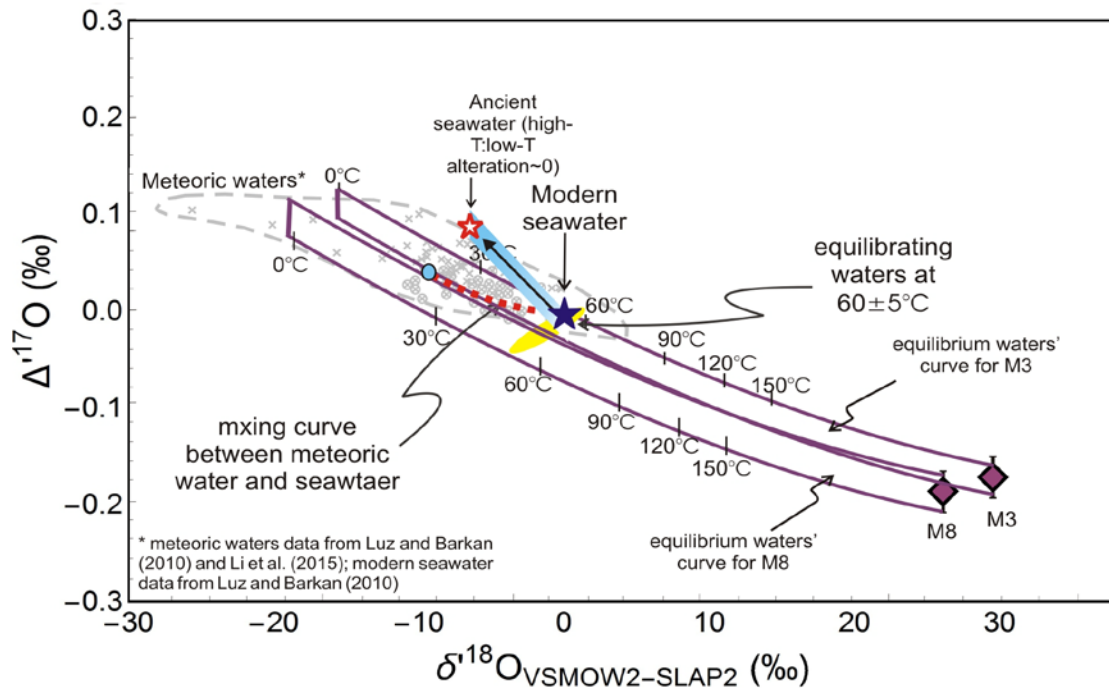
Figure 42 Phanerozoic bedded chert samples (purple diamonds) in Δ'¹⁷O vs δ'¹⁸O space, along with feasible water compositions that the cherts could be in equilibrium with at various temperatures, lying along the purple curves. Sample M3 is in equilibrium with seawater at 60 ± 5°C, in agreement with its marine character. The radiolarite chert M8 could also be in equilibrium with seawater at same temperature but also with a mixture of meteoric and marine waters (red dotted curve) at around 50°C.

Figure 42 shows the PBC samples (purple dots) in Δ'¹⁷O vs δ'¹⁸O space, along with feasible water compositions the cherts could be in equilibrium with at various temperatures. The purple curves show the boundaries (taking into account uncertainties of the δ¹⁸O and Δ'¹⁷O data for the sample) of the two equilibrium waters' curves for the M3 and M8 cherts. The curve for M8 passes by close to seawater but not exactly through it at 60°C. But modern meteoric waters' field (Luz and Barkan, 2010; Li et al., 2015) is also encountered from 0 to ~50°C. In order to estimate the δ¹⁸O of an equilibrating meteoric water, consider a mixture of meteoric water of δ¹⁸O = -10‰ with seawater (along the red dotted curve in Fig...). Sample M8 could then be in equilibrium with a

160

mixture of meteoric and marine waters along this curve, of composition $\delta^{18}O = \sim 5‰$ at $50 \pm 15°C$.

The equilibrium waters' curve corresponding to sample M3 clearly passes through modern seawater at $60 \pm 5°C$. Alternatively, it can be in equilibrium with meteoric waters at lower temperatures around 30 - 50°C. Thus, at least for this sample, solely marine water composition is sufficient to explain the observed $\delta^{17}O$ and $\delta^{18}O$ values. But it is not possible to entirely rule out interaction of these cherts with meteoric waters. It is possible that meteoric waters were involved in post-depositional diagenesis of the sample. The inferred high temperatures of $\sim 50°C$, which was certainly not the open seawater temperature during Carboniferous ($\sim 25°C$, Came et al., 2007), are more likely to be diagenetic temperatures of conversion of biogenic opal-A to opal-CT ($\sim 45°C$ suggested by Kastner, 1981).

At least one sample M3 retains signature of equilibrium with water at temperatures of $\sim 60°C$ (most likely diagenetic temperatures). The other chert M8 shows equilibrium neither with modern (ice-free world) seawater nor with decreasing $\delta^{18}O^{SW}$ values on the curve from the mass balance model, at any temperature. But both cherts could have equilibrated with meteoric waters, lower in $\delta^{18}O$ and $\delta^{17}O$ than modern values, corresponding to a slightly lower $\delta^{18}O^{SW}$ in the Carboniferous at temperatures $\sim 30°C$. However, this situation is not distinguishable from modern equilibration with modern meteoric waters at higher temperatures ($\sim 50°C$). Thus, a meteoric water component is viable for both M8 and M3. The temperature estimates for both cherts are probably diagenetic.

4.5.3.1.2   Phanerozoic nodular cherts (PNC)

4.5.3.1.2.1   Samples M1 and M6

The PNC samples are S-type replacement cherts found as siliceous nodules within carbonate layers. They have very low concentrations (0.03 ppm to 0.2 wt%) of crustal and shale contamination indicators like TiO_2 (~ 0.2 wt%), Zr (~ 1.1-2 ppm), Th (~ 0.06-0.19 ppm), Sc (~ 0.2 ppm) and Hf (~ 0.03 ppm) (Figure 40). However, their REE patterns do not mimic modern seawater REE patterns very well. All samples have very similar shale normalized REE+Y patterns

(Figure 23) show some depressed modern marine seawater features, i.e., small LREE depletion ([Pr/Yb]$_{PAAS}$ and [Sn/Yb]$_{PAAS}$ ranging from 0.71 to 0.90 and 0.9 to 1.10 respectively), slightly superchondritic Y/Ho ratios (38 to 40), small negative Ce anomalies (0.39 to 0.57), indicating that there is a partial marine origin. A mixture of marine and meteoric water is possible (Knauth, 1979). Small amounts of terrestrial contamination can easily obliterate original seawater signatures of marine precipitates (Bolhar et al., 2004), so a minor non-marine contamination or interaction with meteoric waters is suspected.
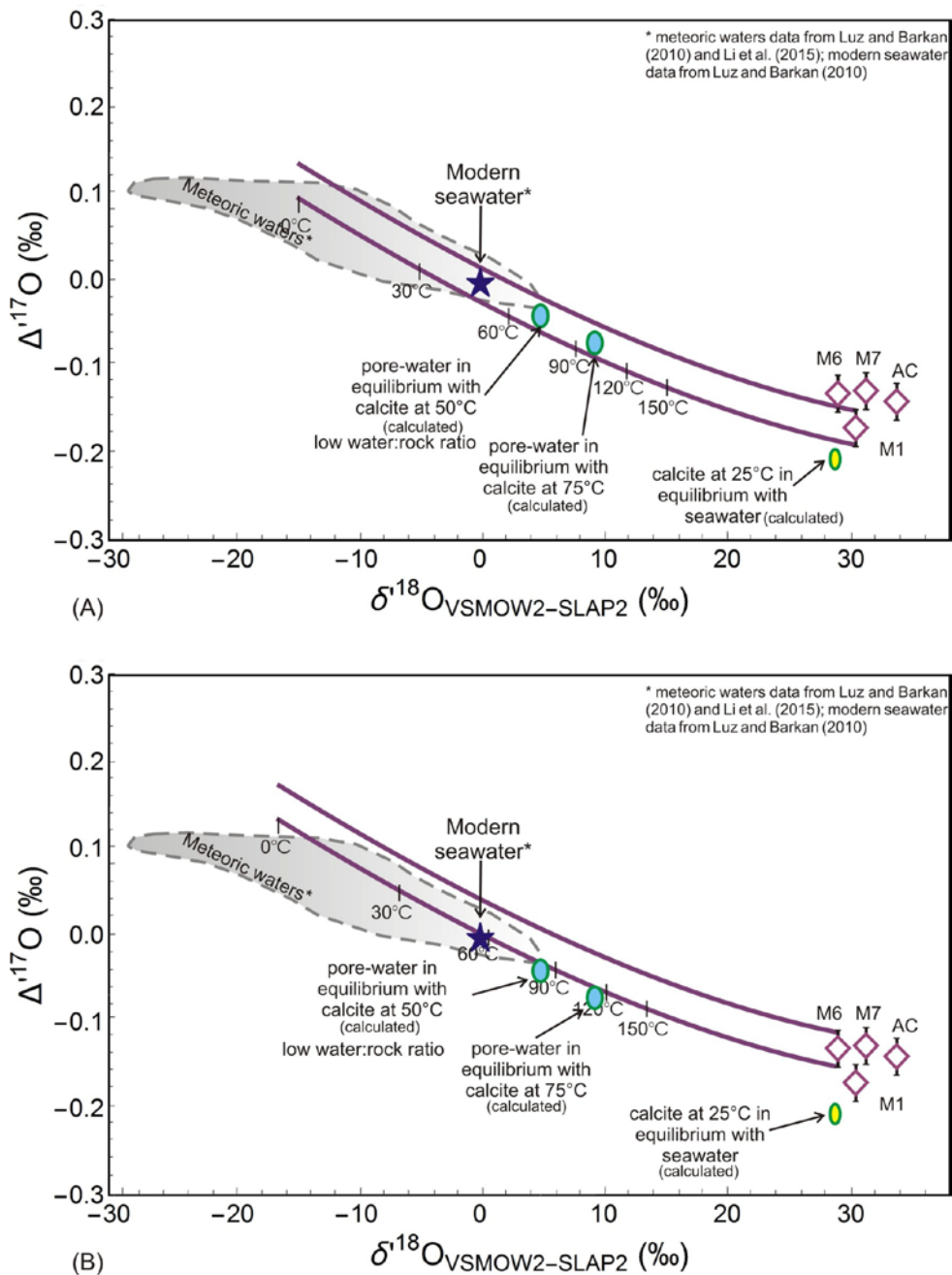
Figure 43 Phanerozoic nodular chert samples M1 and M6 (open diamonds), in Δ'¹⁷O vs δ'¹⁸O space. Feasible water compositions that the cherts could be in equilibrium with, at various temperatures, lie along the area bounded by the purple curves. Cherts M1 and M6 are in equilibrium with modern seawater at ~60°C. They could also be in equilibrium with modelled pore waters (blue dots) inside the host limestone (yellow dot) at higher temperatures. Pore water compositions were modelled using $\alpha_{calcite-H_2O}^{equilibrium}$ (O'Neil et al., 1969) and theoretical $\theta_{SiO_2-H_2O}^{equilibrium}$ values (Cao and Liu, 2011).
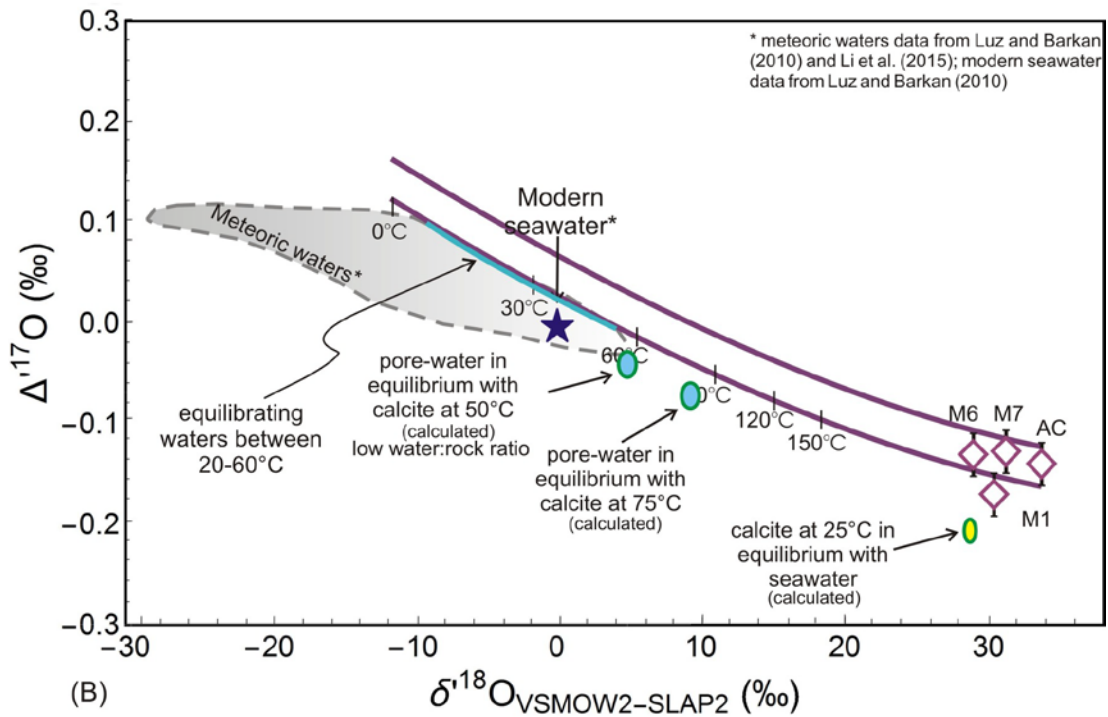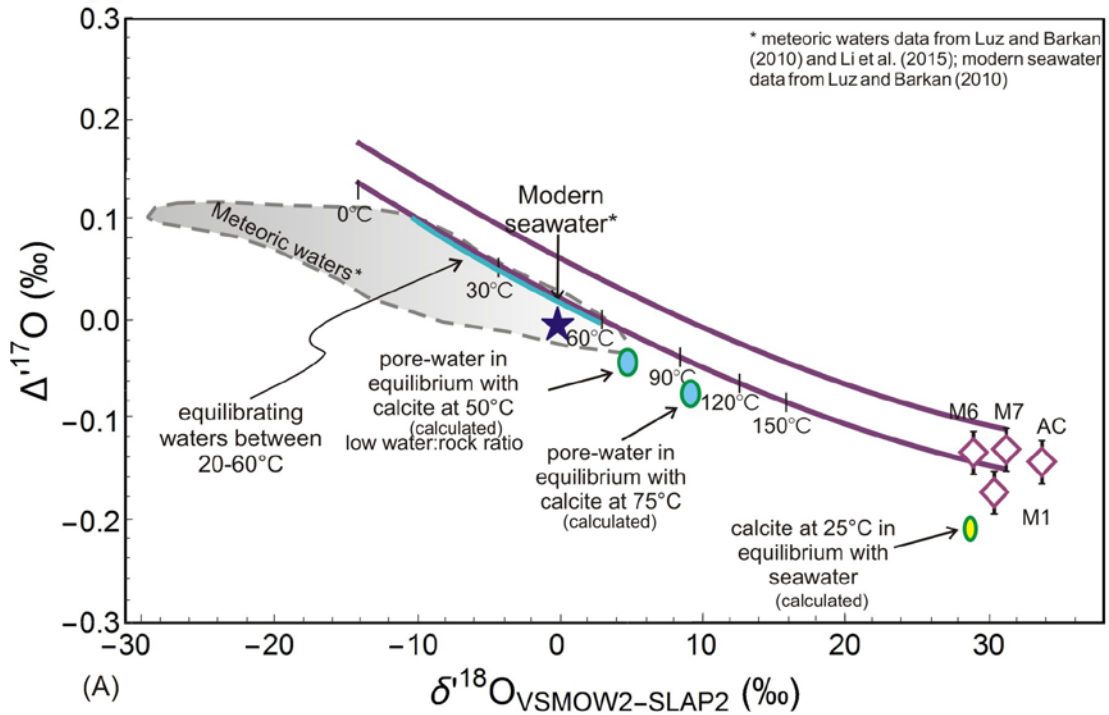
Figure 44 Plot showing Phanerozoic nodular cherts M7 and AC in equilibrium with only a very limited range of meteoric waters in the triple isotope space (denoted by light blue shaded zone in Figure 44) between 20-60°C. The equilibrium water curves for the two samples do not pass through seawater (blue star) or modelled pore water (blue dots) values.

Nodular cherts M1 and M6 are in equilibrium with modern day ocean water at a temperature of 40-60°C as seen in Figure 43. They could potentially also have equilibrated with meteoric waters at slightly lower temperatures, ~30-40°C. Cherts M7 and AC, on the other hand, are in equilibrium with only a very limited range of meteoric waters in the triple isotope space (denoted by light blue shaded zone in Figure 44) between 20-60°C. These are the two possible equilibrium conditions for the samples; below we attempt to resolve between the two.

Knauth and Epstein (1976) observed the involvement of large proportions of meteoric water in the formation of Phanerozoic bedded and nodular cherts studied by them. Most nodular cherts within limestones form by replacing the carbonate and it was postulated by Knauth (1979) that a mixture of meteoric and marine waters, undersaturated in calcite but oversaturated with respect to quartz and opal-CT precipitate such nodule. The study specifically stated that "Cherts forming nearer the marine side of the mixing zone (of marine and meteoric waters) would have isotopic ratios more nearly reflecting precipitation from sea water. Others would show varying degrees of meteoric-water influence". Thus, the findings in this study are in agreement with Knauth (1979).

As an additional step, a set of pore water compositions for these cherts have been modelled. The aim is to find out if the cherts equilibrated with pore waters instead of the meteoric-marine water mixture as postulated earlier (Knauth, 1979). Let us consider a limestone that forms at 25°C from seawater (yellow dot in Figures Figure 43 and Figure 44). Using equilibrium fractionation factor for calcite-water $^{18}O/^{16}O$ fractionation, a $\delta^{18}O$ value of 30.6‰ is calculated at 25°C (Friedman and O'Neil, 1977). For the ^{17}O composition, the theoretically calculated $\theta_{calcite-water}$ = 0.5235 at 25°C by Cao and Liu (2011) is used. Thus, a $\Delta'^{17}O$ = -0.222‰ is determined for the limestone. After precipitation the rock undergoes burial and diagenesis within a closed system, i.e., it gets cut off from seawater and only contains some pore water within interstitial spaces of the rock. The pore water initially has the same composition as seawater. With increasing burial depth and temperatures, the pore waters and the calcite re-equilibrate with each other. Because equilibration now occurs in a close system with low water : rock ratio the pore waters become heavier in $\delta^{18}O$ and have lower $\Delta'^{17}O$ values, and move towards the calcite composition. The $\delta^{18}O$ and $\Delta'^{17}O$ of the calcite remains unchanged because the amount of pore waters is too low to alter the composition of the carbonate. The two blue dots in Figure 43 and Figure 44 represent the

triple isotope compositions of pore waters if reequilibration were to occur at 50°C and 75°C.

Sample M1 chert could have been in equilibrium with either of the two pore water compositions at 70 and 100°C, whereas M6 shows equilibrium with the waters at slightly higher temperatures of 80 and 120°C. For both samples it is not possible to clearly distinguish between equilibrium with meteoric-marine water mixture (between 30-60°C) or pore waters (between 70-120°C). However, the former option is more probable based on opal-CT to microquartz transitioning temperatures (~45°C) and modeled costal regimes for precipitation of such cherts (Knauth, 1979).

Samples M7 and AC do not have their equilibrium waters' curves passing through the modeled pore water compositions at any temperature. If calcite precipitation was considered at lower temperatures, ~15°C (probably more realistic for seawater) then the final pore waters would plot even further away from the equilibrium curves. These two cherts can only be explained by equilibration with meteoric waters between 20-60°C.

4.5.3.2 Proterozoic cherts

4.5.3.2.1   Doushantuo Fmn cherts (DC)

4.5.3.2.1.1   Sample D3

The D3 chert (from Neoproterozoic Era) is a grayish-black microcrystalline dolostone, with chert. It is composed of scanty continuous to fragmented Fe- rich microbial laminations (Fig. 16 A and B) restricted to certain zones of the thin-section. The fragmented nature of the microbial structures suggests that the silicification event could have occurred at a later stage in the diagaenetic history of the rock, when it was already partially lithified. In that case the signature of the silicifying fluid can be potentially retained by the rock, but the timing of the event could be significantly later than the age estimate on the rock (between 635 and 551 Ma estimated from interbedded ash beds by Condon et al., 2005). The sample reacted vigorously with acid during leaching with 0.1N HCl acid indicating presence of large amount of carbonate. It is an S-type chert.

The D3 cherts' REE+Y patterns should not be used to draw inferences about their precipitating solution chemistry because the rock is moderately contaminated with terrigenous material (total REE content 12.5 ppm, TiO_2 0.066 wt%, Zr 9.20 ppm, Sc 0.97 ppm, Hf 0.21 ppm, Th 0.26 ppm)(Table 3) (Figure 40 shows both cherts from the DC group are more contaminated by most other samples in the current study). Nevertheless, their oxygen isotopes may still be useful for deciphering depositing or "last equilibrium" condition in the sedimentary history of the sample.
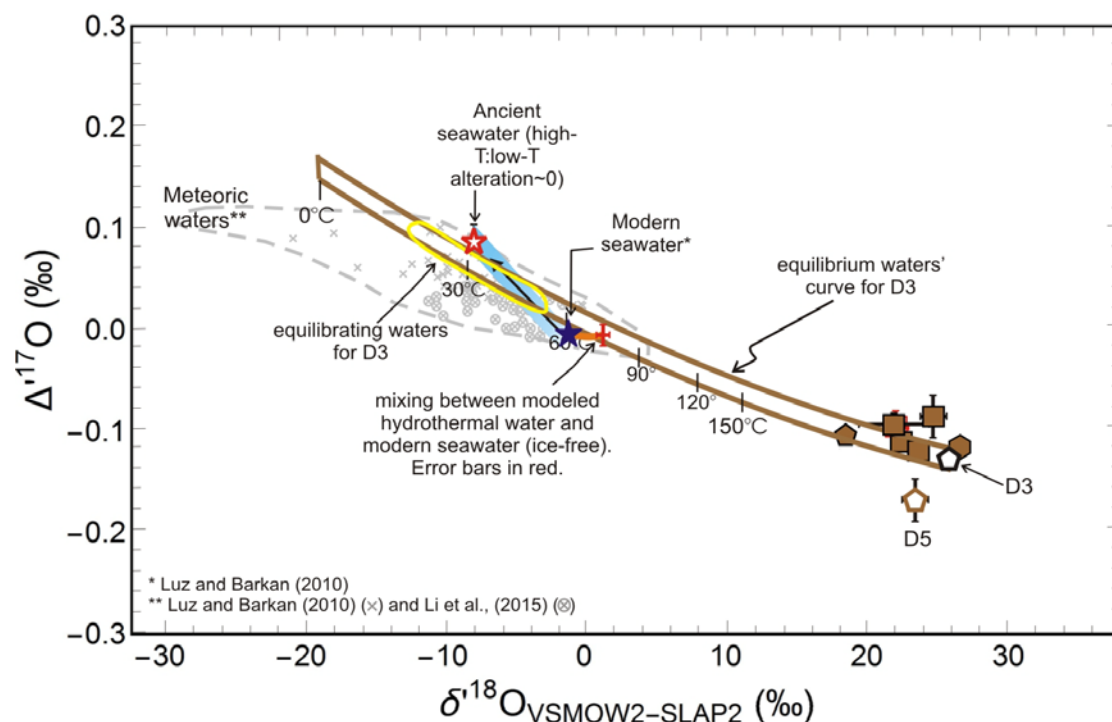
Figure 45 Plot of triple oxygen isotope values of sample D3 and D5 (labeled black and brown symbols respectively, D3 marked black only in this figure for better visibility) along with other Proterozoic samples belonging to the current study (brown symbols). This figure shows the equilibrium waters' curve for sample D3, outlined in brown. The thickness of the curve is due to the uncertainty of oxygen isotope values of D3 (error bars are smaller than size of the symbol). The curve does not pass through modern seawater at any temperature. The yellow outline in the figure outlines the range of modern meteoric waters (-3 to -12‰ $\delta^{18}O$) and temperatures (15-50°C) that the D3 chert may be in equilibrium with. Equilibrium is also possible at ~70°C with mixture of modern hydrothermal fluid (modeled compositions) and seawater.

A large range of equilibrium conditions are possible from the triple oxygen isotope plot showing equilibrium waters' curve (curve with brown outline, the thickness is due to the uncertainties on

167

oxygen isotope measurement) for sample D3 (Figure 45). The yellow outline in the figure outlines the range of waters the chert may potentially be in equilibrium with – from -3 to -12‰ between 50 and 15°C.

Here, the possibility of a hydrothermal signature in the oxygen isotope ratios of the sample is explored. Hydrothermal fluids have $\delta^{18}O$ values in the range 0.5 to 2.3‰ $\delta^{18}O$ (Jean-Baptiste et al., 1997). In order to calculate $\delta^{17}O$ of the hydrothermal fluid, let us consider a $\delta^{18}O$ of +2‰ to start with. Taking a high-T slope of 0.5305 and considering equilibrium with high-T altered oceanic crust samples (Chapter 3, values of sample 504b-50-57: $\delta^{18}O$ = 4.7‰ and $\delta^{17}O$ = 2.484‰) the following value is calculated for the hydrothermal fluid: $\Delta'^{17}O$ = -0.005‰. Upon release from mid-oceanic ridge such a fluid would mix with seawater and the marine sediments are expected to show signatures of this mixed water composition. Such a mixture is shown in Figure 45, marked by a small orange curve. Equilibrium is also possible with such a mixture of modern hydrothermal water and seawater at around 2‰ $\delta^{18}O$ and 70°C temperature. The temperature is low for a hydrothermal fluid, but reasonable for mixtures with cool seawater.

The curve does not pass through modern seawater (ice-free, -1 ± 0.1‰) at any temperature, thus the sample was not in equilibrium with seawater at high T. This information is directly derived from the $\Delta'^{17}O$ values of the chert. If only $\delta^{18}O$ values were considered, equilibrium with seawater could be suspected, thus the $\Delta'^{17}O$ decreases ambiguity for this sample.

4.5.3.2.1.2   Sample D5

This sample is a medium-bedded, laminated, grayish-black, microcrystalline dolostone, with chert from the Neoproterozoic era. An abundance of dark kerogenous material seen in petrographic thin-section but without preservation of microbial structures, possibly indicate a late silification event that destroyed organic structures (Fig. 16 C). Sample D5 is slightly more contaminated with terrestrial material (total REE content 11.7 ppm, TiO2 0.068 wt%, Zr 12.49 ppm, Sc 1.10 ppm, Hf 0.30 ppm, Th 0.35 ppm), than the previous sample (D3) (Table 3). Figure 40 shows that both cherts from the DC group (D3 and D5) are more contaminated than most other samples in the current study. This influences the sample's REE+Y patterns and renders

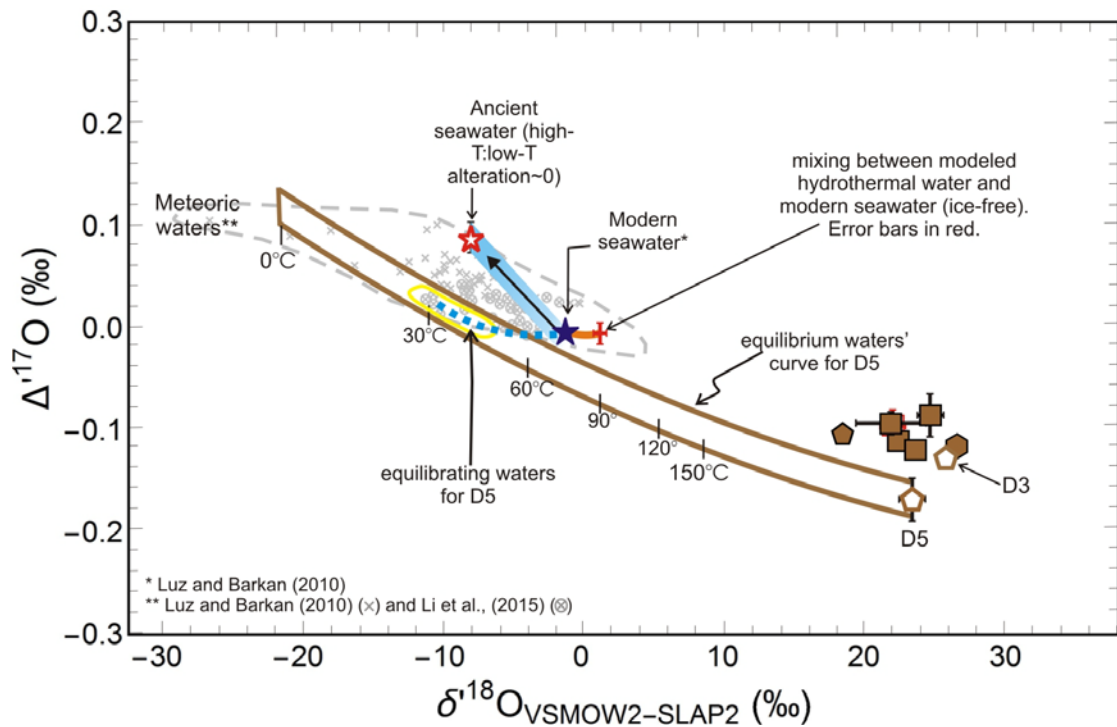them ineffective for inferring depositional fluid characteristics.

Figure 46 Plot of triple oxygen isotope values of sample D3 and D5 (labeled brown symbols) along with other Proterozoic samples belonging to the current study (brown symbols). This figure shows the equilibrium waters' curve for sample D5, outlined in brown. The thickness of the curve is due to the uncertainty of triple oxygen isotope analysis of D5. The curve does not pass through modern seawater at any temperature, excluding equilibration with it. Equilibrium with modeled modern hydrothermal waters is also not possible (mixture of seawater and hydrothermal water marked in orange). The yellow outline in the figure shows the relatively small range of modern meteoric waters (-5 to -12‰ δ^{18}O) and temperatures (40-20°C) that the D5 chert may be in equilibrium with. Equilibrium is also possible with mixture of modern meteoric waters and modern seawater (blue dotted mixing curve) of around -4 to -10‰ δ^{18}O, between 60 and 30°C.

It is evident from Figure 46 that the sample is not in equilibrium with modern seawater (solid blue star) or with a mixture of modern seawater with modern hydrothermal waters (modeled values, orange mixing curve) at any temperature. The sample has a larger error bar on the Δ'^{17}O value compared to the other Proterozoic cherts but the information from its ^{17}O composition still

clearly excludes a modern seawater and hydrothermal fluids' signature.

Figure 46 shows the relatively small range of modern meteoric waters (-5 to -12‰ $\delta^{18}O$) and temperatures (40-20°C) that the D5 chert may be in equilibrium with. Equilibrium is also possible with mixture of modern meteoric waters and modern seawater (blue dotted mixing curve) of around -4 to -10‰ $\delta18O$, between 60 and 30°C.

The equilibrium curve for this sample does not intersect the decreasing $\delta^{18}O^{SW}$ curve obtained from the mass balance model (Ch-3). Hence equilibrium with any low $\delta^{18}O^{SW}$ ocean is not plausible at any temperature. However, if $\delta^{18}O^{SW}$ was slightly lower, say around -2-3‰ not only the corresponding $\Delta'^{17}O^{SW}$ would move up but also the $\Delta'^{17}O$ of meteoric waters would move upwards in the figure. The triple oxygen isotope composition of meteoric waters is coupled to the seawater composition via the process of evaporation. Hence, meteoric waters derived from a low $\delta^{18}O^{SW}$ could also potentially be in equilibrium with D5.

4.5.3.2.2   Dahongyu Formation, Jixian County chert (JC)

4.5.3.2.2.1   Sample JC

The JC chert (from the Mesoproterozoic Era) is a silicified carbonate flat-pebble conglomerate and grainstone, with relict dolomite grains visible in thin section (S-type chert) (Figure 10 and personal study by Stanley Awramik). The sample is contaminated with shale, as reflected by its high Zr (11.5 ppm) (Figure 40 E) and its REE+Y patterns may not reflect true depositional signatures.
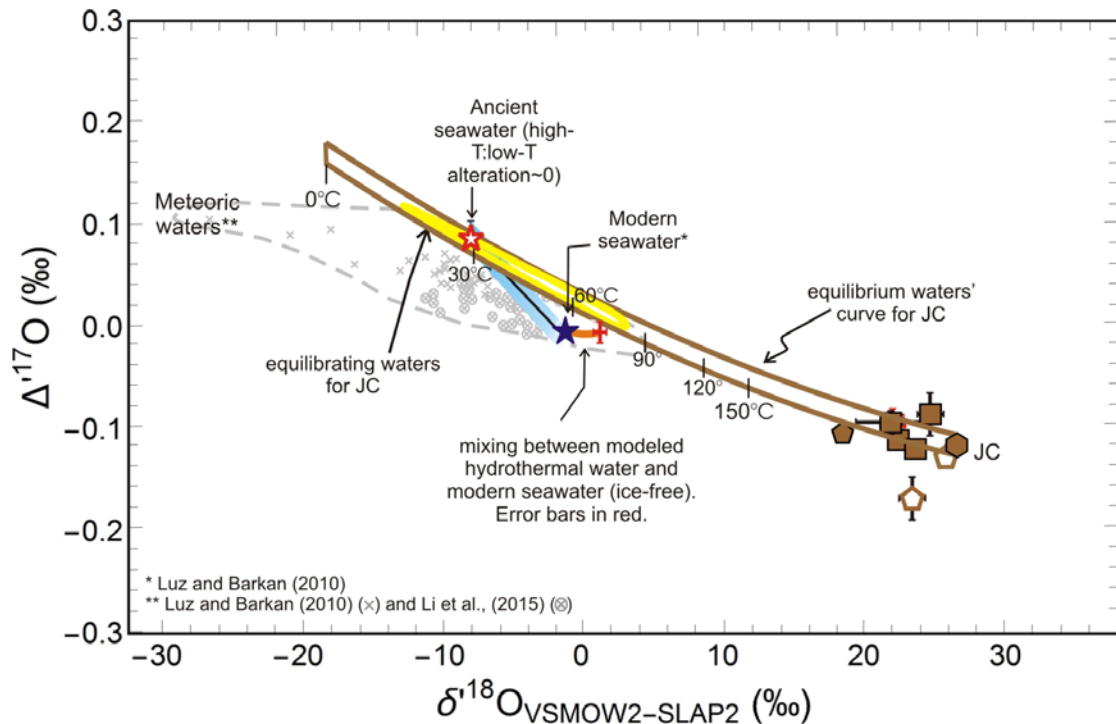
Figure 47 $\Delta'^{17}O$ vs $\delta'^{18}O$ plot of JC chert and its equilibrium waters' curve (thick curve with brown boundaries) shows that the sample could potentially be in equilibrium with a large range of modern meteoric water compositions (+2 to -12‰ $\delta^{18}O$ over temperatures 90-15°C). Equilibration with a light $\delta^{18}O^{SW}$ is also possible as part of the mass balance model curve also falls within the feasible equilibrium waters' range (marked by yellow boundary) (more details can be found in text, section 5.4.3.1).

The oxygen isotope composition of JC suggests (Figure 47) that the sample could be in equilibrium with a large range of modern meteoric water compositions ranging from evaporitic (+2‰ $\delta^{18}O$) to rain or river water (-12‰ $\delta^{18}O$) over temperatures 90-15°C.

Equilibration with a light $\delta^{18}O^{SW}$ is also possible as the mass balance model curve is also intersected over $\delta^{18}O^{SW}$ values from -3‰ to -9‰ by the equilibrium waters' curve for this sample. If $\delta^{18}O^{SW}$ was indeed low, it is more probable that the sample equilibrated with water not as light as -8‰ but rather with -3 to -4‰ $\delta^{18}O^{SW}$, ~0.110 $\Delta'^{17}O^{SW}$ (based on modeling outcomes in this study, Figure 38 and Figure 39).

4.5.3.2.3   Bitter Springs Cherts (BS)

4.5.3.2.4   Sample BS

Only one sample from the Bitter Springs Fmn., Amadeus Basin, Australia has been analyzed in this study– the BSC sample. This is a fine grained, dark coloured sample containing blocky chalcedony cement with rosette patterns inside individual cement blocks and within fenstral structures – features typical of diagenesis. It also shows presence of relict carbonate crystals (Figure 8). This sample shows no LREE depletion ([Pr/Yb]$_{PAAS}$ and [Sm/Yb]$_{PAAS}$ values are 1.34 to 1.79 repectively), negative La/La* of 0.89, small positive Ce/Ce* of 1.05, negative Eu/Eu* of 0.66 and nearly chondritic Y/Ho molar ratio of 29, i.e., no seawater patterns are observed. It classifies as an S-type chert from both petrographic and geochemical evidences (e.g., van den Boorn et al., 2007). The precursor of the rock is likely a carbonate.
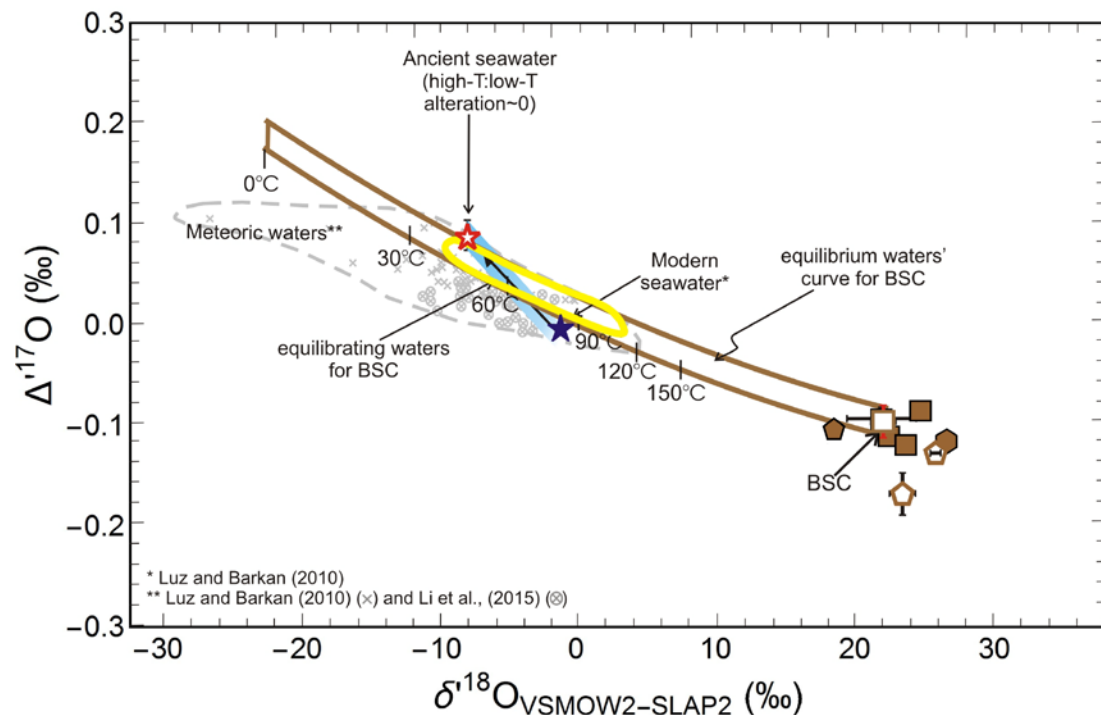
Figure 48 Δ'¹⁷O vs δ'¹⁸O plot for BS chert sample (brown hollow square, with error bars in red, labeled as BSC) from Bitter Springs Fmn., Amadeus Basin, Australia and equilibrium waters' curve for it (bounded by the brown curves). The yellow mark shows the zone of meteoric waters the sample may be in equilibrium with (+2 to --10‰ δ¹⁸O, temperatures 110-40°C). The sample is not in equilibrium with modern ice-free world seawater at any temperature.

The triple oxygen isotopes composition of sample BSC (brown symbol) and its equilibrium waters' curve (bounded by brown curves, taking into account the uncertainty on the measurement of the chert data point) has been plotted in Figure 48. The sample is not in equilibrium with modern seawater at any temperature because the equilibrium curve for the sample passes by ~10 ppm higher than the $\Delta'^{17}O$ of seawater (ice-free). The sample could be in equilibrium with modeled low $\delta^{18}O^{SW}$ values between -7 and -5‰, with $\Delta'^{17}O^{SW}$ between +0.090 and +0.030‰ (temperatures 50-70°C). If seawater $\delta^{18}O$ values varied from -13‰ to present day ice-free values of -1‰ (over last 3.4 Ga, Jaffres et al., 2007), ~850 Ma old seawater could have a $\delta^{18}O$ value as low as -7‰, with temperatures between 10 and 32°C (Jaffres et al., 2007). The mass balance model from the present study (Ch. 3) yields variation of only -8‰ to -1‰ $\delta^{18}O^{SW}$ (and ~0.100‰ to -0.004‰ $\Delta'^{17}O^{SW}$) over the last 3.8 Ga, (red hollow star to blue solid star in Figure 48). According to this, $\delta^{18}O^{SW}$ is expected to be ~ -2‰ (and the $\Delta'^{17}O^{SW}$ ~ 0.014‰) around 850 m.y. ago (Figure 38 and Figure 39). From the model described herein (Ch 3), the ~ BSC sample cannot be in equilibrium with seawater with $\delta^{18}O$ as low as -5‰ and $\Delta'^{17}O$ as high as +0.030‰.

A more feasible range of equilibrium conditions for this chert would be modern day meteoric waters from +2 to -10‰ over a temperature range of 110-40°C. The lack of length-slow chalcedony fibres within the chert (e.g., Folk and Pittman, 1971) supports equilibration with relatively heavy meteoric water (e.g. $\delta^{18}O$ <~-1‰), rather than an evaporitic setting.

4.5.3.2.5   Gunflint bedded cherts – GFBC

4.5.3.2.5.1   Sample GFC-1

The chert is a stromatolitic chert with well preserved microbial laminations suggesting that the rock encountered a silicifying fluid at relatively early stage in its lithification history, while the sediments were still in a semi-soft condition (Carrigan and Cameron,1991; Winter and Knauth, 1992). Such samples are good candidates for seawater history of the past, i.e., in this case ~ 1.88 b.y. (Fralick et al., 2002). This sample was extracted from the hand specimen chert in the form of a mini drill. So, it avoids later formed quartz veins and coarser fenestral quartz, i.e., silica not

related to the deposition of the chert itself. A more precise characterization of the depositing or last equilibrating solution for this sample may, therefore, be possible compared to samples where bulk rock powders have been used. This sample was not available for REE analysis because it was exhausted.
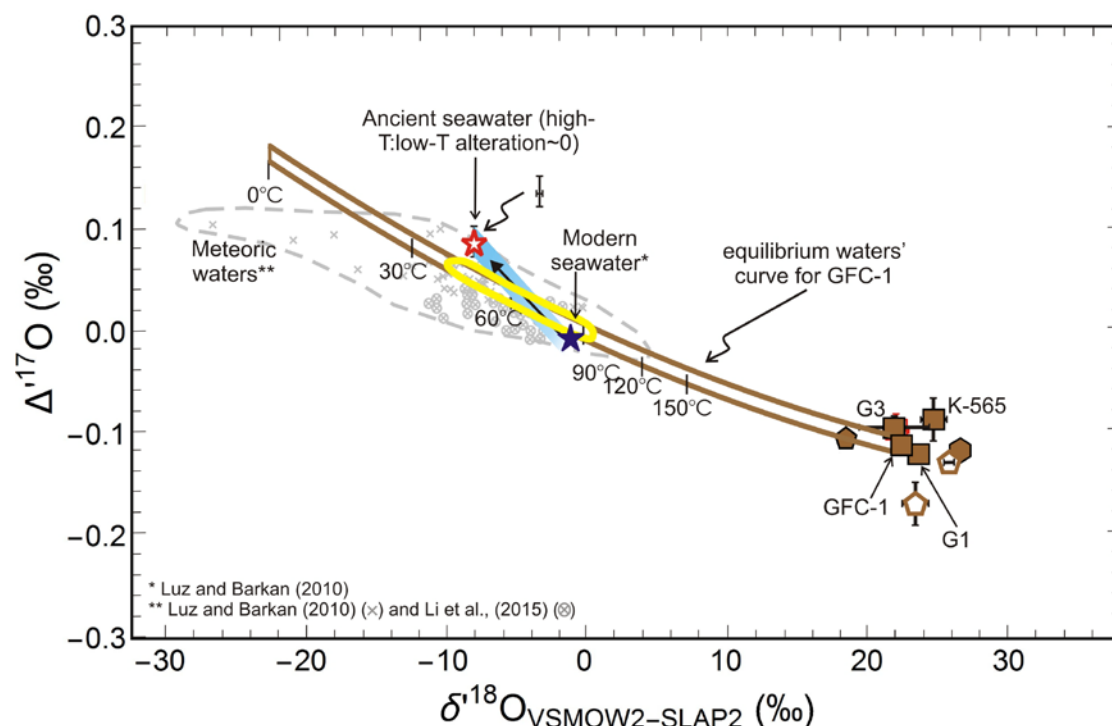
Figure 49 Gunflint bedded cherts (GFBC) in $\Delta'^{17}O$ vs $\delta'^{18}O$ space. The equilibrium waters' curve for the sample GFC-1 is bounded by the brown curves. It is a thick curve taking into account the uncertainties on $\delta'^{18}O$ and $\Delta'^{17}O$ of the data point. The error bars are exactly the size of the symbol for GFC-1 in the y-direction and half the size in the x-direction. The sample may be in equilibrium with a range of possible water compositions (range of water compositions marked in yellow) from modern seawater (blue solid star) (~0‰) at high temperatures (90°C) to waters with lower $\delta^{18}O$ values (~-9‰) at temperatures of 50°C.

Figure 49 shows all Proterozoic samples analyzed in this study (brown symbols), with the Gunflint cherts labeled in $\Delta'^{17}O$ vs $\delta'^{18}O$ space. The size of error bar for Gunflint chert sample GFC-1 is exactly the same as the symbol height on the y-scale and half the symbol width in the x-direction. The brown curves show the boundaries (taking into account uncertainties of the $\delta^{18}O$ and $\Delta'^{17}O$ data for the sample) for the equilibrium waters' curve for the GFC-1 chert. The

equilibrium waters' curve for the GFC-1 chert sample passes through a range of feasible water compositions, including modern seawater and meteoric water field (marked by yellow outline in Figure 49). It also intersects with the mass balance model curve. Overall it is in equilibrium with seawater (0‰) at 90°C to water with $\delta^{18}O \approx$ -9‰ at 50°C. A large part of the meteoric waters' field overlaps with the decreasing $\delta^{18}O$ trend of seawater and for water compositions in this region, making it difficult to distinguish between the two. Meteoric water $\delta^{18}O$ values of -4 to -12‰ are very common today (Dansgaard 1964, Luz and Barkan, 2010; Li et al.,). This implies that a mixture of marine and meteoric waters of present day composition may have been in equilibrium with the chert. Interestingly, temperatures of equilibration are high both for equilibration with meteoric waters/lower $\delta^{18}O$ oceans (50-90°C) as well as with modern seawater (~90°C). Previously, studies supporting low $\delta^{18}O^{SW}$ have used the equilibrium temperatures of marine sediments to suggest much lower temperatures of open seawater (e.g., 10 to 32°C by Jaffres et al. (2007) based on modeling and carbonates' oxygen isotope values. For the sample studied here, however, equilibrium cannot be achieved with any kind of low $\delta^{18}O$ waters at temperatures below 50°C. Therefore this sample either points to a hotter ocean in the past or to a diagenetic signature.

4.5.3.2.5.2   Sample G1

This is also a stromatolitic S-type chert showing excellent preservation of columnar stromatolites with ooids in intercolumnar spaces, within a matrix of microcrystalline quartz. Thus, silicification was contemporaneous with diagenesis (e.g., Winter and Knauth, 1992).
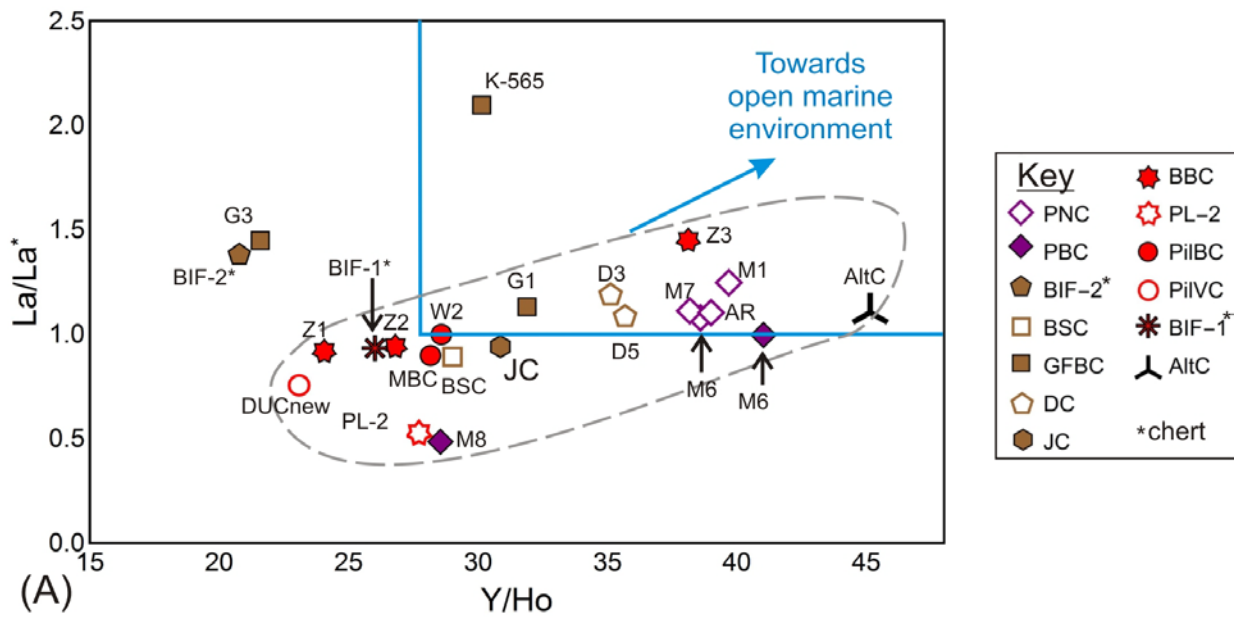
Figure 50 Plot of La anomalies of samples belonging to this study against their Y/Ho ratios. Even though samples come from different geological locations and settings, most of them show a weak correlation (excluding samples BIF-2 chert, G3 and K-565). The correlation suggests small detrital impurities of various amounts within our samples.
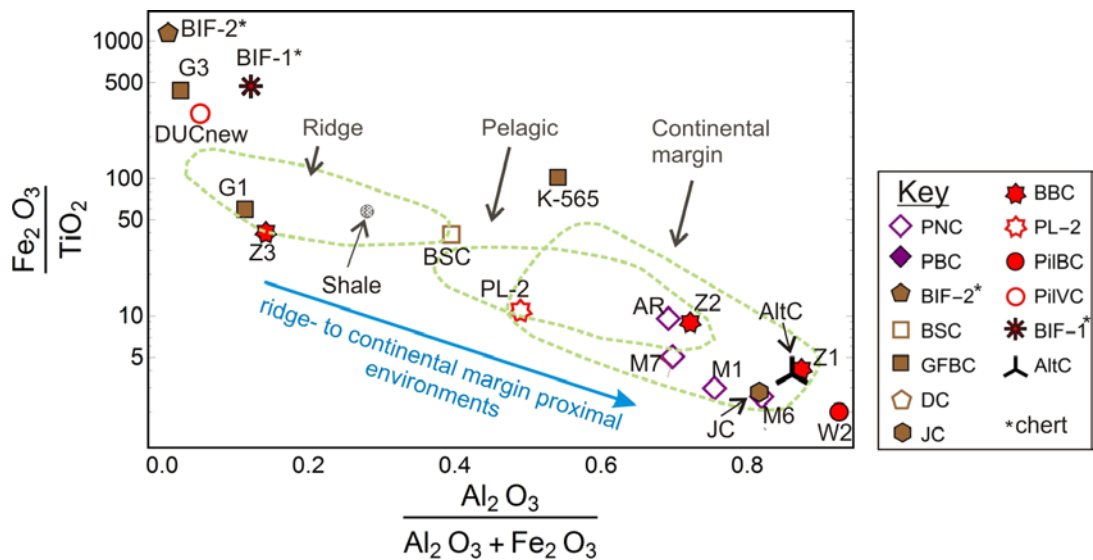

Figure 51 Plot of Fe_2O_3 / TiO_2 vs Al_2O_3/($Al_2O_3 + Fe_2O_3$) The fields in which the ridge-proximal, pelagic and continental margin cherts from Murray (1994) plot have been marked by dashed lines (also in plot (B)). The chert samples G1 and Z3 plot in the field for ridge-proximal cherts,

176

The detrital component of the chert is low (TiO$_2$ ~0.01 wt%, Zr 3.46 ppm, Th 0.05 ppm, Sc 0.11 ppm and Hf 0.05 ppm) and the Y/Ho ratio of 32 is slightly superchondritic. The sample has strong Eu anomaly of 1.68, indicating a hydrothermal input. The hydrothermal imprint on this chert is further confirmed in Figure 51 where according to the classification by Murray (1994) this chert sample falls in the region of "ridge-proximal cherts".

Figure 50 shows a plot of La/La* against Y/Ho ratios of measured cherts in this study and may be used to assess some detrital contamination as well as depositional setting for the samples. The field for superchondritic Y/Ho ratios and positive La anomalies has been bounded by blue lines. Sample G1, along with other cherts, appears to approach values expected for an open marine environment (direction marked with blue arrow). Thus, the data may indicate deposition in a mixed regime, where marine waters with high Y/Ho mix with meteoric or hydrothermal waters having lower Y/Ho values, for e.g., a restricted marine environment (Sugahara et al., 2010).
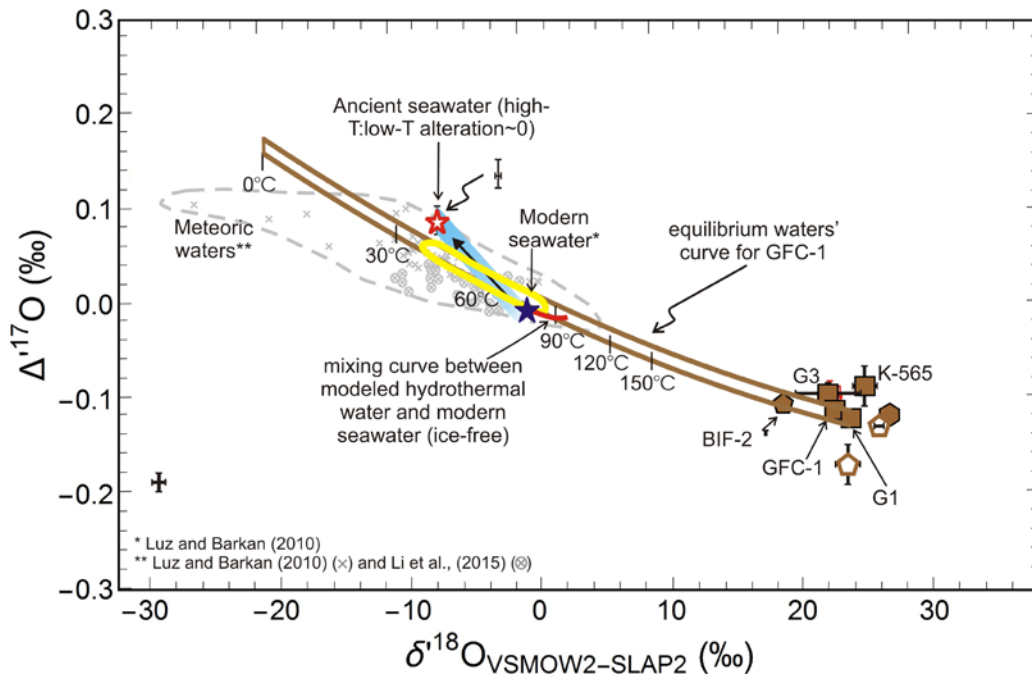
Figure 52 Plot showing equilibrium waters' curve for G1 (bounded by the brown curves). The sample is in equilibrium with meteoric waters from +2 (evaporitic) to -9‰ (rain or river derived) $\delta^{18}O$ or with low $\delta^{18}O$ ancient seawater between -2 and -8‰. The temperatures of equilibration vary between 40-80°C. The sample could also be in equilibrium with a mixture ($\delta^{18}O$ = +2 to 0‰) of modeled hydrothermal water and modern ice-free world seawater at around 90°C. The sample is not in equilibrium with modern ice-free world seawater alone at any temperature.

Marin et al., 2009 performed Ion probe micrometer scale $\delta^{18}O$ analyses on the microquartz of this chert sample and obtained a range of 20 – 25.5‰ $\delta^{18}O$ values (at 20µm scale). They also measured bulk values of the leached sample and obtained +23.2 ± 0.4. This is identical to bulk values of 0.1N HCl leached sample obtained in the current study = 23.940 ± 0.5‰.

The equilibrium waters' curve for the G1 chert sample (bounded by the brown curves is Figure 52) does not pass through modern seawater (ice-free) because it goes through $\Delta'^{17}O$ values that are slightly higher than seawater. This is an example of additional information provided by measuring the $\delta^{17}O$ of a sample. With respect to $\delta^{18}O$ the sample and seawater would be in equilibrium with each other at ~80°C but with the additional $\Delta'^{17}O$ parameter the two are found to be out of equilibrium.

The curve passes through a range of feasible water compositions (marked by yellow outline in

Figure 52) in the meteoric water field (+2 to -9‰) as well as in the mass balance model curve of decreasing $\delta^{18}O$ (-2 to -8‰). The temperatures of equilibration are again quite high, about 40-80°C.

Sample G1 is a hydrothermally affected chert. The chert G1 is seen to be in equilibrium with water compositions on hydrothermal water-seawater mixing curve at $\delta^{18}O$ +2 to 0‰ at temperatures around 90°C.

Summing up, there are two possible sets of equilibrium condition for this chert – either with meteoric waters down to -9‰ $\delta^{18}O$ (indistinguishable from mass balance curve) between 40-80°C or with hydrothermal water of +2 - 0‰ $\delta^{18}O$ at around 90°C.

Marin et al. (2010) observed an isotopic heterogeneity on the micrometer scale (20 – 25.5‰ $\delta^{18}O$ values at 20µm scale) within this sample. The lower $\delta^{18}O$ values (25.5‰) are interpreted to recording the oxygen isotope composition of the amorphous precursor silica (that was precipitated in equilibrium with seawater at that time). The higher $\delta^{18}O$ values (20‰) are interpreted to reflect the temperature of diagenesis (130-170°C). Marin et al. (2010) calculated, via modelling, a final seawater temperature between 37 to 52°C and considered this sample unsuitable for inferring seawater temperatures. With the technique used in this study such high temperatures (130-170°C) are not obtained.

4.5.3.2.5.3   Sample G3

The G3 chert sample is very similar to the previous sample G1, in that it is a stromatolitic chert with excellent preserved microbial laminations. Thus, early silicification, contemporaneous with diagenesis is true for this S-type chert too. The laminations are found within a groundmass of only microquartz, small amount of mesoquartz, but no macroquartz. In contrast to G1 sample G3 lacks oolitic components. In terms of trace element compositions, the sample displays a small positive Eu anomaly (1.40) which indicates that it comprises silica from a hydrothermal source. Detrital components are present in very minor amounts (TiO$_2$ ~0.003 wt%, Zr 1.74 ppm, Th 0.02 ppm, Sc 0.08 ppm and Hf 0.02 ppm) and are not expected to disturb the original REE+Y patterns. The amounts are less than that in G1. However, G3 has a sub-chondritic Y/Ho ratio of 22, in

contrast to slightly superchondritic values of G1 - this is consistent with a hydrothermal REE source.
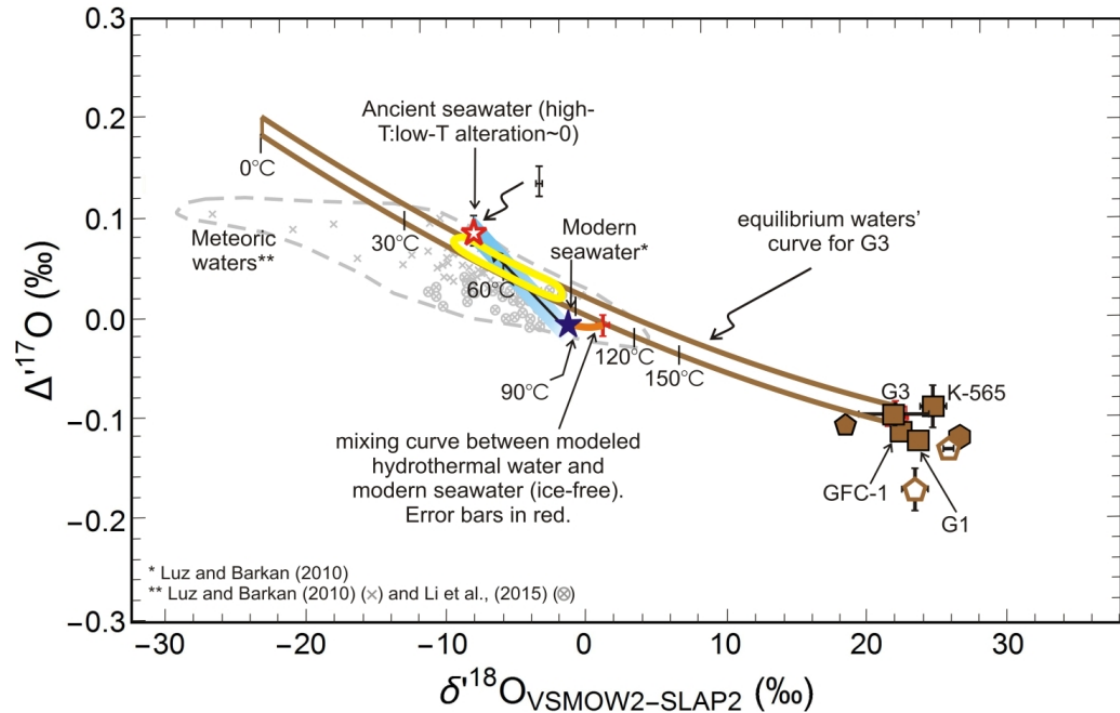

Figure 53 Plot of equilibrium waters' curve for G3 (bounded by the brown curves) in $\Delta'^{17}O$ vs $\delta'^{18}O$ space. The G3 chert may be in equilibrium with modern meteoric waters (-1 to -7‰ $\delta^{18}O$, temperatures 85-45°C), modeled ancient seawater (-3 and -7‰ $\delta^{18}O$, temperatures 80-50°C) or with a mixture ($\delta^{18}O$ = +2‰) of modeled hydrothermal water and modern ice-free world seawater at ~ 100°C. The sample is not in equilibrium with modern ice-free world seawater at any temperature.

The triple oxygen isotope signature of this chert and the equilibrium waters' curve (Figure 53) show very multiple possible equilibrium situations. The sample is in equilibrium with meteoric waters from -1 to -7‰ $\delta^{18}O$ (temperatures 85-45°C) or with low $\delta^{18}O$ ancient seawater between -3 and -7‰ (modeled water values, temperature range 80-50°C). The sample could also be in equilibrium with a mixture ($\delta^{18}O$ = +2‰) of modeled hydrothermal water and modern ice-free world seawater at ~ 100°C. The sample is not in equilibrium with modern ice-free world seawater at any temperature.

This is a fine grained black chert from the Gunflint formation. Geochemical analysis shows that this sample comprises negligible amounts of detrital material (TiO$_2$ ~0.0003 wt%, Zr 1.74 ppm, Th 0.02 ppm, Sc 0.08 ppm and Hf 0.02 ppm). This is also the lowest compared to all other cherts in the study (e.g., one order of magnitude lower TiO$_2$ content compared to others). Thus contamination of the REE+Y pattern by a detrital component is insignificant. Sample K-565 shows a pronounced positive Eu anomaly (3.63) and slightly elevated Y/Ho molar ratio (30), both are indicative of a hydrothermal effect on the depositional history of this chert. These values classify it as a C-type chert (van den Boorn et al., 2007, 2010). The chert also displays very high positive La anomaly (2.097), which is an indicator of open ocean conditions (Figure 50).
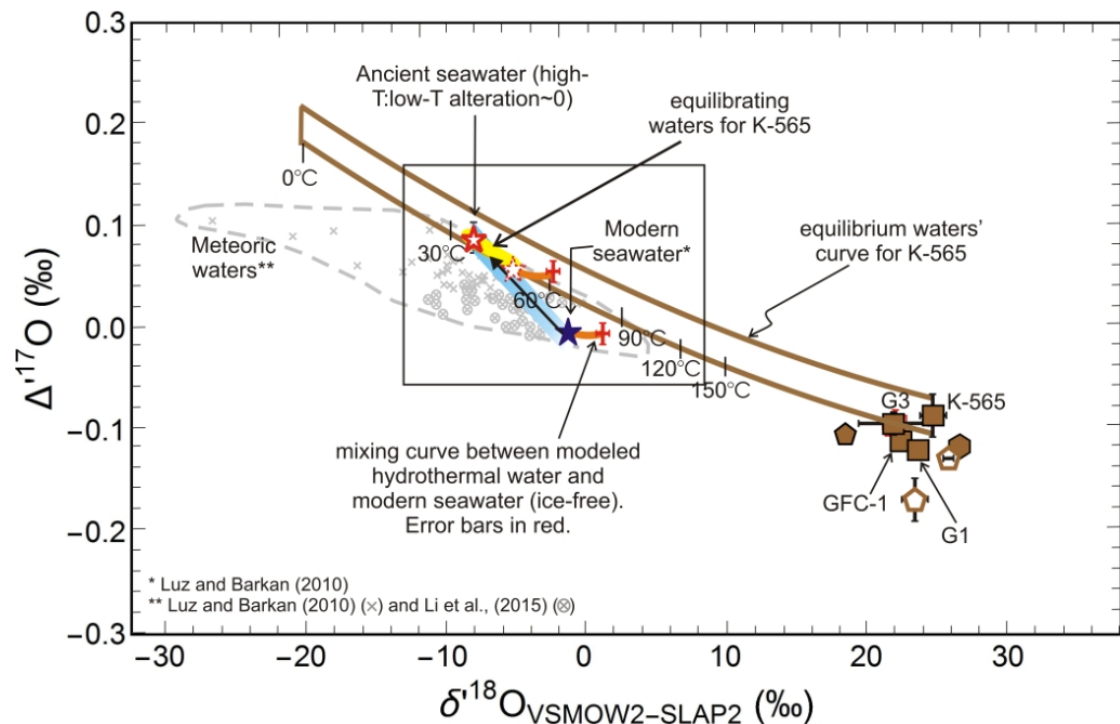

Figure 54 Δ'^{17}O vs δ'^{18}O plot of K-565 chert sample (brown symbol with black error bars) is in equilibrium with meteoric water or low δ^{18}O ancient oceans between -5 to -9‰, over a temperature range of 35-50°C. This is not a feasible equilibrium range for this hydrothermal chert. A magnified view of the region marked by a rectangle in the plot is shown in the next figure.
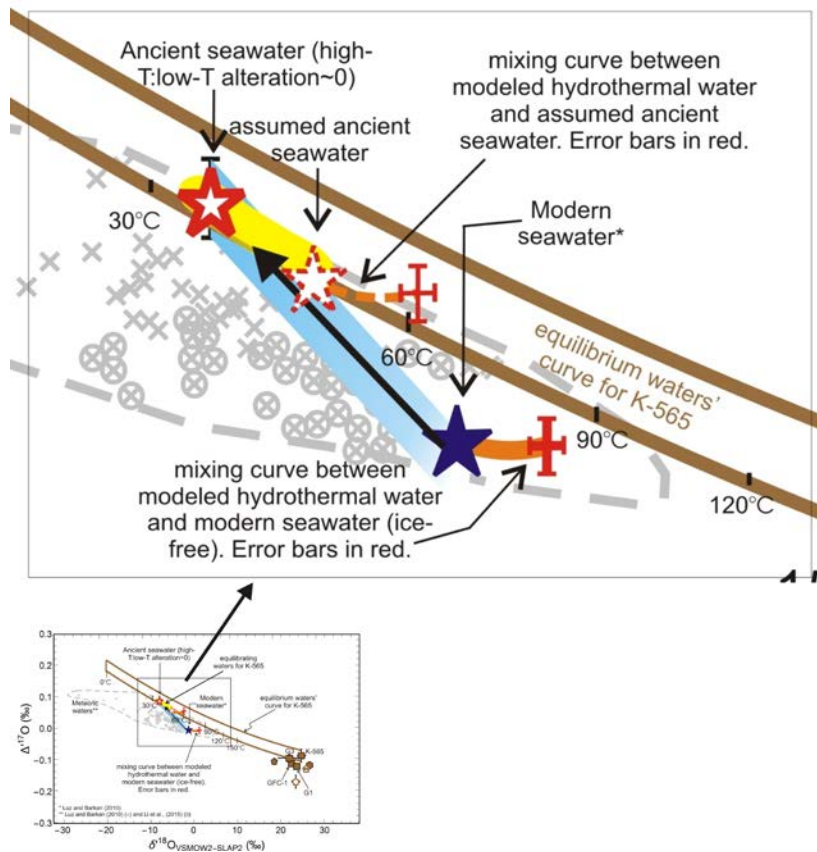
Figure 55 Figure shows a magnification of a part of the previous figure, showing feasible equilibrium conditions for hydrothermal sample K-565. Assuming a light $\delta^{18}O$ seawater of -5‰ (hollow dashed red star), hydrothermal waters of -3‰ with $\Delta'^{17}O$ identical within uncertainty to that of the ancient seawater can be modeled. A mixture of the hydrothermal and marine waters of a lighter $\delta^{18}O$ ocean at temperatures around 40-60°C is the only possible equilibrium solution for this chert sample.

The equilibrium waters' curves for the K-565 chert sample pass through modern meteoric water or low $\delta^{18}O$ ancient oceans between -5 to -9‰, over a temperature range of 35-50°C (yellow zone in Figure 54). However, these are not suitable equilibrium conditions for this particular chert sample based on its trace element evidence (see below).

The K-565 sample shows strong characteristics of a hydrothermal chert in its geochemical signatures, such as very low total REE content (0.536 ppm) and high positive La anomaly (2.097), which is an indicator of marine conditions. These features suggest that a detrital component is insignificant and that the $\delta^{18}O$ of the equilibrating water should be a mixture of hydrothermal

water and seawater (solid orange curve in Figure 55) (unless the chert suffered alteration and complete resetting of microquartz oxygen isotope values). However, the equilibrium curve for the chert does not pass through modern seawater-hydrothermal water mixture. Instead, the case for a lower $\delta^{18}O^{SW}$ in the past is considered next.

Assuming that the oceans 1.88 b.y. ago had $\delta^{18}O$ values of -5‰ (Figure 55), the corresponding ancient hydrothermal water would be ~2‰ heavier, i.e., -3‰. Considering high-T θ values of 0.5305, high-T altered oceanic crust (MORB value remains constant throughout Earth's history, e.g., Kasting et al., 2006 and references therein) in equilibrium with seawater would have the same $\Delta'^{17}O$ value as that of the ancient seawater, i.e., ~0.050‰. If we consider hydrothermal fluids in equilibrium with such an altered rock, they would also have within uncertainty identical $\Delta'^{17}O$ values. An uncertainty of 10 ppm has been assigned. A mixture of ~4‰ $\delta^{18}O$ between such hydrothermal fluids and seawater is a good candidate for equilibrium. Temperature obtained for such equilibrium is ~50°C. These conditions appear to best satisfy the K-565 data.

To sum up, the modeling of ancient hydrothermal fluids for a low $\delta^{18}O$ ocean of ~-5‰ was inspired by sample K-565 because no other feasible equilibrium conditions could be deduced for it. Only this chert, amongst the four studied samples from the Gnflint Fmn. requires the existence of a light $\delta^{18}O$ ancient ocean (~-5‰). Equilibrium curves for all the four individual samples, in fact, also pass through this modeled mixed – water composition (~-4‰ $\delta^{18}O$ and temperatures of ~50°C) and thus, can be a common setting for all the four Gunflint cherts.

4.5.3.2.6　BIF-2

4.5.3.2.6.1　Chert layers from BIF-2

The BIF-2 sample (from the time shortly after the Great Oxygenation Event, i.e., ~1.8 Ga old) from Barberton is dark gray to black chert interbanded with Collenia stromatolites. The chert from the rock (BIF-2-chert) was analyzed in the current study. The BIF-2-chert does not show signs of significant detrital contamination (according to trace element contents, Figure 40). The BIF-2 chert layers display positive La (1.38) and Eu (1.59) anomalies, which indicate marine depositional conditions and a hydrothermal input respectively.
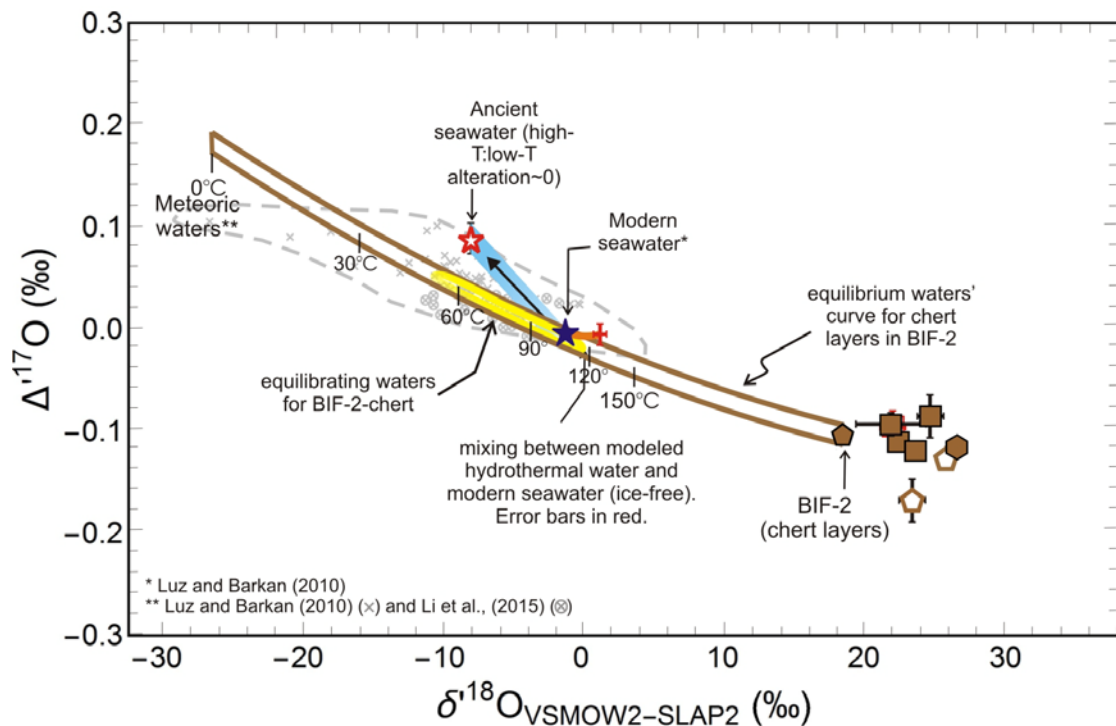
Figure 56 Plot of BIF-2-chert and the feasible equilibrium conditions (yellow outline) in the Δ'¹⁷O vs δ'¹⁸O space. The chert can be in equilibrium with modern seawater or its mixture with hydrothermal waters at 100-120°C. Also a large range of modern meteoric water compositions (-2 to -11‰ δ¹⁸O and 100-50°C) satisfy equilibrium conditions for the chert layers.

The chert layers within the BIF-2 sample yield the lowest $\delta^{18}O$ amongst the Proterozoic samples (i.e., 18.7‰). This could be because it is the oldest Proterozoic sample that has been analyzed or because contamination of iron oxide pulls down the $\delta^{18}O$ values of the chert. Figure 56 shows that the chert is in equilibrium with modern seawater or with a mixture of modern seawater and hydrothermal waters (up to ~2‰ $\delta^{18}O$) at a temperature range of 120-100°C. Alternatively, the BIF-2-chert could also be in equilibrium with modern meteoric waters over the range -2 to -11‰ $\delta^{18}O$ and 100-50°C temperatures.

4.5.3.3 Archean cherts

4.5.3.3.1 Pilbara Bedded Cherts (PilBC)

From this section onwards we move on to the Archean chert samples of the study, ordered roughly in according to increasing age. However, samples of similar geological settings or emplacements have been grouped together (**Error! Reference source not found.**). In the following figures only the samples belonging to the particular group being discussed have been plotted because all samples together plot too close to each other for good visibility.

4.5.3.3.1.1   Sample MBC

This is a chert sample from the white chert layers of the Marble Bar Chert member of the Pilbara Craton, W. Australia. This unit is found in field as thick bedded multicoloured interlayered cherts. Positive Eu anomaly (2.33) classifies it as hydrothermal chert, in agreement with previous studies which use their positive $\delta^{30}Si$ values as additional evidence (van den Boorn et al., 2007). It is a C-type chert (high positive Eu anomaly and slightly superchondritic Y/Ho ratio, van den Boorn et al., 2007, 2010). No significant terrigenous contamination is observed.
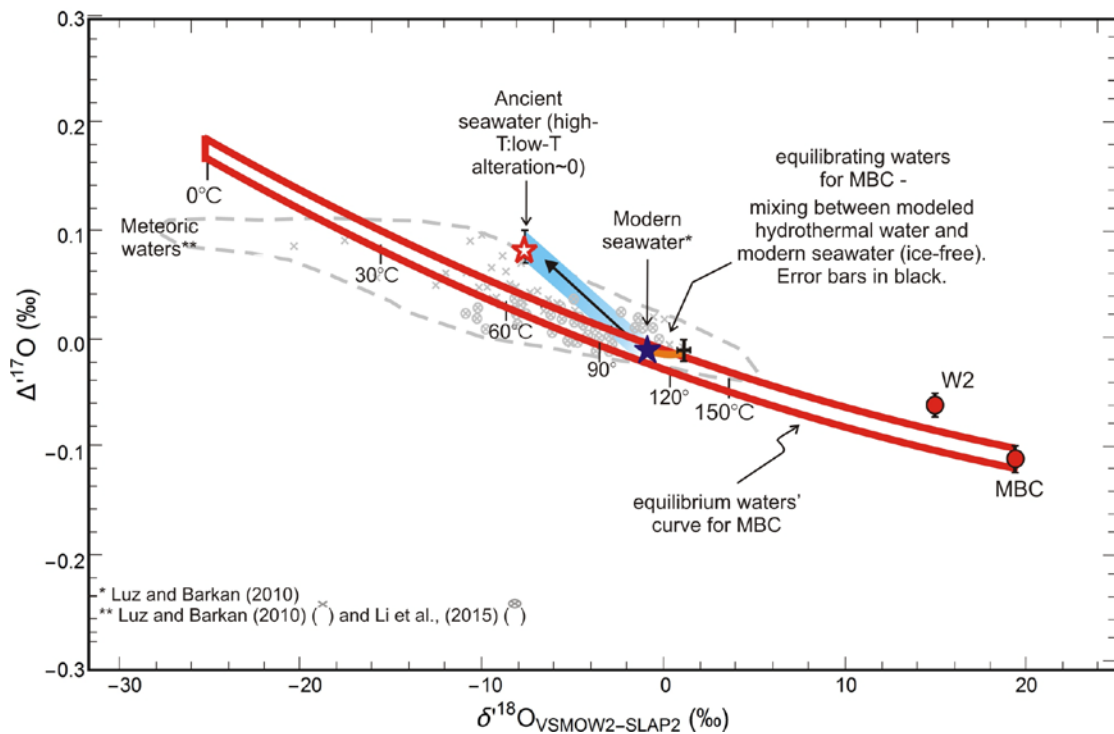
Figure 57 The MBC sample plotted in $\Delta'^{17}O$ vs $\delta'^{18}O$ space along with its corresponding equilibrium waters' curve (red outline) and feasible waters it may have equilibrated with – hydrothermal fluids –modern seawater mixture (orange curve) at ~120°C.

The sample is in equilibrium with modern seawater and a mixture of modern seawater and hydrothermal fluids at ~110°C, as seen in Figure 57 (equilibrium waters' curve marked in red outline). This is consistent with the hydrothermal character of the chert. Stratiform C-cherts at Marble Bar have previously been described as direct silica precipitation on the seafloor due to mixing of hydrothermal fluids with seawater close to seafloor active vent systems at high T (van den Boorn et al., 2007). Rapid silica precipitation upon mixing with cool seawater is thought to be promoted by elevated initial silica concentrations of the hydrothermal fluids. This study also notes the absence of terrigenous components within Marble Bar stratiform cherts and concludes that such active vent systems in the Archean would have operated in regions starved of sediments. These hypotheses are consistent with our results.

The triple oxygen isotopic composition of the cherts allow for alternative possibilities of equilibrium. A large range of modern meteoric waters (-1 to -12‰) over 100-50°C could also explain the triple oxygen isotope composition of the chert. Equilibrium with slightly lower $\delta^{18}O^{SW}$

of ca. -3% at 90°C would also be consistent with the mass balance model.

4.5.3.3.1.2   Sample W2

This sample is a bedded black chert from Dresser Formation in the Pilbara Craton. It shows a small positive Eu anomaly (1.47) indicating hydrothermal origin.
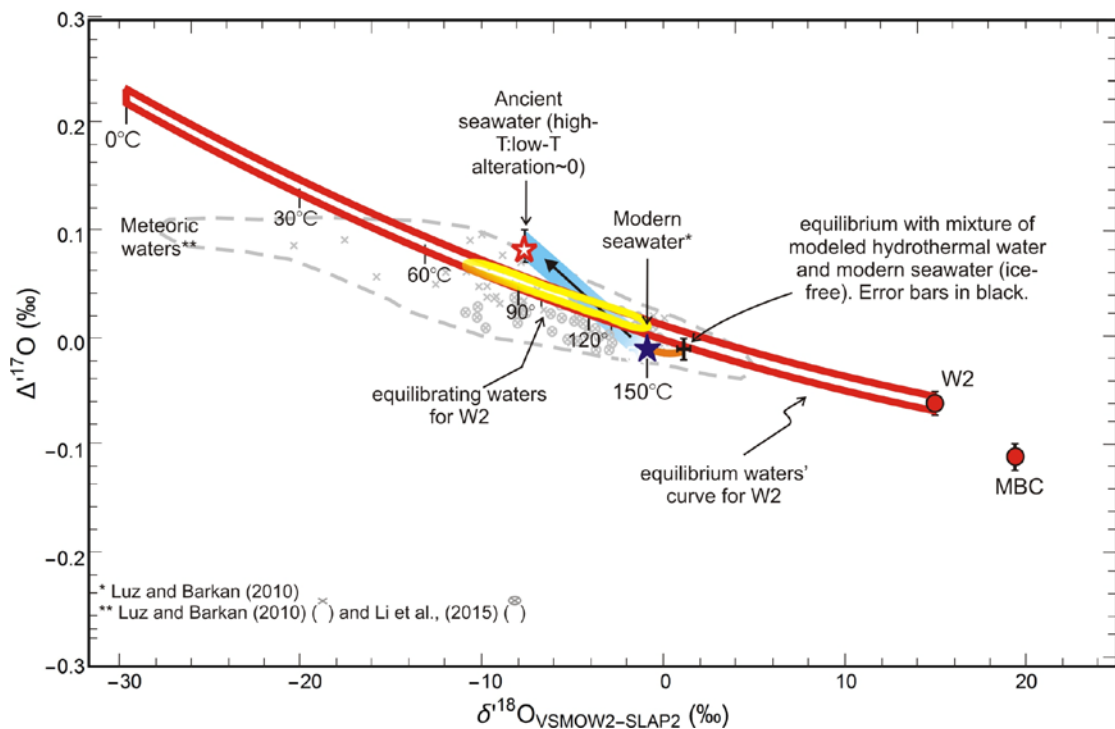
Figure 58 Plot of sample W2 (red symbol) in Δ'¹⁷O vs δ'¹⁸O space along with its corresponding equilibrium waters' curve (red outline) and waters it may have equilibrated with (yellow mark). Because it shows a strong hydrothermal signature , equilibration with hydrothermal fluids (modeled present day compositions) and modern seawater appears more probable (orange curve).

Sample W2 is plotted in Figure 58 along with its equilibrium curve for water compositions (red outlines curve). The curve passes through a range of low δ¹⁸O (-1.5 to -11) and positive Δ'¹⁷O (~0.010-0.070 ppm) water compositions (range marked in yellow) between 150 and 70°C. This could be modern meteoric waters or low δ¹⁸O seawater (up to ~ -7‰) resulting from decreased high-T:low-T ratio in the Archean. The most feasible conditions would be equilibration with

modern seawater and hydrothermal fluids mixture (orange curve) at ~160°C, in accordance with
the hydrothermal event recorded in the sample.

4.5.3.3.1.3   Chert within pillow basalt, Mt. Ada, Pilbara Craton (PL-2)

4.5.3.3.1.4   Sample PL-2

PL-2 is cryptocrystalline silica, in the form of white agate, encased in the interpillow spaces of a
pillow basalt from Mt Ada, Pilbara Craton, Australia. The sample has very low REE concentration,
in the range of a few ppb, which indicates it contains no contamination. It shows high positive
Eu/Eu* of 2.20 and a chondritic Y/Ho ratio of 28, signs of hydrothermal origin.
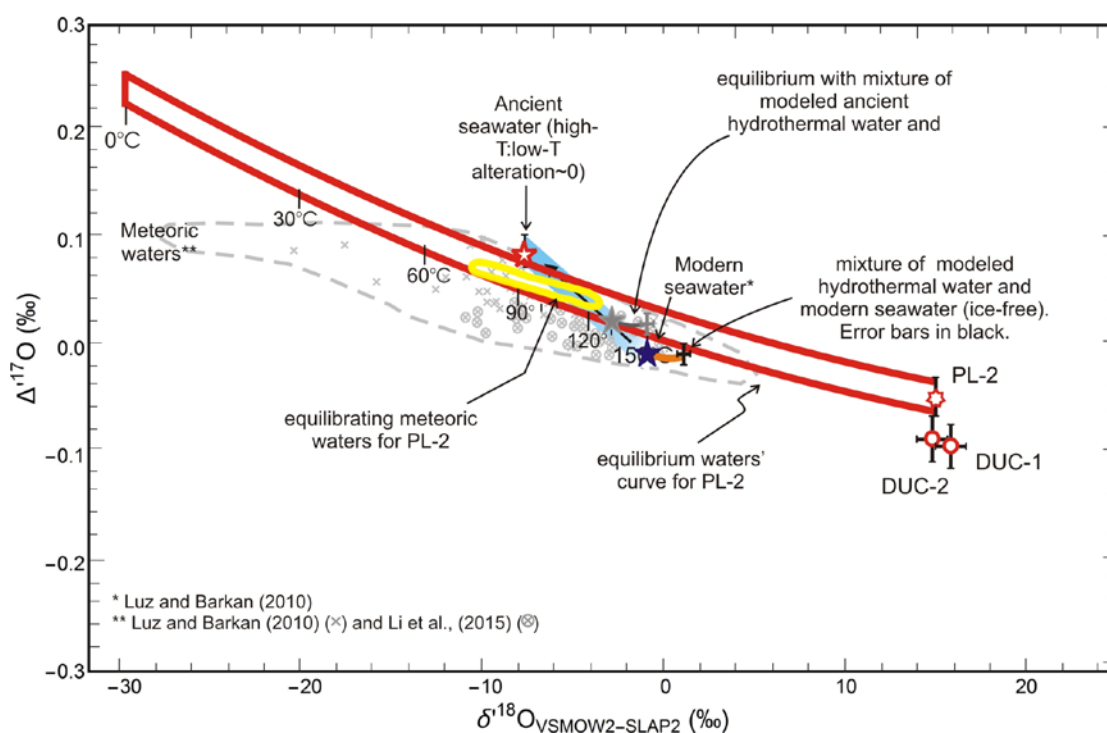

**Figure 59 Samples of two groups are plotted here – PL-2 (with only one sample, PL-2) and PilVC
(vein cherts from Dresser Formation – DUC-1 and DUC-2, but their equilibrium conditions are
described in Figure 60 later on). Waters' equilibrium curve for only PL-2 is shown here. PL-2 is most
likely in equilibrium with hydrothermal – seawater mixture (gray curve) corresponding to a low
$\delta^{18}O^{SW}$ of ~-3‰ (gray solid star) between 120 and 150°C. Equilibration with meteoric waters is also
possible but not probable.**

The possible equilibrium situations for sample PL-2 have been presented in Figure 59 (samples DUC-1 and DUC-2 data points are also plotted along with it). Because of the hydrothermal trace element signature of PL-2 the most probable equilibrium scenario is equilibrium with hydrothermal – seawater mixture (gray curve) corresponding to a low $\delta^{18}O^{SW}$ of ~-3‰ (gray solid star) between 120 and 150°C. The sample supports a slightly lighter $\delta^{18}O^{SW}$ but is not in equilibrium with it at present day-like temperatures.

4.5.3.3.2   Vein cherts from Pilbara Craton (PilVC)

4.5.3.3.2.1   Samples DUC-1 and DUC-2

Both DUC-1 and DUC-2 are cherts from the same sample, at a distance of ~10 cm from each other, belonging to the Dresser Formation. Their representative sample (another vein chert from nearby, same stratigraphic position) shows no positive Eu anomaly, instead shows small negative Ce anomaly, moderate LREE depletion and sub-chondritic Y/Ho ratio.

The possible equilibrium conditions for the vein chert, with both DUC-1 and DUC-2, have been shown in Figure 60 (also data point PL-2 plotted along with it). A mixture of modern hydrothermal fluids and seawater mixture (orange curve), corresponding to $\delta^{18}O$ range of ~-1 to +2‰ between temperatures ~140 and 160°C is the most feasible explanation for this hydrothermal chert sample. Alternatively, equilibrium with a slightly lighter $\delta^{18}O^{SW}$ of ~-3‰ at ~120°C or with modern meteoric waters of $\delta^{18}O$ -2 to -11‰, $\Delta'^{17}O$ -0.020 to 0.040‰ (temperatures 120-70°C) is also possible. This sample indicates that a lower $\delta^{18}O$ ocean could have been possible in the past, but not lower than -3‰.
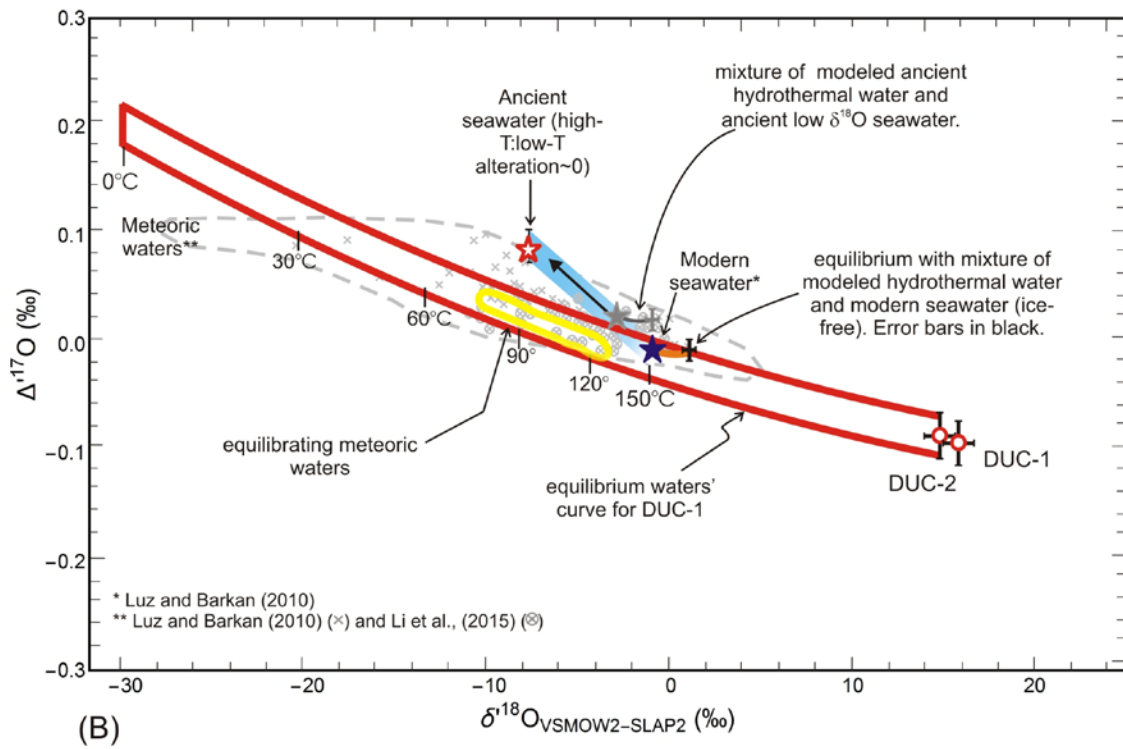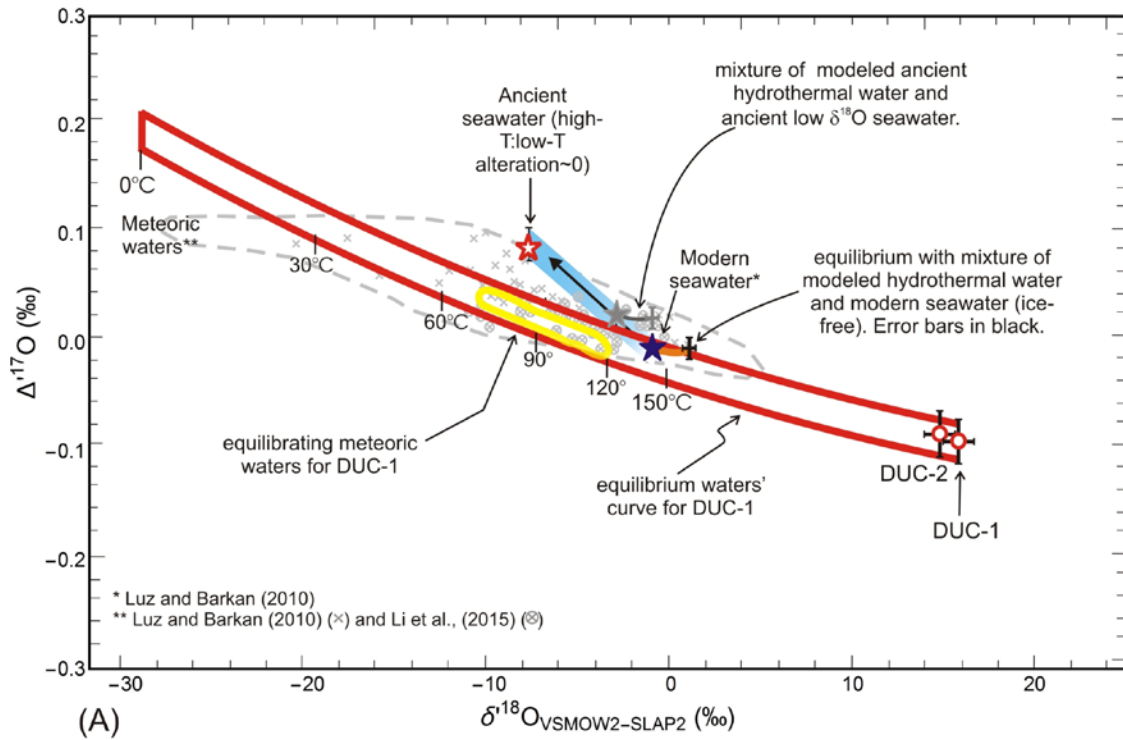
(A)

(B)

190

4.5.3.3.3 Barberton bedded cherts (BBC)

All three samples in this group, Z1, Z2 and Z3 have positive Eu anomalies. They are all possibly of hydrothermal origin.

4.5.3.3.3.1 Sample Z1

This sample is a black chert containing preserved microbial mat laminations relative early silica impregnation of host rock, contemporaneous with diagenesis. It has the smallest Eu anomaly amongst the three samples (1.9). Detrital contamination is negligible.
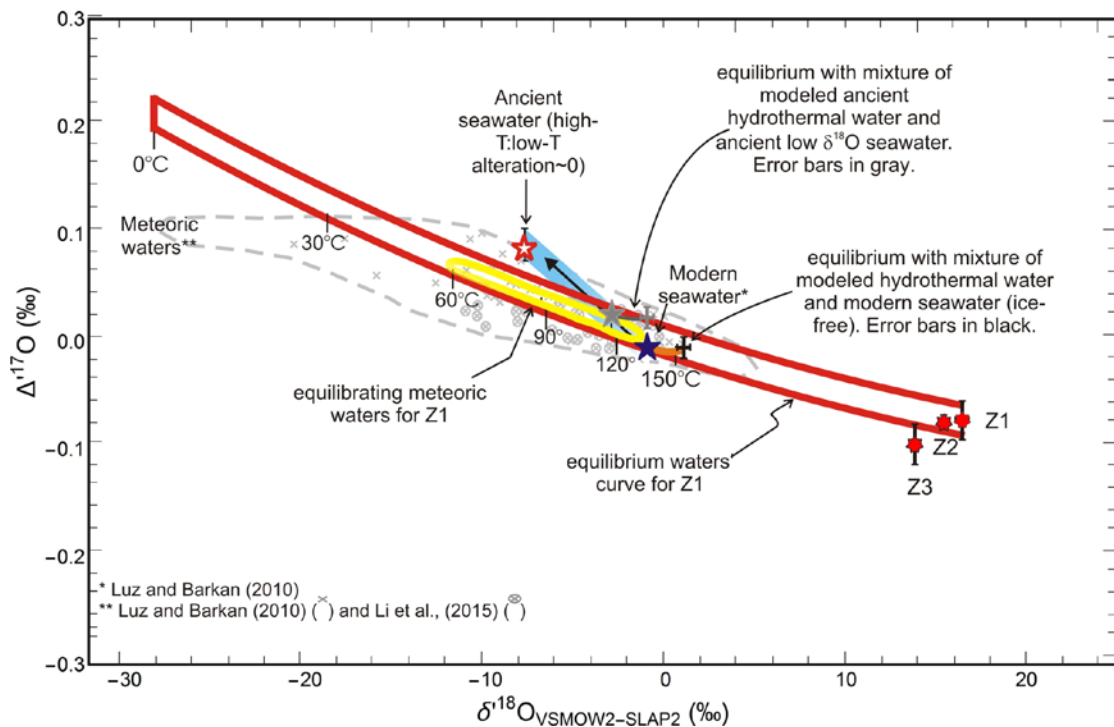
Figure 61 Plot of Δ'17O vs δ'18O of Barberton bedded cherts shows Z1 can be in equilibrium with meteoric waters of modern day (yellow zone). Hydrothermal waters mixing with modern seawater (blue star and orange mixing curve) could be in equilibrium with the chert. Mixing between such ancient light δ18O hydrothermal and seawater (gray solid star and curve) could explain the isotopic composition of Z1 as well.

The Z1 chert shows possible equilibrium with meteoric waters of modern day (over zone marked in yellow in Figure 61) but due to the marine character of this chert this is considered unlikely. Due to its hydrothermal character, equilibrium with hydrothermal waters at elevated temperatures is expected for this chert. A mixture of modern (ice-free world) seawater (blue solid star) and modern day hydrothermal fluids (modeled values, depicted by orange curve and black error bars at end) is feasible at temperatures of (~130-150°C). If $\delta^{18}O^{SW}$ was indeed lower in the Archean than today, then let's assume it plotted along the intersection of the mass balance model curve and equilibrium waters' curve for Z1 (say at point marked by gray solid star in Figure 61, ~-3‰ $\delta^{18}O$). The corresponding hydrothermal water would also have lighter $\delta^{18}O$, higher Δ'17O values than today (gray mixing curve with error bars). Mixing between such ancient light $\delta^{18}O$ hydrothermal and seawater could also explain the isotopic composition of Z2 at

temperatures of ~120-130°C. Minimum $\delta^{18}O^{SW}$ for this sample is ca. -6‰ at equilibration temperatures of ca. 90°C. This $\delta^{18}O^{SW}$ is not as low as suggested by previous studies (e.g.,Jaffres et al., 2007 suggested -13‰ in the Archean).

4.5.3.3.3.2   Sample Z2

This is a fine grained black chert with strong positive Eu anomaly (5.76) indicative of hydrothermal origin.
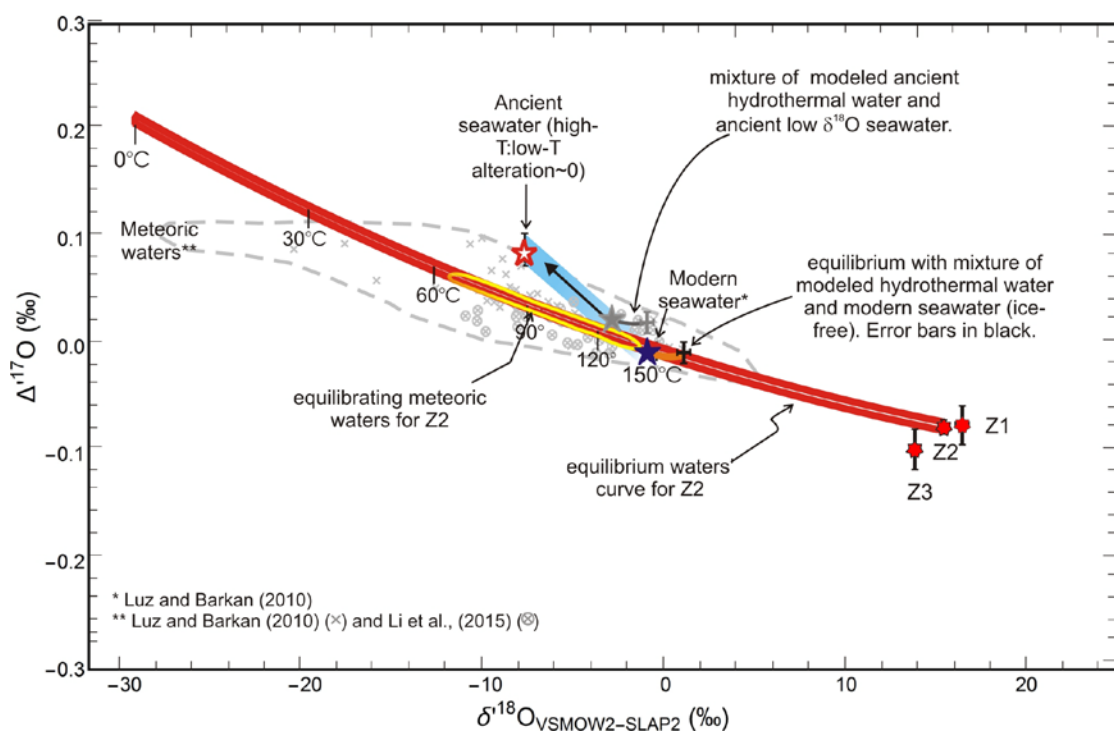
Figure 62 Z2 The triple oxygen isotope composition and equilibrium conditions of Z2 in Δ'^{17}O vs δ'^{18}O space. Equilibrium is possible but not probable with meteoric waters, given that it is most probably a hydrothermal chert. Modern hydrothermal fluid + seawater mixture at ~150°C is the best equilibrium situation for Z2. Slightly depressed δ^{18}O^{SW} values and hydrothermal waters also work for the sample.

The equilibrium situations are similar to Z1. A smaller range of lighter $\delta^{18}O^{SW}$ is covered due to smaller uncertainty in Δ'^{17}O. Most suitable equilibrium conditions are ~150°C with seawater and hydrothermal water mixtures of present day $\delta^{18}O$ and Δ'^{17}O values or slightly lower $\delta^{18}O^{SW}$. The

lowest feasible $\delta^{18}O^{SW}$ for this sample is -2‰, far higher than predicted by Jaffres et al., 2007 (-13‰ in the Archean).

4.5.3.3.3.3   Sample Z3

The sample is a black and gray chert with visibly well preserved stromatolitic laminations, indicating early silicification. The hydrothermal nature of the sample is indicated by positive Eu anomaly of 2.23.
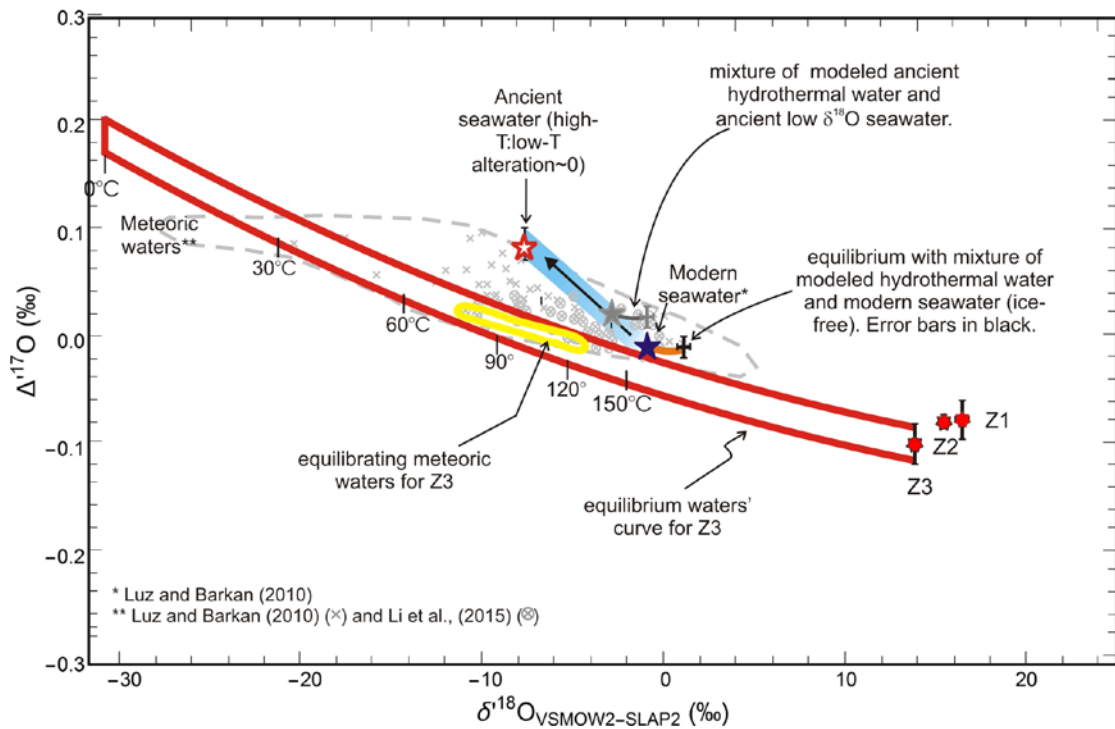
Figure 63 The Z3 chert plotted in Δ'¹⁷O vs δ'¹⁸O space along with its corresponding equilibrium waters' curve (red outline) and feasible waters it may have equilibrated with (yellow). The sample is only in equilibrium with meteoric waters of modern day composition

Z3 chert is only in equilibrium with meteoric waters of modern day composition (Figure 63). The $\delta^{18}O$ values range from -4 to -11‰ whereas the $\Delta'^{17}O$ values range from -0.020 to 0.020‰.. Feasible equilibration temperatures fall between 130 and 70°C. The sample composition cannot be explained in terms of modern seawater or hydrothermal water, or a mixture of both.

4.5.3.3.4 Other samples from the Barberton Greenstone Belt

4.5.3.3.4.1 Sample K-1100

This sample is a "quartz stalactite" sample from the Barberton Greenstone Belt. Trace element data or petrographic details of this chert are not available.

The possible equilibrium conditions for the quartz stalactite have been shown in Figure 64. The equilibrium curve for the sample (red curve) intersects the mass balance model trend between -3 and -6‰, over 90-70°C. This low "$\delta^{18}O$ range" is indistinguishable from modern day meteoric waters. So, the isotopic compositions indicated need not reflect a low $\delta^{18}O$ ocean. Nevertheless, even if they do, the temperatures seen are not of modern day earth near surface values, but rather point toward a diagenetic signature.

A mixture of hydrothermal fluids and seawater mixture (gray curve), corresponding to $\delta^{18}O$ range of ~-3‰, between temperatures 90 and 110°C is also possible for this sample.
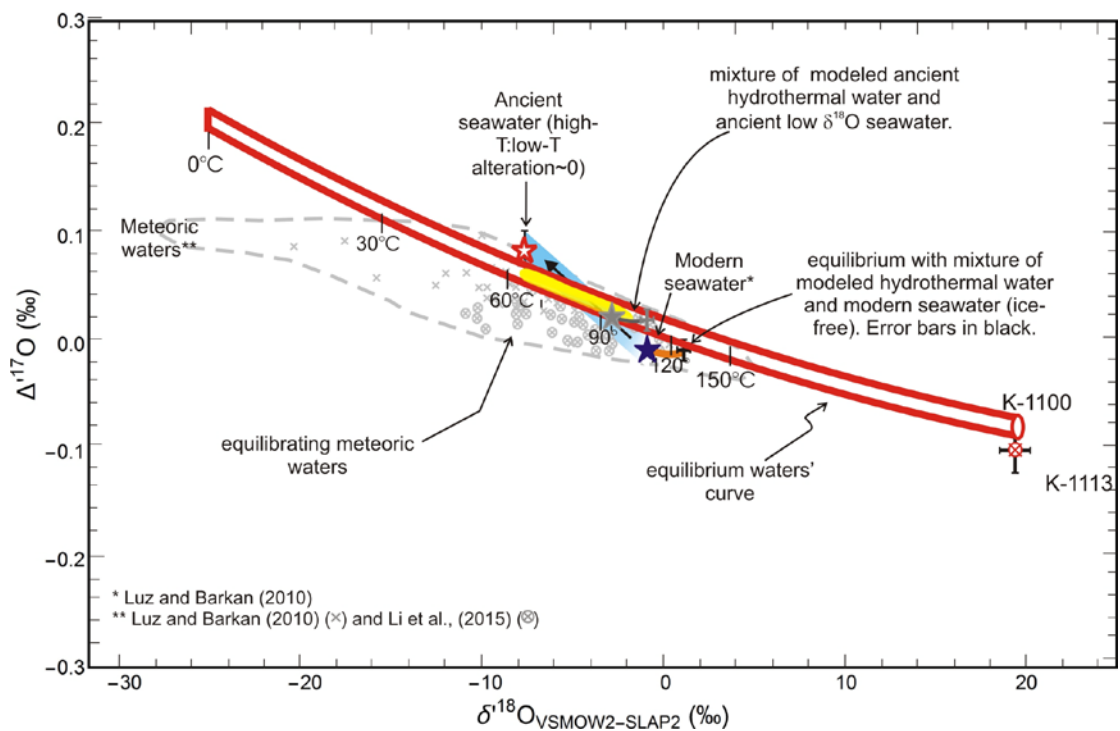
Figure 64 Quartz stalactite sample shows different possible equilibrium conditions in the $\Delta'^{17}O$ vs $\delta'^{18}O$ space. The equilibrium waters' curve for the sample (red curve) intersects the mass balance model trend between -3 and -6‰, over 90-70°C, which is indistinguishable from modern day meteoric waters – thus, not necessarily reflecting a low $\delta^{18}O$ ocean. Alternatively equilibrium with hydrothermal waters corresponding to low $\delta^{18}O$ ocean (~-3‰) is also possible.

This sample is a nodular sample from the Barberton Greenstone Belt. Trace element data or petrographic details of this chert are not available.

The possible equilibrium conditions for the chert have been shown in Figure 65. The equilibrium curve for the sample (red curve) intersects the mass balance model trend between -3 and -6‰, over 90-70°C. This low "$\delta^{18}O$ range" is indistinguishable from modern day meteoric waters. So, the isotopic compositions indicated need not reflect a low $\delta^{18}O$ ocean. Nevertheless, even if they do, the temperatures seen are not of modern day earth near surface values, but rather point toward a diagenetic signature.

A mixture of hydrothermal fluids and seawater mixture of modern day composition and up to -3‰ $\delta^{18}O$ for ancient seawater (orange and gray curves, respectively), satisfy the composition of the chert.

Archean cherts that as heavy as 22‰ have been reported from the Barberton Greenstone Belt and any chert lower than 16‰ have been deemed not likely to provide information about earth surface conditions (Knauth and Lowe, 2003). The K-1100 and K-1113 (~20‰ $\delta^{18}O$) cherts should be good representatives of early earth hydrosphere chemistry and temperature. Sample K-1100 points towards lighter $\delta^{18}O$ (-6‰) values of equilibrating water than K-1113. The latter being a nodular chert would have probably formed from a marine and freshwater mixture, the way Phanerozoic nodular cherts are postulated to have formed (e.g., Knauth and Lowe, 2003). The K-1100 stalactite, on the other hand, might have encountered more meteoric waters and thus retained a lighter $\delta^{18}O$ signature. So, a light $\delta^{18}O^{SW}$ of -3‰ is a suitable scenario for both. However, extremely high temperatures are recorded by both samples (~70°C) even though they appear to be equilibrating with lighter $\delta^{18}O$ waters than present day seawater.
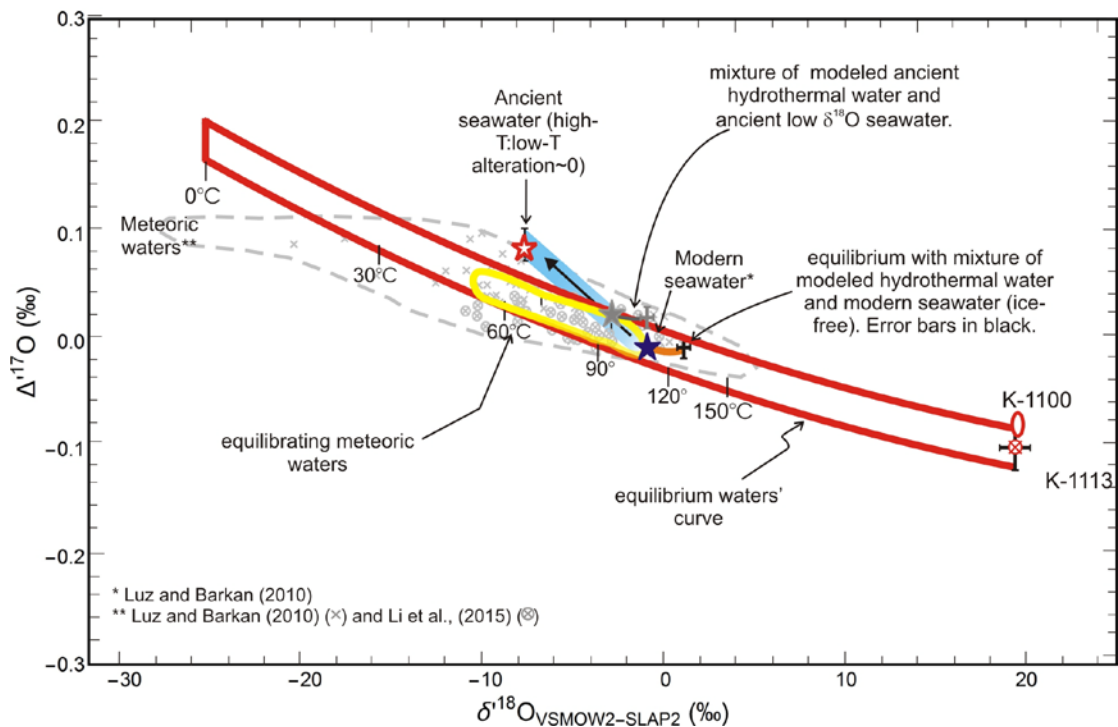
Figure 65 Sample K-1113, a nodular chert in a siderite bed, shows smilar equilibrium conditions as K-1100. It is, however, in equilibrium with δ¹⁸O waters as light as only -3‰ on the mass balance trend. Equilibrium with lower δ¹⁸O water belonging to modern day meteoric water field is possible. Hydrothermal conditions for both a modern ocean (blue star) as well as a lighter -3‰ δ¹⁸O ocean can explain the chert composition.

4.5.3.3.4.3   Sample BIF-1-chert

Chert layers from BIF-1 chert from the Barberton retain hydrothermal signatures, as indicated by their high positive Eu anomaly.

The equilibrium conditions for chert from BIF-1 have been shown in Figure 66. The equilibrium conditions are ambiguous in the sense that the ancient modeled seawater from values and the equilibrium waters' curve for the sample overlap from -3 to -8‰ δ¹⁸O. But these could also be modern meteoric waters. Additionally, equilibrium with hydrothermal waters mixing with -3‰ δ¹⁸O ancient ocean could also be possible. Lower uncertainty in the $\Delta'^{17}O$ value would help better constrain the equilibrium conditions of chert-water, and help distinguish between -3 and -8‰ δ¹⁸O values along the modeled trend from the mass balance model. A decrease in the uncertainty of the mass balance model trend (0.015‰ uncertainty at present) would also help obtain more conclusive results.
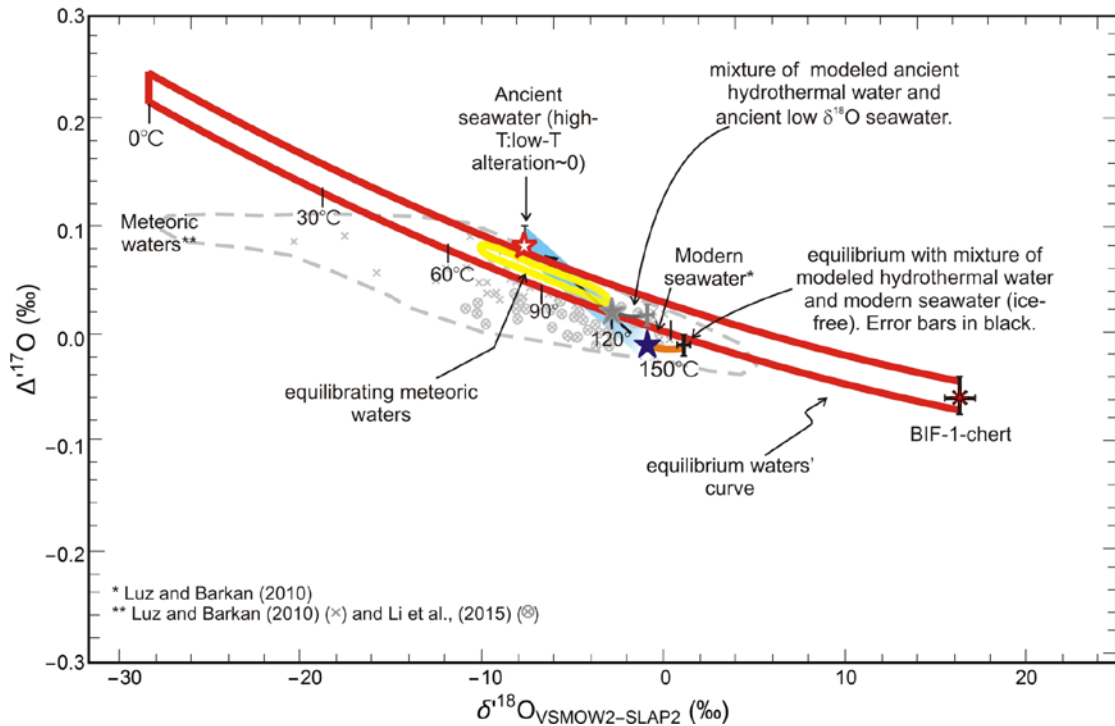
Figure 66 Figure ahows the equilibrium conditions possible for chert layers (red symbol with black borders) of Archean BIF-1 sample from Barberton belt, South Africa. The chert shows equilibrium with ancient modeled seawater from -3 to -8‰, these could also be modern meteoric waters. Equilibrium with hydrothermal waters mixing with -3‰ $\delta^{18}O$ ancient ocean is also possible.

4.6 Summary and Conclusions

Covariation of $\delta'^{18}O$ vs. $\delta'^{17}O$ values of ancient seawater over time, when gradually decreasing the low-T:high-T alteration ration, falls on a slope of 0.515 according to the mass balance model presented in this study. In the reference frame used herein, the corresponding $\Delta'^{17}O$ values of seawater increase with decreasing $\delta'^{18}O$.

The chert samples show a trend of decreasing $\delta^{18}O$ values, decreasing $\delta^{17}O$ and increasing $\Delta'^{17}O$ values with increasing age (from Phanerozoic to Archean). The trend of decreasing $\delta^{18}O^{SW}$ and $\delta^{17}O^{SW}$ (and increasing $\Delta'^{17}O$ with slope 0.5305), obtained in Chapter 3 by gradually decreasing high-T : low-T alteration ratio in the past, follows the trend of changing triple oxygen isotope of the cherts broadly (Figure 38 and Figure 39).

The oxygen isotope values of the Phanerozoic bedded cherts can be explained by modern marine water (M3) or a mixture of modern marine and meteoric waters (for both M3 and M8). The triple oxygen isotopic composition of Phanerozoic nodular cherts is inconsistent with a low-$\delta^{18}O^{SW}$ ocean. The seawater in the Phanerozoic had the same $\delta^{18}O$ as today.

Three Proterozoic cherts (GFC-1, G1 and BIF-2-chert) out of all 10 samples potentially formed in equilibrium with seawater. Respective equilibration temperatures are ~50-100°C with $\delta^{18}O^{SW}$ between 0 to ~-4‰, i.e., slightly lower than present day. Since they are all hydrothermal cherts (as reflected from their positive Eu anomalies) these high temperatures do not necessarily point toward a hotter ocean in the past. These cannot give us information on the average temperature of seawater during their deposition.

A pure seawater origin can be excluded for the other 7 samples based on the additional $\Delta'^{17}O$ parameter in the current study. Judging only by their $\delta^{18}O$ values these cherts could have been interpreted to form from high-T seawater, just like similar chert samples from previous studies (e.g., Winter and Knauth, 1992a; Marin et al., 2010; Cunningham et al., 2012), but the $\Delta'^{17}O$ parameter helps to exclude this possibility for these samples. The REE patterns of the samples also suggest a hydrothermal input (positive Eu anomaly) and open marine regime (superchondritic Y/Ho ratios). So, these samples likely formed in equilibrium with a mixture of hydrothermal water and modern seawater mixtures. A hot Proterozoic ocean is not supported.

Only one Proterozoic sample, i.e., K-565 requires the presence of a lighter $\delta^{18}O^{SW}$ of -5‰. This is a C-type chert with hydrothermal input (high positive Eu anomaly) and open marine depositional regime (superchondritic Y/Ho values). This sample can only be explained by equilibrium with hydrothermal waters corresponding to this light seawater. This scenario would be valid also for the other Gunflint cherts. However, equilibration temperatures are ~50°C which is only possible at sites where hydrothermal waters mix with cooler seawater. This would mean a low $\delta^{18}O^{SW}$ in the Proterozoic with similar temperatures as today. So, the case for a lighter $\delta^{18}O$ and $\delta^{17}O$ seawater cannot be completely excluded at this point.

Almost all Archean cherts are of hydrothermal origin, which can be inferred based on their positive Eu anomalies and near chondritic Y/Ho values. Nevertheless, they can be used to identify the composition of hydrothermal fluids they would have equilibrated with. The

composition of hydrothermal fluids are expected to be a couple of per mil heavier than ambient seawater $\delta^{18}O$ values and within uncertainty identical to seawater $\Delta'^{17}O$ values, considering a high-T slope (0.5305) of equilibrium between hydrothermal fluids and altered oceanic crust. The cherts record equilibration with mixtures of hydrothermal fluids and corresponding seawater that could not be lighter in $\delta^{18}O$ than ~-3 to -5‰. Samples like MBC-1, W2, Z2 can be explained with modern day seawater and hydrothermal fluid mixture compositions, without invoking any light $\delta^{18}O^{SW}$ values. The cherts alternatively also show equilibrium with water compositions lighter in $\delta^{18}O$ and heavier in $\Delta'^{17}O$ than present day seawater. This could be either modern meteoric water or in some cases, past $\delta^{18}O^{SW}$ values. However, equilibrium temperatures obtained are always much higher (~50-130°C) than present day. Thus, the cherts are not in equilibrium with a light $\delta^{18}O^{SW}$ at modern day near-surface ambient temperatures.

As an overall result, it is safe to assume that Precambrian oceans never had drastically low $\delta^{18}O_{SMOW}$ values (in the tune of -13‰). Seawater may have reached values like -5‰ $\delta^{18}O$ and some of the samples studied herein are only consistent with $\delta^{18}O^{SW} > -2$ (Z2). In an unchanged $\delta^{18}O^{SW}$ world, the $\Delta'^{17}O$ of ancient oceans would also remain similar to present day average of -0.004‰ for an ice-free world. The case for a hot Precambrian ocean also seems unlikely, because the hydrothermal hot waters require mixing with cooler seawater to yield temperatures <100°C. The possibility of elevated seawater temperatures in the past cannot be completely ruled out.

Thus, the trend observed in the $\Delta'^{17}O$ vs $\delta'^{18}O$ space for the chert samples is a result of the interplay of more than one factor. The isotopic compositions of the cherts may vary due to a combination of 1) slightly lower $\delta^{17}O^{SW}$ and $\delta^{18}O^{SW}$ and thus 2) lighter corresponding meteoric water compositions, which cherts may at least partially form from (i.e. mixtures of meteoric water and seawaters), 3) warmer ambient temperatures in which the cherts were forming (e.g., close to hydrothermal vents) and 4) diagenetic temperatures associated with formation of microquartz (independent of seawater temperature). Therefore, cherts are not good candidates for inferring average temperatures of the ancient oceans. Some of these reasons can be excluded using the triple oxygen isotope systematics, but clearly not all. Applying the same techniques to other marine sediments like carbonate or phosphates may be useful to narrow the feasible range of processes further down.

4.7 References

Addison, W. D., Brumpton, G. R., Vallini, D. A., McNaughton, N. J., Davis, D. W., Kissin, S. A., ... & Hammond, A. L. (2005). Discovery of distal ejecta from the 1850 Ma Sudbury impact event. Geology, 33(3), 193-196.

Awramik, S. M., & Barghoorn, E. S. (1977). The Gunflint microbiota. Precambrian Research, 5(2), 121-142.

Barghoorn, E. S., & Tyler, S. A. (1965). Microorganisms from the Gunflint Chert These structurally preserved Precambrian fossils from Ontario are the most ancient organisms known. Science, 147(3658), 563-575.

Becker, R. H., & Clayton, R. N. (1976). Oxygen isotope study of a Precambrian banded iron-formation, Hamersley Range, Western Australia. Geochimica et Cosmochimica Acta, 40(10), 1153-1165.

Black, L. P., Shaw, R. D., & Offe, L. A. (1980). The age of the Stuart Dyke Swarm and its bearing on the onset of late Precambrian sedimentation in central Australia. Journal of the Geological Society of Australia, 27(1-2), 151-155.

Blattner, P. (1975). Oxygen isotopic composition of fissure-grown quartz, adularia, and calcite from Broadlands geothermal field, New Zealand, with an appendix on quartz-K-feldspar-calcite-muscovite oxygen isotope geothermometers. American Journal of Science, 275(7), 785-800.

Bolhar, R., Kamber, B. S., Moorbath, S., Fedo, C. M., & Whitehouse, M. J. (2004). Characterisation of early Archaean chemical sediments by trace element signatures. Earth and Planetary Science Letters, 222(1), 43-60.

Bolhar, R., Kamber, B. S., Moorbath, S., Fedo, C. M., & Whitehouse, M. J. (2004). Characterisation of early Archaean chemical sediments by trace element signatures. Earth and Planetary Science Letters, 222(1), 43-60.

Bottinga, Y., & Javoy, M. (1973). Comments on oxygen isotope geothermometry. Earth and

Planetary Science Letters, 20(2), 250-265.

Brandriss, M. E., O'Neil, J. R., Edlund, M. B., & Stoermer, E. F. (1998). Oxygen isotope fractionation between diatomaceous silica and water. Geochimica et Cosmochimica Acta, 62(7), 1119-1125.

Brandriss, M. E., O'Neil, J. R., Edlund, M. B., & Stoermer, E. F. (1998). Oxygen isotope fractionation between diatomaceous silica and water. Geochimica et Cosmochimica Acta, 62(7), 1119-1125.

Buick, R., & Dunlop, J. S. R. (1990). Evaporitic sediments of early Archaean age from the Warrawoona Group, North Pole, Western Australia. Sedimentology, 37(2), 247-277.

Buick, R., & Dunlop, J. S. R. (1990). Evaporitic sediments of early Archaean age from the Warrawoona Group, North Pole, Western Australia. Sedimentology, 37(2), 247-277.

Byerly, G. R., Kröner, A., Lowe, D. R., Todt, W., & Walsh, M. M. (1996). Prolonged magmatism and time constraints for sediment deposition in the early Archean Barberton greenstone belt: evidence from the Upper Onverwacht and Fig Tree groups. Precambrian Research, 78(1), 125-138.

Came, R. E., Eiler, J. M., Veizer, J., Azmy, K., Brand, U., & Weidman, C. R. (2007). Coupling of surface temperatures and atmospheric CO_2 concentrations during the Palaeozoic era. Nature, 449(7159), 198-201.

Cao, X., & Liu, Y. (2011). Equilibrium mass-dependent fractionation relationships for triple oxygen isotopes. Geochimica et Cosmochimica Acta, 75(23), 7435-7445

Carrigan, W. J., & Cameron, E. M. (1991). Petrological and stable isotope studies of carbonate and sulfide minerals from the Gunflint Formation, Ontario: evidence for the origin of early Proterozoic iron-formation. Precambrian Research, 52(3), 347-380.

Clayton, R. N., & Kieffer, S. W. (1991). Oxygen isotopic thermometer calibrations. In Stable isotope geochemistry: A tribute to Samuel Epstein (Vol. 3, pp. 3-10). Geochem. Soc.

Clayton, R. N., O'Neil, J. R., & Mayeda, T. K. (1972). Oxygen isotope exchange between quartz and water. Journal of Geophysical Research, 77(17), 3057-3067.

Clayton, R. N., O'Neil, J. R., & Mayeda, T. K. (1972). Oxygen isotope exchange between quartz and water. Journal of Geophysical Research, 77(17), 3057-3067.

Collins,W.J., & Van Kranendonk, M.J. (1999). Model for the development of kyanite during partial convective overturn of Archean granite-greenstone terranes: the Pilbara Craton, Australia. Journal of Metamorphic Geology, 17, 145–156.

Condon, D., Zhu, M., Bowring, S., Wang, W., Yang, A., & Jin, Y. (2005). U-Pb ages from the neoproterozoic Doushantuo Formation, China. Science, 308(5718), 95-98.

Craig, H., & Gordon, L. I. (1965). Deuterium and oxygen 18 variations in the ocean and the marine atmosphere.

Criss, R. E. (1991). Temperature dependence of isotopic fractionation factors. Stable Isotope Geochemistry: A Tribute to Samuel Epstein, 3, 11-16.

Criss, R. E. (1999). Principles of stable isotope distribution. Oxford University Press.

Cunningham, L. C., Page, F. Z., Simonson, B. M., Kozdon, R., & Valley, J. W. (2012). Ion microprobe analyses of $\delta^{18}O$ in early quartz cements from 1.9 Ga granular iron formations (GIFs): A pilot study. Precambrian Research, 214, 258-268.

Dansgaard, W. (1964). Stable isotopes in precipitation. Tellus, 16(4), 436-468.

Dodd, J. (2011). Oxygen isotopes in diatom silica: a new understanding of silica-water oxygen isotope fractionation in diatom frustules and an application of diatom $\delta^{18}O$ values as a record of paleohydrologic variability in a middle-Pleistocene lacrustine core from the Valles Caldera, New Mexico.

Dodd, J. P., & Sharp, Z. D. (2010). A laser fluorination method for oxygen isotope analysis of biogenic silica and a new oxygen isotope calibration of modern diatoms in freshwater environments. Geochimica et Cosmochimica Acta, 74(4), 1381-1390.

Eugster, H. P. (1967). Hydrous sodium silicates from Lake Magadi, Kenya: precursors of bedded chert. Science, 157(3793), 1177-1180.

Eugster, H. P., & Jones, B. F. (1968). Gels composed of sodium-aluminium silicate, Lake Magadi, Kenya. Science, 161(3837), 160-163.

Floran, R. J., & Papike, J. J. (1978). Mineralogy and petrology of the Gunflint Iron Formation, Minnesota-Ontario: correlation of compositional and assemblage variations at low to

moderate grade. Journal of Petrology, 19(2), 215-288.

Folk, R. L., & Weaver, C. E. (1952). A study of the texture and composition of chert. American Journal of Science, 250(7), 498-510.

Folk, R. L., & Weaver, C. E. (1952). A study of the texture and composition of chert. American Journal of Science, 250(7), 498-510.

Forman, D. J., Ranford, L. C., & Cook, P. J. (1970). Geology of the Amadeus basin, central Australia (p. 100). Australia: Bureau of Mineral Resources, Geology and Geophysics.

Fralick, P., & Barrett, T. J. (1995). Depositional controls on iron formation associations in Canada. Sedimentary Facies Analysis: A Tribute to the Research and Teaching of Harold G. Reading, 137-156.

Fralick, P., & Barrett, T. J. (1995). Depositional controls on iron formation associations in Canada. Sedimentary Facies Analysis: A Tribute to the Research and Teaching of Harold G. Reading, 137-156.

Fralick, P., Davis, D. W., & Kissin, S. A. (2002). The age of the Gunflint Formation, Ontario, Canada: single zircon U Pb age determinations from reworked volcanic ash. Canadian Journal of Earth Sciences, 39(7), 1085-1091.

Fralick, P., Davis, D. W., & Kissin, S. A. (2002). The age of the Gunflint Formation, Ontario, Canada: single zircon U Pb age determinations from reworked volcanic ash. Canadian Journal of Earth Sciences, 39(7), 1085-1091.

Friedman, I., & O'Neil, J. R. (1977). Data of geochemistry: Compilation of stable isotope fractionation factors of geochemical interest (Vol. 440). US Government Printing Office.

Gersonde, R., Hodell, D. A., & Blum, P. (1999). 1. Leg 177 summary: southern ocean paleoceanography1. In Proceedings of the Ocean Drilling Program, Initial Reports (Vol. 177).

Goodwin, A. M. (1956). Facies relations in the Gunflint iron formation [Ontario]. Economic Geology, 51(6), 565-595.

Hay, R. L. (1968). Chert and its sodium-silicate precursors in sodium-carbonate lakes of East Africa. Contributions to Mineralogy and Petrology, 17(4), 255-274.O'Neil, J. R., & Hay, R. L.

(1973). 18O/16O ratios in cherts associated with the saline lake deposits of East Africa. Earth and Planetary Science Letters, 19(2), 257-266.

Heaney, P. J. (1993). A proposed mechanism for the growth of chalcedony. Contributions to Mineralogy and Petrology, 115(1), 66-74.

Herwartz, D., Pack, A., Krylov, D., Xiao, Y., Muehlenbachs, K., Sengupta, S., & Di Rocco, T. (2015). Revealing the climate of snowball Earth from Δ17O systematics of hydrothermal rocks. Proceedings of the National Academy of Sciences, 112(17), 5337-5341.

Hickman, A. H. (1983). Geology of the Pilbara Block and its environs (Vol. 127). Geological Survey of Western Australia.

Hickman, A. H., & Van Kranendonk, M. J. (2012). A Billion Years of Earth History: A Geological Transect Through the Pilbara Craton and the Mount Bruce Supergroup-a Field Guide to Accompany 34th IGC Excursion WA-2. Geological Survey of Western Australia.

Holmden, C., & Muehlenbachs, K. (1993). The 18O/16O ratio of 2-billion-year-old seawater inferred from ancient oceanic crust. Science, 259(5102), 1733-1736.

Ingall, E. Drew. (1888). *Report on mines and mining on Lake Superior.* Montreal: Dawson.

Jaffrés, J. B., Shields, G. A., & Wallmann, K. (2007). The oxygen isotope evolution of seawater: a critical review of a long-standing controversy and an improved geological water cycle model for the past 3.4 billion years. Earth-Science Reviews, 83(1), 83-122.

Jiang, G., Sohl, L.E., Christie-Blick, N., 2003. Neoproterozioc stratigraphic comparison ofthe Lesser Himalaya (India) andYangtze Block (South China): paleogeographic implications. Geology 31, 917–920

Kato, Y., & Nakamura, K. (2003). Origin and global tectonic significance of Early Archean cherts from the Marble Bar greenstone belt, Pilbara Craton, Western Australia. Precambrian Research, 125(3), 191-243.

Kawabe, I. (1978). Calculation of oxygen isotope fractionation in quartz-water system with special reference to the low temperature fractionation. Geochimica et Cosmochimica Acta, 42(6), 613-621.

Keller, W. D., Viele, G. W., & Johnson, C. H. (1977). Texture of Arkansas Novaculite indicates thermally induced metamorphism. *Journal of Sedimentary Research*, *47*(2).

Kita, I., Taguchi, S., & Matsubaya, O. (1985). Oxygen isotope fractionation between amorphous silica and water at 34–93 C.

Knauth, L. P. (1973). Oxygen and hydrogen isotope ratios in cherts and related rocks (Doctoral dissertation, California Institute of Technology).

Knauth, L. P. (1979). A model for the origin of chert in limestone. Geology, 7(6), 274-277.

Knauth, L. P. (1992). Origin and diagenesis of cherts: an isotopic perspective. In *Isotopic signatures and sedimentary records* (pp. 123-152). Springer Berlin Heidelberg.

Knauth, L. P. (1994). Petrogenesis of chert. Reviews in Mineralogy and Geochemistry, 29(1), 233-258.

Knauth, L. P., & Epstein, S. (1976). Hydrogen and oxygen isotope ratios in nodular and bedded cherts. Geochimica et Cosmochimica Acta, 40(9), 1095-1108.

Knauth, L. P., & Epstein, S. (1976). Hydrogen and oxygen isotope ratios in nodular and bedded cherts. Geochimica et Cosmochimica Acta, 40(9), 1095-1108.

Knauth, L. P., & Lowe, D. R. (2003). High Archean climatic temperature inferred from oxygen isotope geochemistry of cherts in the 3.5 Ga Swaziland Supergroup, South Africa. Geological Society of America Bulletin, 115(5), 566-580.

Knoll, A. H., Barghoorn, E. S., & Golubić, S. (1975). Paleopleurocapsa wopfnerii gen. et sp. nov.: A Late Precambrian alga and its modern counterpart. Proceedings of the National Academy of Sciences, 72(7), 2488-2492.

Landais, A., Barkan, E., Yakir, D., & Luz, B. (2006). The triple isotopic composition of oxygen in leaf water. Geochimica et cosmochimica acta, 70(16), 4105-4115.

Leclerc, A. J., & Labeyrie, L. (1987). Temperature dependence of the oxygen isotopic fractionation between diatom silica and water. Earth and Planetary Science Letters, 84(1), 69-74.

Leng, M. J., & Barker, P. A. (2006). A review of the oxygen isotope composition of lacustrine diatom silica for palaeoclimate reconstruction. Earth-Science Reviews, 75(1), 5-27.

Li, S., Levin, N. E., & Chesson, L. A. (2015). Continental scale variation in 17 O-excess of meteoric waters in the United States. Geochimica et Cosmochimica Acta, 164, 110-126.Luz, B., & Barkan, E. (2005). The isotopic ratios 17 O/16 O and 18 O/16 O in molecular oxygen and their significance in biogeochemistry. Geochimica et Cosmochimica Acta, 69(5), 1099-1110.

Li, Z., Li, X., Kinny, P.D., Wang, J., Zhang, S., Zhou, H., 2003. Geochronology of Neoproterozoic syn-rift magmatism in the Yangtze Craton, South China and correlation with other continents: evidence for a mantle superplume that broke up Rodinia. Precambrian Research 122, 85–109.

Liu, P., Yin, C., Chen, S., Tang, F., & Gao, L. (2013). The biostratigraphic succession of acanthomorphic acritarchs of the Ediacaran Doushantuo Formation in the Yangtze Gorges area, South China and its biostratigraphic correlation with Australia. Precambrian Research, 225, 29-43.

Luz, B., & Barkan, E. (2010). Variations of 17 O/16 O and 18 O/16 O in meteoric waters. Geochimica et Cosmochimica Acta, 74(22), 6276-6286.

Maliva, R. G., Knoll, A. H., & Simonson, B. M. (2005). Secular change in the Precambrian silica cycle: insights from chert petrology. Geological Society of America Bulletin, 117(7-8), 835-845.

Marin-Carbonne, J., Chaussidon, M., & Robert, F. (2012). Micrometer-scale chemical and isotopic criteria (O and Si) on the origin and history of Precambrian cherts: implications for paleo-temperature reconstructions. Geochimica et Cosmochimica Acta, 92, 129-147.

Marin-Carbonne, J., McKeegan, K. D., Davis, A. M., MacPherson, G. J., Mendybaev, R. A., & Richter, F. M. (2012). O, Si and Mg isotopic compositions of FUN inclusion Vigarano 1623–5. Lunar Planet. Sci, 43, 1687.

Matheney, R. K., & Knauth, L. P. (1989). Oxygen-isotope fractionation between marine biogenic silica and seawater. Geochimica et Cosmochimica Acta, 53(12), 3207-3214.Craig, H. (1957). Isotopic standards for carbon and oxygen and correction factors for mass-spectrometric analysis of carbon dioxide. Geochimica et cosmochimica acta, 12(1), 133-149.

Matheney, R. K., & Knauth, L. P. (1989). Oxygen-isotope fractionation between marine biogenic silica and seawater. Geochimica et Cosmochimica Acta, 53(12), 3207-3214.

Matsuhisa, Y., Goldsmith, J. R., & Clayton, R. N. (1978). Mechanisms of hydrothermal crystallization of quartz at 250 C and 15 kbar. Geochimica et Cosmochimica Acta, 42(2), 173-182.

Matsuhisa, Y., Goldsmith, J. R., & Clayton, R. N. (1978). Mechanisms of hydrothermal crystallization of quartz at 250 C and 15 kbar. Geochimica et Cosmochimica Acta, 42(2), 173-182.

Matsuhisa, Y., Goldsmith, J. R., & Clayton, R. N. (1979). Oxygen isotopic fractionation in the system quartz-albite-anorthite-water. Geochimica et Cosmochimica Acta, 43(7), 1131-1140.

Matthews, A., & Beckinsale, R.D. (1979). Oxygen isotope equilibration systematics between quartz and water. American Mineralogist, 64,232–240.

Matthews, A., Goldsmith, J. R., & Clayton, R. N. (1983). Oxygen isotope fractionations involving pyroxenes: the calibration of mineral-pair geothermometers. Geochimica et Cosmochimica Acta, 47(3), 631-644.

Micheelsen, H. (1966). *The structure of dark flint from Stevns, Denmark* (Doctoral dissertation, Andelsbogtr., Odense).

Miller, M. F. (2002). Isotopic fractionation and the quantification of 17 O anomalies in the oxygen three-isotope system: an appraisal and geochemical significance. Geochimica et Cosmochimica Acta, 66(11), 1881-1889.

Minami, M., Shimizu, H., Masuda, A., & Adachi, M. (1995). Two Archean Sm-Nd ages of 3.2 and 2.5 Ga for the Marble Bar Chert, Warrawoona Group, Pilbara Block, Western Australia. Geochemical Journal, 29(6), 347-362.

Moschen, R., Lücke, A., & Schleser, G. H. (2005). Sensitivity of biogenic silica oxygen isotopes to changes in surface water temperature and palaeoclimatology. Geophysical Research Letters, 32(7).

Moschen, R., Lücke, A., Parplies, J., Radtke, U., & Schleser, G. H. (2006). Transfer and early diagenesis of biogenic silica oxygen isotope signals during settling and sedimentation of diatoms in a temperate freshwater lake (Lake Holzmaar, Germany). Geochimica et

cosmochimica acta, 70(17), 4367-4379.

Moschen, R., Lücke, A., Parplies, J., Radtke, U., & Schleser, G. H. (2006). Transfer and early
diagenesis of biogenic silica oxygen isotope signals during settling and sedimentation of
diatoms in a temperate freshwater lake (Lake Holzmaar, Germany). Geochimica et
cosmochimica acta, 70(17), 4367-4379.

Murray, R. W. (1994). Chemical criteria to identify the depositional environment of chert: general
principles and applications. Sedimentary Geology, 90(3), 213-232.

Murray, R. W., ten Brink, M. R. B., Jones, D. L., Gerlach, D. C., & Russ, G. P. (1990). Rare earth
elements as indicators of different marine depositional environments in chert and shale.
Geology, 18(3), 268-271.

Nijman, W., & Valkering, M. E. (1999). Growth fault control of Early Archaean cherts, barite
mounds and chert-barite veins, North Pole Dome, Eastern Pilbara, Western Australia.
Precambrian Research, 95(3), 247-274.

O'Neil, J. R. (1963). Oxygen isotope fractionation studies in mineral systems.

O'neil, J. R., & Clayton, R. N. (1964). Oxygen isotope geothermometry. Isotopic and cosmic
chemistry, 157-168.

O'Neil, J. R., & Hay, R. L. (1973). 18O/16O ratios in cherts associated with the saline lake deposits
of East Africa. *Earth and Planetary Science Letters*,*19*(2), 257-266.

O'Neil, J. R., Clayton, R. N., & Mayeda, T. K. (1969). Oxygen isotope fractionation in divalent metal
carbonates. Univ. of Chicago.

Pack, A., & Herwartz, D. (2014). The triple oxygen isotope composition of the Earth mantle and
understanding variations in terrestrial rocks and minerals. Earth and Planetary Science
Letters, 390, 138-145.

Pack, A., Russell, S. S., Shelley, J. M. G., & Van Zuilen, M. (2007). Geo-and cosmochemistry of the
twin elements yttrium and holmium. Geochimica et Cosmochimica Acta, 71(18), 4592-4608.

Pack, A., Tanaka, R., Hering, M., Sengupta, S., Peters, S., & Nakamura, E. (2016). The oxygen
isotope composition of San Carlos olivine on the VSMOW2-SLAP2 scale. Rapid

Communications in Mass Spectrometry, 30(13), 1495-1504.

Perry, E. C. (1967). The oxygen isotope chemistry of ancient cherts. Earth and Planetary Science Letters, 3, 62-66.

Pourmand, A., Dauphas, N., & Ireland, T. J. (2012). A novel extraction chromatography and MC-ICP-MS technique for rapid analysis of REE, Sc and Y: Revising CI-chondrite and Post-Archean Australian Shale (PAAS) abundances. Chemical Geology, 291, 38-54.

Preiss, W. V., Walter, M. R., Coats, R. P., & Wells, A. T. (1978). Lithological correlations of Adelaidean glaciogenic rocks in parts of the Amadeus, Ngalia, and Georgina basins. BMR Journal of Australian Geology and Geophysics, 3, 43-53.

Rumble, D., Miller, M. F., Franchi, I. A., & Greenwood, R. C. (2007). Oxygen three-isotope fractionation lines in terrestrial silicate minerals: An inter-laboratory comparison of hydrothermal quartz and eclogitic garnet. Geochimica et Cosmochimica Acta, 71(14), 3592-3600.

Runnegar, B., Dollase, W. A., Ketcham, R. A., Colbert, M., & Carlson, W. D. (2001, November). Early Archean sulfates from Western Australia first formed as hydrothermal barites not gypsum evaporites. In Geol. Soc. Am. Abstracts with Programs (Vol. 33).

Schmidt, M., Botz, R., Rickert, D., Bohrmann, G., Hall, S. R., & Mann, S. (2001). Oxygen isotopes of marine diatoms and relations to opal-A maturation. Geochimica et Cosmochimica Acta, 65(2), 201-211.

Schopf, J. W. (1968). Microflora of the Bitter Springs formation, late Precambrian, central Australia. Journal of Paleontology, 651-688.

Schopf, J. W. (1983). Earth's earliest biosphere: its origin and evolution.

Schopf, J. W. (1992). The Proterozoic biosphere: a multidisciplinary study. Cambridge University Press.

Schrag, D. P., Adkins, J. F., McIntyre, K., Alexander, J. L., Hodell, D. A., Charles, C. D., & McManus, J. F. (2002). The oxygen isotopic composition of seawater during the Last Glacial Maximum. Quaternary Science Reviews, 21(1), 331-342.

Sharp, Z. D., & Kirschner, D. L. (1994). Quartz-calcite oxygen isotope thermometry: A calibration based on natural isotopic variations. Geochimica et Cosmochimica Acta, 58(20), 4491-4501.

Sharp, Z. D., & Kirschner, D. L. (1994). Quartz-calcite oxygen isotope thermometry: A calibration based on natural isotopic variations. Geochimica et Cosmochimica Acta, 58(20), 4491-4501.

Sharp, Z. D., Gibbons, J. A., Maltsev, O., Atudorei, V., Pack, A., Sengupta, S., Shock, E.L., & Knauth, L. P. (2016). A calibration of the triple oxygen isotope fractionation in the SiO_2–H_2O system and applications to natural samples. Geochimica et Cosmochimica Acta, 186, 105-119.

Shemesh, A., Charles, C. D., & Fairbanks, R. G. (1992). Oxygen isotopes in biogenic silica: global changes in ocean temperature and isotopic composition. Science, 256(5062), 1434-1436.

Shiro, Y., & Sakai, H. (1972). Calculation of the reduced partition function ratios of α-, β-quartzs and calcite. Bulletin of the Chemical Society of Japan, 45(8), 2355-2359.

Simonson, B. M., & Lanier, W. P. (1987). Early silica cementation and microfossil preservation in cavities in iron formation stromatolites, early Proterozoic of Canada. Precambrian Iron-Formations, 187-213.

Southgate, P. N. (1989). Relationships between cyclicity and stromatolite form in the Late Proterozoic Bitter Springs Formation, Australia. Sedimentology, 36(2), 323-339.

Stiegler, M. T., Lowe, D. R., & Byerly, G. R. (2008). Abundant pyroclastic komatiitic volcanism in the 3.5–3.2 Ga Barberton greenstone belt, South Africa. Geology, 36(10), 779-782.

Sugahara, H., Sugitani, K., Mimura, K., Yamashita, F., & Yamamoto, K. (2010). A systematic rare-earth elements and yttrium study of Archean cherts at the Mount Goldsworthy greenstone belt in the Pilbara Craton: Implications for the origin of microfossil-bearing black cherts. Precambrian Research, 177(1), 73-87.

Sugahara, H., Sugitani, K., Mimura, K., Yamashita, F., & Yamamoto, K. (2010). A systematic rare-earth elements and yttrium study of Archean cherts at the Mount Goldsworthy greenstone belt in the Pilbara Craton: Implications for the origin of microfossil-bearing black cherts. Precambrian Research, 177(1), 73-87.

Thorpe, R. I., Hickman, A. H., Davis, D. W., Mortensen, J. K., & Trendall, A. F. (1992). U-Pb zircon

geochronology of Archaean felsic units in the Marble Bar region, Pilbara Craton, Western

Australia. Precambrian Research, 56(3), 169-189.

Thorpe, R. I., Hickman, A. H., Davis, D. W., Mortensen, J. K., & Trendall, A. F. (1992). U-Pb zircon

geochronology of Archaean felsic units in the Marble Bar region, Pilbara Craton, Western

Australia. Precambrian Research, 56(3), 169-189.

Trendall, A. F. (1968). Three great basins of Precambrian banded iron formation deposition: a

systematic comparison. *Geological Society of America Bulletin*, *79*(11), 1527-1544.

van den Boorn, S. H. J. M., Van Bergen, M. J., Vroon, P. Z., De Vries, S. T., & Nijman, W. (2010).

Silicon isotope and trace element constraints on the origin of~ 3.5 Ga cherts: implications for

Early Archaean marine environments. Geochimica et Cosmochimica Acta, 74(3), 1077-1103.

van den Boorn, S. H., van Bergen, M. J., Nijman, W., & Vroon, P. Z. (2007). Dual role of seawater

and hydrothermal fluids in Early Archean chert formation: evidence from silicon isotopes.

Geology, 35(10), 939-942.

Van Kranendonk, M. J. (2000). Geology of the North Shaw 1: 100 000 Sheets: Sheets 2755.

Geological Survey of Western Australia.

Van Kranendonk, M. J., & Pirajno, F. (2004). Geological setting and geochemistry of metabasalts

and alteration zones associated with hydrothermal chert±barite deposits in the ca. 3.45 Ga

Warrawoona Group, Pilbara Craton, Australia. Geochemistry: Exploration, Environment,

Analysis, 4, 253-278.

Van Kranendonk, M. J., Collins, W. J., Hickman, A., & Pawley, M. J. (2004). Critical tests of vertical

vs. horizontal tectonic models for the Archaean East Pilbara granite–greenstone terrane,

Pilbara craton, western Australia. Precambrian Research, 131(3), 173-211.

Van Kranendonk, M. J., Hickman, A. H., Smithies, R. H., Nelson, D. R., & Pike, G. (2002). Geology and

tectonic evolution of the archean North Pilbara terrain, Pilbara Craton, Western Australia.

Economic Geology, 97(4), 695-732.

Van Kranendonk, M. J., Webb, G. E., & Kamber, B. S. (2003). Geological and trace element evidence

for a marine sedimentary environment of deposition and biogenicity of 3.45 Ga stromatolitic

carbonates in the Pilbara Craton, and support for a reducing Archaean ocean. Geobiology, 1(2), 91-108.

Viljoen, M. J., & Viljoen, R. (1969). The geology and geochemistry of the lower ultramafic unit of the Onverwacht Group and a proposed new class of igneous rocks. Geological Society of South Africa Special Publication, 2, 55-86.

Walter, M. R. (1983). Archean stromatolites- Evidence of the earth's earliest benthos. Earth's earliest biosphere: Its origin and evolution(A 84-43051 21-51). Princeton, NJ, Princeton University Press, 1983,, 187-213.

Walter, M. R., Buick, R., & Dunlop, J. S. R. (1980). Stromatolites 3,400–3,500 Myr old from the North Pole area, Western Australia.

Walter, Malcolm R. *Stromatolites and the biostratigraphy of the Australian Precambrian and Cambrian*. No. 11. Palaeontological Association, 1972.

Wang, J., Li, Z., 2003. History of Neoproterozoic rift in South China: implications for Rodinia break-up. Precambrian Research 122, 141–158

Winter, B. L., & Knauth, L. P. (1992). Stable isotope geochemistry of cherts and carbonates from the 2.0 Ga Gunflint Iron Formation: implications for the depositional setting, and the effects of diagenesis and metamorphism. Precambrian Research, 59(3), 283-313.

Winter, B. L., & Knauth, L. P. (1992). Stable isotope geochemistry of cherts and carbonates from the 2.0 Ga Gunflint Iron Formation: implications for the depositional setting, and the effects of diagenesis and metamorphism. Precambrian Research, 59(3), 283-313.

Winter, B. L., & Knauth, L. P. (1992). Stable isotope geochemistry of cherts and carbonates from the 2.0 Ga Gunflint Iron Formation: implications for the depositional setting, and the effects of diagenesis and metamorphism. Precambrian Research, 59(3), 283-313.

Yin, L., 1987. Microbiotas of latest Precambrian sequences in China. In: Nanjing of Geology and Palaeontology, Academia Sinica (Ed.), Stratigraphy and Palaeontology of Systemic boundaries in China, Precambrian—Cambrian boundary (1). Nanjing University Publishing House, pp. 415–494.

Yin, L., Zhu, M., Knoll, A.H., Yuan, X., Zhang, J., Hu, J., 2007. Doushantuo embryos preserved inside diapause egg cysts. Nature 446, 661–663

Young, E. D., Galy, A., & Nagahara, H. (2002). Kinetic and equilibrium mass-dependent isotope fractionation laws in nature and their geochemical and cosmochemical significance. Geochimica et Cosmochimica Acta, 66(6), 1095-1104.

Yun, Z. (1984). A Gunflint type of microfossil assemblage from early Proterozoic stromatolitic cherts in China.

Zheng Y.F. (1993) Calculation of oxygen isotope fractionation in anhydrous silicate minerals. Geochimica et Cosmochimica Acta, 57,1079–1091.

Zhu, M., Strauss, H., & Shields, G. A. (2007). From snowball earth to the Cambrian bioradiation: calibration of Ediacaran–Cambrian earth history in South China. Palaeogeography, Palaeoclimatology, Palaeoecology, 254(1), 1-6.

5. Conclusion

This thesis demonstrates how high-precision triple oxygen isotope data of cherts add additional information to the calssic $\delta^{18}O$ scale for evaluating the temperature and $\delta^{18}O$ values of seawater through time. Only a restricted range of water compositions solve both $\alpha_{\mathrm{SiO_2-Water}}^{18/16\mathrm{O}}$-T and $\theta_{\mathrm{SiO_2-Water}}^{\mathrm{equilibrium}} - T$ temperature relationships at the same time. Thus, the range of water compositions that can satisfy equilibrium conditions can be constrained better than when using the classical $\delta^{18}O$ – T relation alone. Water compositions that do not satisfy both thermometers can be excluded.

To enable a thorough interpretation of measured isotope data, a mass balance model was constructed to predict the triple oxygen isotopic composition of the ocean at variable isotopic flux rates (see Chapter 3). It was shown that variable high-T : low-T alteration of the crust is the most important geological process potentially affecting triple oxygen isotopic steady state over Earth's history. If the $\delta^{18}O$ of seawater did change due to fluctuations in the high-T : low-T alteration ratio over time, the $\delta^{17}O$ of such a 'low $\delta^{18}O$ ocean' can be predicted within narrow bounds. Covariation of decreasing $\delta'^{18}O$ vs. $\delta'^{17}O$ of seawater would fall on a slope of 0.516. Hence, $\Delta'^{17}O$ increases with decreasing $\delta'^{18}O$ in the reference frame used herein.

The chert samples show a trend of decreasing $\delta^{18}O$ values and $\delta^{17}O$ values (and increasing $\Delta'^{17}O$) with increasing age, from Phanerozoic to Archean. Comparing these measured data with the model, allows to narrow down the range of feasible water compositions that the cherts may have formed from (see chapter 4). A pure seawater origin can be excluded for some samples based on the additional $\Delta'^{17}O$ parameter in the current study. A hot Proterozoic ocean is not supported, whereas the possibility of higher seawater temperatures in the Archean cannot be ruled out. Overall the Precambrian oceans never had drastically low $\delta^{18}O_{\mathrm{SMOW}}$ values (in the tune of -13‰). Individual samples imply that seawater may have had values like -2‰ or possibly -6‰ $\delta^{18}O$ in the Precambrian.

The range of seawater $\delta^{18}O$ estimates can be narrowed down significantly by improving the uncertainty on the $\Delta'^{17}O$ of the cherts further. Better temperature estimates of the early oceans may be achieved by applying the triple oxygen isotope systematics to other marine sediments like carbonates and phosphates.

Revealing the climate of snowball Earth from Δ¹⁷O systematics of hydrothermal rocks

Daniel Herwartz, Andreas Pack, Dmitri Krylovb, Yilin Xiaoc, Karlis Muehlenbachs, Sukanya Sengupta, and Tommaso Di Rocco

My contribution to the manuscript: Analyzing data and writing some parts of the paper.

Revealing the climate of snowball Earth from $\Delta^{17}O$ systematics of hydrothermal rocks

Daniel Herwartz[a,1,2], Andreas Pack[a], Dmitri Krylov[b], Yilin Xiao[c], Karlis Muehlenbachs[d], Sukanya Sengupta[a], and Tommaso Di Rocco[a]

[a]Abteilung Isotopengeologie, Geowissenschaftliches Zentrum, Georg-August-Universität Göttingen, 37073 Göttingen, Germany; [b]Institute of Precambrian Geology and Geochronology, Russian Academy of Sciences, 199034 St. Petersburg, Russia; [c]CAS Key Laboratory of Crustal-Mantle Materials and Environments, School of Earth and Space Science, University of Science and Technology of China, Hefei, 230026, China; and [d]Department of Earth and Atmospheric Sciences, University of Alberta, Edmonton, AB, Canada T6G 2E3

The oxygen isotopic composition of hydrothermally altered rocks partly originates from the interacting fluid. We use the triple oxygen isotope composition ($^{17}O/^{16}O$, $^{18}O/^{16}O$) of Proterozoic rocks to reconstruct the $^{18}O/^{16}O$ ratio of ancient meteoric waters. Some of these have originated from snowball Earth glaciers and thus give insight into the climate and hydrology of these critical intervals in Earth history. For a Paleoproterozoic [~2.3–2.4 gigayears ago (Ga)] snowball Earth, $\delta^{18}O = -43 \pm 3$‰ is estimated for pristine meteoric waters that precipitated at low paleo-latitudes (≤35°N). Today, such low $^{18}O/^{16}O$ values are only observed in central Antarctica, where long distillation trajectories in combination with low condensation temperatures promote extreme ^{18}O depletion. For a Neoproterozoic (~0.6–0.7 Ga) snowball Earth, higher meltwater $\delta^{18}O$ estimates of −21 ± 3‰ imply less extreme climate conditions at similar paleo-latitudes (≤35°N). Both estimates are single snapshots of ancient water samples and may not represent peak snowball Earth conditions. We demonstrate how $^{17}O/^{16}O$ measurements provide information beyond traditional $^{18}O/^{16}O$ measurements, even though all fractionation processes are purely mass dependent.

triple oxygen isotopes | hydrothermal alteration | snowball Earth | climate | paleo-temperatures

G lacial successions deposited near the paleo-equator (≤15°) suggest that the Earth was entirely covered by ice several times during the Precambrian. Such episodes were termed "snowball Earth" climates. Presumably, the concentration of continents at low latitudes enhanced chemical weathering rates and thus removal of CO_2 from the atmosphere (1). Low pCO_2 led to global cooling and formation of polar and continental ice sheets. Once ice caps extended to latitudes below ~50°, a runaway ice albedo cooling effect occurs (2), global temperatures drop far below zero, and the entire Earth becomes covered with ice (a snowball Earth) (2, 3). At least one "total glaciation" occurred in the Paleoproterozoic era [Makganyene at ~2.4 gigayears ago (Ga)] (1), and at least two more arose in the Cryogenian (Sturtian at 720 Ma; Marinoan at 635 Ma) (3).

The climatic and hydrologic conditions of these critical episodes are poorly understood because classic paleo-thermometers (e.g., marine carbonates) are not viable for snowball Earth states and ancient water samples are missing. The $^{18}O/^{16}O$ ratio of meteoric water (expressed as $\delta^{18}O_{mw}$) can serve as a proxy for paleo-temperature if the hydrogeological context is known (4). A few attempts have been made to reconstruct ancient $\delta^{18}O_{mw}$ (5–8).

Calcite cements that precipitated in methane seeps in the Nuccaleena Formation, Australia, probably sample meltwaters from the ~635 Ma Marinoan snowball Earth with $\delta^{18}O$ ranging around ~−29‰ (5). The upper carbonate unit of the Lantian Formation in Anhui, South China, probably formed during the younger, ~580 Ma Gaskiers glaciation within a meltwater-dominated basin. These carbonates appear to be unaltered, hence low precipitation temperatures imply water compositions of $\delta^{18}O \approx$ −20‰ to −27‰ (6). Barite- and malachite-associated sulfate from a diamictite in Kaiyang, Guizhou, China, reveals meteoric

water compositions of $\delta^{18}O \approx -34 \pm 10$‰, probably representing Marinoan meltwaters (7). Apart from chemical sediments (5, 6) or ancient weathering products (7), it has also been suggested to estimate $\delta^{18}O_{mw}$ from hydrothermally altered rocks that have interacted with meltwater of meteoric origin (8).

Interaction of rocks with meteoric water at hydrothermal conditions (~350 °C) shifts $\delta^{18}O$ of the rocks ($\delta^{18}O_r$) toward lower values. Modern examples for such shifts are known from volcanically active regions such as Iceland (9) or Yellowstone. Fossil Phanerozoic and Precambrian hydrothermal systems like the Dabie−Sulu ultra-high-pressure terrain (China) (10) or the Belomorian Belt (Russia) (11) are suggested to have formed similarly to their modern analogs. The lowest $\delta^{18}O_r$ values provide an upper limit for the $\delta^{18}O_{mw}$ (8). At full equilibration, rocks have a $\delta^{18}O_r$ that is only 2−3‰ higher than the water they interacted with (12), but the degree of equilibration between a rock and a given water is generally unknown, compromising absolute $\delta^{18}O_{mw}$ estimates (8). Here we present a new approach to reconstruct the absolute $\delta^{18}O_{mw}$ from measuring not only $^{18}O/^{16}O$ but also the $^{17}O/^{16}O$ ratios of hydrothermal low $\delta^{18}O_r$ Precambrian rocks.

Concept of Using Triple Oxygen Isotopes

The $\delta^{17}O_{mw}$ is closely coupled with the $\delta^{18}O_{mw}$ (Fig. S1); a relation hereafter called meteoric water line (MWL). The slope of the MWL is a result of equilibrium-dominated fractionation,

whereas the intercept is due to kinetic fractionation in the exogenic water (see SI Text and Fig. S1). Rocks, in general, do not plot on the MWL (13). Rocks that have exchanged to variable degrees with meteoric water will define a mixing trend in a $\Delta'^{17}O$ vs. $\delta'^{18}O$ diagram (Fig. 1). The intersect between the mixing trend and the MWL gives, along with a small offset due to equilibrium hydrothermal water−rock fractionation, the composition of the interacting water (Fig. 1). This allows reconstruction of the $\delta^{18}O_{mw}$ from hydrothermally altered rocks and overcomes the limitation of unknown degree of equilibration, when using $\delta^{18}O_r$ only. Details regarding mass-dependent effects on $\Delta'^{17}O$ in silicates (Fig. S2) and definitions are given in SI Text.

Results and Discussion

We first test the new approach on hydrothermally altered low-$\delta^{18}O$ rocks from Iceland, where the $\delta^{18}O$ of the interacting water is approximately known. Icelandic samples are altered basalts from two boreholes (KG7 and KG10) at the Krafla volcano, taken from variable depths between 978 m and 2,100 m below the surface. The samples fall on a mixing array in the $\Delta'^{17}O$ vs. $\delta'^{18}O$ space between the unaltered Iceland basalt and the altered end-member (Fig. 1A and Fig. S3A). The samples stem from depths where temperatures were mostly ≥300 °C (9) and equilibrium fractionation between water and the alteration product is small [e.g., $\Delta\delta^{18}O_{water-epidote}$ ≤ 2‰, temperature (T) = 350 °C (14)]. Reconstruction of the pristine meteoric water (see Methods) gives a $\delta^{18}O_{mw}$ = −22 ± 4‰ (1σ_{SE}).

This estimate is lower than modern Icelandic meteoric waters with $\delta^{18}O_{mw}$ ≈ −12‰ (14, 15) but agrees with exchange with meteoric water from the Last Glacial Maximum (LGM). Such "ice age" waters are components of modern fumaroles [$\delta^{18}O$ values down to −19.3‰ (15)] and epidote-forming hydrothermal fluids [$\delta^{18}O_{hf}$ ≈ −16‰ (14)] at Krafla. The $\delta^{18}O_{hf}$ of any hydrothermal fluid in Iceland must be higher than the oxygen isotopic composition of the pristine meteoric water (i.e., $\delta^{18}O_{mw}$ < $\delta^{18}O_{hf}$), because water−rock interaction drives the initial meteoric water to higher $\delta^{18}O$. Hence the $\delta^{18}O_{hf}$ reconstructed from epidote [∼−16‰ (14)] will be systematically higher than the pristine $\delta^{18}O_{mw}$ reconstructed by our novel approach (−18 to −26‰). The $\delta^{18}O_{hf}$ would only be equal to $\delta^{18}O_{mw}$ if water/rock ratios (W/R) were infinitely high, because the $\delta^{18}O_{hf}$ is a function of W/R whereas our approach is independent of W/R.

At W/R > 10, the initial water composition would change by less than 10%, implying that the Icelandic basalts had been altered to ∼40−65% (Fig. 2A). However, the respective samples are to 100% mineralogically reconstituted to secondary minerals (clay, chlorite, epidote); hence a W/R = 2 (Fig. 2B) seems more realistic. The water composition would be altered from −22‰ (initial $\delta^{18}O_{mw}$) to −14.5‰ ($\delta^{18}O_{hf}$) along a mixing line between the initial meteoric water and water in equilibrium with the unaltered basalt. Apparent degrees of alteration (up to 95%; Fig. 2B) are then more consistent with the rock mineralogy. If W/R ≈ 2 (Fig. 2B) are representative for other samples from Krafla, the $\delta^{18}O_{hf}$ = −16‰ for the epidote precipitating fluid (14) is several permil higher than the respective initial $\delta^{18}O_{mw}$. We therefore propose that the role of ice age fluids at Krafla has been underestimated and W/R ratios have been overestimated. However, because the water mixing line is parallel to the rock mixing line, estimates of pristine $\delta^{18}O_{mw}$ are independent from assumed W/R ratios. Collectively, the data from Iceland demonstrate that $\delta^{17}O$ along with $\delta^{18}O$ can be used to infer the composition of the pristine meteoric water from hydrothermally altered rocks.

Neoproterozoic samples are eclogites (omphacite, garnet, quartz, rutile) from the Dabie−Sulu ultra-high-pressure terrain, eastern China. The $\Delta\delta^{18}O$ between the metamorphic minerals of these eclogites imply Mesozoic (240−220 Ma) isotopic equilibrium

at 500−900 °C (10), well after the Neoproterozoic hydrothermal alteration (16). However, the metamorphic petrology, the age, the mineral equilibration temperatures, and even the rock type are unimportant for our approach. Despite the later metamorphic overprint, the bulk samples are still low in $\delta^{18}O_r$; hence part of the samples' oxygen still originates from the meteoric waters that had interacted with the samples. All hydrothermally altered samples (whole-rock estimates; Table S1) fall on a mixing trend between the unaltered and the fully altered end-members. This mixing trend crosses the MWL and implies a $\delta^{18}O_{mw}$ = −21 ± 3‰ (Fig. 1B). If the protolith exchanged oxygen not at hydrothermal, but at lower temperatures, a water composition of −22 ± 3‰ is suggested (see Supporting Information).

The Dabie−Sulu is located on the northern margin of the South China block that was drifting between ∼35°N (at 750 Ma) (17) and ∼15°N (at 600 Ma) (18) in the Neoproterozoic. A $\delta^{18}O_{mw}$ of −21 ± 3‰ at such low latitude is probably related to either the Sturtian (∼720 Ma) or the Marinoan (∼635 Ma) glaciation (3), but an origin from one of the smaller events (e.g., the Gaskiers glaciation) is also plausible. Published lower $\delta^{18}O_{mw}$ estimates of ∼−29‰ (5), ∼−20‰ to −27‰ (6), and −34 ± 10‰ (7) differ from ours in space and time. Some estimates are likely related to other Neoproterozoic glaciations; hence large variations between individual studies are expected. Because the hydrological cycle becomes sluggish at very low temperatures (3), it seems plausible that most $\delta^{18}O_{mw}$ estimates do not represent water that had precipitated during the peak of a snowball Earth episode. Maybe none of them does. Therefore, all estimates should be rated as maximum values with respect to peak snowball Earth conditions.

Paleoproterozoic samples from the Belomorian Belt (Hetoostrov Island, Karelia, northwestern Russia) are Al-enriched mafic schists, composed of plagioclase, amphiboles (pargasite and gedrite), biotite, garnet, rutile, staurolite with corundum, or kyanite (11, 19). Coexisting mineral $\Delta\delta^{18}O$ suggest equilibration temperatures between ∼450 °C and 700 °C (11, 20) that relate to the Svecofennian orogeny at ∼1.9 Ga. The regional concentric $\delta^{18}O_r$ zoning around vents are interpreted as signs for a fossil high-temperature hydrothermal system that probably formed at low paleo-latitudes (≤35°) during a Paleoproterozoic snowball Earth around 2.3−2.4 Ga (8). The whole rocks define an array in the $\Delta'^{17}O$ vs. $\delta'^{18}O$ diagram that intersects with the MWL and gives $\delta^{18}O_{mw}$ = −43 ± 3‰ (Fig. 1B). If the alteration occurred not at high but at low temperatures, a $\delta^{18}O_{mw}$ of ∼−49‰ is suggested (Fig. S3C). The maximum $\delta^{18}O_{mw}$ ≈ −30‰ estimate that can be derived from the lowest measured $\delta^{18}O_r$ = −27.3‰ (8) from the same locality is considerably higher, illustrating the value of additional $\delta^{17}O_r$ measurements.

Our reconstructions of $\delta^{18}O_{mw}$ are based on a $\delta^{18}O$ of seawater ($\delta^{18}O_{sw}$) similar to today (21). Higher (8) or lower (22) $\delta^{18}O_{sw}$ values would shift the MWL (Fig. 1C). If $\delta^{18}O_{sw}$ were high, our $\delta^{18}O_{mw}$ estimate would also increase to the same extent. Lower $\delta^{18}O_{sw}$ (22) would not affect $\delta^{18}O_{mw}$ estimates because the position of the MWL would remain similar to today's (Fig. 1C; see Supporting Information for the effects on temperature estimates). Such low $\delta^{18}O_{sw}$ are vigorously debated and are implausible if plate tectonics worked in broadly similar ways to today (21).

Today, $\delta^{18}O_{mw}$ bear information on mean annual temperature (MAT) (4). The only place on Earth where mean annual $\delta^{18}O_{mw}$ values are as low as −43 ± 3‰ is central Antarctica distal from the sea. Using a modern $\delta^{18}O_{mw}$ vs. MAT relationship (8) [e.g., $\delta^{18}O_{mw}$ = 0.69*MAT − 13.6‰ (4)], a $\delta^{18}O_{mw}$ = −43‰ would translate into a MAT estimate of −42.5 °C. However, the hydrology of a fully frozen Earth close to the equator certainly differs from present-day conditions near the poles. Even today, local $\delta^{18}O_{mw}$ vs. MAT relationships show significant deviations from the global trend (23−25). Spatial slopes for Antarctica are generally steeper [e.g., 0.8‰/°C (25)], while ice core $\delta^{18}O$ from the LGM reveal shallow temporal relationships [e.g., ∼0.4‰/°C

Fig. 1. Triple oxygen isotopic compositions of hydrothermally altered samples. (A) Samples from Iceland plot on a mixing line between the Earth mantle and a 100% alteration end-member close to the MWL (assuming infinite W/R). Literature data of meteoric waters mostly plot above the MWL with a slope of 0.5285 (Fig. S1). (B) Samples from the Sulu and Karelia also plot on mixing lines between the predicted composition of meteoric water from snowball Earth events and their unaltered end-members. (C) Estimated compositions for Paleoproterozoic seawater and respective MWLs (stippled lines). The relative offset of the MWL from seawater remains constant. Large points are whole-rock averages with error bars showing 1σ SEM (1σ$_{SE}$). Small points represent individual mineral analysis (no error bars shown).
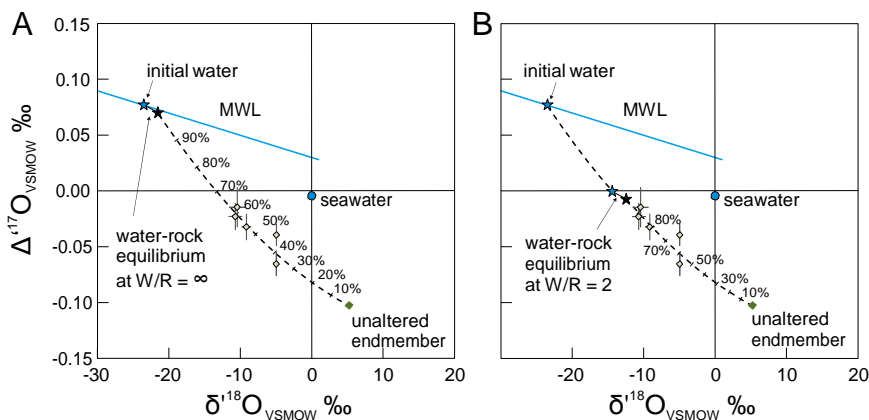
Fig. 2. Estimates of pristine $\delta^{18}O_{mw}$ are independent from W/R ratios. (A) At infinite W/R, the composition of the hydrothermal fluid is identical to the pristine meteoric water. Because the degree of sample alteration are underestimated (see Results and Discussion), this end-member scenario does not apply. (B) Lower W/R ratios (batch model) give more realistic estimates of sample alteration. The $\delta^{18}O_{hf}$ will evolve along a mixing line parallel to the rock mixing line. Therefore, estimates of pristine $\delta^{18}O_{mw}$ are independent of W/R and for simplicity, infinite W/R are assumed for Sulu and Karelia.

(24)]. General Circulation models (GCMs) predict such shallow temporal $\delta^{18}O_{mw}$ vs. MAT slopes mainly due to (i) low source and precipitation temperatures and (ii) a more dominant summer over winter precipitation combined with a stronger drop in summer than in winter temperatures (24). To our knowledge, GCMs have not been examined for the extreme conditions of a snowball Earth, but more simple Rayleigh-type models also predict shallower temporal slopes for a simultaneous drop in source and precipitation temperatures (23). On a snowball Earth, at least the source temperature would be lower than in the LGM, implying that shallow temporal slopes [e.g., 0.4‰/°C (24)] may extrapolate to even colder climates. If so, a modern-day $\delta^{18}O_{mw}$ vs. MAT relationship will overestimate paleo-temperatures not only for the LGM (23–25) but likely also for snowball Earth climates. A robust translation of $\delta^{18}O_{mw}$ into an absolute temperature scale could resolve debates about the extension of ice sheets (3, 26, 27) and sea ice thickness (28) during a snowball Earth (see Supporting Information). Extensive (sub)tropical glaciers on the continents are widely accepted for snowball Earth climates, but it remains a matter of debate whether the entire oceans were also covered by thick ice (3, 28). Climate models predict far lower equatorial temperatures for a "hard" snowball Earth (−45 °C to −20 °C) compared with a "slushball" Earth state (0−10 °C) (3, 26, 27). Thick sea ice > 100 m requires temperatures between −25 °C and −12 °C (28).

Besides low absolute temperatures, large degrees of Rayleigh-type distillation are required to reach such low $\delta^{18}O$ in precipitation. For example, ~ 80% condensation of the initial vapor at temperatures of −40 °C is necessary to reach $\delta^{18}O_{mw}$ values ≤ −40‰ (Figs. S4 and S5). The main source of atmospheric water vapor on a hard snowball Earth is sublimation in equatorial regions (≤10°; Fig. S6) (3) where temperatures are highest. A large degree of distillation thus implies glaciers deposited at some distance from this water source. Empirical correlations from Antarctica imply a decrease of 3‰/1,000 km (25); hence vapor transport over thousands of kilometers (over land or over sea ice) would be required to reach the observed low $\delta^{18}O_{mw}$. Initial precipitation at high altitudes with subsequent transport to the (presumably low-elevation) rift setting suggested for Karelia (8) is also feasible. Presently, $\delta^{18}O_{mw}$ decreases by ca. 2‰ per kilometer in temperate regions (29) and by 7‰ per kilometer in Antarctica (25). This increase in isotopic lapse rate (permil per kilometer) for colder regions is predicted by the thermodynamic model of Rowley et al. (30). Colder and drier climates are expected to yield increased lapse rates (30). For a slushball Earth, with evaporation temperatures ~5 °C at the equator (3, 26, 27), an altitude of ~5 km is sufficient to reach $\delta^{18}O_{mw} \approx$ −40‰. At this lapse rate (8‰ per kilometer), an elevation of only 2.5 km would be required to reach our Neoproterozoic $\delta^{18}O_{mw}$ estimate of ~ −21‰.

On a fully frozen but tectonically active Earth, cryovolcanism (as observed on the icy Jupiter moon Europa) is another potential source of atmospheric water that may help to decrease the overall $\delta^{18}O_{mw}$ compositions at low latitudes. Most of the erupted seawater and vapor would immediately resublimate and freeze in the cold atmosphere with only a small fraction being transported farther away from the source (distillation). Such waters would also have low $\delta^{18}O$ despite short distillation pathways.

Conclusions and Outlook

Our approach offers a way to reconstruct pristine $\delta^{18}O_{mw}$ from samples that had not been isotopically equilibrated with meteoric water. This example demonstrates how measurements of $^{17}O/^{16}O$ expand the traditional $\delta^{18}O$ scheme by another dimension. Being able to discriminate between kinetic fractionation vs. equilibrium fractionation vs. mixing will help quantify individual processes (e.g., diagenesis) or parameters (e.g., temperature). The basic theory is well developed, but applications are mainly restricted to the hydrogeological cycle (see Supporting Information). In principal, these systematics are applicable to all isotope systems with at least three stable isotopes. The sole limitation is currently set by the required high precision of isotope analysis.

Methods

The oxygen isotope ratios of anhydrous whole rock samples and minerals separates were measured using a high-precision laser fluorination technique (13). The hydrous samples from Iceland that could not be analyzed by laser fluorination were conventionally reacted with BrF_5 in Ni bombs. Samples were measured relative to tank O_2 that was calibrated against O_2 released from Vienna Standard Mean Ocean Water (VSMOW). The $\delta^{17}O$ and $\delta^{18}O$ are therefore reported on VSMOW scale (13).

To estimate equilibrium water−rock fractionation in triple-isotope space, we used a $\theta_{water-rock}$ = 0.528 [corresponding to T ≈ 350 °C; see Pack and Herwartz (13)]. Uncertainty in θ has a negligible effect, because fractionation in $\delta^{18}O$ is small (Fig. 1A). For fossil sites (Sulu and Karelia), the temperature of water−rock interaction is uncertain. At lower temperatures, $\theta_{water-rock}$ would decrease. As illustrated in Fig. S3, such low T alteration would slightly reduce $\delta^{18}O_{mw}$ estimates.

1. Hoffman PF (2013) The Great Oxidation and a Siderian snowball Earth: MIF-S based correlation of Paleoproterozoic glacial epochs. Chem Geol 362:143–156.
2. Sellers WD (1969) A global climatic model based on the energy balance of the Earth-atmosphere system. J Appl Meteor 8(3):392–400.
3. Pierrehumbert RT, Abbot DS, Voigt A, Koll D (2011) Climate of the Neoproterozoic. Annu Rev Earth Planet Sci 39(1):417–460.
4. Dansgard BW (1964) Stable isotopes in precipitation. Tellus 16(4):436–468.
5. Kennedy M, Mrofka D, von der Borch C (2008) Snowball Earth termination by destabilization of equatorial permafrost methane clathrate. Nature 453(7195):642–645.
6. Zhao Y-Y, Zheng Y-F (2010) Stable isotope evidence for involvement of deglacial meltwater in Ediacaran carbonates in South China. Chem Geol 271(1-2):86–100.
7. Peng Y, et al. (2013) Oxygen isotope composition of meltwater from a Neoproterozoic glaciation in South China. Geology 41(3):367–370.
8. Bindeman IN, Serebryakov NS (2011) Geology, petrology and O and H isotope geochemistry of remarkably ^{18}O depleted Paleoproterozoic rocks of the Belomorian Belt, Karelia, Russia, attributed to global glaciation 2.4Ga. Earth Planet Sci Lett 306(3-4):163–174.
9. Hattori K, Muehlenbachs K (1982) Oxygen isotope ratios of the Icelandic crust. J Geophys Res 87(B8):6559–6565.
10. Yui T-F, Rumble DI, Lo C-H (1995) Unusually low $\delta^{18}O$ ultra-high-pressure metamorphic rocks from the Sulu Terrain, eastern China. Geochim Cosmochim Acta 59(13):2859–2864.
11. Krylov DP (2007) O^{18} depletion in corundum bearing rocks from North Karelija (the Baltic Shield). Water-Rock Interact 7:87–89.
12. Criss RE, Taylor HP (1986) Meteoric-hydrothermal systems. Rev Mineral Geochem 16(1):373–424.
13. Pack A, Herwartz D (2014) The triple oxygen isotope composition of the Earth mantle and understanding variations in terrestrial rocks and minerals. Earth Planet Sci Lett 390:138–145.
14. Pope EC, Bird DK, Arnórsson S (2014) Stable isotopes of hydrothermal minerals as tracers for geothermal fluids in Iceland. Geothermics 49:99–110.
15. Darling WG, Armannsson H (1989) Stable isotopic aspects of fluid flow in the Krafla, Námafjall and Theistareykir geothermal systems of northeast Iceland. Chem Geol 76(3-4):197–213.
16. Zhang RY, Liou JG, Ernst WG (2009) The Dabie–Sulu continental collision zone: A comprehensive review. Gondwana Res 16(1):1–26.
17. Li ZX, et al. (2008) Assembly, configuration, and break-up history of Rodinia: A synthesis. Precambrian Res 160(1-2):179–210.
18. Macouin M, et al. (2004) Combined paleomagnetic and isotopic data from the Doushantuo carbonates, South China: Implications for the "snowball Earth" hypothesis. Earth Planet Sci Lett 224(3-4):387–398.
19. Bindeman IN, Schmitt AK, Evans DAD (2010) Limits of hydrosphere-lithosphere interaction: Origin of the lowest-known ^{18}O silicate rock on Earth in the Paleoproterozoic Karelian rift. Geology 38(7):631–634.
20. Krylov DP (2008) Anomalous $^{18}O/^{16}O$ ratios in the corundum-bearing rocks of Khitostrov, northern Karelia. Dokl Earth Sci 419A(3):453–456.
21. Muehlenbachs K (1998) The oxygen isotopic composition of the oceans, sediments and the seafloor. Chem Geol 145(3-4):263–273.
22. Veizer J, et al. (1999) $^{87}Sr/^{86}Sr$, $\delta^{13}C$ and $\delta^{18}O$ evolution of Phanerozoic seawater. Chem Geol 161(1-3):59–88.
23. Jouzel J, et al. (1997) Validity of the temperature reconstruction from water isotopes in ice cores. J Geophys Res 102(C1):26471–26487.
24. Lee J-E, Fung I, DePaolo DJ, Otto-Bliesner B (2008) Water isotopes during the Last Glacial Maximum: New general circulation model calculations. J Geophys Res 113(D19):D19109.
25. Masson-Delmotte V, et al. (2008) A review of Antarctic surface snow isotopic composition: Observations, atmospheric circulation, and isotopic modeling. J Clim 21(13): 3359–3387.
26. Abbot DS, Voigt A, Koll D (2011) The Jormungand global climate state and implications for Neoproterozoic glaciations. J Geophys Res 116(D18):D18103.
27. Teitler Y, et al. (2014) Investigating the Paleoproterozoic glaciations with 3-D climate modeling. Earth Planet Sci Lett 395:71–80.
28. Warren SG, Brandt RE, Grenfell TC, McKay CP (2002) Snowball Earth: Ice thickness on the tropical ocean. J Geophys Res 107(C10):3167.
29. Bowen GJ, Wilkinson B (2002) Spatial distribution of $\delta^{18}O$ in meteoric precipitation. Geology 30(4):315–318.
30. Rowley DB, Pierrehumbert RT, Currie BS (2001) A new approach to stable isotope-based paleoaltimetry: Implications for paleoaltimetry and paleohypsometry of the High Himalaya since the Late Miocene. Earth Planet Sci Lett 188(1-2):253–268.

EARTH, ATMOSPHERIC, AND PLANETARY SCIENCES

A calibration of the triple oxygen isotope fractionation in the SiO$_2$–H$_2$O system and applications to natural samples

Z.D. Sharp, J.A. Gibbons, O. Maltsev, V. Atudorei, A. Pack, S. Sengupta, E.L. Shock, L.P. Knauth

My contribution to the manuscript: Measurements of triple oxygen isotope values of diatom samples via laser fluorination using F$_2$.

A calibration of the triple oxygen isotope fractionation in the SiO$_2$–H$_2$O system and applications to natural samples

Z.D. Sharp [a,b,⇑], J.A. Gibbons [a], O. Maltsev [a], V. Atudorei [a,b], A. Pack [c],
S. Sengupta [c], E.L. Shock [d,e], L.P. Knauth [d]

[a] Department of Earth and Planetary Sciences, University of New Mexico, 200 Yale Blvd, Albuquerque, NM 87131, USA
[b] Center for Stable Isotopes, University of New Mexico, 200 Yale Blvd, Albuquerque, NM 87131, USA
[c] Geowissenschaftliches Zentrum, Georg-August-Universität, Goldschmidtstraße 1, D-37073 Göttingen, Germany
[d] School of Earth and Space Exploration, Arizona State University, PO Box 871404, Tempe, AZ 85287-1404, USA
[e] School of Molecular Sciences, Arizona State University, PO Box 871404, Tempe, AZ 85287-1404, USA

Abstract

It is now recognized that variations in the $\Delta^{17}O$ of terrestrial materials resulting from purely mass dependent fractionations, though small, have geological significance. In this study, the $\delta^{18}O$ and $\delta^{17}O$ values of selected low temperature quartz and silica samples were measured in order to derive the quartz-water fractionation–temperature relationship for the three oxygen isotope system. A $^{18}O/^{16}O$ quartz-water fractionation equation valid for all temperatures was generated from published high temperature exchange experiments and low temperature empirical estimates and is given by
$1000 \ln \alpha^{18O=16O}_{qz-H_2O} = \frac{4.200 \times 10^6}{T^2} - \frac{3.500 \times 10^3}{T}$ (T in Kelvins). The equilibrium $\delta^{17}O$–$\delta^{18}O$ relationship is given by the equation
$\ln \alpha^{17O=16O} = \theta \ln \alpha^{18O=16O}$. The variation of θ with temperature for the quartz-water system was determined empirically using low temperature marine diatoms, microcrystalline quartz and a modern sinter sample. A best fit to the data give the equation
$\theta_{SiO_2-H_2O} = \frac{-1.85 \pm 0.04}{T} + 0.5305$, indistinguishable from an earlier theoretical estimate.

Application of the quartz-water triple isotope system to low temperature samples provides constraints on both temperature and composition of the water with which the silica last equilibrated. Authigenic quartz crystallization temperatures cluster around 50 °C, which are lower than many previous estimates. The combined $\delta^{18}O$ and $\delta^{17}O$ values of samples considered to be in equilibrium with ocean or meteoric waters can be used to estimate both formation temperatures and the $\delta^{18}O$ value of the meteoric water. Unlike other multiple isotopes systems, such as combined H and O isotopes in cherts, the oxygen source and diagenetic potential for both $^{17}O/^{16}O$ and $^{18}O/^{16}O$ ratios are identical, simplifying interpretations from ancient samples.
© 2016 Elsevier Ltd. All rights reserved.

Keywords: Triple oxygen isotopes; Isotope thermometry; Quartz; Diatoms; Isotope fractionatoin

1. INTRODUCTION

The foundations of stable isotope geochemistry can be traced to the pioneering work by Harold Urey almost 70 years ago (Urey, 1947). There, he laid out the theory of stable isotope fractionation as it pertains to natural systems and within several years, his team published its first estimate of paleo-ocean temperatures using the oxygen isotope ratio of ancient carbonates (Urey et al., 1951). Urey's paleotemperature equation is based on the temperature dependence of the stable oxygen isotope ($^{18}O/^{16}O$) fractionation between calcite and water. In the case of ancient samples, the oxygen isotope composition of the water is

---

⇑ Corresponding author at: Department of Earth and Planetary Sciences, University of New Mexico, 200 Yale Blvd, Albuquerque, NM 87131, USA. Tel.: +1 505 277 0742.
E-mail address: zsharp@unm.edu (Z.D. Sharp).

inferred. Urey recognized this problem, stating "Throughout our discussion we have neglected the possibility and even probability of some variation of the isotopic composition of the waters..." so that "these temperatures are regarded as preliminary" (Urey et al., 1951). Almost 3/4 of a century later, knowledge of the $d^{18}O$ value of ancient waters remains elusive. A number of approaches have been used to address the problem: multiple isotope systems have been combined to constrain the ocean composition (e.g., Knauth, 1973; Hren et al., 2009) and clumped isotope thermometers have been used to eliminate the uncertainties in estimating the $d^{18}O$ value of water (Eiler, 2007).

In this work we add the rare ^{17}O stable isotope as a further constraint on mineral–water fractionation and paleotemperature reconstruction. The early practitioners recognized that

$$d^{17}O \approx \emptyset \, d^{18}O, \left(\text{where } d = \left(\frac{R_{sample}}{R_{standard}} - 1 \right) \times 1000, \text{ and R is the} \right.$$

ratio of the heavy to light isotope) so that measuring the $d^{17}O$ value of a substance provided no additional information to $d^{18}O$ alone (Bigeleisen, 1952; Craig, 1957). In detail, the equilibrium fractionation of ^{17}O relative to ^{16}O between any two phases A and B is given by

$$a^{17}O_{A-B} = (a^{18}O_{A-B})^{h} \tag{1}$$

where

$$a_{A-B} = \frac{R_A}{R_B} \tag{2}$$

and R is the $^{17}O/^{16}O$ or $^{18}O/^{16}O$ ratio of the phase. Because of the near constancy of $h \approx 0.5$ for both equilibrium and kinetic reactions (Craig, 1957), a plot of $d^{17}O$ vs. $d^{18}O$ values of Earth-derived materials gives a near-linear relationship, termed the terrestrial fractionation line or TFL (Clayton, 2003; Rumble et al., 2007). When recast in a linearized format where $d^0 = 1000 \ln \left(\frac{d}{1000} + 1 \right)$ (Miller, 2002), $d_A - d_B = 1000 \ln(a_{A-B})$, and h is given by

$$h_{A-B} = \frac{d^{07}O_A - d^{07}O_B}{d^{08}O_A - d^{08}O_B} \tag{3}$$

The general terrestrial fractionation line using linearized delta values is given as $d^{017}O = k \times d^{018}O + c$. Here, k is the empirical slope of the best fit line and c is the y-intercept, which is often assumed to be equal to 0.

Departures from the terrestrial fractionation line, (which can be very large for extraterrestrial materials and byproducts of stratospheric photochemical reactions, e.g., McKeegan and Leshin, 2001; Thiemens et al., 2012), are expressed in $D^{017}O$ notation. $D^{017}O$ is illustrated in Fig. 1 and given by

$$D^{017}O = d^{017}O - k \times d^{018}O + c \tag{4}$$

The $D^{017}O$ notation was introduced to display small deviations from an otherwise tight correlation between $d^{17}O$ and $d^{18}O$ for terrestrial materials, which is considered as the reference line (RL), with a slope of k_{RL} and y-intercept of c. In the case of equilibrium fractionation between two phases A and B, k is replaced by the more specific term h (Eq. (1)). The intercept c of the RL is chosen as zero in this work in order to obtain a $D^{017}O = 0$ for VSMOW. Various slopes (k) have been suggested for the reference line.
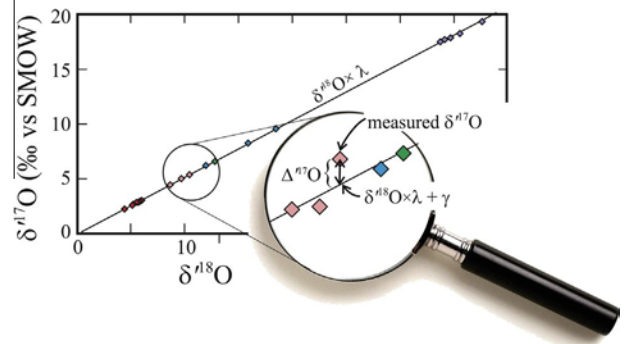

Fig. 1. Illustration of the mathematical significance of $D^{017}O$. The $d^{018}O$–$d^{017}O$ values define a line with a slope k_{RL} and y intercept of c. The difference in the measured $d^{017}O$ value and the $d^{017}O$ value calculated from $d^{018}O \times k + c$ is given by the $D^{017}O$.

Barkan and Luz (2012) and Schoenemann et al. (2013) proposed using the VSMOW and SLAP (Standard Light Antarctic Precipitate) points for the definition of a suitable reference line. The advantage of this procedure is that non-linearity issues (for $d^{18}O$, but also for $d^{17}O$) of the mass spectrometer are eliminated. Under such standardization, the k value is 0.528. We follow this procedure in this communication, where SMOW has $d^{18}O$ and $d^{17}O$ values 0‰, SLAP has $d^{18}O$ value 55.5‰ and a $d^{17}O$ value of 29.699‰. Normalized to a reference line with $k_{RL} = 0.528$ gives a $D^{017}O$ value of 0‰ for both SMOW and SLAP (Schoenemann et al., 2013).

If the k parameter in Eq. (4) were constant under all conditions and all terrestrial materials evolved from a single uniform reservoir, then all samples on Earth would lie on a single curve in $d^{18}O$–$d^{17}O$ space (straight line in $d^{017}O$–$d^{018}O$ space) and the $d^{17}O$ value would provide no additional information to the $d^{18}O$ value alone. Bindeman et al. (2014) demonstrate the near linear relationship between $d^{017}O$ and $d^{018}O$ values for a single locality in Karelia, Russia, with a total spread of $d^{18}O$ values of 30‰ and a k value of 0.5274 ($r^2 = 0.9999$).

For any two minerals in equilibrium, we substitute h for k, indicating a mass-dependent fractionation. From theoretical consideration, h is not constant (Matsuhisa et al., 1978; Young et al., 2002; Cao and Liu, 2011), so that slight variations in $D^{017}O$ occur. For oxygen, h varies between 0.5 and 0.5305 (at T = 1). (Matsuhisa et al., 1978; Young et al., 2002). From theory, Cao and Liu (2011) calculated the temperature dependence of h for various oxides and determined that h decreases with decreasing T. Only a few empirical estimates for equilibrium h values have been reported. Liquid water and water vapor have $h = 0.529$ (Meijer and Li, 1998; Barkan and Luz, 2005), whereas CO_2–water has a $h = 0.523$ (Barkan and Luz, 2012; Hofmann et al., 2012). For the pair biogenic apatite–water, Pack et al. (2013) determined a h value at 37 °C = 0.523. High-T (600–1150 °C) empirical mineral–mineral equilibria for a granite and mantle peridotite give h values of 0.528–0.529 (Pack and Herwartz, 2014). Generally low h values are observed for fractionation processes dominated by kinetics (e.g., Luz et al., 1999; Landais et al., 2006). Mete-

oritic waters scatter around a trend with a slope of 0.528 suggesting fractionation controlled by liquid–vapor equilibrium and a small kinetic component with $h < 0.529$ (Meijer and Li, 1998; Luz and Barkan, 2010). The overall significance of the variable h is that materials which may have evolved from a single homogenized reservoir by different processes and temperatures do not end up falling on a single $d^{17}O$–$d^{18}O$ curve. Subtle, but resolvable departures from a single curve provide information about the formation history of the minerals (e.g., Levin et al., 2014; Passey et al., 2014).

Here, we focus on the quartz/silica–water equilibrium. For the purposes of this paper, we assume that the fractionation between quartz-water and amorphous silica–water are the same (see discussion in Section 5.1). Cao and Liu (2011) calculated $h_{qz\text{-}water}$ as a function of temperature ranging from 0.5242 at 0 oC to 0.5255 at 100 oC. Pack and Herwartz (2014) made an empirical estimate of the quartz-water fractionation using modern sponge spicules. Their h estimate was 0.5212 at rv8 oC. The $d^{18}O$ values of the sponge spicules, however, are lower than expected for the equilibrium silica–water fractionation at 8 oC, likely because they did not remove the light hydration water by stepwise fluorination (Matheney and Knauth, 1989; Dodd and Sharp, 2010). We present data from new samples in order to empirically constrain the temperature dependence of h for silica–water.

2. METHODS

2.1. Analytical procedure

All samples were analyzed by fluorination using BrF_5. Evolved O_2 gas was passed through a 5 Å mol sieve GC column in order to remove traces of NF_3 that would otherwise cause an isobaric interference at mass 33. We have found that this method provides more complete purification than the more commonly employed cryogenic purification technique (Clayton and Mayeda, 1983). Quartz (and silica) were fluorinated using the conventional laser extraction technique (Sharp, 1990) and water was fluorinated in 1/4" nickel tubes heated to rv300 oC for four minutes (O'Neil and Epstein, 1966). Sample size was between 1 and 2 mg for solids and water. In order to achieve high precision $D^{17}O$ analyses, counting times were long, consisting of 3–4 repetitions of 20–30 cycles between reference gas and sample gas in dual inlet. Sample and standard voltages were balanced before each analysis block. Analysis of diatom sample 1094–4073 was made at the University of Göttingen, Germany using a ThermoFinnigan MAT 253 mass spectrometer with amplifier resistors matched for O_2 analysis (300 MX resistor, mass 32, 300 GX resistor, mass 33, 100 GX resistor, mass 34). All other samples were measured at the Center for Stable Isotopes, University of New Mexico using either a ThermoFinnigan MAT 253 or Delta XL Plus mass spectrometer with the same combination of amplifier resistors as above. No differences were observed between data collected on the Delta or MAT 253 mass spectrometers.

Diatoms contain 'structural water' which needs to be removed before analysis. We followed the procedure of Dodd (2011) for our amorphous silica analysis. Samples were reacted with F_2 gas for 30–60 min to remove non-tetrahedral oxygen (H_2O or OH). Samples were then fluorinated using BrF_5. In cases where prefluorination was insufficient to remove all non-tetrahedral oxygen, $d^{18}O$ values were lower than for samples that were completely dehydrated. The $d^{18}O$ values of successive analyses of a single sample reach a 'plateau' value after all water was removed. Nevertheless, even with incomplete water removal, the calculated h values are essentially constant (Fig. A1). The validity of our methodology is demonstrated in a round-robin comparative study by Chapligin et al. (2011).

2.2. Standardization

Standardization is critical when comparing the triple oxygen isotope values of rocks with water. The water community has adopted a two-point calibration based on the standards VSMOW and SLAP. VSMOW, by definition has $d^{17}O = d^{18}O$ 0‰ (and $D^{17}O$ 0‰). SLAP has a $d^{18}O$ value of 55.5‰ (Hut, 1987; Coplen, 1994) and a $D^{17}O = 0$‰ relative to VSMOW for $h = 0.528$, such that the $d^{17}O$ value of SLAP is 29.699 (Schoenemann et al., 2013). Data should be normalized to this scale taking into account possible 'compression' ($D^{18}O_{VSMOW-SLAP} < 55.5$‰) using standard protocols (e.g., Sharp, 2007, Appendix B).

The 'rock' triple-isotope community is generally only peripherally tied to the VSMOW–SLAP scale. This is because very few laboratories routinely measure the triple oxygen isotope compositions of both water and minerals. There are only two published studies in which VSMOW, SLAP and mantle olivine were measured using fluorination (Kusakabe and Matsuhisa, 2008; Tanaka and Nakamura, 2013). Our and previous measurements of VSMOW, SLAP and mantle olivine are given in Table A1 (Appendix A). Data are normalized to VSMOW = 0‰ for $d^{18}O$ and $d^{17}O$. The average $d^{18}O$ and $D^{17}O$ values of SLAP are 55.4‰ and 0.009‰, obviating the need for any stretching correction. The correction for all samples is made by subtracting the difference between the $d^{0x}O_{measured\text{-}SMOW}$–$d^{0x}O_{SMOW}$ from the measured $d^{0x}O$ value of the sample. d^{0x}-O is the linearized value of the sample, $d^{0x}O_{measured\text{-}SMOW}$ is the linearized value of the measured SMOW relative to reference gas and $d^{0x}O_{SMOW}$ is the accepted value of SMOW (=0‰). Uncertainties for SMOW and San Carlos olivine are 0.1‰ for $d^{18}O$ and 0.05‰ for $d^{17}O$ (1r). Because $d^{18}O$ and $d^{17}O$ errors track with each other, the uncertainties for $D^{17}O$ are less than 0.009‰. Errors for $d^{18}O$ and $d^{17}O$ for SLAP are greater than for VSMOW and San Carlos olivine, due to the light nature of the water sample and potential memory effects associated with analyzing a material with such an anomalously low $d^{18}O$ value. The precision of $D^{17}O$ values are as good as for the other materials, demonstrating again the coupled uncertainties of $d^{18}O$ and $d^{17}O$.

The $d^{18}O$ values of San Carlos olivine are higher than the generally assumed value of rv5.3‰ (e.g., Eiler et al., 1995; Ahn et al., 2012; Pack and Herwartz, 2014). It is not clear why there is a discrepancy. Nevertheless, the

$D^{17}O$ value of 0.054 ± 0.008 ‰ is robust because this value is does not vary with the $d^{18}O$ value. All silicate analyses in this work are normalized to a $d^{18}O$ value for San Carlos Olivine of 5.3‰ and a $D^{17}O$ value of 0.054.

3. SAMPLES

Samples analyzed in this study are either silica or quartz that formed at low temperatures. Diatoms from ocean drill cores, microcrystalline quartz from a dredge sample, authigenic quartz crystals from limestone, a water-filled quartz-lined concretion (geode), and modern sinter sample and its formation waters represent our data set. Sample descriptions are given in Appendix B and isotope data are presented in Table 1. For the calibration of the h–T relationship for SiO_2–H_2O, five well-characterized samples were used: diatoms from three high latitude ODP cores in the Southern Ocean, a microcrystalline quartz (MCQ) sample from the Horizon Guyot in the North Central Pacific Ocean and a modern sinter sample from Yellowstone

National Park, WY. For the modern sinter, the $d^{17}O$ and $d^{18}O$ value of the sinter and coexisting water were measured and the water temperature was recorded during sample collection. For the marine samples, $d^{18}O$ and $d^{17}O$ values of 0‰ were assumed. The calibration based on these samples was applied to the other less-well constrained samples to estimate formation conditions.

4. RESULTS

The $d^{18}O$ and $d^{17}O$ values, their linearized equivalents and the $D^{0\,17}O$ values are presented in Table 1. Expected geologic temperatures and those calculated from the $1000 \ln a_{SiO_2-H_2O}^{18O=^{16}O}$ T relationship are also presented in Table 1.

5. DISCUSSION

The goal of this work is to determine the relationship between a_{qz-H_2O} and temperature for both $^{18}O/^{16}O$ and

Table 1
Triple oxygen isotope data for selected materials. The bold samples were used for the best fit of h vs. T. Calculated temperatures from quartz-water fractionations. All data relative to VSMOW. Sample 1094–4073 was analyzed at the U. of Goettingen; all other analyses were made at the UNM.

Sample	Material	T (oC) Calc./assumed	$d^{17}O$	$d^{18}O$	$d^{0\,17}O$	$d^{0\,18}O$	$D^{0\,17}O$ h = 0.528	h
1094–4073-1	Diatom	9/0	21.877	42.208	21.641	41.342	0.187	0.5235
-2		7/0	22.233	42.921	21.989	42.025	0.200	0.5232
-3		4/0	22.823	44.010	22.566	43.069	0.174	0.5240
1093_leg 177-1	Diatom	6/4	22.416	43.170	22.168	42.264	0.147	0.5245
-2		8/4	22.031	42.502	21.792	41.623	0.186	0.5235
-3		7/4	22.208	42.854	21.965	41.961	0.190	0.5235
PS1772-1	Diatom	5/0	22.546	43.465	22.296	42.547	0.169	0.5240
-2		6/0	22.267	42.936	22.023	42.040	0.174	0.5239
-3		5/0	22.437	43.271	22.189	42.361	0.178	0.5237
Horizon Guyot	Chert	17	20.537	39.573	20.329	38.810	0.161	0.5238
				39.4[*]				
1207225 N	Sinter		10.678	20.518	10.621	20.311	0.103	
			9.299	17.797	9.256	17.640	0.058	
			10.953	20.988	10.893	20.771	0.074	
			9.719	18.578	9.672	18.408	0.047	
	Average		10.162	19.470	10.111	19.283	0.047	
120722SN	Water		6.49	12.29	6.51	12.36	0.02	
			6.93	13.20	6.95	13.29	0.06	
			6.57	12.51	6.59	12.59	0.06	
	Average		6.663	12.667	6.683	12.747	0.047	
120722SN 1000 ln(qz-H₂O)		42/47			16.794	32.030	0.117	0.5243
Herkimer diamond	Euhedral quartz		12.433	23.838	12.357	23.558	0.081	
				23.8[**]				
			12.648	24.209	12.569	23.921	0.061	
	Average		12.541	24.023	12.463	23.739	0.071	
Triassic DC609	Euhedral quartz		15.575	29.886	15.455	29.448	0.094	
DC9044	Euhedral quartz		15.390	29.591	15.272	29.161	0.124	
Dover	Chert		13.323	25.465	13.235	25.146	0.042	
Morocco stalactite	Euhedral quartz		13.636	26.113	13.544	25.787	0.071	
Keokuk Geode	Euhedral quartz		14.481	27.716	14.377	27.339	0.057	
	Water		2.57	4.96	2.57	4.97	0.05	

[*] Measurement from Knauth (1973), corrected to VSMOW.
[**] Measurement from Clayton and Epstein (1958).

$^{17}O/^{16}O$. The ratio of these two, namely $\ln a^{18}O_{qz\text{-}H_2O}/\ln a^{17}O_{qz\text{-}H_2O}$ is equal to h. If we measure the $d^{18}O$ and $d^{17}O$ values of silica and water for a sample equilibrated at a known temperature, then we can calculate the h value at that temperature. A best fit of the data passing through $h = 0.5305$ at $T = 1$ gives the h–T relationship.

5.1. The $^{18}O/^{16}O$ quartz-water temperature dependence

In order to expand the $a_{qz\text{-}water}$–T relationship to $^{17}O/^{16}O$, it is first necessary to define a temperature dependent fractionation equation for $a^{18}O_{qz\text{-}water}$. A large number of quartz-water fractionation equations have been published. Here we synthesize published data to obtain an equation that is valid over a full range of temperatures. The quartz-water fractionation has been determined experimentally (O'Neil and Clayton, 1964; Clayton et al., 1972; Matsuhisa et al., 1978, 1979; Matthews and Beckinsale, 1979; Matthews et al., 1983; Hu and Clayton, 2003), theoretically (Shiro and Sakai, 1972; Becker and Clayton, 1976; Kawabe, 1978; Clayton and Kieffer, 1991; Zheng, 1991), empirically (Blattner, 1975; Sharp and Kirschner, 1994), or using a hybrid approach, combining theory and experiments (Bottinga and Javoy, 1973). Temperature of experimental quartz-water fractionation experiments are all above 250 oC. Amorphous biogenic and abiogenic silica-water fractionations have also been determined experimentally or empirically (Knauth and Epstein, 1976; Kita et al., 1985; Leclerc and Labeyrie, 1987; Matheney and Knauth,

1989; Shemesh et al., 1992; Brandriss et al., 1998; Dodd, 2011). The literature data used for our quartz-water oxygen isotope fractionation equation are given in Table 2. We include the results of exchange experiments above 250 oC, inorganic silica precipitation in geothermal waters at intermediate temperatures, and cold-water diatom samples from ocean cores. Where multiple experiments were made at a particular temperature, only the average value of that study was used for our fit. The data of Clayton et al. (1972) were corrected to an $a_{CO_2-H_2O} = 1.0412$ (O'Neil et al., 1975) in place of 1.0407 used in the original study. This puts the $d^{18}O$ value of water (measured as CO_2 equilibrated with water) on the same scale as the other experimental studies.

The fractionation $\ln a$ is proportional to T at high temperatures and T^{-1} at low temperatures (e.g., Criss, 1991). There is no theoretical basis for any one 'correct' mineral–water fractionation equation. High temperature mineral–water fractionation data have been fit to equations of the form

$$1000 \ln a = \frac{a \times 10^6}{T^2} + \frac{b \times 1000}{T} \qquad (5)$$

or

$$1000 \ln a = \frac{a \times 10^6}{T^2} + c; \qquad (6)$$

or a hybrid of these two

$$1000 \ln a = \frac{a \times 10^6}{T^2} + \frac{b \times 1000}{T} + c; \qquad (7)$$

Table 2
Published oxygen isotope data for quartz (silica)–water fractionation. Diatom samples (n = 17, not listed) are from Leclerc and Labeyrie (1987).

1000 ln a	T (oC)	Reference	Notes
9.03	250	Matsuhisa et al. (1978)	
0.64	800	Matsuhisa et al. (1979)	Average of 2 experiments
1.05	700	Matsuhisa et al. (1979)	Average of 9 experiments
1.49	600	Matsuhisa et al. (1979)	Average of 7 experiments
2.31	500	Matsuhisa et al. (1979)	Average of 6 experiments
4.11	400	Matsuhisa et al. (1979)	Average of 6 experiments
6.64	300	Matsuhisa et al. (1979)	1 experimental pair
8.6	265	Matthews and Beckinsale (1979)	Synthesis experiments from silicic acid
5.3	360	Matthews and Beckinsale (1979)	Synthesis experiments from silicic acid
3.6	465	Matthews and Beckinsale (1979)	Synthesis experiments from silicic acid
0.91	750	Clayton et al. (1972)	Corrected $a_{qz\text{-}H_2O}$ from 1.0407 to 1.0412. Used only 100% exchanged results
1.48	650	Clayton et al. (1972)	Corrected $a_{qz\text{-}H_2O}$ from 1.0407 to 1.0412
2.04	580	Clayton et al. (1972)	Corrected $a_{qz\text{-}H_2O}$ from 1.0407 to 1.0412
2.28	550	Clayton et al. (1972)	Corrected $a_{qz\text{-}H_2O}$ from 1.0407 to 1.0412
2.8	490	Clayton et al. (1972)	Corrected $a_{qz\text{-}H_2O}$ from 1.0407 to 1.0412
1.14	750	Hu and Clayton (2003)	Reacted at 1.5 GPa
1.84	600	Hu and Clayton (2003)	Reacted at 1.5 GPa
2.73	500	Hu and Clayton, 2003	Reacted at 1.5 GPa
1.43 ± 0.18	600	Matthews et al. (1983)	Run at multiple pressures. Only partial exchange.
3.99	400	Matthews et al. (1983)	Run at multiple pressures. Only partial exchange
9.12	250	Matthews et al. (1983)	One experiment only
20.65	92.7	Kita et al. (1985)	Empirical. Silica precipitated from geothermal waters
22.84	87	Kita et al. (1985)	Empirical. Silica precipitated from geothermal waters
24.99	80	Kita et al. (1985)	Empirical. Silica precipitated from geothermal waters
28.20	58	Kita et al. (1985)	Empirical. Silica precipitated from geothermal waters
32.56	34	Kita et al. (1985)	Empirical. Silica precipitated from geothermal waters

The constants b and c are related to the high normal modes of vibration for the water molecule (Bottinga and Javoy, 1973). At infinite temperatures, 1000 ln a = 0, so that Eqs. (6) and (7) break down at some temperature above 1000 oC.

A best fit to the high temperature data is shown in Fig. 2a. The data can be fit equally well to Eqs. (5) or (7). The best fit to Eq. (5) over the temperature interval 250–800 oC is given by

$$1000 \ln a_{qz-H_2O}^{18O=16O} \ 1/4 \ \frac{4:20ð0:11Þ \times 10^6}{T^2} \quad \frac{3:3ð0:2Þ \times 1000}{T}$$

$$R^2 \ 1/4 \ 0:9977; \qquad\qquad\qquad ð8Þ$$

where numbers in parentheses represent standard error of each temperature coefficient. We prefer the form of Eq. (5) because it satisfies the necessary condition that a = 1 at infinite temperature. It does suggest, however, that there is a crossover at 1000 oC with 1000ln a_{qz-H_2O} becoming negative above this temperature. Such crossovers are well known in some mineral–water systems (e.g., O'Neil and Taylor, 1969; Saccocia et al., 2009) and are not unexpected. The difference between the measured fractionation and the best fit data are shown by the red points in Fig. 3. All measured and calculated data agree to within 0.4‰ and generally better than 0.3‰.

A best fit over the entire temperature range, including the low temperature inorganic samples (Kita et al., 1985) and diatom data (Leclerc and Labeyrie, 1987; Schmidt et al., 2001, present study) gives the equation

$$1000\ln a_{qz-H_2O}^{18O=16O} \ 1/4 \ \frac{4:28ð0:07Þ \times 10^6}{T^2} \quad \frac{3:5ð0:2Þ \times 1000}{T}$$

$$R^2 \ 1/4 \ 0:9978 \qquad\qquad\qquad ð9Þ$$

shown in Fig. 2b. The best fit for the entire data range is almost identical to the high temperature fit alone (black vs. red curve, Fig. 2a). Eq. (9) gives very similar results to that of Zheng (1993), using a semi-theoretical approach.
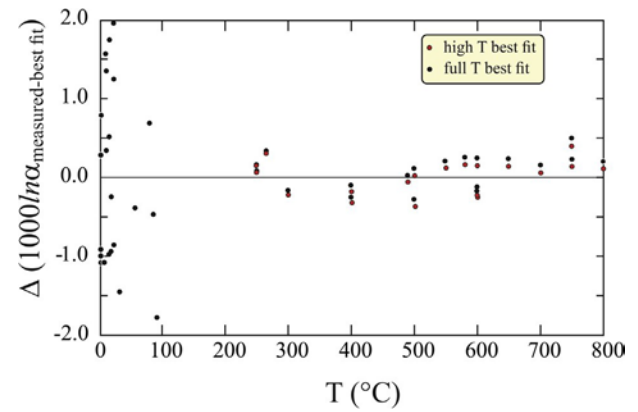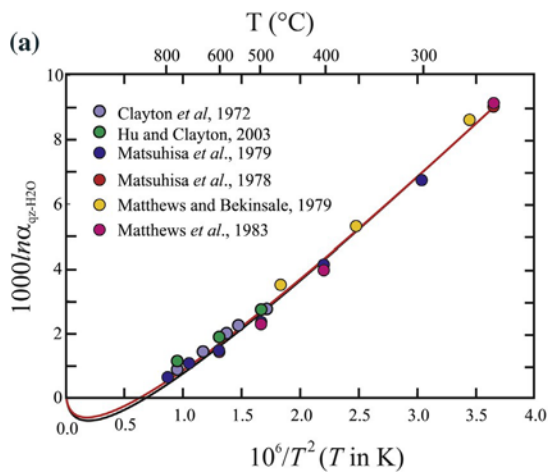

Fig. 3. Difference in the measured 1000 ln $a_{SiO_2-H_2O}$ values and those calculated using Eq. (8) (red circles) and 9 (black circles). The 3‰ scatter at the low temperature end is due to the variability of published $d^{18}O_{diatom}$ data. The best-fit curve over the entire temperature range (Eq. (9)) gives a 1000 ln a value of 44.6‰ at 0 oC, which is within 1‰ of the highest $d^{18}O$ values measured for Antarctic diatoms (Shemesh et al., 1995). (For interpretation of the references to color in this figure legend, the reader is referred to the web version of this article.)

The differences between measured and calculated 1000 ln a values over the entire temperature range are shown as the black points in Fig. 3. The low temperature diatom data have an overall spread of almost 4‰. Shemesh et al. (1992) argued that only diatom data from high latitude sites should be included in a temperature-fractionation calibration to avoid the effects of local upwelling in the more tropical sites. Of equal importance is the possibility that glacial melt water lowered the $d^{18}O$ value of the seawater so that the assumption that the $d^{18}O$ value of the water = 0‰ is not correct. The highest 1000ln $a_{diatom-H_2O}$ values from Antarctic cores are 44–44.5‰ (Shemesh et al., 1995). Our best fit calibration curve passes through 44.6‰ at 0 oC,
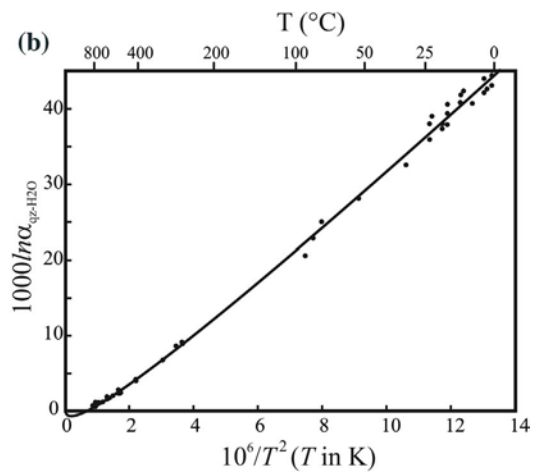
Fig. 2. Best fit for temperature ($10^6/T^2$) vs. 1000 ln a_{qz-H_2O} from published fractionation data (Table 2). (a) Best fit to the experimental data above 250 oC. The best fit is given by the red curve (Eq. (8)). (b) Best fit to the experimental high-T data and the low temperature empirical data (from geothermal sinters and ocean diatom samples) over the entire temperature range (Eq. (9), black curve). (For interpretation of the references to color in this figure legend, the reader is referred to the web version of this article.)

demonstrating that our calibration is applicable to low temperature amorphous silica (diatoms).

A final concern is whether amorphous silica and quartz have the same fractionation. Stolper and Epstein (1991) and Matthews et al. (1994) measured the CO_2–amorphous SiO_2 fractionation from 550 to 950 oC. They compared their measured fractionations to the CO_2–quartz fractionation obtained from a combination of reduced partition function ratios of quartz (Clayton et al., 1989) and CO_2 (Chacko et al., 1991). There was a systematic offset of rv0.3‰, although no difference was seen between measured albite-CO_2 and albitic glass–CO_2 fractionations. Given the uncertainty in the reduced partition functions for quartz, a conclusion regarding the isotopic effect of amorphization of quartz is ambiguous. The lack of fractionation between albite and albite glass in these sample studies (Stolper and Epstein, 1991; Matthews et al., 1994) suggests that amorphization has a negligible effect. We would argue that because the quartz-water and diatom-water data agree so well with each other, that any non-zero fractionation between amorphous silica and quartz can safely be ignored for the purpose of this study. The excellent agreement of the semi-theoretical quartz-water calibration of Zheng (1993) with our diatom-based calibration further validates the assumption that the quartz-water and amorphous silica–water fractionations are very nearly the same.

5.2. Triple oxygen isotope analyses

5.2.1. h–T relationship

Our empirical calibration of $h_{qz-water}$ is based on five samples: two diatom samples from the Antarctic Zone of the Southern Ocean where the ocean temperature and water isotope composition are well constrained, a microcrystalline quartz sample from the Central Pacific in equilibrium with ocean water and a modern sinter with coexisting water and a measured formation temperature. Diatoms were analyzed following the method of Dodd (2011). Multiple aliquots of the same sample were loaded into a sample holder and pre-fluorinated to remove hydroxyl and H_2O oxygen. Nevertheless, we found that the $d^{18}O$ and $d^{17}O$ values of the two diatom samples increased with each successive analysis (Table 1), indicating that not all of the water was removed during prefluorination in the early analyses. The last-analyzed samples should be closest to the true values and indeed give formation temperatures closer to those expected for growth in Antarctic waters. These were used for our calibration. Regardless of the measured $d^{18}O$ values, the h values determined for each successive analysis are identical within ±0.0002 (Fig. A1), a finding also observed by Rumble et al. (2007). Therefore, although there may be some uncertainty in the true $d^{18}O$ value of the diatoms, the calculated h values are robust.

Temperature estimates for the diatoms depend on the corresponding $d^{18}O$ value of the ocean. Assuming modern $d^{18}O$ values for seawater, temperature estimates range from 4 oC (sample 1094) to 17 oC (1093 and Horizon Guyot). Both diatom samples are from glacial periods when increased continental ice should increase the $d^{18}O$ value of the ocean. Schrag et al. (2002) measured the $d^{18}O$ value

of pore waters from Leg 177, Hole 1093 and calculated $d^{18}O$ values of seawater during the Last Glacial Maximum to be 1‰ higher than the modern. Assuming a similar increase during Marine Isotope Stage 10 for sample 1093, temperature estimates for both diatom samples are increased by 3 oC. These temperatures are clearly too high and suggest that either the quartz-water calibration is incorrect, a fraction of H_2O remained in the diatom during fluorination, or sample purification was not 100%. The Horizon Guyot MCC sample could be as old as mid-Eocene, with $d^{18}O_{ocean\ water}$ of rv 0.6‰. If it equilibrated with this lighter water, the temperature estimate decreases by 2 oC. The error introduced by the uncertainties in the $d^{18}O_{water}$ value is a factor of 6 less than the error of the best fit.

A final consideration is the corresponding change in $d^{17}O$ value of the ocean during transfer of ice to the continents during glacial periods. We assume that the $d^{18}O$ value of continental ice is 30‰. Removing rv3% of the ocean to continental ice with a $d^{18}O$ value of 30‰ and corresponding $d^{17}O$ value of 15.973‰ (Luz and Barkan, 2010) will change the calculated h value by only 0.0002. The transfer of a few percent of water to the continents has a trivial effect on our h determinations.

A best fit of h vs. temperature using the low temperature diatom, microcrystalline quartz and sinter data (Fig. 4), as well as a h = 0.5305 at T = 1, gives the following equation for qz-H_2O:

$$h_T \ \frac{1}{4} \ \frac{\eth 1:85 \ \pm \ 0:04\th}{T} \ \th 0:5305 \quad R^2 \ \frac{1}{4} \ 0:9998; \qquad \eth 10\th$$
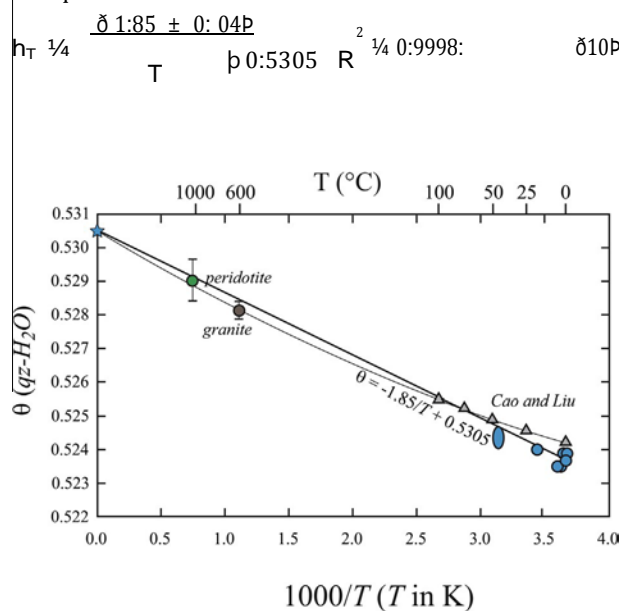
Fig. 4. Temperature–h plot for low-temperature samples. Our data (Table 1 and shown as blue circles) are fit with a curve passing through the high temperature theoretical limit (h = 0.5305, shown by blue star) with a slope of 1.85/T (T in K). The published theoretical values for quartz-water are from Cao and Liu (2011, gray triangles) and their best fit (curved line). Error in h estimate for the diatom samples is ±0.0001, smaller than the size of the symbols. Also shown are the empirical h estimates for silicate mineral fractionations from a granite (assumed T = 620 oC) and mantle xenolith (assumed T = 1050 oC) from Pack and Herwartz (2014). (For interpretation of the references to color in this figure legend, the reader is referred to the web version of this article.)

The temperature for each sample was estimated using the measured $1000 \ln a_{SiO_2-H_2O}$ value and Eq. (9). If instead we use the assumed temperatures of formation for these samples (e.g., near-zero for Antarctic diatoms), the constant in Eq. (10) changes from 1.85 to 1.81. This difference corresponds to change in θ at 0 oC of only 0.0002.

The θ values for mineral–mineral pairs in a granite and peridotite are also shown in Fig. 4. These values are based on the fractionation between coexisting silicates (Pack and Herwartz, 2014) and have moderately large uncertainties. Nevertheless they plot precisely on our θ–T curve even though they are for anhydrous mineral fractionation. This result suggests that mineral–mineral and mineral–water θ values converge at temperatures above 600 oC. What is clear is that the effect of temperature on θ is most dramatic at low temperatures (Fig. 5). The $d\theta/dT$ value at 700 oC is an order of magnitude less than at 0 oC. All igneous and high-grade metamorphic rocks should fractionate with a θ value between 0.528 and 0.529.

The theoretical quartz-water data from Cao and Liu (2011) are also shown in Fig. 4. They are identical to our results within analytical uncertainty. The Cao and Liu data show that the θ–T relationship is a function of $1/T$ and $1/T^2$. Given the limited temperature range of our calibration, we are able to fit our data equally well with only a $1/T$ term, although a second-order term may be required when data from intermediate temperature (250–500 oC) samples are acquired.

5.2.2. Application to natural samples

Combining Eqs. (9) and (10) gives the fractionation for $^{17}O/^{16}O$ as a function of temperature. From the relationship $\ln a^{17O=16O} = \theta \ln a^{18O=16O}$, the quartz-water $^{17}O/^{16}O$ fractionation is given by

$$1000 \ln a^{17O=16O}_{qz-H_2O} = \left(\frac{4.28 \times 10^6}{T^2} - \frac{3500}{T} \right)\left(0.5305 - \frac{1.85}{T} \right); \tag{11}$$

and

$$D^{0^{17}}O = \left(\frac{4.28 \times 10^6}{T^2} - \frac{3500}{T} \right)\left(0.5305 - \frac{1.85}{T} - k_{RL} \right) \tag{12}$$
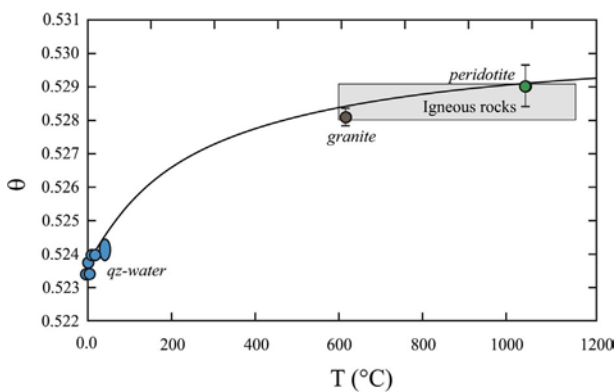

Fig. 5. Plot of θ vs. T (oC) showing the dramatic effect of changing θ at low temperatures. Above 600 oC, the θ value is nearly constant at 0.528–0.529 (gray rectangle). Data as in Fig. 4.

where k_{RL} is the chosen slope of the RL. A number of different k_{RL} values have been used in the literature. There is no 'correct' k_{RL} value, and presently no agreement on a 'standard' k_{RL} value. We wish to point out that in fact, all interpretations and conclusions are completely independent of assumed k_{RL}. It is simply a bookkeeping tool for illustrating small differences in the measured and expected $d^{17}O$ values (e.g., Pack and Herwartz, 2014). Appendix C illustrates this concept. We adopt a value of $k = 0.528$ in keeping with the hydrology literature and because it is close to the high temperature limit seen in natural materials.

Our data for samples equilibrated with ocean water can be plotted as $1000 \ln a^{18O=16O}_{qz-H_2O}$ vs. $D^{0\,17}O$ (Fig. 6), where each point on the curve gives the equilibrium values for a particular temperature. (Note that $1000 \ln a_{x-y} = d^0_x - d^0_y = D^0_{x-y}$, where the ^{0} indicates a linearized d value). In this plot, T is removed as a variable, which allows for the $D^{0\,17}O$ value to be computed as a function of $\ln a^{18O=16O}_{qz-H_2O}$ for all temperatures. (See Appendix D for derivation.). The utility of the three-isotope system is clear. With the $d^{18}O$ value alone, it is impossible to ascertain whether a sample was in equilibrium with ocean water or underwent later diagenesis with a meteoric component. When plotted in $D^{0\,17}O$–$d^{0\,18}O$ space, additional information is gained. If a particular sample does not lie on the curve in Fig. 6, it cannot have been in equilibrium with ocean water at any temperature.

A second example of the utility of the three isotope system is in an application to authigenic quartz crystals from an 'unaltered' Triassic limestone from Romania. The $d^{13}C$ and $d^{18}O$ values of the limestone are consistent with formation from ocean water at rv20–22 oC with minimal diagenesis (Appendix B). Conodonts, agglutinated foraminifera and mm-size doubly-terminated authigenic quartz crystals are found as trace phases in the limestone. The $d^{18}O$ values of quartz crystals are only 1‰ higher than the calcite, clearly indicating that the two phases are not in equilibrium (Sharp and Kirschner, 1994). The source of the diagenetic
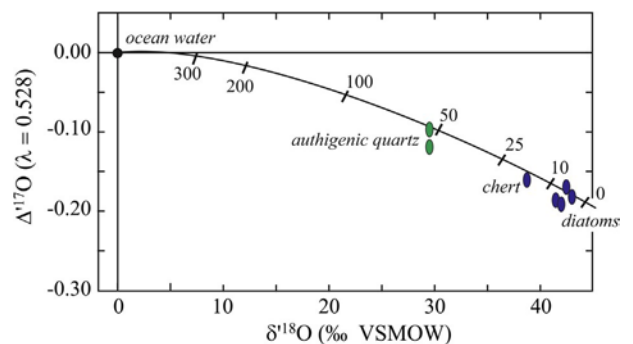
Fig. 6. $D^{0\,17}O$–$d^{0\,18}O$ plot of quartz or amorphous silica in equilibrium with ocean water. The curved line is the equilibrium quartz values as a function of temperature. Any sample that does not plot on the line cannot be in equilibrium with ocean water. The position of a sample on the curve provides the equilibrium temperature. Note: the samples plotted in this figure were used to generate the curve. Oval shapes illustrate 1r errors in $D^{0\,17}O$ values. Errors in $d^{018}O$ values are less than the thickness of each point.

fluid responsible for the authigenic quartz crystals is indeterminate from the $d^{18}O_{qz}$ values alone. When taken together, however, the $d'^{18}O$–$d'^{17}O$ values of the quartz plot precisely in equilibrium with seawater at rv50 oC (Fig. 6). These results suggest that the quartz formed by dissolution of metastable sponge spicules (e.g., Williams et al., 1985) and re-precipitation as quartz at 50 oC in non-lithified, bioturbated sediments with porewaters that had a seawater isotopic composition. The 50 oC recrystallization value is in good agreement with independent estimates for opal-A to opal-CT transition temperatures (Keller and Isaacs, 1985), but considerably below an estimate of 80 oC for the opal-CT to quartz transition (Murata et al., 1977). Interestingly, the calcite has not isotopically re-equilibrated at 50 oC presumably because the calcite was in chemical equilibrium with the porewater and therefore did not undergo any recrystallization during heating (e.g., O'Neil, 1977).

The curve in Fig. 6 can be 'flipped' so that it represents the $D'^{17}O$–$d'^{18}O$ values of water in equilibrium with quartz of a particular composition. In Fig. 7, the average oxygen isotope composition of sinter sample 120722SN and corresponding water are plotted along with the global meteoric water line (Luz and Barkan, 2010; Li et al., 2015). Also shown is the range of $d^{18}O$ values for Yellowstone cold and hot waters (Kharaka et al., 2002). The sinter and coexisting thermal water plot in $^{18}O/^{16}O$ and $^{17}O/^{16}O$ equilibrium with each other at rv42 oC, in excellent agreement with the measured temperature of 47 oC. The water is at the high end of the $d^{18}O$ values for thermal waters for Yel-
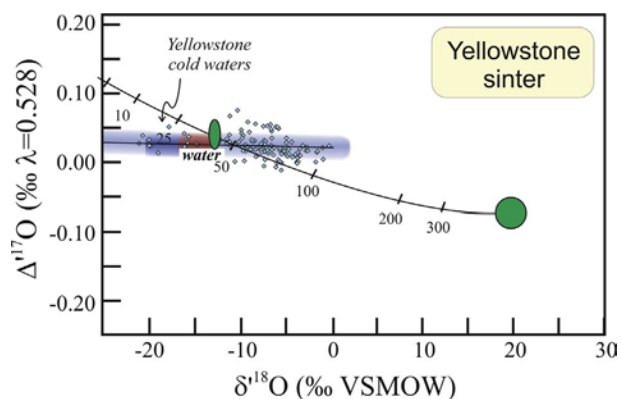
lowstone and suggests that boiling has modified the $d^{18}O$ and $d^{17}O$ water values from the primary meteoric value.

For samples that are thought to have formed in equilibrium with meteoric water, the triple oxygen isotope composition of a single mineral can be used to estimate both the temperature and $d^{18}O$ value of the meteoric water. The concept is illustrated for two crystalline quartz-filled nodules (geodes) and the famous doubly-terminated Herkimer Diamond quartz samples (New York, USA) in Fig. 8. The first sample is a 'stalagtitic' quartz geode (Fig. 9) from Morocco (precise locality unknown). The optical-grade quartz is oriented as parallel crystalline 'stalactites' or fingers, each with a central microcrystalline core. It appears that the crystal fingers formed from water migrating through the core (tube?), leading to crystallizing at the tip of the growing finger. The second is a Keokuk geode from Hancock County, Illinois. This geode contained liquid water, so that we were able to measure the isotopic composition of both the water and quartz. We recognize that there is a reasonable possibility that the water may postdate the formation of the quartz. Nevertheless, the combined isotope data allow us to assess possible equilibrium and temperature of formation.

The equilibrium water curve for the Moroccan sample crosses the field of meteoric water at rv50 oC and a $d^{18}O$ value of meteoric water between 7.5‰ and 4.0‰ (green point, heavy black curve in Fig. 8). By assuming only that the mineralizing fluid was meteoric water, we are able to determine both the formation temperature and local meteoric water value of this sample. Our estimate for the $d^{18}O$ value of meteoric water is precisely in the range of modern meteoric water in Morocco (Winckel et al., 2002; Ettayfi

Fig. 7. $D'^{17}O$–$d'^{18}O$ plot of water in equilibrium with quartz/silica. This plot is similar to that shown in Fig. 6 except that the origin is now the mineral, and the curve represents the $D'^{17}O$–$d'^{18}O$ values of water in equilibrium with a specific quartz/silica sample. Sample 120722SN is a modern sinter sample. The curve originating at the silica $D'^{17}O$–$d'^{18}O$ values passes through the measured $d'^{18}O$–$D'^{17}O$ water values at 42 oC, in good agreement with the measured temperature in the spring of 47 oC. The curve also shows published $d'^{18}O$–$D'^{17}O$ values for meteoric water (Luz and Barkan, 2010; Li et al., 2015) and the range of hot (red) and cold (blue) $d'^{18}O$ values for Yellowstone waters (Kharaka et al., 2002). The large uncertainties in $d'^{18}O$ and $D'^{17}O$ values for sinter probably reflect sample heterogeneity due to variable isotopic composition of water and temperature. (For interpretation of the references to color in this figure legend, the reader is referred to the web version of this article.)

Fig. 8. Triple isotope values of three authigenic quartz samples. Waters in equilibrium with the Moroccan geode (shown in Fig. 9) are defined by the thick black curve. They cross the meteoric water band in the range 7‰ to 4‰ at 40 to 50 oC. This is in good agreement with the $d'^{18}O$ values of modern Moroccan meteoric water (gray band, Winckel et al., 2002; Ettayfi et al., 2012). The Keokuk geode and included water plot in near equilibrium at rv40 oC (red curve). The Herkimer diamond samples could be in equilibrium with meteoric water at rv50 oC, or could be a mixture of meteoric waters and pore waters at at higher temperature rv80 oC (curves not shown). (For interpretation of the references to color in this figure legend, the reader is referred to the web version of this article.)

Fig. 9. Moroccan geode showing stalagtitic 'fingers' of quartz. The appearance suggests that the quartz precipitated from drip waters that migrated through the open tubes in the center of each finger. Red oval highlights a cut section showing the microcrystalline core of the 'fingers'. Width of geode is 13 cm. (For interpretation of the references to color in this figure legend, the reader is referred to the web version of this article.)

et al., 2012). The 50 °C temperature is the same as the authigenic quartz crystals from the Triassic limestone.

The Keokuk geode and the water filling the cavity appear to be in near-equilibrium with each other. The $D^{18}O_{qz-H_2O}$ value alone would be ambiguous, but the near perfect fit of the geode and water for both isotope systems (red curve in Fig. 8) suggests that the water could be formation water, or at least has the same isotopic composition of formation water. The Herkimer diamond sample also appears to be in equilibrium with meteoric water at 50 °C (curve not shown). In all, the Romanian authigenic quartz, the Keokuk geode, the Moroccan 'stalactite' and the Herkimer diamond all have a near 50 °C formation temperature, suggesting that in general, amorphous silica may transform to quartz at rv50 °C.

6. CONCLUSIONS

Adding $^{17}O/^{16}O$ ratios to the oxygen isotope mix takes the oxygen isotope system from a one dimensional line to a curve in a two dimensional plane. The $d^{18}O$ values of solid samples have long been used to estimate the temperature by assuming a formation water value, but obviously, there is an unavoidable ambiguity in the temperature estimate because the actual $d^{18}O_{water}$ value is not known. A $d^{18}O_{silica}$ value of 35‰ could be in equilibrium with ocean water at 30 °C, but it could also be in equilibrium with a lighter meteoric water at a lower temperature. There simply is no unique solution. In the three-isotope system, a measured $d^{18}O$ value requires a specific corresponding $d^{17}O$ value to be in equilibrium with water of a specific composition. For a measured $d^{18}O_{silica}$ value of exactly 30‰, the $d^{17}O$ value must be 15.63‰ to satisfy the condition that it could have been in equilibrium with ocean water. Any other $d^{17}O$ value would conclusively demonstrate that this silica sample was not in equilibrium with ocean water under any

temperature conditions. Similarly, if a sample is thought to have equilibrated with meteoric water, then the intersection of the $d^{18}O–D^{17}O$ curve with the meteoric water field (as in Fig. 8) provides both the $d^{18}O_{water}$ values and formation temperature. We recognize that the $d^{18}O–D^{17}O$ meteoric water line is actually a band and not a discreet line, but as more data are obtained regionally, the meteoric water line will become further constrained for a given geographic location and time period (Li et al., 2015).

Multiple isotope systems have been used to constrain temperature and/or meteoric water values of authigenic minerals. For example, researchers have combined H and O isotopes from cherts to place further constraints on formation conditions (e.g., Knauth and Epstein, 1976; Hren et al., 2009). This approach has a number of complicating factors. Are both isotope systems in equilibrium with the formation waters? Were both isotope systems inherited from the same source at the same time? Has one or both undergone later diagenesis? The 'diagenetic potential' of these two elements could be vastly different. For example, hydrogen may be more easily exchanged than oxygen. For $d^{18}O$ and $d^{17}O$, the diagenetic potential as well as source are identical. None of the abovementioned problems exist in the triple oxygen isotope system.

Most laboratories that have laser fluorination systems for traditional oxygen isotope analysis can relatively easily modify their system for simultaneous analysis of $^{16}O^{16}O$, $^{17}O^{16}O$, and $^{18}O^{16}O$. As more data are collected, the picture for nascent triple oxygen isotope system will become clearer and better defined.

APPENDIX A. STANDARDIZATION

Data for standards VSMOW, SLAP and San Carlos olivine are shown in Table A1. Data are normalized to VSMOW, such that the $d^{17}O$, $d^{18}O$ and $D^{17}O$ values are all 0‰. All other data are corrected by subtracting the $d^{0x}O_{ref\ gas}–d^{0x}O_{VSMOW}$ (or $D^{017}O_{ref\ gas}–D^{017}O_{VSMOW}$) from each analysis. $d^{0x}O_{ref\ gas}$ is the linearized measured $d^{0x}O$ (or calculated $D^{017}O_{ref\ gas}$) of VSMOW and $d^{0x}O_{VSMOW}$ (and $D^{017}O_{VSMOW}$) are the accepted values of VSMOW   0‰. Uncertainties for $d^{17}O$ and $d^{18}O$ analyses are ±0.05 and ±0.1‰ (1r). Uncertainties for $D^{017}O$ are less than 0.01‰ (1r). The higher precision for $D^{17}O$ is due to the

Table A1

Measured oxygen isotope compositions for water and olivine standards with corrected reference to give VSMOW = 0‰. $D^{17}O^0$ values are for the equation $D^{17}O^0 = d'^{17}O^0 - 0.528 \times d'^{18}O^0$. Also shown are published values for SLAP and olivine. Bold values are averages.

	$d^{17}O$	$d^{18}O$	$d'^{17}O^0$	$d'^{18}O^0$	$D'^{17}O^0$
VSMOW	0.113	0.210	0.113	0.210	0.002
	0.038	0.088	0.038	0.088	0.008
	0.052	0.100	0.052	0.100	0.001
	0.022	0.021	0.022	0.021	0.011
	0.018	0.046	0.018	0.046	0.007
	0.015	0.052	0.015	0.052	0.013
	0.003	0.018	0.003	0.018	0.007
	0.030	0.079	0.030	0.079	0.012
Average	**0.000**	**0.000**	**0.000**	**0.000**	**0.000**
Stdev	0.052	0.103	0.052	0.103	0.009
SLAP	29.488	55.080	29.932	56.655	0.018
	29.213	54.580	29.648	56.126	0.014
	29.758	55.589	30.210	57.194	0.012
	29.915	55.896	30.372	57.519	0.002
	29.875	55.823	30.331	57.442	0.001
Average	**29.650**	**55.394**	**30.099**	**56.987**	**0.009**
Stdev	0.296	0.556	0.305	0.588	0.007
SLAP[a]	29.21	54.65	29.645	56.200	0.029
SLAP[b]	29.44	55.02	29.882	56.592	0.002
SCO	2.835	5.493	2.831	5.478	0.061
	2.850	5.488	2.846	5.473	0.043
	2.819	5.455	2.815	5.440	0.057
	2.922	5.656	2.918	5.640	0.060
	2.907	5.604	2.903	5.588	0.047
	2.907	5.646	2.903	5.630	0.069
	2.913	5.633	2.909	5.618	0.057
	2.943	5.687	2.939	5.670	0.055
	2.956	5.689	2.952	5.672	0.043
	2.883	5.553	2.879	5.538	0.045
	2.900	5.610	2.896	5.595	0.058
	2.798	5.409	2.794	5.394	0.054
Average	**2.886**	**5.577**	**2.882**	**5.561**	**0.054**
Stdev	0.050	0.095	0.050	0.094	0.008
SCO[a]	2.89	5.26	2.886	5.246	0.116
Olivine[b]	2.70	5.28	2.696	5.266	0.084

[a] (Kusakabe and Matsuhisa, 2008).
[b] (Tanaka and Nakamura, 2013).

covariance of $d^{17}O$ and $d^{18}O$ such that the $D^{17}O$ remains constant regardless of small variations in the measured $d^{18}O$ value.

Fig. A1 plots the measured $d^{17}O$ and $d^{18}O$ values of three analyses of diatom sample 1094–4073. The $d^{18}O$ values increase with increasing degrees of prefluorination, but all samples lie on the same line passing through the ocean water value (assumed $d^{17}O = d^{18}O = 0‰$). The slope of the line is h and is the same for all three analyses.

APPENDIX B. DESCRIPTION OF SELECTED SAMPLES

1093-Leg 177–A-23-H-4-W – From ODP Leg 177, Hole 1093. Located farther to the north than Hole 1094 at the present day polar front zone, with $d^{18}O$ values of carbonate rv0.5–1‰ heavier than sample 1094 (Hodell et al., 2003). Sample from 109.0 to 111.0 meters composite depth (mcd). Age: rv400 ka, MIS 10.

1094–4073 – From ODP Leg 177. Hole 1094 drilled at 53oS. Water depth – 2807 m. Location is in the present ice-free Antarctic Zone, but was covered by sea ice during last glaciation (Gersonde et al., 1999). The $d^{18}O_{calcite}$ for this core range from 3.5‰ to 4.5‰ (Hodell et al., 2003) relative to PDB, consistent with a 0 oC temperature and $d^{18}O_{ocean}$ of 1‰ to 0‰. From 21.77 m depth rv111 k.a MIS 5d. Donated by Aldo Shemesh. Measured in Goettingen. All other samples measured at UNM.

120722SN: Hot spring sinter and water – Sampled in 22 July 2012 from a mid-range temperature spring (44o41^{0}58.43^{00}N, 110o46^{0}1.94^{00}W) at Sylvan Springs in Yellowstone National Park as part of a long-term project to quantify connections between the geochemical compositions of hot springs and the microbial communities they support. Additional data from an earlier sample of this spring are reported by Windman et al. (2007) (sample 040718U).

Chert from Horizon Guyot – Dredged during an investigation of Horizon Guyot, Pacific Ocean. 168o52.3^{0}W, 10o 28.0^{0}N, 1700 m water depth. Transmitted to Paul Knauth by Harmon Craig. Greater than 98% granular microcrystalline quartz. $d^{18}O = 38.85‰$ by Knauth (1973).
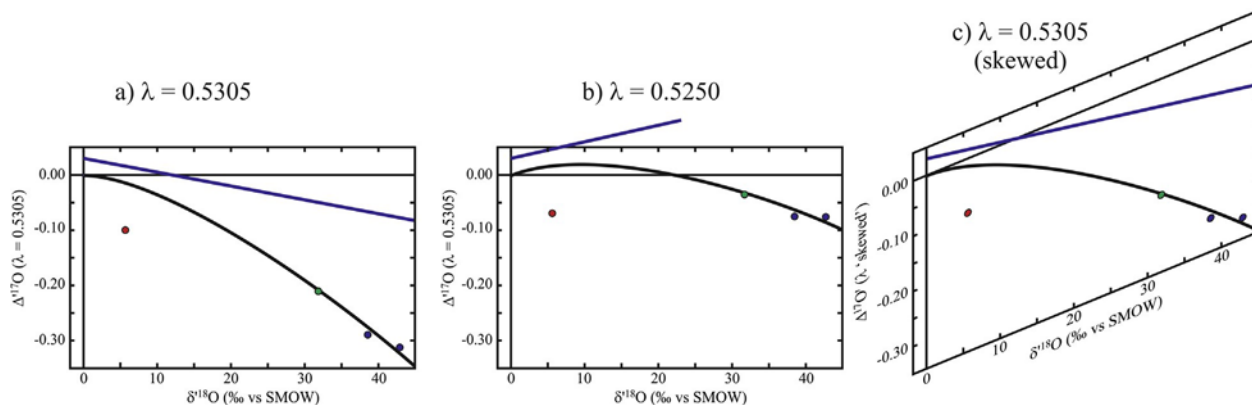

Fig. A1. Graphical illustration of k. (a) and (b) are the same data with different k_{RL} values. (c) Is the result of (a) sheared upward on the right side. The curves in (b) and (c) are identical. Data points are not representative of any sample, but illustrate how sample data scale proportionally with equilibrium curves regardless of assumed k.

DC 609, 9044 – Early-Middle Triassic transition marine pelagic limestone from North Dobrogea, Romania (Atudorei, 1999). Trace phases include minor conodonts, agglutinated foraminifera and mm-sized doubly-terminated euhedral quartz crystals. These samples do not contain sponge spicules, although they are found in equivalent lithologies elsewhere. The lithologies are strongly bioturbated. Carbonate isotope values: DC 9044; d^{13}C = 4.53 and d^{18}O = 2.35‰ PDB. DC 9045; d^{13}C = 4.40 and d^{18}O = 2.48‰ PDB. d^{18}O$_{calcite}$ values correspond to a temperature of 20–22 oC for a d^{18}O$_{ocean}$ = 1‰ (vs. SMOW).

Herkimer diamond – Cambro-Ordovician silicified dolomite hosted quartz crystals. Optically pure doubly terminated glassy crystals.

Keokuk geode – Keokuk geode from the lower Warsaw formation, Hancock County, Illinois. Sample contained liquid water which was extracted by drilling through the geode wall.

Moroccan stalagtitic geode – sample of unknown origin. Purchased in Morocco by K. Zielger. The geode is filled with parallel coarsely crystalline quartz fingers forming in an open cavity (Fig. 9). Each finger has a tube-like central shaft which presumably acted as a conduit for water migration to the growing tip of each stalagtitic finger. The outer layers of the stalactites are composed of optically pure quartz crystals, whereas the interior shaft is microcrystalline. We analyzed the coarse optically pure material.

PS1772-8 – Diatom-rich section of a sediment core from the Southern Ocean (Lat: 55.4583, Long: 1.1633 (Gersonde and Hempel, 1990). The sample was deposited in Marine Isotope Stage 5. The purified diatom sample is 99.49% silica (Chapligin et al., 2011) with a d^{18}O value from a laboratory intercomparison of 42.8‰. Our value of 43.5‰ is identical to our previous analysis (UNM: 43.5 ± 0.1‰, n = 10) of this sample (Chapligin et al., 2011).

APPENDIX C. THE (LACK OF) SIGNIFICANCE OF k$_{RL}$

A triple isotope reference line (RL), whether it be considered as a Terrestrial Fractionation Line (Clayton, 2003; Kusakabe and Matsuhisa, 2008), a meteoric water line (Luz and Barkan, 2010) or a more generic format, is used to illustrate small displacements of a particular sample from that reference line (Fig. 1). The choice of the reference line does not have any mathematical or geological significance in and of itself. Temperatures, etc. are all based on Eqs.

(1)–(5) and (8)–(12). The reference k is not in the mathematics. This is illustrated in Fig. C1, where the same data are plotted in D$^{0 17}$O–d$^{0 18}$O space for three different k values. The points are arbitrary values. The red spot is a typical mantle composition, the green and blue points are low temperature samples. The curved line is the quartz-water equilibrium curve and the straight blue line is an extension of the MWL to positive d^{18}O values. Although Fig. C1a (k = 0.5305) and Fig. C1b (k = 0.525) appear very different, they actually convey identical information. Fig. C1c is generated by taking Fig. C1a and skewing the right edge upward. The lines and points in Fig. C1c exactly match those in curve C1b.
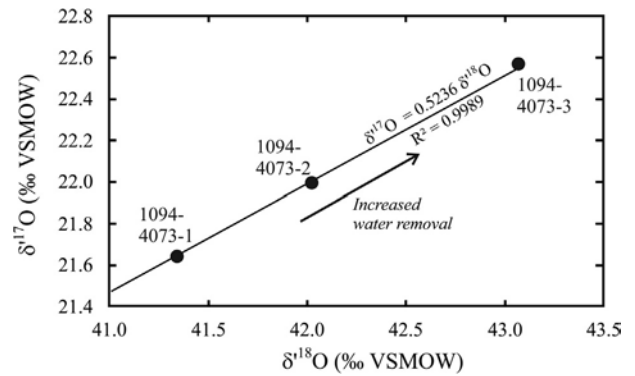

Fig. C1. d$^{0 17}$O–d$^{0 18}$O plot of multiple analyses of diatom sample 1094–4073. Each successive analysis gave a higher d^{18}O value due to more complete removal of structural 'water'. Nevertheless, all samples plot on a curve passing through the origin with a resultant h value of 0.5236 ± 0.0004, illustrating the covariance of d$^{0 17}$O and d$^{0 18}$O.

APPENDIX D. DERIVATION OF THE D$^{0 17}$O–D$^{0 18}$O CURVE

The fractionation between phases x and y is given by

$$1000 \ln a^{18O}_{x\ y} = \frac{a \times 10^6}{T^2} - \frac{b \times 10^3}{T} \quad :; \qquad (D1)$$

and

$$1000 \ln a^{17O}_{xy} = \left(\frac{a \times 10^6}{T^2} - \frac{b \times 10^3}{T} \right) h_{xy} \qquad (D2)$$

From Eq. (4),

$$D^{0 17}O = \frac{\left(\frac{a \times 10^6}{T^2} - \frac{b \times 10^3}{T} \right) h_{xy}}{\left(\frac{a \times 10^6}{T^2} - \frac{b \times 10^3}{T} \right) k_{RL}} \qquad (D3)$$

For

$$h_{x\ y} = \frac{c}{T} + 0.5305 \qquad (D4)$$

Equation (D3) can be rewritten as

$$D^{d7}O = \frac{\left(\frac{a \times 10^6}{T^2} - \frac{b \times 10^3}{T} \right) \left(\frac{c}{T} + 0.5305 \right)}{k_{RL}} \qquad (D5)$$

k$_{RL}$ is the chosen value in order to display D$^{0 17}$O. Commonly, k$_{RL}$ is taken as 0.52, 0.528 or 0.5305, although the choice of k$_{RL}$ is discretionary and does not affect any of the results.

Equation (D1) can be rearranged to solve for temperature, given by the following equation where D^0 = 1000 ln a$_{x-y}$ = d$^{0 18}$O$_x$–d$^{0 18}$O$_y$

$$T (K) = \frac{b \pm \sqrt{b^2 + 4 a D^0}}{2D^0} \qquad (D6)$$

Substituting the right side of equation D6 into D5 gives the solution for D$^{0 17}$O as a function of D^0.

REFERENCES

Ahn I., Lee J. I., Kusakabe M. and Choi B.-G. (2012) Oxygen isotope measurements of terrestrial silicates using a CO_2-laser BrF_5 fluorination technique and the slope of terrestrial fractionation line. Geosci. J. **16**, 7–16.

Atudorei V. (1999) Constraints on the Upper Permian to Upper Triassic Marine Carbon Isotope Curve. Case Studies from the Tethys. University of Lausanne, p. 161.

Barkan E. and Luz B. (2005) High precision measurements of $^{17}O/^{16}O$ and $^{18}O/^{16}O$ ratios in H_2O. Rapid Commun. Mass Spectrom. **19**, 3737–3742.

Barkan E. and Luz B. (2012) High-precision measurements of $^{17}O/^{16}O$ and $^{18}O/^{16}O$ ratios in CO_2. Rapid Commun. Mass Spectrom. **26**, 2733–2738.

Becker R. H. and Clayton R. N. (1976) Oxygen isotope study of a Precambrian banded iron-formation, Hamersley Range, Western Australia. Geochim. Cosmochim. Acta **40**, 1153–1165.

Bigeleisen J. (1952) The effects of isotopic substitution on the rates of chemical reactions. J. Phys. Chem. **56**, 823–828.

Bindeman I. N., Serebryakov N. S., Schmitt A. K., Vazquez J. A., Guan Y., Azimov P. Y., Astafiev B. Y., Palandri J. and Dobrzhinetskaya L. (2014) Field and microanalytical isotopic investigation of ultradepleted in ^{18}O Paleoproterozoic "Slushball Earth" rocks from Karelia, Russia. Geosphere **10**, 308–339.

Blattner P. (1975) Oxygen isotopic composition of fissure-grown quartz, adularia, and calcite from Broadlands geothermal field, New Zealand, with an appendix on quartz-K-feldspar-calcite-muscovite oxygen isotope geothermometers. Am. J. Sci. **275**, 785–800.

Bottinga Y. and Javoy M. (1973) Comments on oxygen isotope geothermometry. Earth Planet. Sci. Lett. **20**, 250–265.

Brandriss M. E., O'Neil J. R., Edlund M. B. and Stoermer E. F. (1998) Oxygen isotope fractionation between diatomaceous silica and water. Geochim. Cosmochim. Acta **62**, 1119–1125.

Cao X. and Liu Y. (2011) Equilibrium mass-dependent fractionation relationships for triple oxygen isotopes. Geochim. Cosmochim. Acta **75**, 7435–7445.

Chacko T., Mayeda T. K., Clayton R. N. and Goldsmith J. R. (1991) Oxygen and carbon isotope fractionations between CO_2 and calcite. Geochim. Cosmochim. Acta **55**, 2867–2882.

Chapligin B., Leng M. J., Webb E., Alexandre A., Dodd J. P. and Sharp Z. D., et al. (2011) Inter-laboratory comparison of oxygen isotope compositions from biogenic silica. Chem. Geol. **75**, 7242–7256.

Clayton R. N. (2003) Oxygen isotopes in meteorites. In Treatise on Geochemistry (eds. H. D. Holland and K. K. Turekian), pp. 129–142.

Clayton R. N. and Epstein S. (1958) The relationship between O^{18}/O^{16} ratios in coexisting quartz, carbonate, and iron oxides from various geological deposits. J. Geol. **66**, 352–373.

Clayton R. N. and Kieffer S. W. (1991) Oxygen isotopic thermometer calibrations. In Stable Isotope Geochemistry: A Tribute to Samuel Epstein (eds. H. P. J. Taylor, J. R. O'Neil and I. R. Kaplan). Lancaster Press Inc., San Antonio, pp. 3–10.

Clayton R. N. and Mayeda T. K. (1983) Oxygen isotopes in eucrites, shergottites, nakhlites, and chassignites. Earth Planet. Sci. Lett. **62**, 1–6.

Clayton R. N., O'Neil J. R. and Mayeda T. K. (1972) Oxygen isotope exchange between quartz and water. J. Geophys. Res. **77**, 3057–3066.

Clayton R. N., Goldsmith J. R. and Mayeda T. K. (1989) Oxygen isotope fractionation in quartz, albite, anorthite and calcite. Geochim. Cosmochim. Acta **53**, 725–733.

Coplen T. B. (1994) Reporting of stable hydrogen, carbon, and oxygen isotopic abundances (Technical Report). Pure Appl. Chem. **66**, 273–276.

Craig H. (1957) Isotopic standards for carbon and oxygen and correction factors for mass-spectrometric analysis of carbon dioxide. Geochim. Cosmochim. Acta **12**, 133–149.

Criss R. E. (1991) Temperature dependence of isotopic fractionation factors. In Stable Isotope Geochemistry: A Tribute to Samuel Epstein (eds. H. P. J. Taylor, J. R. O'Neil and I. R. Kaplan). The Geochemical Society, San Antonio, pp. 11–16.

Dodd J. P. (2011) Oxygen isotopes in diatom silica: a new understanding of silica–water oxygen isotope fractionation in diatom frustules and an application of diatom $d^{18}O$ values as a record of paleohydrological variability in a middle Pleistocene lacustrine core from the Valles Caldera. Department of Earth and Planetary Sciences. University of New Mexico, Albuquerque, p. 108.

Dodd J. P. and Sharp Z. D. (2010) A laser fluorination method for oxygen isotope analysis of biogenic silica and a new oxygen isotope calibration of modern diatoms in freshwater environments. Geochim. Cosmochim. Acta **74**, 1381–1390.

Eiler J. M. (2007) "Clumped-isotope" geochemistry—the study of naturally-occurring, multiply-substituted isotopologues. Earth Planet. Sci. Lett. **262**, 309–327.

Eiler J. M., Farley K. A., Valley J. W., Stolper E. M., Hauri E. H. and Craig H. (1995) Oxygen isotope evidence against bulk recycled sediment in the mantle sources of Pitcairn Island lavas. Nature **377**, 138–141.

Ettayfi N., Bouchaou L., Michelot J. L., Tagma T., Warner N., Boutaleb S., Massault M., Lgourna Z. and Vengosh A. (2012) Geochemical and isotopic (oxygen, hydrogen, carbon, strontium) constraints for the origin, salinity, and residence time of groundwater from a carbonate aquifer in the Western Anti-Atlas Mountains, Morocco. J. Hydrol. **438–439**, 97–111.

Gersonde R. and Hempel G. (1990) Die Expeditionen ANTARKTIS-V11113 und Vllll4 mit FS ''Polarstern'' 1989. Alfred Wegener Institute for Polar and Marine Research, Bremerhaven, p. 178.

Gersonde R., Hodell D. A., Blum P., et al. (1999) Proc. ODP, Init. Repts., 177 [Online]. Available from World Wide Web: <http://www-odp.tamu.edu/publications/177_IR/177TOC.HTM>.

Hodell D. A., Charles C. D., Curtis J. H., Mortyn P. G., Ninnemann U. S. and Venz K. A. (2003) Data report: Oxygen isotope stratigraphy of ODP Leg 177 Sites 1088, 1089, 1090, 1093, and 1094. In: Proc. ODP, Scientific Results, 177 [Online] (eds. R. Gersonde, D. A. Hodell and P. Blum). <http://www-odp.tamu.edu/publications/177_SR/chap_109/chap_109.htm>.

Hofmann M. E. G., Horváth B. and Pack A. (2012) Triple oxygen isotope equilibrium fractionation between carbon dioxide and water. Earth Planet. Sci. Lett. **319–320**, 159–164.

Hren M. T., Tice M. M. and Chamberlain C. P. (2009) Oxygen and hydrogen isotope evidence for a temperate climate 3.42 billion years ago. Nature **462**, 205–208.

Hu G. and Clayton R. N. (2003) Oxygen isotope salt effects at high pressure and high temperature and the calibration of oxygen isotope geothermometers. Geochim. Cosmochim. Acta **67**, 3227–3246.

Hut G. (1987) Consultants' group meeting on stable isotope reference samples for geochemical and hydrological investigations. International Atomic Energy Agency, Vienna.

Kawabe I. (1978) Calculation of oxygen isotope fractionation in quartz-water system with special reference to the low temperature fractionation. Geochim. Cosmochim. Acta **42**, 613–622.

Keller M. A. and Isaacs C. M. (1985) An evaluation of temperature scales for silica diagenesis in diatomaceous sequences including

a new approach based on the Miocene Monterey Formation, California. Geo-Mar. Lett. **5**, 31–35.

Kharaka Y. K., Thordsen J. J. and White L. D. (2002) Isotope and chemical compositions of meteoric and thermal waters and snow from the greater Yellowstone National Park region, Open-File Report, - ed. p. 70.

Kita I., Taguchi S. and Matsubaya O. (1985) Oxygen isotope fractionation between amorphous silica and water at 34–93 oC. Nature **314**, 83–84.

Knauth L. P. (1973) Oxygen and Hydrogen Isotope Ratios in Cherts and Related Rocks, p. 378.

Knauth L. P. and Epstein S. (1976) Hydrogen and oxygen isotope ratios in nodular and bedded cherts. Geochim. Cosmochim. Acta **40**, 1095–1108.

Kusakabe M. and Matsuhisa Y. (2008) Oxygen three-isotope ratios of silicate reference materials determined by direct comparison with VSMOW-oxygen. Geochem. J. **42**, 309–317.

Landais A., Barkan E., Yakir D. and Luz B. (2006) The triple isotopic composition of oxygen in leaf water. Geochim. Cosmochim. Acta **70**, 4105–4115.

Leclerc A. J. and Labeyrie L. (1987) Temperature dependence of oxygen isotopic fractionation between diatom silica and water. Earth Planet. Sci. Lett. **84**, 69–74.

Levin N. E., Raub T. D., Dauphas N. and Eiler J. M. (2014) Triple oxygen isotope variations in sedimentary rocks. Geochim. Cosmochim. Acta **139**, 173–189.

Li S., Levin N. E. and Chesson L. A. (2015) Continental scale variation in ^{17}O-excess of meteoric waters in the United States. Geochim. Cosmochim. Acta **164**, 110–126.

Luz B. and Barkan E. (2010) Variations of ^{17}O/^{16}O and ^{18}O/^{16}O in meteoric waters. Geochim. Cosmochim. Acta **74**, 6276–6286.

Luz B., Barkan E., Bender M. L., Thiemens M. H. and Boering K. A. (1999) Triple-isotope composition of atmospheric oxygen as a tracer of biosphere productivity. Nature **400**, 547–550.

Matheney R. K. and Knauth L. P. (1989) Oxygen-isotope fractionation between marine biogenic silica and seawater. Geochim. Cosmochim. Acta **53**, 3207–3214.

Matsuhisa Y., Goldsmith J. R. and Clayton R. N. (1978) Mechanisms of hydrothermal crystallization of quartz at 250 o C and 15 kbar. Geochim. Cosmochim. Acta **42**, 173–182.

Matsuhisa Y., Goldsmith J. R. and Clayton R. N. (1979) Oxygen isotopic fractionation in the system quartz-albite-anorthite-water. Geochim. Cosmochim. Acta **43**, 1131–1140.

Matthews A. and Beckinsale R. D. (1979) Oxygen isotope equilibration systematics between quartz and water. Am. Mineral. **64**, 232–240.

Matthews A., Goldsmith J. R. and Clayton R. N. (1983) On the mechanisms and kinetics of oxygen isotope exchange in quartz and feldspars at elevated temperatures and pressures. Geol. Soc. Am. Bull. **94**, 396–412.

Matthews A., Palin J. M., Epstein S. and Stolper E. (1994) Experimental study of ^{18}O/^{16}O partitioning between crystalline albite, albitic glass, and CO_2 gas. Geochim. Cosmochim. Acta **58**, 5255–5266.

McKeegan K. D. and Leshin L. A. (2001) Stable isotope variations in extraterrestrial materials. In Stable Isotope Geochemistry (eds. J. W. Valley and D. R. Cole). Mineralogical Society of America, Washington, D.C., pp. 279–318.

Meijer H. A. J. and Li W. J. (1998) The use of electrolysis for accurate d^{17}O and d^{18}O isotope measurements in water. Isot. Environ. Health Stud. **34**, 349–369.

Miller M. F. (2002) Isotopic fractionation and the quantification of ^{17}O anomalies in the oxygen three-isotope system: an appraisal and geochemical significance. Geochim. Cosmochim. Acta **66**, 1881–1889.

Murata K. J., Friedman I. and Gleason J. D. (1977) Oxygen isotope relations between diagenetic silica minerals in Monterey Shale, Temblor Range, California. Am. J. Sci. **277**, 259–272.

O'Neil J. R. (1977) Stable isotopes in mineralogy. Phys. Chem. Miner. **2**, 105–123.

O'Neil J. R. and Clayton R. N. (1964) Oxygen isotope geothermometry. In Isotopic and Cosmic Chemistry. North Holland Publishing Co., Amsterdam, pp. 157–168.

O'Neil J. R. and Epstein S. (1966) A method for oxygen isotope analysis of milligram quantities of water and some of its applications. J. Geophys. Res. **71**, 4955–4961.

O'Neil J. R. and Taylor H. P. (1969) Oxygen isotope equilibrium between muscovite and water. J. Geophys. Res. **74**, 6012–6022.

O'Neil J. R., Adami L. H. and Epstein S. (1975) Revised value for the O(18) fractionation between CO_2 and H_2O at 25 oC. J. Res. U.S. Geol. Survey **3**, 623–624.

Pack A. and Herwartz D. (2014) The triple oxygen isotope composition of the Earth mantle and D^{17}O variations in terrestrial rocks. Earth Planet. Sci. Lett. **390**, 138–145.

Pack A., Gehler A. and Süssenberger A. (2013) Exploring the usability of isotopically anomalous oxygen in bones and teeth as paleo-CO_2-barometer. Geochim. Cosmochim. Acta **102**, 306–317.

Passey B. H., Hu H., Ji H., Montanari S., Li S., Henkes G. A. and Levin N. E. (2014) Triple oxygen isotopes in biogenic and sedimentary carbonates. Geochim. Cosmochim. Acta **141**, 1–25.

Rumble D., Miller M. F., Franchi I. A. and Greenwood R. C. (2007) Oxygen three-isotope fractionation lines in terrestrial silicate minerals: an inter-laboratory comparison of hydrothermal quartz and eclogitic garnet. Geochim. Cosmochim. Acta **71**, 3592–3600.

Saccocia P. J., Seewald J. S. and Shanks, III, W. C. (2009) Oxygen and hydrogen isotope fractionation in serpentine–water and talc–water systems from 250 to 450 oC, 50 MPa. Geochim. Cosmochim. Acta **73**, 6789–6804.

Schmidt M., Botz R., Rickert D., Bohrmann G., Hall S. R. and Mann S. (2001) Oxygen isotopes of marine diatoms and relations to opal-A maturation. Geochim. Cosmochim. Acta **65**, 201–211.

Schoenemann S. W., Schauer A. J. and Steig E. J. (2013) Measurement of SLAP2 and GISP d^{17}O and proposed VSMOW–SLAP normalization for d^{17}O and ^{17}O excess. Rapid Commun. Mass Spectrom. **27**, 582–590.

Schrag D. P., Adkins J. F., McIntyre K., Alexander J. L., Hodell D. A., Charles C. D. and McManus J. F. (2002) The oxygen isotopic composition of seawater during the Last Glacial Maximum. Quatern. Sci. Rev. **21**, 331–342.

Sharp Z. D. (1990) A laser-based microanalytical method for the in situ determination of oxygen isotope ratios of silicates and oxides. Geochim. Cosmochim. Acta **54**, 1353–1357.

Sharp Z. D. (2007) Principles of Stable Isotope Geochemistry. Pearson Prentice Hall, Upper Saddle River.

Sharp Z. D. and Kirschner D. L. (1994) Quartz-calcite oxygen isotope thermometry; a calibration based on natural isotopic variations. Geochim. Cosmochim. Acta **58**, 4491–4501.

Shemesh A., Charles C. D. and Fairbanks R. G. (1992) Oxygen isotopes in biogenic silica; global changes in ocean temperature and isotopic composition. Science **256**, 1434–1436.

Shemesh A., Burckle L. H. and Hays J. D. (1995) Late Pleistocene oxygen isotope records of biogenic silica from the Atlantic sector of the Southern Ocean. Paleoceanography **10**, 179–196.

Shiro Y. and Sakai H. (1972) Calculation of the reduced partition function ratios of a-, b-quartz and calcite. Bull. Chem. Soc. Jpn. **45**, 2355–2359.

Stolper E. and Epstein S. (1991) An experimental study of oxygen isotope partitioning between silica glass and CO_2 vapor. In

(eds. , Jr.H. P. Taylor, J. R. O'Neil and I. R. Kaplan). The Geochemical Society, San Antonio, pp. 35–51.

Tanaka R. and Nakamura E. (2013) Determination of ^{17}O-excess of terrestrial silicate/oxide minerals with respect to Vienna Standard Mean Ocean Water (VSMOW). Rapid Commun. Mass Spectrom. **27**, 285–297.

Thiemens M. H., Chakraborty S. and Dominguez G. (2012) The physical chemistry of mass-independent isotope effects and their observation in Nature. Annu. Rev. Phys. Chem. **63**, 155–177.

Urey H. C. (1947) The thermodynamic properties of isotopic substances. J. Chem. Soc., 562–581.

Urey H. C., Epstein S. and McKinney C. R. (1951) Measurement of paleotemperatures and temperatures of the Upper Cretaceous of England, Denmark, and the southeastern United States. Geol. Soc. Am. Bull. **62**, 399–416.

Williams L. A., Parks G. A. and Crerar D. A. (1985) Silica diagenesis; I, Solubility controls. J. Sediment. Res. **55**, 301–311.

Winckel A., Marlin C., Dever L., Morel J.-L., Morabiti K., Makhlouf M. B. and Chalouan A. (2002) Apport des isotopes stables dans l'estimation des altitudes de recharge de sources thermales du Maroc. C.R. Geosci. **334**, 469–474.

Windman T., Zolotova N., Schwandner F. and Shock E. (2007) Formate as an energy source for microbial metabolism in chemosynthetic zones of hydrothermal ecosystems. Astrobiology **7**, 873–890.

Young E. D., Galy A. and Nagahara H. (2002) Kinetic and equilibrium mass-dependent isotope fractionation laws in nature and their geochemical and cosmochemical significance. Geochim. Cosmochim. Acta **66**, 1095–1104.

Zheng Y. F. (1991) Calculation of oxygen isotope fractionation in metal oxides. Geochim. Cosmochim. Acta **55**, 2299–2307.

Zheng Y.-F. (1993) Calculation of oxygen isotope fractionation in anhydrous silicate minerals. Geochim. Cosmochim. Acta **57**, 1079–1091.

Associate editor: Edwin Schauble

The oxygen isotope composition of San Carlos olivine on the VSMOW2-SLAP2 scale

Andreas Pack1*, Ryoji Tanaka2†, Markus Hering1, Sukanya Sengupta1, Stefan Peters1 and

Eizo Nakamura2†

My contribution to the manuscript: Running SMOW2 and SLAP2 water extractions and measurements in the laboratory.

Research Article

The oxygen isotope composition of San Carlos olivine on the VSMOW2-SLAP2 scale

Andreas Pack[1]*, Ryoji Tanaka[2†], Markus Hering[1], Sukanya Sengupta[1], Stefan Peters[1] and Eizo Nakamura[2†]

[1]Georg-August Universität, Geowissenschaftliches Zentrum (GZG), Abteilung Isotopengeologie, Goldschmidtstrasse 1, 37083 Göttingen, Germany
[2]The Pheasant Memorial Laboratory for Geochemistry and Cosmochemistry, Institute for Study of the Earth's Interior (ISEI), Okayama University, Misasa, Tottori 682-0193, Japan

RATIONALE: The precise determination of $\Delta'^{17}O$ values in terrestrial material is becoming increasingly important to understand the mass-dependent fractionation processes that cause variations in oxygen isotope ratios. San Carlos olivine is widely used as the reference material for oxygen isotope measurements of terrestrial and extraterrestrial materials. We report new $\Delta'^{17}O$ values for San Carlos olivine that were independently determined in two different laboratories (Geoscience Center [GZG], University of Göttingen) and Institute for Study of the Earth's Interior [ISEI], Okayama University, Misasa) in direct comparison with VSMOW2 and SLAP2 water standards.

METHODS: The $\delta^{17}O$ and $\delta^{18}O$ values of VSMOW2, SLAP2, GISP, and San Carlos olivine were determined relative to reference gas. In both laboratories, water and San Carlos olivine samples were prepared by BrF_5 fluorination. In both laboratories, the O_2 released from water and olivine samples was passed through the same purification system and measured using the same mass spectrometer relative to the same reference gas.

RESULTS: In both laboratories, the $\delta^{17}O_{VSMOW2}$ and $\delta^{18}O_{VSMOW2}$ scales were slightly compressed with respect to the recommended composition of VSMOW2 and SLAP2. The new $\Delta'^{17}O_{0.528}$ value (calculated from the VSMOW2-SLAP2 scaled δ values) of San Carlos olivine from GZG was -36 ± 9 ppm and, from ISEI, a value of -40 ± 7 ppm (1σ standard deviation) was determined. These values are ~50 ppm higher than previously reported from the same laboratories. Possible causes for the observed discrepancies are discussed.

CONCLUSIONS: The results of this study in comparison with previous data from the same laboratories demonstrated that for high accuracy determination of $\Delta'^{17}O$ values: (i) calibration of the reference gas relative to O_2 released from primary standards (VSMOW2, SLAP2) in the same laboratory is highly recommended, (ii) non-linearity of the mass spectrometer may not only affect $\delta^{17}O$ and $\delta^{18}O$ values but also $\Delta'^{17}O$ values, and (iii) the VSMOW2-SLAP2 scaling should also be applied to analyses of rocks and minerals. Studies that are concerned with small differences in $\Delta'^{17}O$ at similar $\delta^{18}O$ values, however, are not affected by non-linearity of the mass spectrometer. Copyright © 2016 John Wiley & Sons, Ltd.

Different techniques have been developed for the high-precision measurement of $^{17}O/^{16}O$ and $^{18}O/^{16}O$ ratios in water,[1–5] and rocks and minerals.[5–13] The oxygen isotope composition ($\delta^{17}O$ and $\delta^{18}O$ values; for definition, see McKinney et al.[14]) of water can be measured with high precision on O_2 extracted by fluorination (CoF_3,[2] BrF_5[4,5]), electrolysis,[1] or laser-based spectroscopic techniques (e.g., Steig et al.[15] and references cited therein). The extraction of O_2 from rocks and minerals requires fluorination in Ni reactors at high temperature,[16] or fluorination with the assistance of an infrared laser.[17]

* Correspondence to: A. Pack, Georg-August Universität, Geowissenschaftliches Zentrum (GZG), Abteilung Isotopengeologie, Goldschmidtstrasse 1, 37083 Göttingen, Germany.
E-mail: apack@uni-goettingen.de

† Present address: Institute for Planetary Materials, Okayama University, Misasa, Tottori 682–0193, Japan.

Pack and Herwartz[13] reported that the high precision $\Delta'^{17}O$ values of rocks and minerals obtained from different laboratories show variability outside the respective error intervals. This variability was attributed to systematic errors related to extraction (e.g., NF_3 contamination) and/or standardization of $\delta^{17}O$ values (i.e. the $\delta^{17}O$ values may not have been reported strictly on the VSMOW or VSMOW2 scale). While reporting precisions in $\Delta'^{17}O$ of <10 ppm, Pack and Herwartz[13] stated that the accuracy in $\Delta'^{17}O$ values was in the range of ±10 ppm. For comparison of $\Delta'^{17}O$ values between different reservoirs with similar $\delta^{18}O$ values (e.g.,[7,8,11,18,19]), exact scaling of $\delta^{17}O$ values on VSMOW2 or VSMOW2-SLAP2 is not required. However, when comparing measurements with theory (e.g.,[20,21]), it is necessary to apply accurate δ values. Also, when studying interaction between rocks and water (e.g.,[22]), accurate determination of δ values is necessary.

San Carlos olivine is a widely used reference material for studies of $\Delta'^{17}O$ in terrestrial and extraterrestrial solid materials. It is suggested by the data in Pack and Herwartz[13]

and references cited therein that the $\Delta'^{17}O$ value of San Carlos olivine is representative within a few ppm of the composition of the Earth's upper mantle. Tanaka and Nakamura[5] and Pack and Herwartz[13] reported $\Delta'^{17}O$ values that were identical within 3 ppm, but some few tens of ppm lower than those in most other studies (see Fig. 3 in Pack and Herwartz[13]). In contrast to other studies (e.g.,[3,5,23]), Pack and Herwartz[13] did not measure VSMOW or VSMOW2 water in their laboratory, but used a reference gas bottle that was calibrated with a now exhausted O_2 tank that had been externally calibrated.[24]

Here, we present new data for VSMOW2, SLAP2, GISP, and San Carlos olivine from our attempt to report accurate $\Delta'^{17}O$ values from two different laboratories. We propose revised $\delta^{18}O$ and $\Delta'^{17}O$ values of San Carlos olivine and discuss possible causes for discrepancies with previously reported values.

MATERIALS, DEFINITIONS, AND METHODS

Sampling

Geoscience Center, Göttingen University (GZG)

Fresh VSMOW2, GISP, and SLAP2 water samples were acquired from the International Atomic Energy Agency (IAEA, Vienna, Austria). The original water ampoules were opened and distributed in ~1 mL aliquots in flame-sealed 6 mm o.d. glass ampoules. For each analytical session, a new ampoule was opened immediately before injection and the remaining water was discarded. Subsamples of San Carlos olivine were prepared from a commercially traded ~1 cm single crystal. This is a different sample from those that were analyzed by Pack and Herwartz.[13]

Institute for Study of the Earth's Interior, Okayama University (ISEI)

The original 20 mL ampoules of VSMOW2 and SLAP2 reference waters and a ~ 5 mL aliquot of GISP water stored in 5-mL flame-sealed glass ampoules were used in this study. Each of these reference waters was transferred to a 4-mL septum-sealed glass vial just before the analysis. Subsamples of San Carlos olivine (MSOL-1) were prepared from a ~ 1 cm single crystal, the same material as was analyzed by Tanaka and Nakamura.[5]

Definitions

The oxygen isotope ratios are expressed in δ notation in ‰[14] relative to a given reference.

We report the raw ratios (δ^iO_{WG}, δ^iO_{raw}; i = { 17, 18 }) relative to the reference gases (WG), along with the normalized ratios relative to the measured values for VSMOW2 (δ^iO_{VSMOW2}) and VSMOW2-SLAP2 ($\delta^iO_{VSMOW2-SLAP2}$). The δ^iO_{raw} values from GZG are reported using the previously assigned $\delta^{17}O_{VSMOW} = 5.906$ ‰ and $\delta^{18}O_{VSMOW} = 11.986$ ‰ values of the reference gas that were also used by Pack and Herwartz.[13] These values were determined by measurement of the reference gas relative to a now expired reference gas bottle that had been externally calibrated.[24] This means that the δ^iO_{raw} value from this study can

directly be compared with the "δ^iO_{VSMOW}" value reported in the literature.[13,18,22] The difference between the assigned δ and the true δ values, however, is small (<0.1 ‰) for both $\delta^{17}O$ and $\delta^{18}O$. The δ^iO_{raw} values from the ISEI are reported relative to the previously assigned $\delta^{17}O_{VSMOW} = 7.36$ ‰ and $\delta^{18}O_{VSMOW} = 14.63$ ‰ values calibrated relative to O_2 released from VSMOW.[5]

The δ^iO_{VSMOW2} values are calculated as:

$$\delta^iO_{VSMOW2}^{sample} = \delta^iO_{raw}^{sample} - \delta^iO_{raw}^{VSMOW2} \tag{1}$$

In order to account for non-linearity of the mass spectrometers and improve inter-laboratory comparability, it was suggested that a two-point calibration strategy with reference materials with a large difference in δ values should be used. The two reference materials of choice were VSMOW2 and SLAP2 waters.[25] In this study, we broadly follow the strategy by Schoenemann et al.[26] with separate scaling for $\delta^{17}O$ and $\delta^{18}O$ values and assigned SLAP2 values of -29.6987 ‰[26] and -55.5 ‰,[27] respectively:

$$\delta^iO_{VSMOW2-SLAP2}^{sample} = \frac{-\delta^iO_{VSMOW2}^{SLAP2;assigned}}{\delta^iO_{raw}^{VSMOW2} - \delta^iO_{raw}^{SLAP2}} \cdot \left(\delta^iO_{raw}^{sample} - \delta^iO_{raw}^{VSMOW2} \right) \tag{2}$$

Deviations from the correlation between the $\delta^{17}O$ and $\delta^{18}O$ values are expressed as $\Delta'^{17}O_{ref}$ with:

$$\Delta'^{17}O_{ref}^{sample} = 10^3 \cdot \ln\left(\frac{\delta^{17}O_{ref}^{sample}}{10^3} + 1 \right) - \lambda RL \cdot 10^3 \cdot \ln\left(\frac{\delta^{18}O_{ref}^{sample}}{10^3} + 1 \right) \tag{3}$$

The index ref indicates to what the δ values have been normalized (VSMOW2, VSMOW2-SLAP2). Here, we report $\Delta'^{17}O$ in parts per million (molar, ppm). Various reference lines (RL) have been suggested for reporting $\Delta'^{17}O$ depending on the materials that were studied. We choose a reference line that passes through the origin with slopes $\lambda_{RL} = 0.5280$ and $\lambda_{RL} = 0.5305$. The former value is the assigned slope defined by VSMOW2 and SLAP2. The 0.5305 slope is identical to the high-temperature equilibrium isotope fractionation exponent.[28] An index x on the $\Delta'^{17}O_x$ notation indicates which reference line has been chosen. All the δ values are reported to 3 decimal places so that recalculation of $\Delta'^{17}O$ to any other reference frame is possible. It has been confirmed that the $\delta^{17}O_{VSMOW-SLAP}$ and $\delta^{18}O_{VSMOW-SLAP}$ values of VSMOW2 and SLAP2 are identical to those of VSMOW and SLAP, respectively, within the uncertainty of the measurement.[2,4]

EXPERIMENTAL

GZG

The extraction line that was used for fluorination and subsequent purification of O_2 from water and the San Carlos olivine samples is shown schematically in Fig. 1.
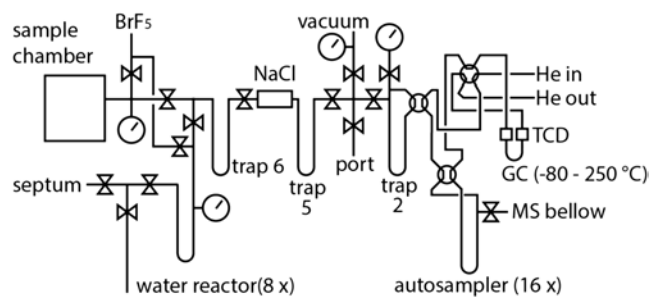
Figure 1. Sketch of the extraction line that allows extraction of O$_2$ from water and rocks, oxides and silicates. The line is made of stainless steel with Swagelock and Valco valves and is fully computer operated (LabView, National Instruments, Austin, TX, USA). The base vacuum of the line is ~10^{-6} mbar. The extracted O$_2$ can be transferred offline in glass vials (filled with 5 Å molecular sieve pellets) that are connected to the port or can be transferred to a 16-port autosampler for automatic measurement.

The water samples were analyzed using a procedure similar to that described by O'Neil and Epstein.[29] Between 1.5 and 5 µL of water was injected with a gas-tight syringe through a septum into a water reactor (see Fig. 1). The entire reactor head and injection unit was heated to 90°C. The vapor was cryo-trapped in 6 mm stainless steel fingers. An excess of BrF$_5$ was then added to the frozen water samples. In order to avoid BrF$_5$ coming into contact with ice, the liquid N$_2$ level was raised by ~1 cm before trapping BrF$_5$. The isolated reaction tubes were then heated for ~10 min to about 350°C using a heat gun.

After reaction, excess BrF$_5$ and HF were cryo-trapped in trap 6. Using NaCl, traces of F$_2$ were reacted to produce Cl$_2$ that was cryo-trapped in trap 5 (Fig. 1). The purified O$_2$ sample was then transferred for ~10 min to trap 2 that was filled with 5 Å molecular sieve beads. From trap 2, the sample O$_2$ was transported via a He carrier gas stream (10–20 mL min^{-1}) through a Hewlett Packard 5890 Series II gas chromatograph (Agilent Technologies, Santa Clara, CA, USA) for separation of O$_2$ from contaminating NF$_3$ and N$_2$. The gas chromatograph was equipped with a 1/8", 3 m long packed 5 Å molecular sieve column (Restek, Bellefonte, PA, USA). Separation was conducted at 50°C. Before each run, the GC column was heated for 10 min to 250°C. After separation of contaminating NF$_3$ and N$_2$, the sample O$_2$ was either back collected in trap 2 or transported to a 16-port autosampler located at the mass spectrometer. If O$_2$ was trapped in trap 2, He was evacuated. The sample O$_2$ was then transferred to glass vials filled with 5 Å molecular sieve (~10–20 1/8″ beads) that were attached with an UltraTorr connection to the port of the extraction line (Fig. 1). When the sample O$_2$ had been transported to the autosampler, He carrier gas was evacuated from the respective molecular sieve trap through the pumping system of the mass spectrometer. Before expanding the sample O$_2$ gas into the sample bellows of a Thermo MAT253 (Thermo Fisher Scientific, Bremen, Germany) gas source isotope ratio mass spectrometer, the sample and molecular sieve were heated to ~90°C for ~5 min (glass vials) and 30 min (autosampler). The gas was then automatically measured in dual inlet mode relative to the reference gas (WG) in four successive blocks (20 cycles with 8 s counting time for sample and reference gas) for ~90 min. The mass spectrometric noise in Δ'^{17}O was

~6 ppm (1σ SEM, 80 cycles). There was no correlation between the scatter in the δ^{17}O and δ^{18}O values. The reproducibility in Δ'^{17}O values for different extractions of O$_2$ was in the same range as the mass spectrometric noise. The extraction of O$_2$ from San Carlos olivine was performed using the same line and protocol as used for the water samples (Fig. 1). The extraction was performed by infrared laser fluorination with BrF$_5$ as the oxidation agent.[17] About 2 mg of olivine was placed in a 18-place sample holder. Each sample was reacted under an atmosphere of ~45 mbar BrF$_5$. After all the silicate had reacted, the sample O$_2$ was purified and transferred into the bellows of the mass spectrometer using the same line and protocol as for water samples (Fig. 1). All the San Carlos samples were analyzed using the autosampler.

ISEI

The fluorination and gas purification methods that were used for analysis of water and mineral samples were modified after O'Neil and Epstein[29] and Sharp,[17] respectively. Details of these methods were described in Tanaka and Nakamura.[5] For this study, the water fluorination line was re-built using a new stainless steel tube, new bellows-sealed valves, and a new 30 mm o.d. Ni reaction tube. To reduce the possible source of procedural blank for the water fluorination method, the septum at the water injection port was changed after every five injections. For the water samples, 3 µL of water was injected through the septum using a gas-tight syringe. The vapor was frozen in the bottom of the Ni reaction tube. Approximately 300 µmol of BrF$_5$ was then trapped near the top of the Ni tube. The water and BrF$_5$ were then reacted at 250°C for 30 min using a mantle heater. For the extraction of O$_2$ from the San Carlos olivine, about 1–1.5 mg of sample was placed in a Ni sample holder. The O$_2$ was extracted using a CO$_2$ laser with BrF$_5$ as the oxidation agent. Extracted O$_2$ from both water and San Carlos olivine was purified using the same purification line, comprising liquid N$_2$ cold traps and hot KBr for the removal of BrF$_5$, HF, SiF$_4$, Br$_2$, and F$_2$. The purified O$_2$ was then trapped with 13 Å molecular sieve at liquid N$_2$ temperature.

The isotope ratios in the extracted O$_2$ gas were determined using a Thermo MAT253 gas source isotope ratio mass spectrometer in dual inlet mode with simultaneous detection of m/z 32, 33 and 34. The ion beams were collected in Faraday collectors attached to amplifiers with 3×10^8, 3×10^{11} and 1×10^{11} Ω feedback resistors. For each sample, 8 blocks of 11 cycles each were measured with a total measurement time of ~90 min. The mass spectrometric error (1σ SE) in the Δ'^{17}O values was 5–10 ppm for each run.

The interfering ^{14}N^{19}F interference on ^{33}O$_2$ was monitored with ^{14}N^{19}F$_2$ at m/z 52. The ion intensity ratio of m/z 33/52 was the same for the sample and the reference gases. The intensities of N$_2$ at m/z 28 and Ar at m/z 40 relative to m/z 33 were also monitored and were the same for the sample and the reference gas. The total procedural O$_2$ blanks for water and silicate extractions were 50–70 nmol and <1 nmol, respectively. The blank for the water extractions was 3× lower than in previous experiments.[5] Because no significant effect of the blank on the result was observed, no blank correction was performed in this study.

RESULTS AND DISCUSSION

The data for VSMOW2, SLAP2, GISP, and San Carlos olivine are listed in Tables 1 and 2. The measured data (Tables 1 and 2) are illustrated in Fig. 2.

The $\delta^{18}O_{VSMOW2}$ value of SLAP is -55.1 ± 0.2 ‰ (GZG) and -55.37 ± 0.04 ‰ (ISEI). Published $\delta^{18}O_{VSMOW2}$ values for SLAP2 vary between 53.9 and 56.5 ‰.[5,26,27] Thus, data from this study are well within the range of published data and are furthermore close to the latest (2009) IAEA recommended value of -55.50 ± 0.02 (SD) ‰. The effect of VSMOW2-SLAP2 scaling on $\Delta'^{17}O_{0.528}$ has to be taken into account for the GZG data (Fig. 2(A)), but is negligibly small for the ISEI data (Fig. 2(B)). This, however, is a coincidence that results from the choice of the slope λ_{RL} of the reference line in the definition of $\Delta'^{17}O$. The measured VSMOW2-scaled $\Delta'^{17}O_{0.528}$ value for SLAP2 varies between -29 and 58 ppm (see compilation in Schoenemann et al.[26]). The data from this study are within the reported range but clearly show that a two-point strategy is necessary for high precision $\Delta'^{17}O$ studies if $\delta^{18}O$ shows > ~5 ‰ variations. To ensure inter-laboratory comparability, we are adhering to the recommendation that $\delta^{17}O$ and $\delta^{18}O$ data should be reported on the VSMOW2-SLAP2 scale.[26,30]

The VSMOW2-SLAP2 scaled $\delta^{18}O$ values of GISP are -24.6 ± 0.2 (GZG) and -24.87 ± 0.04 ‰ (ISEI, Table 1). Within uncertainty, both values are identical to the values of -24.76 ± 0.09 (SD) ‰ and -24.82 ± 0.09 (SD) ‰ recommended by the IAEA[31] and compiled by Schoenemann et al.,[26] respectively. The VSMOW2-SLAP2 scaled $\Delta'^{17}O_{0.528}$ values for GISP from this study are 32 ± 9 (GZG) and 19 ± 6 ppm (ISEI; Fig. 2). Schoenemann et al.[26] originally reported a value of 22 ± 11 ppm for GISP while Steig et al.[15] reported an updated value of 28 ± 2 ppm for GISP that was obtained by gas source mass spectrometry. The VSMOW2-SLAP2 scaled $\Delta'^{17}O_{0.528}$ value from cavity ring down spectroscopy is 27 ± 4 ppm.[15] The weighted mean (this study and the updated value of Schoenemann et al.[26] and new data reported in Steig et al.[15]) for GISP is 27 ± ~5 ppm. The good agreement between data from this study and literature data demonstrates the robustness of a VSMOW2-SLAP2 calibration when reporting high precision $\Delta'^{17}O$ data.

For San Carlos olivine, the VSMOW2-SLAP2 scaled $\Delta'^{17}O_{0.528}$ values are -36 ± 9 (GZG) and -40 ± 8 ppm (ISEI), respectively (Fig. 2). These values differ considerably from the values of -89 and -85 ppm previously reported, respectively, by Pack and Herwartz[13] and Tanaka and Nakamura[5] and need explanation.

Pack and Herwartz[13] did not apply VSMOW2-VSLAP scaling for their data. The effect of non-linearity on the $\Delta'^{17}O$, however, is only ~1 ppm per ‰ change in the $\delta^{18}O$ value (Fig. 2). Therefore, the observed ~50 ppm shift in $\Delta'^{17}O$ for San Carlos olivine cannot be explained by non-linearity in $\Delta'^{17}O$. Pack and Herwartz,[13] in their study, did not analyze standard waters but reported the values relative to a reference gas that had been measured relative to an externally calibrated O_2 gas (see Hofmann et al.[24]). The $\Delta'^{17}O_{0.5305,raw}$ value of San Carlos olivine calculated from the "δ^iO_{VSMOW}"value from Pack and Herwartz[13] is -103 ppm, which is identical to the value of $\Delta'^{17}O_{0.5305,raw}$ = -104 ppm (Table 2) obtained from the $\delta^{18}O_{raw}$ value in this study. The mass spectrometer and the reference gas (and the assigned reference gas $\delta^{17}O_{VSMOW2}$ and $\delta^{18}O_{VSMOW2}$ values) were identical in this study to those of Pack and Herwartz.[13] The extraction of O_2 in this study was performed with a new extraction line (Fig. 1) that differs in many parts from that used by Pack and Herwartz.[13] The fact that the $\Delta'^{17}O$ values (without VSMOW2/SLAP scaling) are identical within 1 ppm may indicate that the observed ~50 ppm shift in $\Delta'^{17}O$ is not due to a systematic error related to silicate fluorination. Instead, we conclude that the discrepancy is due to uncertainties related to the internal and/or external reference gas calibration.

The $\Delta'^{17}O_{raw}$ values of San Carlos olivine from ISEI relative to the reference gas agree with those of Tanaka and Nakamura.[5] However, the $\Delta'^{17}O$ values of the water samples show a systematic offset towards ~45 ppm higher values than previously measured by Tanaka and Nakamura.[5] This result implies that the systematic difference in $\Delta'^{17}O_{0.528}$ values for San Carlos olivine between Tanaka and Nakamura[5] (-85 ppm) and this study (-40 ppm) was caused by the calibration of the $\delta^{17}O$ value of the reference gas determined by VSMOW-extracted oxygen. This may be caused by impurities in the extracted O_2 gas. Although the measured signal intensity of the $^{14}N^{19}F_2$ peak at m/z 52 relative to m/z 33 did not change between this and previous studies, the total procedure blank of O_2 in this study was one-third of that in previous experiments. The minor modification of the water fluorination line in this study considerably reduced the blank for the water fluorination line. In Tanaka and Nakamura,[5] a blank correction was performed to the raw data. Since the $\delta^{17}O$ and $\delta^{18}O$ values of the oxygen blank could not be measured, the isotopic composition of the blank oxygen was assumed to be identical to that of the air O_2. The discrepancy between this study and Tanaka and Nakamura[5] could be caused by this assumption. In this present study, the oxygen blank was significantly reduced to a level at which blank correction is not needed. Another possible cause for the discrepancy between this study and that of Tanaka and Nakamura[5] is the presence of impurities in the sample gas during mass spectrometry (e.g., N_2 or Ar; e.g.,[32]). Tanaka and Nakamura[5] did not monitor the signal intensities of N_2 and Ar. However, the higher oxygen blank in Tanaka and Nakamura[5] than in this study may suggest that the N_2 and Ar contents were higher, resulting in systematically higher $\delta^{17}O$ values. Thus, we revise the $\Delta'^{17}O_{0.528}$ value of San Carlos olivine determined at ISEI to -40 ± 8 ppm.

Similar experiments (measurement of VSMOW2, SLPA2 and San Carlos olivine) have recently been conducted by Sharp et al.,[33] who obtained a $\delta^{18}O$ value of 5.56 ‰ and a $\Delta'^{17}O_{0.528}$ value of -54 ± 8 ppm, which is 16 ppm lower than the mean of -38 ppm from this study. The cause for the discrepancy is not clear, but it is of the same order of magnitude as the discrepancy of 13 ppm in the $\Delta'^{17}O_{0.528}$ value of GISP water from this study. This demonstrates that accurate determination of $\Delta'^{17}O$ of rocks and minerals relative to VSMOW2 and SLAP2 remains difficult and more studies should be undertaken to obtain accurate $\Delta'^{17}O$ values on the ppm scale.

An implication from this study is that the $\Delta'^{17}O_{0.5305}$ value of the Earth's mantle is not -100 ppm,[5,13] but $\Delta'^{17}O_{0.5305} \approx$ -50 ppm ($\Delta'^{17}O_{0.528} \approx$ -40 ppm) and this revised value is now in better agreement with data from other studies (see[34,35]). Analysis

San Carlos olivine on the VSMOW2-SLAP2 scale

Table 1. Measured data ($\delta^{17}O$, $\delta^{18}O$ and $\Delta'^{17}O$ values) for VSMOW2, SLAP2 and GISP water													
		$\delta^{17}O$	$\delta^{18}O$	$\delta^{17}O$	$\delta^{18}O$	$\delta^{17}O$	$\delta^{18}O$	$\Delta'^{17}O$	$\Delta'^{17}O$	$\delta^{17}O$	$\delta^{18}O$	$\Delta'^{17}O$	$\Delta'^{17}O$
Standard 1		WG	WG	raw	raw	VSMOW2	VSMOW2	VSMOW2	VSMOW2	VSMOW2	VSMOW2	VSMOW2	VSMOW2
Standard 2		-	-	-	-	-	-	-	-	SLAP2	SLAP2	SLAP2	SLAP2
slope of RL		-	-	-	-	-	-	0.5280	0.5305	-	-	0.5280	0.5305
Laboratory	Sample name	‰	‰	‰	‰	‰	‰	ppm (mol)	ppm (mol)	‰	‰	ppm (mol)	ppm (mol)
GZG	VSMOW2	-5.962	-11.899	-0.091	-0.056	-0.006	0.010	-11	-11	-0.006	0.010	-11	-11
GZG	VSMOW2	-5.961	-11.901	-0.090	-0.058	-0.005	0.008	-9	-9	-0.005	0.008	-9	-9
GZG	VSMOW2	-5.908	-11.828	-0.037	0.016	0.048	0.082	5	5	0.049	0.082	5	5
GZG	VSMOW2	-5.842	-11.700	0.029	0.146	0.114	0.212	2	2	0.115	0.213	2	2
GZG	VSMOW2	-5.876	-11.769	-0.005	0.076	0.080	0.142	5	5	0.081	0.143	5	5
GZG	VSMOW2	-5.834	-11.684	0.038	0.162	0.123	0.228	3	2	0.124	0.229	3	2
GZG	VSMOW2	-6.184	-12.338	-0.315	-0.500	-0.230	-0.434	-1	0	-0.232	-0.437	-1	0
GZG	VSMOW2	-6.080	-12.153	-0.210	-0.313	-0.125	-0.247	6	6	-0.126	-0.249	5	6
Mean				-0.085	-0.066	0.000	0.000	0	0	0.000	0.000	0	0
SD				0.123	0.231	0.123	0.231	7	7	0.124	0.232	7	7
SEM				0.043	0.082	0.043	0.082	2	2	0.044	0.082	2	2
ISEI	VSMOW2	-7.337	-14.417	-0.031	0.002	0.008	0.006	5	5	0.008	0.006	5	5
ISEI	VSMOW2	-7.341	-14.416	-0.035	0.004	0.004	0.008	0	0	0.004	0.008	0	0
ISEI	VSMOW2	-7.345	-14.425	-0.039	-0.006	0.000	-0.002	1	1	0.000	-0.002	1	1
ISEI	VSMOW2	-7.339	-14.410	-0.033	0.009	0.006	0.014	-1	-1	0.006	0.014	-1	-1
ISEI	VSMOW2	-7.346	-14.429	-0.040	-0.010	-0.001	-0.006	2	2	-0.001	-0.006	2	2
ISEI	VSMOW2	-7.363	-14.442	-0.057	-0.023	-0.018	-0.019	-8	-8	-0.018	-0.019	-8	-8
Mean				-0.039	-0.004	0.000	0.000	0	0	0.000	0.000	0	0
SD				0.009	0.012	0.009	0.012	4	4	0.009	0.012	4	4
SEM				0.004	0.005	0.004	0.005	2	2	0.004	0.005	2	2
GZG	SLAP2	-35.366	-66.686	-29.669	-55.499	-29.584	-55.433	81	223	-29.832	-55.792	25	169
GZG	SLAP2	-35.176	-66.290	-29.478	-55.099	-29.393	-55.033	54	196	-29.640	-55.389	-1	141
GZG	SLAP2	-35.738	-67.322	-30.043	-56.143	-29.958	-56.077	56	200	-30.209	-56.440	-1	144
GZG	SLAP2	-35.720	-67.288	-30.025	-56.109	-29.940	-56.043	55	199	-30.191	-56.406	-1	144
GZG	SLAP2	-35.384	-66.670	-29.687	-55.483	-29.602	-55.417	53	196	-29.850	-55.776	-2	141
GZG	SLAP2	-35.047	-66.052	-29.348	-54.858	-29.263	-54.792	53	194	-29.508	-55.147	-2	140
GZG	SLAP2	-35.079	-66.075	-29.380	-54.881	-29.295	-54.815	33	174	-29.541	-55.170	-22	120
GZG	SLAP2	-35.046	-66.033	-29.347	-54.838	-29.262	-54.772	43	184	-29.507	-55.126	-12	130
GZG	SLAP2	-34.986	-65.958	-29.287	-54.763	-29.202	-54.697	63	204	-29.447	-55.051	8	150
GZG	SLAP2	-34.802	-65.618	-29.102	-54.419	-29.017	-54.353	62	201	-29.260	-54.705	7	148
Mean				-29.537	-55.209	-29.451	-55.143	55	197	-29.699	-55.500	0	143
SD				0.314	0.582	0.314	0.582	12	13	0.316	0.585	12	13
SEM				0.099	0.184	0.099	0.184	4	4	0.100	0.185	4	4

(Continues)

Table 1. (Continued)

		$\delta^{17}O$	$\delta^{18}O$	$\delta^{17}O$	$\delta^{18}O$	$\delta^{17}O$	$\delta^{18}O$	$\Delta'^{17}O$	$\Delta'^{17}O$	$\delta^{17}O$	$\delta^{18}O$	$\Delta'^{17}O$	$\Delta'^{17}O$
Standard 1		WG	WG	raw	raw	VSMOW2	VSMOW2	VSMOW2	VSMOW2	VSMOW2	VSMOW2	VSMOW2	VSMOW2
Standard 2		-	-	-	-	-	-	-	-	SLAP2	SLAP2	SLAP2	SLAP2
slope of RL		-	-	-	-	-	-	0.5280	0.5305	-	-	0.5280	0.5305
Laboratory	Sample name	‰	‰	‰	‰	‰	‰	ppm (mol)	ppm (mol)	‰	‰	ppm (mol)	ppm (mol)
ISEI	SLAP2	-36.736	-68.934	-29.646	-55.312	-29.607	-55.308	-13	130	-29.672	-55.442	-5	137
ISEI	SLAP2	-36.809	-69.053	-29.720	-55.434	-29.681	-55.430	-21	121	-29.747	-55.564	-14	129
ISEI	SLAP2	-36.757	-68.997	-29.668	-55.377	-29.629	-55.373	1	143	-29.694	-55.507	9	151
ISEI	SLAP2	-36.758	-68.993	-29.669	-55.373	-29.630	-55.369	-3	140	-29.695	-55.503	5	148
ISEI	SLAP2	-36.748	-68.975	-29.659	-55.355	-29.620	-55.350	-2	140	-29.685	-55.484	5	148
Mean				-29.672	-55.370	-29.633	-55.366	-8	135	-29.699	-55.500	0	143
SD				0.028	0.044	0.028	0.044	9	9	0.028	0.044	9	9
SEM				0.013	0.020	0.013	0.020	4	4	0.013	0.020	4	4
GZG	GISP	-18.992	-36.400	-13.198	-24.850	-13.113	-24.784	51	114	-13.223	-24.944	27	90
GZG	GISP	-18.728	-35.912	-12.933	-24.356	-12.848	-24.290	52	114	-12.956	-24.447	28	90
GZG	GISP	-18.644	-35.774	-12.848	-24.217	-12.763	-24.151	63	124	-12.870	-24.307	39	101
Mean				-12.993	-24.474	-12.908	-24.408	56	117	-13.016	-24.566	31	94
SD				0.183	0.333	0.183	0.333	7	6	0.184	0.335	7	6
SEM				0.105	0.192	0.105	0.192	4	3	0.106	0.193	4	4
ISEI	GISP	-20.369	-38.800	-13.159	-24.738	-13.120	-24.734	16	79	-13.149	-24.794	20	82
ISEI	GISP	-20.358	-38.774	-13.148	-24.711	-13.109	-24.707	13	76	-13.138	-24.766	16	79
ISEI	GISP	-20.422	-38.895	-13.212	-24.834	-13.173	-24.830	15	78	-13.202	-24.890	18	81
ISEI	GISP	-20.449	-38.942	-13.240	-24.881	-13.201	-24.877	13	76	-13.230	-24.938	16	79
ISEI	GISP	-20.442	-38.946	-13.233	-24.886	-13.194	-24.882	22	85	-13.223	-24.942	26	89
Mean				-13.198	-24.810	-13.159	-24.806	16	79	-13.188	-24.866	19	82
SD				0.042	0.081	0.042	0.081	4	4	0.042	0.082	4	4
SEM				0.019	0.036	0.019	0.036	2	2	0.019	0.037	2	2

		δ17O	δ18O	δ17O	δ18O	δ17O	δ18O	Δ'17O	Δ'17O	δ17O	δ18O	Δ'17O	Δ'17O
	Standard 1	WG	WG	raw	raw	VSMOW2	VSMOW2	VSMOW2	VSMOW2	VSMOW2	VSMOW2	VSMOW2	VSMOW2
	Standard 2	-	-	-	-	-	-	-	-	SLAP2	SLAP2	SLAP2	SLAP2
	slope of RL	-	-	-	-	-	-	0.528	0.5305	-	-	0.528	0.5305
Laboratory	Sample name	‰	‰	‰	‰	‰	‰	ppm (mol)	ppm (mol)	‰	‰	ppm (mol)	ppm (mol)
GZG	SC olivine	-3.194	-6.635	2.693	5.271	2.778	5.337	-36	-50	2.801	5.371	-31	-45
GZG	SC olivine	-3.279	-6.799	2.607	5.106	2.693	5.172	-35	-48	2.715	5.205	-30	-43
GZG	SC olivine	-3.338	-6.907	2.548	4.997	2.633	5.062	-36	-49	2.655	5.095	-32	-44
GZG	SC olivine	-3.417	-7.052	2.468	4.849	2.554	4.915	-39	-51	2.575	4.947	-34	-46
GZG	SC olivine	-3.291	-6.815	2.596	5.089	2.681	5.155	-38	-51	2.703	5.189	-33	-46
GZG	SC olivine	-3.386	-7.001	2.500	4.901	2.585	4.967	-34	-47	2.607	4.999	-29	-42
GZG	SC olivine	-3.230	-6.706	2.657	5.200	2.742	5.266	-35	-48	2.765	5.300	-30	-43
GZG	SC olivine	-3.350	-6.909	2.536	4.994	2.621	5.060	-47	-60	2.643	5.093	-42	-55
GZG	SC olivine	-3.299	-6.819	2.588	5.085	2.673	5.151	-43	-56	2.696	5.184	-38	-51
GZG	SC olivine	-3.268	-6.779	2.619	5.126	2.704	5.192	-34	-47	2.727	5.225	-29	-42
GZG	SC olivine	-3.396	-7.013	2.490	4.889	2.575	4.955	-38	-50	2.597	4.987	-33	-46
GZG	SC olivine	-3.267	-6.776	2.620	5.129	2.705	5.195	-34	-47	2.728	5.228	-29	-42
GZG	SC olivine	-3.256	-6.734	2.631	5.171	2.716	5.237	-45	-58	2.739	5.271	-40	-54
GZG	SC olivine	-3.342	-6.893	2.544	5.010	2.629	5.076	-48	-60	2.651	5.109	-43	-56
GZG	SC olivine	-3.242	-6.729	2.645	5.177	2.730	5.242	-34	-47	2.753	5.276	-29	-42
GZG	SC olivine	-3.281	-6.795	2.606	5.109	2.691	5.175	-38	-51	2.714	5.209	-33	-46
GZG	SC olivine	-3.185	-6.621	2.702	5.286	2.787	5.351	-35	-48	2.811	5.386	-29	-43
GZG	SC olivine	-3.229	-6.700	2.658	5.205	2.743	5.271	-36	-49	2.766	5.305	-31	-44
GZG	SC olivine	-3.196	-6.615	2.691	5.292	2.776	5.358	-49	-63	2.799	5.393	-44	-58
GZG	SC olivine	-3.143	-6.520	2.745	5.388	2.830	5.454	-46	-60	2.854	5.489	-41	-55
GZG	SC olivine	-3.390	-6.971	2.496	4.932	2.581	4.998	-55	-67	2.603	5.030	-50	-63
GZG	SC olivine	-3.357	-6.914	2.529	4.989	2.614	5.055	-51	-64	2.636	5.087	-47	-59
GZG	SC olivine	-3.261	-6.736	2.625	5.170	2.711	5.235	-50	-63	2.733	5.269	-45	-58
GZG	SC olivine	-3.298	-6.826	2.588	5.079	2.673	5.144	-40	-52	2.696	5.178	-35	-48
GZG	SC olivine	-3.348	-6.905	2.538	4.998	2.623	5.064	-47	-60	2.645	5.097	-43	-55
GZG	SC olivine	-3.422	-7.040	2.464	4.862	2.549	4.928	-50	-62	2.571	4.960	-45	-57
GZG	SC olivine	-3.430	-7.057	2.456	4.845	2.541	4.911	-49	-61	2.562	4.943	-44	-57
GZG	SC olivine	-3.444	-7.104	2.441	4.797	2.527	4.863	-38	-50	2.548	4.894	-33	-45
GZG	SC olivine	-3.439	-7.082	2.447	4.819	2.532	4.885	-44	-56	2.553	4.916	-39	-52
GZG	SC olivine	-3.413	-7.058	2.472	4.843	2.558	4.909	-31	-44	2.579	4.941	-27	-39
Mean						2.658	5.119	-41	-54	2.681	5.153	-36	-49
SD						0.085	0.160	7	7	0.086	0.161	7	7
SEM						0.016	0.029	1	1	0.016	0.029	1	1

Table 2. Oxygen isotope composition (δ17O, δ18O and Δ'17O values) of San Carlos olivine analyzed in the Göttingen (GZG) and the Institute for Study of the Earth's Interior (ISEI) laboratories

(Continues)

Table 2. (Continued)

Standard 1	Standard 2	slope of RL	Laboratory						W2			δ'17O VSMOW2 SLAP2 -	δ18O VSMOW2 SLAP2 -	Δ'17O VSMOW2 SLAP2 0.528	Δ'17O VSMOW2 SLAP2 0.5305
									5			-	-	0.528	0.5305
MSOL–1			ISEI	−4.587			.355	5.231	−59	−46	2.723	2.784	5.368	−47	−60
MSOL–1			ISEI	−4.642	−9.264	2.684	5.235		−50	−37		2.729	5.247	−38	−51
MSOL–1			ISEI	−4.636			.261		−59	−46		2.735	5.274	−46	−60
MSOL–1			ISEI	−4.623	−9.242	2.703	5.257	5.253	−44	−31	2.742	2.748	5.270	−31	−44
MSOL–1			ISEI	−4.624			.263		−47	−34		2.747	5.275	−34	−48
Mean							5.274		−52	−39	2.743	2.749	5.287	−39	−53
SD							.047		7	7		0.021	0.047	7	7
SEM							.021		3	3		0.010	0.021	3	3

Figure 2. Plot of $\Delta'^{17}O$ values (based on $\delta^{i}O_{VSMOW2}$ and a reference line with slope $\lambda_{RL} = 0.528$) vs $\delta^{18}O_{VSMOW2}$ values of SLAP2, VSMOW2, GISP, and San Carlos olivine from the GZG (Göttingen) laboratory (A) and the ISEI (Misasa) laboratory (B). Only 1σ uncertainties are reported. The VSMOW2-SLAP2 regression line was calculated by Monte Carlo simulation. The uncertainties given for GISP and San Carlos include the uncertainty of the VSMOW2-SLAP2 scaling.

of a more expanded suite of mantle-derived rocks than analyzed by Pack and Herwartz,[13] however, may be useful to verify the homogeneity of the Earth's mantle.

The non-linearity of the mass spectrometer with respect to VSMOW2-SLAP2 requires correction of the equilibrium fractionation slopes reported in Pack and Herwartz.[13] The slope defined by minerals (olivine, low- and high-Ca pyroxene, spinel) of San Carlos peridotite ($T_{eq} = 1050°C$) becomes 0.530 ± 0.06, the slope for the granite (plagioclase − quartz, $T_{eq} = 620°C$) becomes 0.529 ± 0.003, and the minerals (quartz, hedenbergite, magnetite) of a metamorphic banded iron formation ($T_{eq} = 600°C$) defined a slope of 0.530 ± 0.001. The slopes are now very close to the high-T approximation for equilibrium fractionation of 0.5305.[20,28]

The recalculated VSMOW2- and VSMOW2-SLAP2-scaled values of Tanaka and Nakamura[5] do not change significantly. The slope defined by mantle peridotite minerals (olivine, low- and high-Ca pyroxenes, and spinel) analyzed at ISEI is 0.527 ± 0.014 for both VSMOW2- and VSMOW2-SLAP2-scaled data, the same value as that calculated from the original data of Tanaka and Nakamura.[5]

CONCLUSIONS

High precision $\Delta'^{17}O$ data of rocks and minerals should be reported on the basis of VSMOW2-SLAP2 scaled $\delta^{17}O$ and $\delta^{18}O$ values. The $\Delta'^{17}O_{0.5305}$ value of San Carlos olivine is ~ -50 ppm ($\Delta'^{17}O_{0.528} \approx$ -40 ppm). The non-linearity of the mass spectrometer should be determined by the analysis of O_2 extracted from VSMOW2 and VSLAP2 in the same laboratory. Working reference materials with known $\delta^{17}O$ values, but very different $\delta^{18}O$ values, may be prepared for every-day monitoring of the non-linearity. The data from this study show that the determination of the $\Delta'^{17}O$ values of rocks and minerals relative to VSMOW2 and SLAP2 with an accuracy <10–15 ppm remains challenging.

Acknowledgements

REFERENCES

[1] H. A. J. Meijer, W. J. Li. The use of electrolysis for accurate $\delta^{17}O$ and $\delta^{18}O$ isotope measurements in water. Isot. Environ. Health Stud. 1998, 34, 349.

[2] E. Barkan, B. Luz. High precision measurements of $^{17}O/^{16}O$ and $^{18}O/^{16}O$ ratios in H_2O. Rapid Commun. Mass Spectrom. 2005, 19, 3737.

[3] M. Kusakabe, Y. Matsuhisa. Oxygen three-isotope ratios of silicate reference materials determined by direct comparison with VSMOW-oxygen. Geochem. J. 2008, 42, 309.

[4] Y. Lin, R. N. Clayton, M. Gröning. Calibration of $\delta^{17}O$ and $\delta^{18}O$ of international measurement standards – VSMOW, VSMOW2, SLAP, and SLAP2. Rapid Commun. Mass Spectrom. 2010, 24, 773.

[5] R. Tanaka, E. Nakamura. Determination of ^{17}O-excess of terrestrial silicate/oxide minerals with respect to Vienna Standard Mean Ocean Water (VSMOW). Rapid Commun. Mass Spectrom. 2013, 27, 285.

[6] M. F. Miller, I. A. Franchi, A. S. Sexton, C. T. Pillinger. High precision $\delta^{17}O$ isotope measurements of oxygen from silicates and other oxides: method and applications. Rapid Commun. Mass Spectrom. 1999, 13, 1211.

[7] U. Wiechert, A. N. Halliday, D. C. Lee, G. A. Snyder, L. A. Taylor, D. Rumble. Oxygen isotopes and the Moon-forming giant impact. Science 2001, 339, 780.

[8] M. J. Spicuzza, J. M. D. Day, L. A. Taylor, J. W. Valley. Oxygen isotope constraints on the origin and differentiation of the Moon. Earth Planet. Sci. Lett. 2007, 253, 254.

[9] A. Pack, C. Toulouse, R. Przybilla. Determination of oxygen triple isotope ratios of silicates without cryogenic separation of NF_3 − technique with application to analyses of technical O_2 gas and meteorite classification. Rapid Commun. Mass Spectrom. 2007, 21, 3721.

[10] D. Rumble, M. F. Miller, I. A. Franchi, J. P. Greenwood. Oxygen three-isotope fractionation lines in terrestrial silicate minerals: an inter-laboratory comparison for hydrothermal quartz and eclogite garnet. Geochim. Cosmochim. Acta 2007, 71, 3592.

[11] L. J. Hallis, M. Anand, R. C. Greenwood, M. F. Miller, I. A. Franchi, S. S. Russell. The oxygen isotope composition, petrology and geochemistry of mare basalts: Evidence for large-scale compositional variation in the lunar mantle. Geochim. Cosmochim. Acta 2010, 74, 6885.

[12] D. Rumble, S. Bowring, T. Iizuka, T. Komiya, I. Lepland, M. T. Rosing, Y. Ueno. The oxygen isotope composition of earth's oldest rocks and evidence of a terrestrial magma ocean. Geochem. Geophys. Geosyst. 2013, 14, 1929.

[13] A. Pack, D. Herwartz. The triple oxygen isotope composition of the Earth mantle and understanding $\Delta^{17}O$ variations in terrestrial rocks and minerals. Earth Planet. Sci. Lett. 2014, 390, 138.

[14] C. R. McKinney, J. M. McCrea, S. Epstein, H. A. Allen, H. C. Urey. Improvements in mass spectrometers for the measurement of small differences in isotope abundance ratios. Rev. Sci. Instrum. 1950, 21, 724.

[15] E. J. Steig, V. Gkinis, A. J. Schauer, S. W. Schoenemann, K. Samek, J. Hoffnagle, K. J. Dennis, S. M. Tan. Calibrated high-precision ^{17}O-excess measurements using cavity ring-down spectroscopy with laser-current-tuned cavity resonance. Atm. Meas. Techn. 2014, 7, 2421.

[16] P. Baertschi, S. R. Silverman. The determination of relative abundances of the oxygen isotopes in silicate rocks. Geochim. Cosmochim. Acta 1951, 39, 569.

[17] Z. D. Sharp. A laser-based microanalytical technique for in situ determination of oxygen isotope ratios of silicates and oxides. Geochim. Cosmochim. Acta 1990, 54, 1353.

[18] D. Herwartz, A. Pack, B. Friedrichs, A. Bischoff. Identification of the giant impactor Theia in lunar rocks, Science 2014, 344, 1146.

[19] I. E. Kohl, P. H. Warren, E. D. Young. Earth and Moon are indistinguishable in $\Delta^{17}O$ to several parts per million. 46th Lunar and Planetary Science Conference (Houston), 2015, abstract 2867.

[20] Y. Matsuhisa, J. R. Goldsmith, R. N. Clayton. Mechanisms of hydrothermal crystallization of quartz at 250°C and 15 kbar. Geochim. Cosmochim. Acta 1978, 42, 173.

[21] X. Cao, Y. Liu. Equilibrium mass-dependent fractionation relationships for triple oxygen isotopes. Geochim. Cosmochim. Acta 2011, 75, 7435.

[22] D. Herwartz, A. Pack, D. Krylov, Y. Xiao, K. Muehlenbachs, S. Sengupta, T. Di Rocco. Revealing the climate of 'snowball Earth' from $\Delta^{17}O$ systematics of hydrothermal rocks. Proc. Natl. Acad. Sci. 2015, 112, 5337.

[23] I. Ahn, J. I. Lee, M. Kusakabe, B.-G. Choi. Oxygen isotope measurements of terrestrial silicates using a CO_2-laser BrF_5 fluorination technique and the slope of terrestrial fractionation line. Geosci. J. 2012, 16, 7.

[24] M. Hofmann, B. Horváth, A. Pack. Triple oxygen isotope equilibrium fractionation between CO_2 and water. Earth Planet. Sci. Lett. 2012, 319/320, 159.

[25] T. B. Coplen. Discontinuance of SMOW and PDB. Nature 1995, 54, 349.

[26] S. W. Schoenemann, A. J. Schauer, E. J. Steig. Measurement of SLAP2 and GISP $\delta^{17}O$ and proposed VSMOW-SLAP normalization for $\delta^{17}O$ and $^{17}O_{excess}$. Rapid Commun. Mass Spectrom. 2013, 27, 582.

[27] R. Gonfiantini. Standards for stable isotope measurements in natural compounds. Nature 1978, 271, 534.

[28] E. D. Young, A. Galy, H. Nagahara. Kinetic and equilibrium mass-dependent isotope fractionation laws in nature and their geochemical and cosmochemical significance. Geochim. Cosmochim. Acta 2002, 66, 1095.

[29] J. R. O'Neil, S. Epstein. A method for oxygen isotope analysis of milligram quantities of water and some of its applications. J. Geophys. Res. 1966, 71, 4955.

[30] T. B. Coplen. Reporting of stable hydrogen, carbon, and oxygen isotopic abundances. Pure Appl. Chem. 1994, 66, 273.

[31] IAEA. Reference sheet for international measurement standards VSMOW2 and SLAP2. IAEA, Vienna, Austria, 2009. Available: https://nucleus.iaea.org/rpst/Documents/VSMOW2_SLAP2.pdf.

[32] E. Barkan, B. Luz. High-precision measurements of $^{17}O/^{16}O$ and $^{18}O/^{16}O$ of O_2 and O_2/Ar ratio of air. Rapid Commun. Mass Spectrom. 2003, 17, 2809.

[33] Z. D. Sharp, J. A. Gibbons, O. Maltsev, A. Pack, S. Sengupta, E. L. Shock, L. P. Knauth. A calibration of the triple oxygen isotope fractionation in the SiO_2–H_2O system and applications to natural samples. Geochim. Cosmochim. Acta 2016, in press.

[34] M. F. Miller, R. C. Greenwood, I. A. Franchi. Comment on "The triple oxygen isotope composition of the Earth mantle and understanding $\Delta^{17}O$ variations in terrestrial rocks and minerals" by Pack and Herwartz [Earth Planet. Sci. Lett. 2014, 390, 138–145]. Earth Planet. Sci. Lett. 2015, 418, 181.

[35] A. Pack, D. Herwartz. Observation and interpretation of $\Delta^{17}O$ variations in terrestrial rocks − Response to the comment by Miller et al. on the paper by Pack & Herwartz (2014). Earth Planet. Sci. Lett. 2015, 418, 184.

Tracing the oxygen isotope composition of the upper Earth's atmosphere using cosmic spherules

Andreas Pack, Andres Höweling, Dominik C. Hezel, Maren Stefanak, Anne-Katrin Beck, Stefan T. M. Peters, Sukanya Sengupta, Daniel Herwartz

and

Luigi Folco

My contribution to the manuscript: Running extraction and measurement of triple oxygen isotope composition of air O_2 with Maren Stefanak and Anne Beck as a part of their Bachelor's thesis

Tracing the oxygen isotope composition of the upper Earth's atmosphere using cosmic spherules

Andreas Pack[1], Andres Höweling[1,2], Dominik C. Hezel[3], Maren T. Stefanak[1], Anne-Katrin Beck[1], Stefan T.M. Peters[1], Sukanya Sengupta[1], Daniel Herwartz[3] & Luigi Folco[4]

Molten I-type cosmic spherules formed by heating, oxidation and melting of extraterrestrial Fe,Ni metal alloys. The entire oxygen in these spherules sources from the atmosphere. Therefore, I-type cosmic spherules are suitable tracers for the isotopic composition of the upper atmosphere at altitudes between 80 and 115 km. Here we present data on I-type cosmic spherules collected in Antarctica. Their composition is compared with the composition of tropospheric O_2. Our data suggest that the Earth's atmospheric O_2 is isotopically homogenous up to the thermosphere. This makes fossil I-type micrometeorites ideal proxies for ancient atmospheric CO_2 levels.

[1] Universität Göttingen, Geowissenschaftliches Zentrum, Goldschmidtstraße 1, 37077 Göttingen, Germany. [2] Karlsruher Institut für Technologie, Institut für Angewandte Materialien - Werkstoffprozesstechnik, Hermann-von-Helmholtz-Platz 1, 76344 Eggenstein-Leopoldshafen, Germany. [3] Universität Köln, Institut für Geologie und Mineralogie, Greinstraße 4-6, 50939 Köln, Germany. [4] Università di Pisa, Dipartimento di Scienze della Terra, Via Santa Maria 53, 56126 Pisa, Italy. Correspondence and requests for materials should be addressed to A.P. (email: apack@uni-goettingen.de).

Free molecular oxygen (O_2) is released by photosynthesis into the atmosphere and is essential for all breathing animals. With exception of data for the last 800,000 years from air inclusions in polar ice, little direct information is available about concentration and isotope composition of ancient atmospheric O_2. This is due to the limited interaction between air molecular oxygen and the lithosphere.

Among the rare rocky materials that contain atmospheric oxygen[1–3] there are particular types of micrometeorites (microscopic extraterrestrial dust particles) called cosmic spherules[4]. Roughly 10 tons of small extraterrestrial particles are deposited onto the Earth's surface per day[5]. The particles collide with the Earth's atmosphere at velocities of $11-70 km s^{-1}$ (ref. 6) and are visible as shooting stars when they are decelerated and at altitudes up to Ḃ$80-115$ km[7,8]. A portion of these extraterrestrial particles totally melts during the atmospheric entry and is termed cosmic spherules. Cosmic spherules that are composed of Fe,Ni oxides are termed 'I-type cosmic spherules' (in the following, we use the short version 'I-type spherules'[9–11]. These I-type spherules formed by oxidation of extraterrestrial Fe,Ni metal alloys, which are ubiquitous components of meteorites.

Because oxygen in I-type spherules originates entirely from the atmosphere, they are excellent probes for the isotopic composition of upper atmospheric oxygen. The isotopic composition of atmospheric oxygen, in turn, is a proxy for the global primary production (GPP) and atmospheric CO_2 levels[1,2,12–14]. It is not clear, however, if the atmospheric oxygen is isotopically homogenous up to the meso- and thermosphere, where cosmic spherules interact with air.

The stable isotope composition of tropospheric O_2 (99.8% ^{16}O, 0.04% ^{17}O, 0.2% ^{18}O) is controlled by the steady state between photosynthesis and respiration (mass-dependent Dole effect[15]), evapotranspiration and mass-independent fractionation in the stratosphere[14,16]. For the composition of the modern troposphere values of $23.4 rd^{18}O r 24.2\%$ and $-0.566 r D'^{17}O r -0.430\%$ have been reported in the literature[14,17–20] (for definitions, see Methods) with little variations up to 61 km (ref. 17). The high $d^{18}O$ of tropospheric O_2 is caused by the Dole effect, whereas the low $D'^{17}O$ value reflects mass-independent fractionation effects in the stratosphere. The higher the atmospheric CO_2 levels, the lower the $D'^{17}O$ values[12,14]; a relation that was used as paleo-CO_2 barometer[1,2,13].

No experimental oxygen isotope data are available for the upper atmosphere at altitudes 461 km. To obtain information about the $D'^{17}O$ heterogeneity of the atmosphere, we measured the oxygen ($d^{17}O$, $d^{18}O$) and iron ($d^{56}Fe$, $d^{57}Fe$; see Methods for definition) isotope composition of I-type spherules from the Transantarctic Mountains that have ages o2 Ma (ref. 21). For this time interval, atmospheric CO_2 levels as well as $D'^{17}O$ of O_2 did not deviate much from the modern level[22,23] and data can be used to test whether the atmosphere is isotopically homogenous. Because of the Ḃ$1,000$ years residence time of atmospheric O_2 (ref. 14), no effect on the man-made increase in CO_2 is yet visible in decreasing $D'^{17}O$.

The oxygen isotope composition of I-type spherules is controlled by the composition of the oxidizing species (for example, atmospheric O_2), the fractionation during oxidation of the Fe,Ni alloys, and the fractionation during atmospheric evaporation.

Cosmic spherules have higher $d^{18}O$ values (up to 56%; ref. 24) than any terrestrial material reported so far. The high $d^{18}O$ led Clayton et al.[4] to propose a heavy oxygen isotope reservoir in the upper atmosphere. Davis et al.[25], however, showed that I-type spherules are also enriched in heavy iron isotopes with extreme $d^{56}Fe$ values of up to 45%. They concluded that high $d^{18}O$ values

are due to evaporation and do not reflect the isotope composition of the upper atmosphere; a conclusion that was supported by further measurements[24,26–29]. From the oxygen and iron isotope composition, Engrand et al.[24] modeled evaporative mass losses for I-type spherules of 54–85%.

Because evaporative fractionation is strictly mass-dependent, I-type spherules still provide unique information about the mass-independent anomaly in $D'^{17}O$ of their upper mesospheric oxygen source. The reconstruction of variations in atmospheric $D'^{17}O$ from fossil cosmic spherules[4,30–33] would be a new paleo-CO_2 proxy. The only published $D'^{17}O$ data on I-type spherules by Clayton et al.[4] and Engrand et al.[24], however, have intrinsic uncertainties that are too large (0.1 to 41%) to provide reliable information on the composition of the upper atmosphere.

We present new high-precision oxygen isotope data of tropospheric O_2 and compare these data with new high-precision oxygen and iron isotope data from Antarctic I-type spherules. These data are combined with results of oxidation and evaporation experiments to test if the Earth atmosphere is isotopically homogenous and if isotope ratios of fossil cosmic spherules are suitable paleo-CO_2 proxies.

Results

Oxygen isotope composition of tropospheric air. The mean composition of air oxygen from our study (series B; Supplementary Table 1) is $d^{18}O$ ¼ $24.15 \pm 0.05\%$ with $D'^{17}O$ ¼ $-0.469 \pm 0.007\%$. An earlier protocol (series A; Supplementary Table 1) gave identical $D'^{17}O$, but slightly lower $d^{18}O$. The datum from this study is within the range reported in the literature and agrees with $D'^{17}O$ values of Thiemens et al.[17] and Young et al.[14]. The measured data of Young et al.[14] have been corrected relative to the San Carlos olivine value reported by Pack et al.[34]. The corrected measured datum of $D'^{17}O$ ¼ $-0.467 \pm 0.005\%$ for air oxygen[14] is then identical to our measured datum of $-0.469 \pm 0.007\%$ (Supplementary Table 1) and agrees with the model datum of -0.469% presented by Young et al.[14] The non-application of VSMOW2-SLAP2 scaling[34] to our air data shifts the $D'^{17}O$ down to Ḃ-0.50%, which would be closer to the values of Barkan and Luz[18][20]. For this study, we adopt $d^{18}O$ ¼ 24.15% and $D'^{17}O$ ¼ -0.47% for the troposphere.

Oxygen and iron isotope composition of cosmic spherules. The isotope composition of the I-type spherules and the oxidation experiment run products are listed in Supplementary Table 2. The $d^{18}O$ of the spherules ranges from 36 to 42%. The corresponding $D'^{17}O$ ranges from -0.72 to -0.62%. The $d^{18}O$ and the $D'^{17}O$ is within the range reported by Clayton et al.[4] and Engrand et al.[24] The $d^{56}Fe$ values are high for all spherules, ranging from 22 to 32% (Supplementary Table 2).

Discussion

The interaction between cosmic Fe,Ni metal and the Earth atmosphere during deceleration is considered to proceed in two consecutive steps. The first step is the atmospheric heating and oxidation of the infalling Fe,Ni metal alloy (fractionation in oxygen isotopes only). The second step is the melting and evaporation of the Fe,Ni oxides (fractionation in both, oxygen and iron isotopes).

Information about the oxygen isotope fractionation that is associated with the oxidation step is obtained from experiments (this study; see Methods) and from iron meteorite fusion crust data[4,35,36]. The products of the high-T metal oxidation experiments have $d^{18}O$ values that are 4% lower than air oxygen (Supplementary Table 2). Clayton et al.[4] reported $d^{18}O$
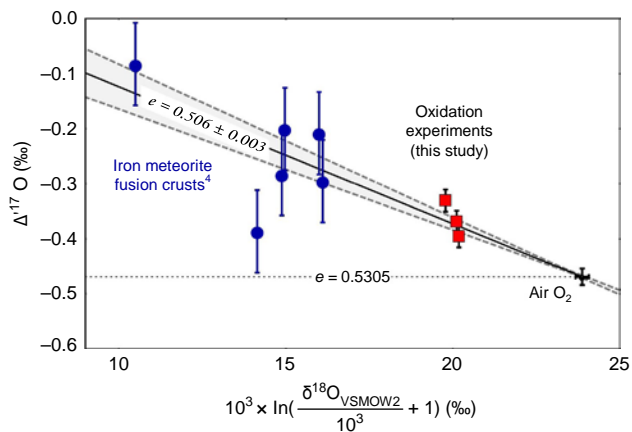
Figure 1 | Triple oxygen isotope fractionation during metal oxidation. Plot of $D'^{17}O$ versus $d'^{18}O$ of the run products of the high-T oxidation experiments (solid red squares) along with air oxygen (this study) and iron meteorite oxide fusion crust (solid blue circles;[4]; the lowest values were not considered as it was likely affected by exchange with low-$d^{18}O$ water). Shown are values with 1s error bars. The oxidation is associated with a kinetic isotope fractionation with slope $y_O \frac{1}{4} 0.506\pm0.003$ (solid line; dashed lines indicate the 1s s.d. uncertainty interval). The high-T equilibrium slope $y \frac{1}{4} 0.5305$ (dotted horizontal line) is shown for comparison.

Figure 2 | Oxygen and iron isotope fractionation during evaporation. Plot of the linearized $d^{18}O$ versus $d^{56}Fe$ of evaporation experiments by Wang et al.[40]. The iron isotope fractionation is a function of fraction f evaporated (Equation 1). The close coupling between $d^{18}O$ and $d^{56}O$ allows prediction of the pre-evaporation $d^{18}O$ of the I-type spherules. The 1s-errors (s.d.) were estimated on base of the scatter of the data. The regression line (solid) is shown with its respective 1s-error envelope (dashed lines).

values of iron meteorite fusion crusts that were B9% lower than air oxygen. They concluded that the atmospheric oxidation of Fe,Ni alloys is associated with kinetic fractionation and formation of isotopically light oxides with $d^{18}O_{Fe,Ni\ oxide} o d^{18}O_{air}$, which we also suggest as the cause of the low $d^{18}O$ of the experimental Fe,Ni oxides. Kinetic fractionation should be associated with a low y_O value (for definition, see Methods). The best-fit line through air, experimental run products and iron meteorite fusion crust[4] has a slope of $y_O \frac{1}{4} 0.506\pm0.003$ (Fig. 1). This low y value clearly supports that kinetic fractionation is the cause for the difference in $d^{18}O_{Fe,Ni\ oxides}$ and $d^{18}O_{air\ O2}$ (ref. 37). Molecular diffusion of O_2 would give a slope of $y_O \frac{1}{4} 0.508$. Iron meteorite fusion crust data[35] suggest that iron isotopes do not fractionate during oxidation.

For the experiments and iron meteorite fusion crusts, atmospheric oxygen is the oxidant. Above the ozone layer, however, a considerable fraction of molecular oxygen is steadily dissociated into atomic oxygen (for example,[38]). Atomic oxygen is a hazard for low Earth orbit space flights due to its highly corrosive nature. Because I-type spherules are oxidized at high altitudes, atomic oxygen may have contributed to the oxidation. However, Clayton et al.[4] and Genge[10] stated that no discrimination between atomic and molecular oxygen is likely during oxidation upon atmospheric entry because the collision energy between infalling meteoroids and air particles is higher than the O_2 bond strength. This implies that I-type spherules sample the bulk upper atmosphere oxygen (O and O_2).

Our experiments and the fusion crust literature data[4] show that $a_{oxidation} o 1$ (for $^{18}O/^{16}O$; see Equation 5), but also reveal considerable variation. For I-type spherules, we assume that $0.9428 r a_{oxidation} r 1$. The lower limit is given by pure Graham's law[39] fractionation with atomic oxygen being the moving species.

The second process affecting the isotopic composition of I-type spherules is evaporation[25]. Because iron isotopes are not affected by oxidation[35] but only by evaporation, $d^{56}Fe$ can be used as monitor for the degree of evaporation f (refs 24,25,40; Equation 1). The $d^{56}Fe$ of the infalling metal is assumed to be
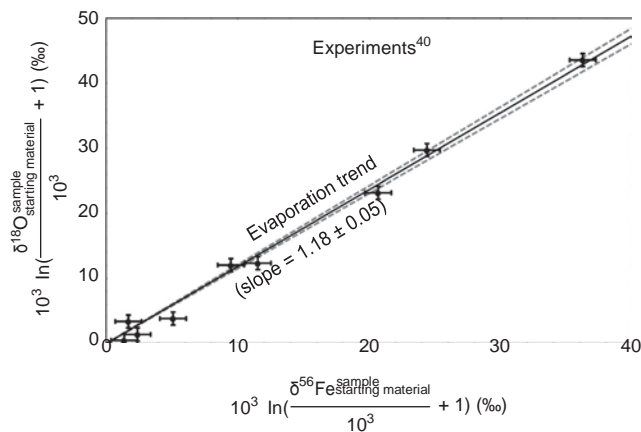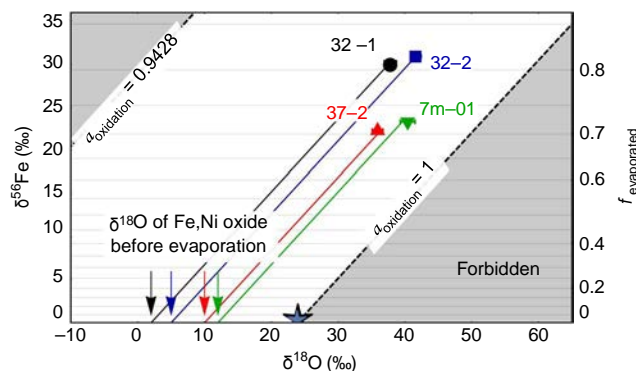

Figure 3 | Model for the triple oxygen isotope fractionation during oxidation. Plot of measured $d^{56}Fe$ versus $d^{18}O$ of spherules for the reconstruction of the pre-evaporative $d^{18}O$ (32-01: black solid circle; 32-02: blue solid square; 37-02: red solid triangle; 7 m-01: rotated green solid triangle). The right axis displays the fraction f that evaporated (70–82%). The slopes of the lines (32-01: black; 32-02: blue; 37-02: red; 7 m-01: green) displayed were taken from the experiments by Wang et al.[40] (Fig. 2. The grey shaded 'forbidden' areas outline cases for unreasonable kinetic fractionation factors a associated with atmospheric oxidation of Fe,Ni metal; all studied spherules fall outside the forbidden areas. The star marks the $d^{18}O$ of modern air oxygen.

$0\pm1\%$ relative to the IRMM-014 standard material[41].

$$d^{56}Fe \frac{1}{4} 10^3 ð1 - f Þ^{a_{evaporation}^{56=54} - 1} - 1 \qquad ð1Þ$$

Wang et al.[40] determined an $a_{evaporation} \frac{1}{4} 0.9820$ ($^{56}Fe/^{54}Fe$). This value in combination with $d^{56}Fe$ allows calculation of f for the I-type spherules (Equation 1). The $d^{56}Fe$ values of the spherules from this study (Supplementary Table 2) indicate evaporative mass loss of 70 r f r 82%, which is well in the range of 54 r f r 85% reported by Engrand et al.[24].

The experimental relation between $d^{18}O$ and $d^{56}Fe$ during evaporation from Wang et al.[40] (Fig. 2) now allows reconstructing the $d^{18}O$ of the I-type spherules before
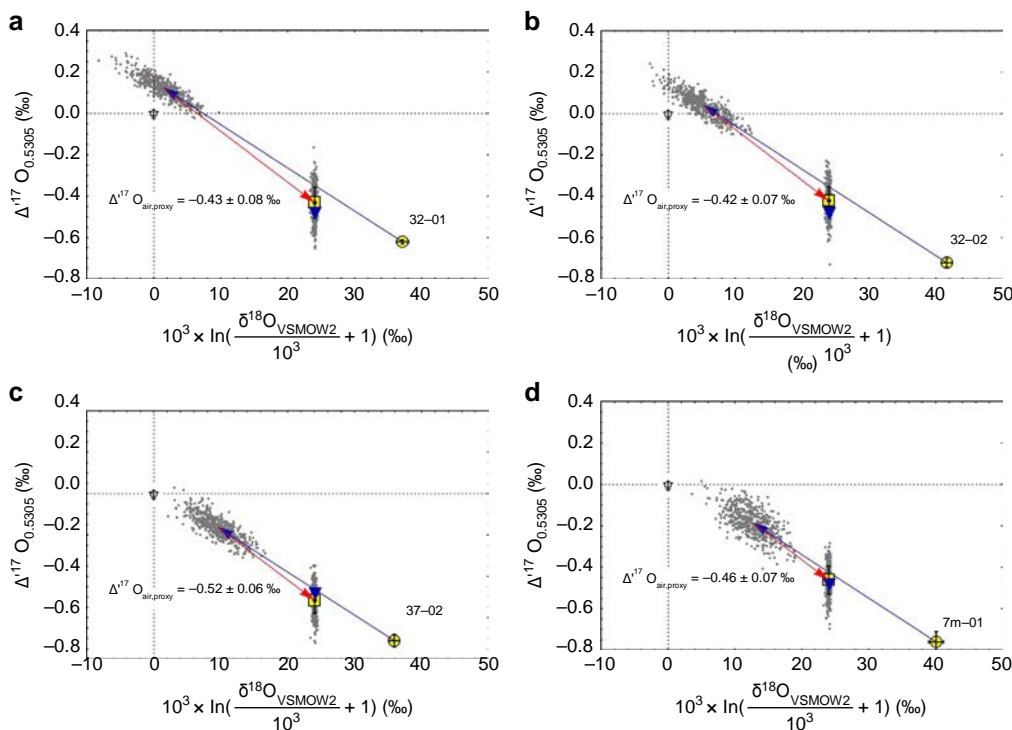
Figure 4 | Reconstruction of the D'17O of upper atmospheric oxygen. Plot of D'17O versus linearized d18O showing the result of the model calculations (including MonteCarlo error calculation (N ¼ 500) grey dots) for I-type spherules 32–01 (a), 32–02 (b), 37–02 (c) and 7 m-01 (d). The measured composition of the I-type spherules is displayed (yellow circle). The oxygen isotope composition is controlled by oxidation (red arrow) and evaporation (blue arrow). The resultant D'17O (at given d18O ¼ 24%; this study) is displayed (yellow square) along with the composition of modern tropospheric O_2 (filled upside–down triangle). Given are 1s-error bars.

evaporation (f ¼ 0; Equation 2).

$$\ln\left(\frac{d^{18}O_{before\;evaporation}}{10^3} + 1\right) \; ¼ \; \ln\left(\frac{d^{18}O_{spherule}}{10^3} + 1\right) \\ -1:18 \cdot \ln\left(\frac{d^{56}Fe_{spherule}}{10^3} + 1\right)$$

ð2Þ

The difference in d18O between the spherules before evaporation and air oxygen gives the degree of fractionation during the oxidation step. We obtained values between −22 and −12% during oxidation of the infalling Fe,Ni alloys (Fig. 3). The greater magnitudes of fractionation compared with our experiments (−4%) and iron meteorite fusion crust (B −9%; ref. 4) is attributed to the much shorter heating time of I-type spherules[10] compared with iron meteorites and experiments. Shorter heating and oxidation time prevents equilibration between oxides and air oxygen.

For the reconstruction of the D'17O of the upper mesospheric oxygen, we need the y_O values for the oxidation (0.506±0.003; Fig. 1) and evaporation. Wang et al.[40] measured y_O ¼ 0.5096 for their evaporation experiments. As in case of oxidation, the low y_O value is indicative of kinetic fractionation during evaporation[37]. The observed y_{Fe} values during evaporation (y_{Fe} ¼ 0.671; ref. 40) and for the I-type spherules from this study (y_{Fe} ¼ 0.674) are significantly lower than the high-T equilibrium value of y_{Fe} ¼ 0.687 (see ref. 37 for details) and support kinetic fractionation.

The results of the calculation are listed in Supplementary Table 3 and illustrated in Fig. 4. The gas that oxidized the studied Antarctic I-type spherules had −0.510rD'17Or−0.420% (mean −0.460±0.020%; this study;[14,17] which is in excellent agreement with measured D'17O¼−0.469% for the modern troposphere (Fig. 4).

Our data from oxygen and iron isotope analyses of Antarctic I-type spherules are consistent with an oxygen source with a D'17O similar to that of modern tropo- and stratospheric molecular oxygen within±0.02%. No oxygen reservoir with a markedly different D'17O participated in the oxidation of I-type spherules, suggesting that the Earth atmosphere is isotopically homogenous up to the mesosphere in B70–80 km (Fig. 5).

Our results imply that the oxygen isotope composition (D'17O) of the bulk atmosphere can be reconstructed from combined oxygen and iron isotope data of I-type cosmic spherules. This has an important implication for the reconstruction of past atmospheric CO_2 levels. Blunier et al.[42] showed that the D'17O of atmospheric molecular oxygen, indeed, varies with CO_2 partial pressures. This is predicted from experiments[12] and mass balance modeling[14]. The oxygen and iron isotope composition of unaltered fossil I-type cosmic spherules[4,30–33] will thus provide information on the D'17O of the ancient atmosphere and past CO_2 levels. The resolution of the calculated D'17O$_{O2}$ isB0.07% (single I-type cosmic spherule; see Fig. 4), which translates (at modern GPP) to an uncertainty in the CO_2 mixing ratio ofB200 p.p.m. Lower than modern GPP levels would lead to an even higher resolution of calculated CO_2 levels. The reconstruction of CO_2 levels based on 17O in I-type spherules is therefore considerably more precise than CO_2 reconstruction from 17O of sulfate[1] and reaches far more back into Earth history than 17O from air inclusions in ice cores[42] and fossil mammal bioapatite[2,13]. However, to use D'17O of air oxygen as paleo-CO_2-barometer the GPP at that time needs to be known[14]. This may limit the usability of the new proxy. The apparent disadvantage, however, can be turned into a fortune. If the atmospheric CO_2 concentration is known from other, independent proxies[43], D'17O of atmospheric molecular oxygen
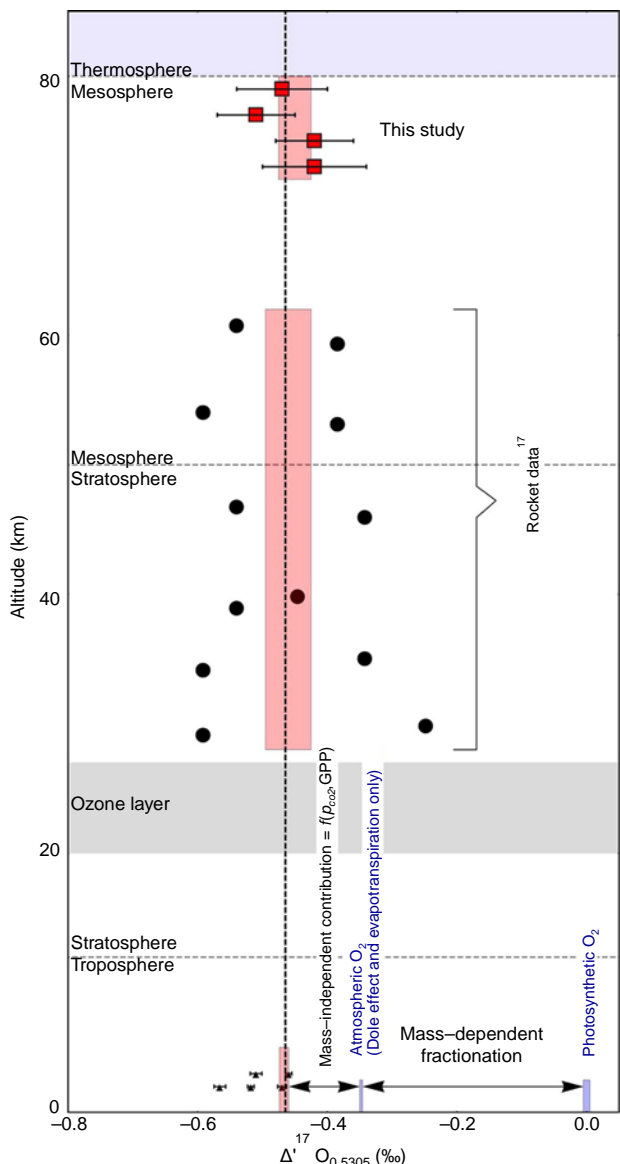
Figure 5 | Isotope profile through the Earth atmosphere. Diagram showing the D'^{17}O profile of the modern atmosphere. The data up to 61 km are measurements on air samples (solid circles: [17]; solid triangles:[14,18–20,54]). These data agree well with the mesospheric I-type spherule proxy data from this study (solid red squares with 1s-error bars).

in combination with mass balance modeling[14] turns into a proxy for the GPP. There is little doubt that I-type cosmic spherules were deposited during the entire geological history of the Earth. The question is whether sufficiently large and unaltered fossil I-type spherules can actually be recovered from sediments. The recent find of unaltered 2.7 Ga old I-type cosmic spherules[33] is very promising in this respect.

Methods

Sampling and experiments. We studied a total of 21 aliquots of four samples for oxygen isotopes and one aliquot of the four samples each for iron isotopes. The samples are part of the Transantarctic Mountain collection[44]. The sample sizes range between 400 and 550 mm with masses between 160 and 370 mg. The samples were inspected for weathering products by optical microscopy. No weathering products (for example, brownish ferrihydride or goethite) were observed.

The spherule densities were determined prior to crushing. Their diameters and masses were measured and from this their densities calculated (Supplementary Table 4). The I-type spherule densities vary between 4.3 and 4.8 g cm^{-3} (Supplementary Table 4).

The density data confirm that the I-type spherules are composed of Fe,Ni oxides with little or no remaining Fe,Ni metal. The studied samples fall within the density range (5.0±0.5 g cm^{-3}) observed by Feng et al.[45]. Wüstite ([Fe,Ni]O$_{0.94}$) has a density of 5.7 and magnetite ([Fe,Ni]$_2$FeO$_4$) of 5.2 g cm^{-3}. In contrast, iron metal has a density of 7.9 g cm^{-3}. The apparent lower density of the spherules compared to wüstite and magnetite is explained by B20 vol.% pore space.

The samples are all spherical due to melting during their atmospheric entry. The bulk elemental composition and the mineralogy of the studied spherules were not determined. Electron microprobe analysis of I-type spherules from the same collection yielded 91±5 wt.% FeO, 2.8±0.5 wt.% NiO, and MgO, Al$_2$O$_3$, and o0.5 wt.% SiO$_2$ (ref. 44). This composition is similar to results of Engrand et al.[24] and Herzog et al.[28] who report values of 92–93 wt.% FeO and 4–5 wt.% NiO.

For isotope analysis, spherules were wrapped in Al foil and gently crushed in a steel mortar. We obtained 21 aliquots (4–8 per spherule) with masses of 20–50 mg. As magnetite is the dominant phase in I-type spherules[24,46], we used terrestrial magnetite along with NBS-28 quartz for tests. For NBS-28, we adopted a d^{18}O¼9.65% and D'^{17}O¼ −0.054% (D'^{17}O from[47], with revision from[34]).

I-type spherules form by oxidation of Fe,Ni alloys at high temperatures during their atmospheric entry. We conducted three metal oxidation experiments at the University of Göttingen to study the oxygen isotope fractionation associated with high temperature oxidation of metal in air. A powdered iron base alloy with 7.5 wt.% Ni and 0.6 wt.% Co was used as an analogue material for I-type spherules. Between 0.8 and 1.1 mg powder was placed on a ceramic plate in the hot zone of a Gero HTRV vertical gas-mixing furnace. The furnace was flushed with 300 ml min^{-1} air. Oxidation occurred between 1,510 and 1,590 °C for 30 min.

Air samples were taken at the Göttingen University North Campus outside the Geoscience Building (51°33023^{00} N 9°56046^{00} E). The air was taken from the balcony on the 4th floor using a 5 ml syringe yielding B1 ml standard temperature and pressure O$_2$ gas.

Oxygen isotope analyses. Variations in stable oxygen isotope ratios of a sample are expressed in form of the d notation relative to the ratios in VSMOW2 water (Equation 3) with i standing for masses 17 and 18:

$$d^i O_{sample} \frac{1}{4} \frac{\frac{^i O}{^{16} O}_{sample}}{\frac{^i O}{^{16} O}_{VSMOW2}} - 1 \qquad \eth 3 \th$$

Deviations from an otherwise close correlation between d^{17}O and d^{18}O are expressed in form of the D'^{17}O notation (Equation 4). We choose a reference line with slope 0.5305 and zero intercept. Deviations of D'^{17}O from zero can be caused by both, non-mass-dependent and mass-dependent processes.

$$D^0 {}^{17} O^{sample} \frac{1}{4} \ln \eth d^{17} O^{sample} \th 1 \th - 0.5305 \cdot \ln \eth d^{18} O^{sample} \th 1 \th \qquad \eth 4 \th$$

The fractionation between two reservoirs (A, B) is expressed in form of the fractionation factor a (Equation 5). The reservoirs could be two phases in equilibrium or products (B) and educts (A) of a kinetic process.

$$a_{A-B}^{i=16} \frac{1}{4} \frac{d^i O^A \th 1000}{d^i O^B \th 1000} \qquad \eth 5 \th$$

The i in Equation 5 stands for isotopes with masses 17 and 18. For mass-dependent processes, the relation between a$^{17/16}$ and a$^{18/16}$ is linked through the triple oxygen isotope fractionation exponent y$_O$ (Equation 6).

$$a_{A-B}^{^{17} O = {}^{16} O} \frac{1}{4} \eth a_{A-B}^{^{18} O = {}^{16} O} \th^{y_O} \qquad \eth 6 \th$$

For oxygen y$_O$ varies between 0.5000 and 0.5305 (refs 37,48,49). Only for very small a values, y values may fall outside the 0.5–0.5305 range[50]. Such effects are neglected here. As a rule, low y values are associated with kinetic effects, whereas higher y values are associated with equilibrium fractionation processes.

The triple oxygen isotope ratios of I-type spherules and the high-T oxidation experiment run products were analysed at the University of Göttingen on O$_2$ extracted by infrared laser fluorination[51], following the protocol described in Pack et al.[2]. In brief, sample O$_2$ was liberated by laser fluorination (F$_2$) and analysed in continuous flow mode in a Thermo MAT253 gas source mass spectrometer. NBS-28 quartz was used for normalisation relative to VSMOW2 scale (d^{17}O¼5.04%, d^{18}O¼9.65%, D^{17}O¼ −0.054%; using the revised calibration of San Carlos olivine from[34]). The total masses of the spheres were 160–370 mg and thus suitable for measurement of multiple aliquots of a single spherule. For the oxidation experiments, B0.6–1 mg aliquots were analysed.

Oxygen from air was extracted using the same line that was described by Pack et al.[34] for their water (including VSMOW2 and SLAP2) and silicate analyses (San Carlos olivine) (Fig. 6).

For each extraction, 5 ml aliquots of air standard temperature and pressure (STP) were injected through a liquid nitrogen cooled glass U-trap (for removal of moisture and CO$_2$; 'trap 7', Fig. 6). The dry, CO$_2$ free mixture of Ar, N$_2$ and O$_2$ was transferred to 'trap 2' that was filled with 5 Å molecular sieve pellets. In an early protocol (S01–S05; Supplementary Table 1), Ar was separated from O$_2$ at −100 °C, which resulted in very long trapping times. In an improved protocol (B01–BP2; Supplementary Table 1), separation of Ar was performed using the cryo unit of the Hewlett-Packard 5890 gas chromatograph at −80 °C. After Ar had passed through the gas chromatograph (monitored using a Pfeiffer Prisma
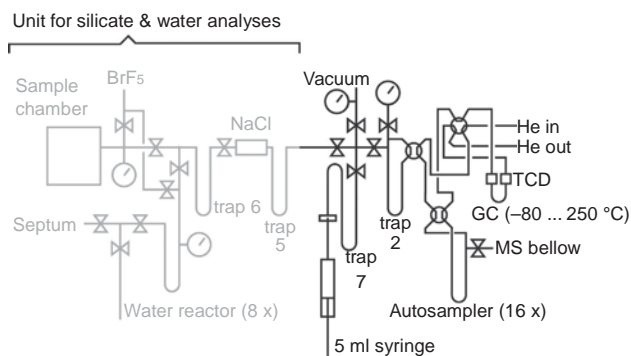
Figure 6 | Illustration of the extraction line. Sketch of the extraction line used for the air measurements. The same line was used for the measurement of VSMOW2, SLAP2 and San Carlos olivine[34].

quadrupole mass spectrometer at the end of the He capillary; 'He out' in Fig. 6), temperature was raised to $-30 °C$ for the elution of O_2 and separation of N_2. The improved protocol is similar to the protocol described by Young et al.[14]. The purified O_2 was analysed for B60–90 min in dual inlet mode.

To test accuracy and precision of laser F_2 in combination with continuous flow mass spectrometry of small samples, a set of experiments were performed on magnetite (as analogues of I-type spherules) and NBS-28 quartz (Fig. 7).

Our tests on NBS-28 quartz and magnetite (Fig. 7) show that precise analyses of $d^{18}O$ and $D'^{17}O$ are possible down to 10 mg samples. The blank intensities corresponded to rB 0.005 mmol O_2 (rB6% of the sample). The tests reveal uncertainties in $d^{18}O$ of±0.6% for quartz and±1% for magnetite. The uncertainties in $D'^{17}O$ were±0.03% for quartz and ±0.05% for magnetite. The higher uncertainty observed for magnetite may be due to heterogeneity on small scale (for example,[52]). For our I-type spherule analyses, we adopt analytical uncertainties of 1% for $d^{18}O$ and 0.06% for $D'^{17}O$. We have not adopted the VSMOW2-SLAP2 scaling for the continuous flow measurements since conditions during the measurement are less controlled (for example, variable peak heights and widths) and VSMOW2-SLAP2 correction for $D'^{17}O$(ref. 34) would be smaller than the uncertainty in $D'^{17}O$. The agreement between the spherule $D'^{17}O$ from this study and conventional F_2 data from Clayton et al.[4] confirm that the continuous flow $d^{17}O$ data are on VSMOW2 scale.

Iron isotopes. Three iron isotopes have been analysed (^{54}Fe, ^{56}Fe, ^{57}Fe). Isotope ratios are expressed relative to the IRMM-014 standard in form of the d notation with:

$$d^i Fe = \frac{\frac{^iFe}{^{54}Fe} \text{sample}}{\frac{^iFe}{^{54}Fe} \text{IRMM-14}} - 1 \qquad (7)$$

and i corresponding to masses 56 and 57. All $d^{56}Fe$ and $d^{57}Fe$ data are reported in % variations. Variations in the three iron isotopes are coupled through the triple iron isotope exponent y_{Fe} (Equation 8).

$$a_{A-B}^{56=54} = (a_{A-B}^{56=54})^{y_{Fe}} \qquad (8)$$

The symbols A and B in Equation 8 can either stand for two phases that are in equilibrium or for educts (B) and products (A) of a reaction with associated kinetic fractionation. The high-T approximation for equilibrium iron isotope fractionation is y_{Fe} = 0.6784 (ref. 37). As in case of oxygen, variations in y_{Fe} provide insights into the fractionation process.

The iron isotope compositions were measured at the University of Bonn using a Thermo Scientific Neptune MC-ICP-MS instrument and glassware for sample introduction. Samples were measured 2–3 times, non-consecutively, during long analytical sessions of around 8 hours. Analyses were carried out in high-resolution mode with sufficient transmission to allow routine analyses of an 1 p.p.m. iron sample solutions. Each sample measurement was bracketed by two analyses of an IRMM-014 iron solution that was made up to closely match the iron concentration of the sample. The external reproducibility of the data was typically±0.07%, whereas the internal reproducibility was generally about a factor of two better. A detailed description on sample preparation and mass spectrometry can be found in Hezel et al.[53] and Hezel et al.[36].

Monte Carlo simulation. The errors in $d^{18}O$ and $D'^{17}O$ of the upper atmospheric oxygen were estimated using a Monte Carlo approach. The composition was computed 500 times. Each input parameter was varied independently for each run (Supplementary Table 5). We used a normal distribution for the variation within the respective error interval. The computation was performed using the Mathematica software.
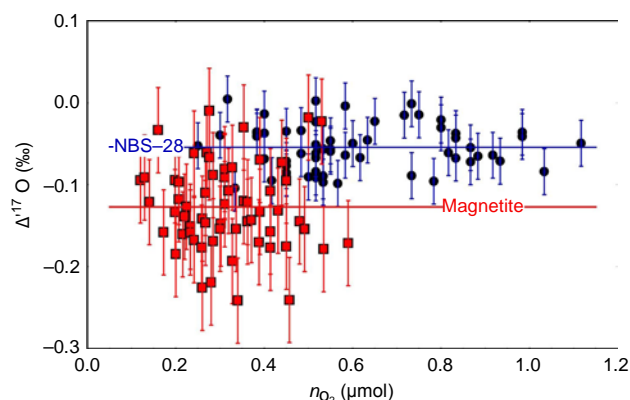
Figure 7 | Results of oxygen isotope analyses of small samples. Plot of $D'^{17}O$ of NBS-28 quartz (solid blue circles) and magnetite (solid red squares) versus amount of O_2 (in moles) in the samples. The continuous flow measurements were normalized to NBS-28 with $D'^{17}O$ ¼ -0.054%. The smallest magnetite samples had masses of only B10 mg. No systematic variation in $D'^{17}O$ is observed with sample size. Errors are 1s standard deviations.

References

1. Bao, H., Lyons, J. & Zhou, C. Triple oxygen isotope evidence for elevated CO_2 levels after a Neoproterozoic glaciation. Nature 54, 349–392 (2008).
2. Pack, A., Gehler, A. & Süssenberger, A. Exploring the usability of isotopically anomalous oxygen in bones and teeth as paleo-CO_2-barometer. Geochim. Cosmochim. Acta 102, 306–317 (2013).
3. Blamey, N. J. F. et al. Paradigm shift in determining neoproterozoic atmospheric oxygen. Geology 44, 651–654 (2016).
4. Clayton, R. N., Mayeda, T. K. & Brownlee, D. E. Oxygen isotopes in deep-sea spherules. Earth Planet. Sci. Lett. 79, 235–240 (1986).
5. Plane, J. M. C. Cosmic dust in the earth's atmosphere. Chem. Soc. Rev. 41, 6507–6518 (2012).
6. Brownlee, D. E. Interplanetary dust. Rev. Geophys. Space Phys 17, 1735–1743 (1979).
7. Love, S. G. & Brownlee, D. E. Heating and thermal transformation of micrometeoroids entering the Earth's atmosphere. Icarus 89, 26–43 (1991).
8. Flynn, G. J. in Accretion of extraterrestrial matter throughout earth's history. (eds Peucker-Ehrenbrink, B. & Schmitz, B.) 107–127 (Springer Scienceþ Business Media, 2001).
9. Genge, M. J., Engrand, C., Gounelle, M. & Taylor, S. The classification of micrometeorites. Meteor. Planet. Sci. 35, 807–816 (2008).
10. Genge, M. J. The origins of I-type spherules and the atmospheric entry of iron micrometeoroids. Meteor. Planet. Sci 51, 1063–1081 (2016).
11. Folco, L. & Cordier, C. in Planetary Mineralogy (eds Lee, M. R. & Leroux, H.) 253–297 (European Mineralogical Union, 2015).
12. Luz, B., Barkan, E., Bender, M. L., Thiemens, M. H. & Boering, K. A. Triple-isotope composition of atmospheric oxygen as a tracer of biosphere productivity. Nature 54, 349–392 (1999).
13. Gehler, A., Gingerich, P. D. & Pack, A. Temperature and atmospheric CO_2 concentration estimates through the PETM using triple oxygenisotope analysis of mammalian bioapatite. Proc. Natl Acad. Sci. USA 113, 7739–7744 (2016).
14. Young, E. D., Yeung, L. Y. & Kohl, I. E. On the $D^{17}O$ budget of atmospheric O_2. Geochim. Cosmochim. Acta 135, 102–125 (2014).
15. Dole, M., Lane, G. A., Rudd, D. P. & Zaukelies, D. A. Isotopic composition of atmospheric oxygen and nitrogen. Geochim. Cosmochim. Acta 6, 65–78 (1954).
16. Thiemens, M. H., Chakraborty, S. & Dominguez, G. The physical chemistry of mass-independent isotope effects and their observation in nature. Annu. Rev. Phys. Chem. 63, 155–177 (2012).
17. Thiemens, M. H., Jackson, T., Zipf, E. C., Erdman, P. W. & van Egmond, C. Carbon dioxide and oxygen isotope anomalies in the mesosphere and stratosphere. Science 339, 780–785 (1995).
18. Barkan, E. & Luz, B. High precision measurements of $^{17}O/^{16}O$ and $^{18}O/^{16}O$ ratios in H_2O. Rapid Commun. Mass Spectrom. 19, 3737–3742 (2005).
19. Barkan, E. & Luz, B. The relationships among the three stable isotopes of oxygen in air, seawater and marine photosynthesis. Rapid Commun. Mass Spectrom. 25, 2367–2369 (2011).

20. Kaiser, J. & Abe, O. Reply to Nicholson's comment on 'Consistent calculation of aquatic gross production from oxygentriple isotope measurements' by Kaiser (2011). Biogeosci 9, 2921–2933 (2012).

21. Sauvet, C., Gattacceca, J., Rochette, P. & Folco, L. Constraining the terrestrial age of micrometeorites using their record of the Earth's magnetic field polarity. Geol 39, 123–126 (2011).

22. Higgins, J. A. et al. Atmospheric composition 1 million years ago from blue ice in the Allan Hills, Antarctica. Proc. Natl Acad. Sci. USa 112, 6887–6891 (2015).

23. Hönisch, B., Hemming, N. G., Archer, D., Siddall, M. & McManus, J. F. Atmospheric carbon dioxide concentration across the mid-pleistocene transition. Science 324, 1551–1554 (2009).

24. Engrand, C. et al. Isotopic compositions of oxygen, iron, chromium, and nickel in cosmic spherules: toward a better comprehension of atmospheric entry heating effects. Geochim. Cosmochim. Acta 39, 569–584 (2005).

25. Davis, A. M., Clayton, R. N., Mayeda, T. K. & Brownlee, D. E. in Proceedings of the XXII Lunar and Planetary Science Conference, 18–22 (Lunar and Planetary Institute, Houston, TX, 1996).

26. Davis, A. M. & Brownlee, D. E. in Proceedings of the XXIV Lunar and Science Conference (Houston). 373–374 (1993).

27. Herzog, G. F., Hall, G. S. & Brownlee, D. E. Mass fractionation of nickel isotopes in metallic cosmic spheres. Geochim. Cosmochim. Acta 58, 5319–5323 (1994).

28. Herzog, G. F. et al. Isotopic and elemental composition of iron, nickel, and chromium in type I deep-sea spherules: Implications for origin and composition of the parent micrometeoroids. Geochim. Cosmochim. Acta 63, 1443–1457 (1999).

29. Yada, T. et al. Oxygen isotopic and chemical compositions of cosmic spherules collected from the Antarctic ice sheet: implications for their precursor materials. Geochim. Cosmochim. Acta 69, 5789–5804 (2005).

30. Deutsch, A., Greshake, A., Pesonen, L. J. & Pihlaja, P. Unaltered cosmic spherules in a 1.4-Gyr-old sandstone from Finland. Nature 395, 146–148 (1998).

31. Onoue, T., Nakamura, T., Haranosono, T. & Yasuda, C. Composition and accretion rate of fossil micrometeorites recovered in Middle Triassic deep-sea deposits. Geology 39, 567–570 (2011).

32. Voldman, G. G., Genge, M. J., Albanesi, G. L., Barnes, C. R. & Ortega, G. Cosmic spherules from the Ordovician of Argentina. Geol. J. 48, 222–235 (2013).

33. Tomkins, A. G. et al. Ancient micrometeorites suggestive of an oxygen-rich Archaean upper atmosphere. Nature 533, 235–238 (2016).

34. Pack, A. et al. The oxygen isotope composition of San Carlos olivine on VSMOW2-SLAP2 scale. Rapid Commun. Mass Spectrom. 30, 1495–1504 (2016).

35. Williams, H. M. et al. Fe isotope fractionation in iron meteorites: new insights into metal-sulphide segregation and planetary accretion. Earth Planet. Sci. Lett. 250, 486–500 (2006).

36. Hezel, D. C. et al. Meteorite fusion crusts as analogues of chondrules: clues from Fe and O isotopes and bulk elemental composition. Meteor. Planet. Sci. 50, 229–242 (2015).

37. Young, E. D., Galy, A. & Nagahara, H. Kinetic and equilibrium mass-dependent isotope fractionation laws in nature and their geochemical and cosmochemical significance. Geochim. Cosmochim. Acta 66, 1095–1104 (2002).

38. Mlynczak, M. G. et al. Atomic oxygen in the mesosphere and lower thermosphere derived from SABER: algorithm theoretical basis and measurement uncertainty. J. Gephys. Res 118, 5724–5735 (2013).

39. Graham, T. On the molecular mobility of gases. Phil. Trans. Roy. Soc. 153, 385–405 (1863).

40. Wang, J., Davis, A. M., Clayton, R. N. & Mayeda, T. K. Kinetic Isotopic Fractionation During the Evaporation of the Iron Oxide from Liquid State. XXV Lunar and Planetary Science Conference (Houston) abstract #1459 (1994).

41. Dauphas, N. & Rouxel, O. Mass spectrometry and natural variations of iron isotopes. Mass Spectr. Rev. 25, 515–550 (2006).

42. Blunier, T., Barnett, B., Bender, M. L. & Hendricks, M. B. Biological oxygen productivity during the last 60,000 years from triple oxygen isotope measurements. Global Biogeochem. Cy. 16, 1029 (2002).

43. Royer, D. L., Berner, R. & Beerling, D. J. Phanerozoic atmospheric CO_2 change: evaluating geochemical and paleobiological approaches. Earth Sci. Rev. 54, 349–392 (2001).

44. Rochette, P. et al. Micrometeorites from the transantarctic mountains. Proc. Natl Acad. Sci. 85, 1727–1731 (2008).

45. Feng, H. et al. Internal structure of type I deep-sea spherules by X-ray computed microtomography. Meteorit. Planet. Sci 40, 195–206 (2005).

46. Brownlee, D. E. Cosmic dust-Collection and Research. Annu. Rev. Earth Planet. Sci. 13, 147–173 (1985).

47. Pack, A. & Herwartz, D. The triple oxygen isotope composition of the Earth mantle and understanding $D^{17}O$ variations in terrestrial rocks and minerals. Earth Planet. Sci. Lett. 390, 138–145 (2014).

48. Matsuhisa, Y., Goldsmith, J. R. & Clayton, R. N. Mechanisms of hydrothermal crystallization of quartz at 250 °C and 15 kbar. Geochim. Cosmochim. Acta 42, 173–182 (1978).

49. Cao, X. & Liu, Y. Equilibrium mass-dependent fractionation relationships for triple oxygen isotopes. Geochim. Cosmochim. Acta 75, 7435–7445 (2011).

50. Bao, H., Cao, X. & Hayles, J. A. The confines of triple oxygen isotope exponents in elementaland complex mass-dependent processes. Geochim. Cosmochim. Acta 170, 39–50 (2015).

51. Sharp, Z. D. A laser-based microanalytical technique for in situ determination of oxygen isotope ratios of silicates and oxides. Geochim. Cosmochim. Acta 54, 1353–1357 (1990).

52. Valley, J. W. & Graham, C. M. Cryptic grain-scale heterogeneity of oxygen isotope ratios in metamorphic magnetite. Science 259, 1729–1733 (1993).

53. Hezel, D. C. et al. A nebula setting as the origin for bulk chondrule Fe isotope variations in CV chondrites. Earth Planet. Sci. Lett. 296, 423–433 (2010).

54. Pack, A., Toulouse, C. & Przybilla, R. Determination of oxygen triple isotope ratios of silicates without cryogenic separation of NF_3 - technique with application to analyses of technical O_2 gas and meteorite classification. Rapid Commun. Mass Spectrom. 21, 3721–3728 (2007).

Acknowledgements

Author contributions

A.P. conceived and supervised the project. A.H., D.C.H., M.T.S., A.-K.B., S.T.M.P., S.S. and D.H. designed the experiments, prepared the samples and conducted the analyses. L.F. provided the samples. A.P. wrote the manuscript.

Additional information

CURRICULUM VITAE

Personal details

Name:	Sukanya Sengupta
Date of birth:	29th November 1987
Gender:	Female
Relationship status:	Married

Permanent Address:

Hiland Park,

Cape Tower, Appt-18B2,

1925 Chakgaria,

Kolkata-700094 ,

West Bengal, India

Contact Address :

Georg-August-Universität-Göttingen,

Geowissenschaftliches Zentrum, Abteilung

Isotopengeologie,

Goldschmidtstraße 1,

37077 Göttingen,

Lower Saxony, Germany

Phone number: **+4917630648530**

Spouse's name: Mr. Sumit Roy

Father's name: Mr. Abhijit Sengupta

Mother's name: Ms. Sucharita Sengupta

Educational Qualifications

- **M.Sc.** in **Applied Geology** in the year 2011 with **78.6%** marks (first division) from Department of Geological Sciences, Jadavpur University.

- **B. Sc. (Geology Hons.**) in the year of 2009 with **80.6%** marks (first class with distinction) from Department of Geological Sciences, Jadavpur University.

- **Indian School Certificate Examination** (Higher Secondary) in year 2006 with **85.5%** marks (first class) from Calcutta Girls' High School, Kolkata, India. Subjects: English, Bengali, Mathematics, Physics, Chemistry, Biology.

- **Indian Certificate of Secondary Education Examination** (Secondary) in year 2004 with **93.3%** marks (first class) from Calcutta Girls' High School, Kolkata, India. Subjects: English, Bengali, Mathematics, Physics, Chemistry, Biology, Geography, History and Civics, Commercial Sciences.

- Currently pursuing a PhD in University of Göttingen, Germany; completion expected in July 2016.

Additional Qualifications and Awards

- Awarded **UGC-NET Junior Research Fellowship** (JRF) with rank 56 in the Joint CSIR-UGC Test held in December 2010.
- Awarded scholarship for full PhD in Germany by **DAAD**, **The German Academic Exchange Service**, in 2012.
- Awarded 'Best Oral Presentation' at the Deutsche Mineralogische Gessellschaft - Sektionstreffen von Geochemie und Petrologie, 27th – 28th June, 2014 in Hannover, Germany for presenting the abstract entitled "High Precision $\Delta^{17}O$ analysis of cherts – implications for the temperature and $\delta^{18}O$ of ancient oceans".

Field Experience

- Structural geology fieldwork and detailed mapping of mesoscopic structures in and around Jashidih-Deogarh area in the Chotanagpur Gneissic Complex (Duration 15 days, M. Sc 1st yr, 2010).
- Modern sedimentary environment and palaeontological studies in Chandipur tidal flat, Orissa (Duration 19 days, B. Sc 3rd yr, 2009).
- Regional mapping, metamorphic petrology and overall geological studies in and around Jabalpur, Madhya Pradesh (Duration 16 days, B. Sc 2nd yr, 2008).
- Overall geological studies in Maithon in the Chotanagpur Gneissic Complex (Duration 15 days, B. Sc 1st yr, 2007).

Current Research Area : Isotope Geology and Geochemistry

<u>Research experience</u>

- Completed MSc. dissertation work entitled *"Textural Modeling of Garnet-Sapphirine-Spinel-Gedrite bearing rocks from Karur, Tamil Nadu, India"* under the guidance of Prof. Pulak Sengupta and Dr. Sanjoy Sanyal, Department of Geological Sciences, Jadavpur University.

- Started work as a research scholar in Georg-August-Universität-Göttingen, Lower Saxony, Germany since October 2012, in the group of Prof. Andreas Pack. My work revolves around measurement of the rare ^{17}O isotope in terrestrial material. I am working on fluorination and subsequent extraction of oxygen from ancient cherts, carbonates and other rock types such as phosphates in the future, in order to analyse the ^{17}O isotope content in the samples. The 17-O content of such sediments from different ages help us infer paleo-temperature and oxygen isotopic compositions of the ancient oceans. The ultimate aim is to arrive at the temperature and isotopic composition of the Archean ocean.

  In this context, I am now experienced in using mass spectrometers for oxygen and carbon isotope measurements. I use the software "Mathematica" for data analysis.

<u>Laboratory experience</u>

As part of my PhD work I have practically been working in the lab every day, handling mass spectrometers and extraction lines. I have participated in the building of parts of the extraction lines we have and also in the preliminary maintenance of our various devices. I have worked with cherts, diatoms, carbonates (both organic and inorganic), olivine, oceanic crust samples, water, and air for their oxygen isotope analyses. Methods I have used for O_2 and CO_2 extraction (the lines are partially manual and partially computer controlled):

- IR-laser in-situ fluorination of silicates and oxides using F_2 as fluorinating agent. After fluorinating the sample and separating the oxygen from other phases we clean the gas by passing it through a gas-chromatography column at a definite temperature, depending on type and amount of sample.

- Fluorination of cherts, carbonates and CO_2 in conventional Ni-bombs using BrF_5 as fluorinating agent. We also have an IR-laser fluorination option on this line where I use F2 and BrF5 alternatively depending on the type of samples I want to analyse. Cleaning the recovered oxygen gas follows similar steps as above.

<u>Devices used:</u>

- **Thermo Electron MAT 253 gas mass spectrometer** - for high precision ^{18}O and ^{17}O measurements of oxygen gas, mass scans for studying the composition of the gas and detecting impurities, if any. One can measure either in continuous flow mode or in the dual-inlet mode. I have used both modes.

- **Finnigan Delta Plus gas mass spectrometer** - for measuring ^{18}O in oxygen and ^{13}C and ^{18}O in carbon dioxide, mass scans of the gas

- **Pfeiffer Vacuum Prisma Plus mass spectrometer** - I use this mainly for scanning my sample gas for its composition.

- **Liquid Water Stable Isotope Analyzer (LGR DT-100)** for laser spectroscopic analysis of liquid water samples for hydrogen and oxygen isotopes.

- **Kiel IV device** for extraction of CO_2 from carbonates via reaction with phosphoric acid.

- Exposure to working with Electron Microprobe Analysis, Laser Ablation and Scanning Electron Microscope

<u>Conference abstracts</u>

- **Sengupta, S.***, Pack, A., Robert, F., Reitner, J, and Herwartz, D., 2014. High Precision Δ^{17}O analysis of cherts – implications for the temperature and δ^{18}O of ancient oceans. Goldschmidt2014 Abstracts, 2248, Sacramento, California, USA.

- Pack, A.*****, Herwartz, D., and **Sengupta, S.**, 2014. The triple oxygen isotope composition of the Earth and mass dependent variations in Δ^{17}O in mantle and crustal rocks. Goldschmidt2014 Abstracts, 1891, Sacramento, California, USA.

- **Sengupta, S.**, Pack, A.*****, Robert, F., Reitner, J, and Herwartz, D., 2014. Triple oxygen isotope analysis of cherts – implications for the temperature and δ^{18}O of ancient oceans. 92nd Annual Meeting, Deutsche Mineralogische Gessellschaft, Jena, Germany.

- **Sengupta, S.***, Pack, A., Robert, F., Reitner, J, and Herwartz, D., 2014. High Precision Δ^{17}O analysis of cherts – implications for the temperature and δ^{18}O of ancient oceans. Deutsche Mineralogische Gessellschaft - Sektionstreffen von Geochemie und Petrologie, Hannover, Germany.

- **Sengupta, S.***, Pack, A.*****, Robert, F., Reitner, J, and Herwartz, D., 2014. New approach towards determining temperature ^{18}o composition of ancient oceans using high precision $\delta^{17}O$ analysis of cherts. Symposium of the Göttingen Academy of Sciences and Humanities, Dating the Origin of Life: Present-Day Molecules and First Fossil Record, Göttingen, Germany.

- **Sengupta, S.*,** Pack, A., Sharp, Z. and Bach, W., 2015. Geochemical modellig of triple oxygen isotope composition of seawater using high precision $\Delta^{17}O$ analyses of oceanic crust. Submitted to Goldschmidt 2015, Prague, Czech Republic (submitted for oral presentation).

- **Sukanya Sengupta***, Göttingen, 2016. High precision triple oxygen isotope analysis of cherts for determining $\delta^{18}O$ and temperature of Precambrian oceans. General Meeting SPP 1833 "Building a Habitable Earth" Department of Geology and Mineralogy, University of Cologne.

* presenting author of the oral presentation

Publications

Herwartz, D., Pack, A., Krylov, D., Xiao, Y., Muehlenbachs, K., **Sengupta, S.**, and Di Rocco, T. (2015). Revealing the climate of snowball Earth from $\Delta^{17}O$ systematics of hydrothermal rocks. Proceedings of the National Academy of Sciences, doi: 10.1073/pnas.1422887112.

Pack, A., Höweling, A., Hezel, D.C. Stefanak, M., Beck, A., Peters, S., Sengupta, S., Herwartz,D., & Folco, L. (In prep.) The triple oxygen isotope composition of the thermosphere derived from measurements of I-type micrometeorites – a new paleo-CO_2 proxy.

Pack, A., Ryoji, T., Hering, M., **Sengupta, S.**, Peters, S., & Nakamura, E. (in press).The oxygen isotope composition of San Carlos olivine on the VSMOW2-SLAP2 scale. Rapid Communications in Mass Spectrometry, 30, 1–10.

Sharp, Z. D., Gibbons, J. A., Maltsev, O., Atudorei, V., Pack, A., **Sengupta, S.**, Shock, E.L., & Knauth, L. P. (2016). A calibration of the triple oxygen isotope fractionation in the SiO_2–H_2O system and applications to natural samples. Geochimica et Cosmochimica Acta, 186, 105-119.

<u>Student Supervision</u>

I have co-supervised one Master's Dissertation and one Bachelor's Dissertation work so far in Göttingen Unviersity, both in laboratory work and data analysis and interpretation. I also worked with three other Bachelor's thesis students, supervising and helping them in laboratory work in Uni. Göttingen.

<u>Internship Projects and university seminars</u>

- Summer internship on "Down Core Variation of Sediments from Central Indian Ocean Basin" under the guidance of Dr.Pranab Das at **National Institute of Oceanography**, Dona Paula, Goa.
- Summer training at ONGC, India on petroleum system sciences during July 2010.
- Talk on "Mystery of Dancing Rocks, Death Valley National Park, California" during B. Sc 3rd yr in the Department of Geological Sciences, Jadavpur University.
- Talk on "Lateral and Vertical Facies Variation In The Chandipur Tidal Complex".
- Talk on "Structural Control on Topography of Jashidih-Deogarh Area".

<u>Extracurricular Activities</u>
Swimming, reading, playing guitar and singing.

Dated: 07th June 2016